University of Canterbury

Department of Electrical and
Computer Engineering

Hydrogen-related effects in the optical and surface electronic properties of ZnO

A thesis submitted in partial fulfilment
of the requirements for the Degree of

Doctor of Philosophy
in Electrical and Electronic Engineering

at the
University of Canterbury

by

Dipl.-Phys. Robert Heinhold

March 2014

Für mein Väterchen.

Abstract

This thesis concerns new hydrogen- and polarity-related effects in the photoluminescence of ZnO single crystal wafers and the relationship between surface electron accumulation and surface hydroxyl coverage on different ZnO surfaces.

A comparative study of the low temperature photoluminescence of various types of hydrothermal and melt-grown ZnO wafers revealed several new hydrogen-related exciton recombination lines and a number of consistent polarity-related differences in the PL emission from different crystallographic surfaces. Temperature-dependent PL measurements were extensively used to distinguish the ground and excited state transitions involved in these effects.

ZnO samples of different surface polarity were annealed in oxygen and nitrogen gases and in hydrogen-containing forming gas mixtures in an attempt to identify the origin of these new PL features. The well known aluminium-related I_6 recombination line was resolved into two separate features in hydrothermal ZnO, and the new component $I_{6-\mathrm{H}}$ (3.36081 eV) was found to repeatedly quench and then re-emerge after annealing in oxygen and forming gas, respectively. A model involving an aluminium - lithium - hydrogen defect complex was proposed for $I_{6-\mathrm{H}}$ and further tested via hydrogen and deuterium implantation experiments on hydrothermal ZnO wafers with different lithium concentrations. These experiments also provided evidence for the involvement of a different lithium-hydrogen defect complex in other hydrogen-related emission lines $I_{4\mathrm{b,c}}$ (3.36219 eV and 3.36237 eV) unique to hydrothermal ZnO. In addition, a broad Gaussian-shaped feature observed in the near-band-edge PL emission from the O-polar $(000\bar{1})$, a-plane $(11\bar{2}0)$ and r-plane $(1\bar{1}02)$ faces of ZnO was shown to be surface sensitive and also related to hydrogen.

The involvement of hydrogen in the chemical and electronic properties of different ZnO surfaces was also investigated. The thermal stability of the hydroxyl termination and the associated downward surface band bending on the polar and non-polar surfaces of ZnO was studied by synchrotron and real-time photoelectron spectroscopy, both during and after annealing and subsequent H_2O/H_2 dosing in ultra-high vacuum conditions. On the O-polar face, the band bending could be reversibly switched over a range of approximately 0.8 eV by adjusting the surface H-coverage using simple UHV heat treatments and atmospheric exposure. A transition from electron accumulation to electron depletion on the O-polar face was observed at a H-coverage of approximately 0.9 monolayers. In contrast, the downward band bending on the Zn-polar face was significantly more resilient and electron-depleted surfaces could not be prepared by heat treatment alone. This was also the case for *in situ* cleaving in UHV conditions which

failed to produce hydroxyl-free surfaces due to migration of hydrogen from the bulk to the cleaved surface. Interestingly, the thermal stability of the hydroxyl termination on the a-plane $(11\bar{2}0)$ and m-plane $(10\bar{1}0)$ surfaces was significantly lower than on the polar faces due to the availability of a lower energy desorption pathway and the electrostatic stability of these non-polar surfaces in their clean, bulk terminated form. The surface band bending on the non-polar ZnO surfaces was also found to be directly related to their OH coverage with a transition from downward to upward band bending, similar to that observed on the O-polar face, as the OH coverage was reduced.

Thermal admittance spectroscopy and deep level transient spectroscopy was used to investigate the effect of lithium removal on the defect nature of hydrothermal ZnO. A number of new defects were introduced by the high temperature (1100–1400 °C) annealing/re-polishing process used to reduce the lithium concentration, particularly E_{190} (also known as T2) which is thought to be related to Zn vacancies. Significantly, both the E_{50} defect level and the I_{6-H} PL emission line were absent after lithium (and hydrogen) removal suggesting an association of both these features with the same aluminium - lithium - hydrogen defect complex.

Acknowledgement

Some men are born posthumously.

Friedrich Nietzsche

First and foremost, I would like to thank my supervisor Dr. Martin Allen for his guidance, support, and advice. The research opportunities he offered me at the University of Canterbury and abroad have been truly outstanding. The time, thought, and encouragement he invested in me helped greatly to shape this work. Without his good old fashioned banter, several years of PhD studies (especially in the aftermath of the February 2011 earthquakes) would not have been so *lovely jubbly*.

I want to thank my Co-supervisor Prof. Roger Reeves as well for sharing his great knowledge about optical spectroscopy and for the time he sacrificed to teach me the ropes. He gave me the certitude that with a $50\,\Omega$ resistor and an oscilloscope anything is possible.

Thanks also go to Prof. Steve Durbin for giving me the opportunity to come to New Zealand in order to undertake my doctoral research within the Department of Electrical and Computer Engineering.

I would like thank to Dr. Scott Choi, Dr. Konstantin Ivanovskikh, and Alex Neimann, who helped me in keeping up with all the laboratory equipment and repairs. Alex may be one of the few who truly understands the agonising futility of realigning the laser optics after every single aftershock.

On the Nanofabrication Laboratory end of things, thanks go to Dr. Jim Partridge, Helen Devereux, and Gary Turner for their support and assistance.

For the excellent user support at the Australian Synchrotron and the Carbon $1s$ peak on my samples, I would like to thank Dr. Anton Tadich, Dr. Lars Thomson, and Dr. Bruce Cowie. Profound thanks are similarly necessary to Dr. Simon Cooil and Prof. Andrew Evans at the University of Aberystwyth and Dr. Colin Doyle from the University of Auckland for their great cooperation and for sharing their extensive experience in all XPS matters.

A very special thanks goes to Prof. Marius Grundmann and Dr. Holger von Wenckstern for allowing me to continue my research at the University of Leipzig following the February 2011 earthquake.

Thanks to Dr. Andreas Markwitz, Dr. Peter Murmu, and Dr. John Kennedy at GNS Science for help with the ion implantation process.

On a personal note, I would like to thank my officemates, good friends, and *triumviri* Salim Elzwawi and Thomas Cronje for the daily discussions about nearly anything and the litres of espresso we enjoyed together. Special thanks also to Dr. Lynn Murray for keeping up with me and all the things that may have been lost in translation. I have to thank Alana Hyland for her patience in explaining youth culture to me and Dr. Volker Nock who, despite his repeated attempts to kill me in some odd backcountry tramp, made my life in NZ way more enjoyable. Thanks to both Janelle Irvine and Kasia Madrzejewska for being amazing friends. And thanks to all the great flatmates of all nationalities with whom I have lived in seven different flats and houses in Christchurch.

Lastly, I am deeply indebted to my mother for constant encouragement, support, and love.

Tēnā koutou Aotearoa

List of international collaborators

Gruffudd T. Williams, Simon P. Cooil, and Andrew D. Evans,
Department of Mathematics and Physics, Aberystwyth University, Aberystwyth SY23 3BZ, United Kingdom.

Holger von Wenckstern, Florian Schmidt, Stefan Müller, and Marius Grundmann,
Institut für Experimentelle Physik II, Universität Leipzig, Linnéstraße 5, 04103 Leipzig, Germany.

Christian M. Schlepütz, and Roy Clarke,
Department of Physics, University of Michigan, Ann Arbor, MI 48109, USA

Steve M. Durbin,
Department of Electrical Engineering and Department of Physics, University at Buffalo, Buffalo, NY 14260, USA

Contents

List of Figures

List of Tables

Publication List

Publications in Peer Reviewed Journals:

[1] R. Heinhold, H.-S. Kim, F. Schmidt, H. v. Wenckstern, M. Grundmann, R. J. Mendelsberg, R. J. Reeves, S. M. Durbin, M. W. Allen. *Optical and defect properties of hydrothermal ZnO with low lithium contamination*. Appl. Phys. Lett. **101**, 062105 (2012). DOI: 10.1063/1.4739515.

[2] R. Heinhold, M. W. Allen. *Polarity-dependent photoemission of in situ cleaved zinc oxide single crystals*. J. Mater. Res. **27**, 2214 (2012). DOI: 10.1557/jmr.2012.181.

[3] C. M. Schlepütz, Y. Yang, N. S. Husseini, R. Heinhold, H.-S. Kim, M. W. Allen, S. M. Durbin, R. Clarke. *The presence of a (1x1) oxygen overlayer on ZnO(0001) surfaces and at Schottky interfaces*. J. Phys.: Condens. Matter **24**, 095007 (2012). DOI: 10.1088/0953-8984/24/9/095007.

[4] S. Elzwawi, H. S. Kim, R. Heinhold, M. Lynam, G. Turner, J. G. Partridge, D. G. McCulloch, R. J. Reeves, M. W. Allen. *Device quality ZnO grown using a Filtered Cathodic Vacuum Arc*. Physica B: Cond. Mat. **407**, 2903 (2012). DOI: 10.1016/j.physb.2011.08.074.

[5] R. Heinhold, G. T. Williams, S. P. Cooil, D. A. Evans, M. W. Allen. *Influence of polarity and hydroxyl termination on the band bending at ZnO surfaces*. Phys. Rev. B **88**, 235315 (2013). DOI: 10.1103/PhysRevB.88.235315.

[6] F. Schmidt, S. Müller, H. Wenckstern, C. P. Dietrich, R. Heinhold, H.-S. Kim, M. W. Allen, M. Grundmann. *Comparative study of deep defects in ZnO microwires, thin films and bulk single crystals*. Appl. Phys. Lett. **103**, 062102 (2013). DOI: 10.1063/1.4817824.

[7] M. W. Allen, R. Heinhold, P. Miller, M. J. H. Henseler, R. J. Mendelsberg, S. M. Durbin, R. J. Reeves. *Polarity effects in the optical properties of hydrothermal ZnO*. Appl. Phys. Lett. **103**, 231109 (2013). DOI: 10.1063/1.4837219.

Conference Contributions

[1] R. Heinhold, F. Schmidt, H. v. Wenckstern, M. Grundmann, J. Chai, T. H. Myers, R. J. Mendelsberg, S. M. Durbin, H. S. Kim, R. J. Reeves, M. W. Allen. *Electrical and Optical Characterization of ZnO Hydrothermal Single Crystals with Low Lithium Concentration.* Material Research Society (MRS) Fall Meeting (2011), Poster.

[2] R. Heinhold, T. Veal, C. McConville, D. Zemlyanov, G. Waterhouse, J. Metson, S. Durbin, M. Allen. *Polarity Effects in X-Ray Photoemission of Wurtzite Semiconductors: ZnO as a Case Study.* Material Research Society (MRS) Fall Meeting (2011), Poster.

[3] R. Heinhold, S. Cooil, A. D. Evans, S. M. Durbin, M. W. Allen. *Surface band bending on ZnO under in-situ annealing and H_2O/H_2 dosing using XPS.* Australian Synchrotron User Meeting (2012), Talk.

[4] R. Heinhold, R. J. Reeves, S. M. Durbin, M. W. Allen. *Photoluminescence Studies on as-received, annealed and metal-covered ZnO single Crystals.* The Sixth International Conference on Advanced Materials and Nanotechnology (AMN-6) (2013), Talk.

1 Introduction

The earliest reported application of ZnO dates back over 2000 years. Initially a by-product of early brass production, it was largely used as a medicine for various skin conditions or as a paint before its re-discovery in the early 20$^{\text{th}}$ century. Today ZnO serves as an ingredient in sun lotions due to its ability to absorb UVA and UVB radiation, as a food additive and vital source of zinc [1], in the production of rubber [2], and a wide range of electronic applications. It is radiation hard [3, 4] and, therefore, suitable for space applications; similarly, it has a high bio-compatibility and low toxicity [5, 6], so it can be used as a material for implantable biosensors. Naturally, the applications of ZnO are determined by its underlying physical and chemical properties. ZnO is a wide bandgap semiconductor with an energy gap of 3.36 eV at room temperature. This makes it transparent in the visible region, but a strong absorber of UV radiation. Therefore, it is an ideal candidate for applications such as solar blind UV photo-detectors or as the transparent conducting front contact in solar cells.

ZnO is also a promising candidate for optoelectronic devices in the UV spectrum, such as UV light emitting diodes or laser diodes, due to its high exciton binding energy of 60 meV, which allows the possibility of room-temperature lasing. The UV responsivity of ZnO can be engineered by alloying with MgO or CdO to increase or decrease the bandgap respectively and also enabling the fabrication of heterostructures and, in particular, quantum wells [7]. Initially, ZnO was considered as a high quality substrate for GaN, due to its closely matched lattice constants and the lack of a high quality GaN single crystal growth process. In contrast, a number of bulk growth processes such as hydrothermal growth, pressurised-melt growth or chemical vapour transport growth are readily available for producing high quality ZnO single crystals [8, 9]. These bulk growth processes differ significantly in growth rate, growth temperature, and incorporated impurity concentrations. With the recent progress in ZnO bulk growth and thin film deposition, ZnO has become a promising candidate for the next generation of transparent optoelectonic devices in its own right.

However, the main obstacle for a wider integration of ZnO-based electronics is the

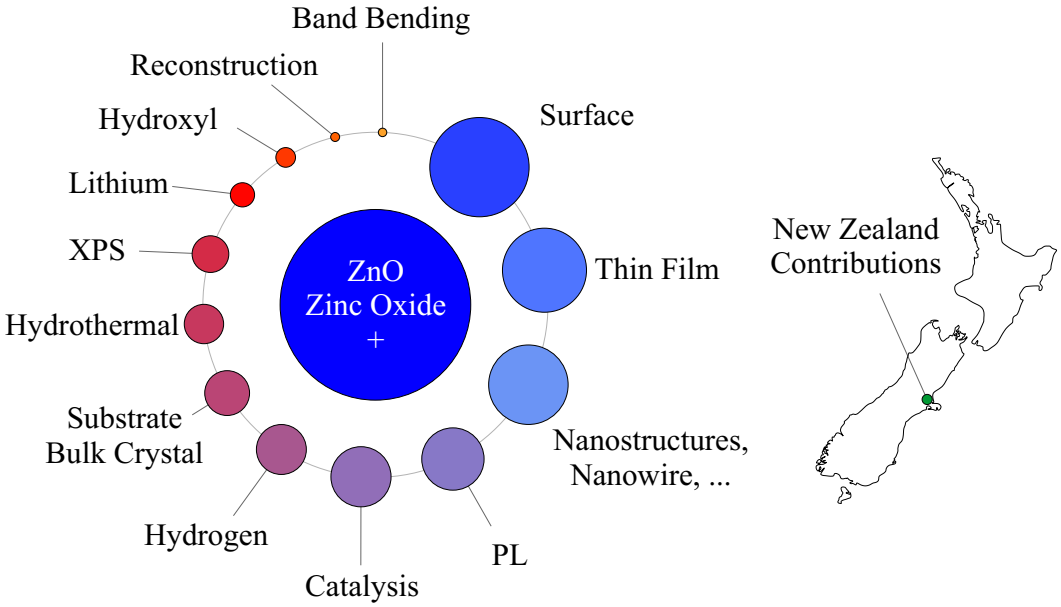

Figure 1.1.: Total number of publications listed by *Scopus* as of January 2014 containing the keywords "ZnO" and "zinc oxide" plus keywords regarding this work represented by area. The keywords "ZnO" and "zinc oxide" yield approximately 77.300 publications compared to 219 with an affiliation from New Zealand. For PL and XPS the unabbreviated names were used.

reliable fabrication of p-type ZnO, as almost all ZnO material exhibits intrinsic, unintentional n-type conductivity [10]. Zinc interstitials and oxygen vacancies are thought to be the source of the prevailing n-type conductivity. More recent findings show that these defects have either a high formation energy or act as deep donors, making them unlikely to contribute significantly to the observed conductivity [11]. Today, the focus has shifted to unintentionally incorporated defects, such as hydrogen. While interstitial hydrogen is an amphoteric defect in most semiconductors [12], it exclusively shows shallow donor characteristics in ZnO [13]. Hydrogen can also take the place of lattice oxygen (i.e. occupy an oxygen vacancy via the formation of multicentred bonds [14]) acting as a shallow donor with a higher temperature stability than interstitial hydrogen. In addition, other shallow donors such as Al, Ga or In are thought to contribute to the unintentional n-type behaviour [15]. On the other hand, acceptor doping is limited by the preferential formation of deep acceptors and/or self-compensation by native donor defects [16].

Considerable effort has been made to identify the bound exciton transitions observed in photoluminescence spectroscopy by introducing shallow donors and acceptors into ZnO by means of diffusion, ion implantation or different growth processes [17–19]. However, only a handful of exciton recombinations in ZnO PL have been identified in the last five decades. A similar situation exists in the case of the capacitance-based defect

spectroscopy of ZnO (i.e. thermal admittance and deep level transient spectroscopy) for which many defect features have been observed but few conclusively identified [20, 21].

Similar to other metal oxides, e.g. In_2O_3, CdO, or SnO_2, ZnO exhibits an electron accumulation layer at its surface which significantly influences device performance and, especially, ohmic and Schottky contact formation [22]. The accumulation layer is a direct result of the downward bending of the near-surface conduction and valence bands in response to donor-like surface states [23]. These surface states can be introduced, for example, by the hydrogenation of the ZnO surface as was shown as early as 1969 [24]. The change in the surface conductivity of ZnO by adsorption of anionic or cationic species allows for the fabrication of efficient gas sensing devices. This effect is even more dramatic in nanostructures as the surface-to-bulk ratio is significantly increased [25]. Chemical reactions on the different surfaces of ZnO are also an area of ongoing research interest, as their interaction with Cu particles forms the basis of today's industrial methanol synthesis [26].

The research conducted in this work impacts a wide range of topics linked to the material system of ZnO. Figure 1.1 shows the total number of publications concerning ZnO as circles of relative area size. Publications which contain the keywords "ZnO" and "zinc oxide", and other keywords relevant to this thesis in their title or abstract are also shown in Fig. 1.1. In comparison, ZnO-related publications with an affiliation to New Zealand are shown on the right. Publications concerning thin films or nanostructures form a large percentage of the total publications on ZnO, as they are associated with an abundance of potential device applications. However, publications on topics such as band bending or surface reconstruction are less frequently found as the underlying physical mechanisms are not yet completely understood.

The work presented here aims to establish a greater understanding of the excitonic photoluminescence emission of ZnO bulk single crystals of different growth methods and post-growth treatments. The focus lies especially on the role of hydrogen and lithium, as both are believed to play an important role in determining the conductivity of ZnO, particularly in the case of hydrothermally grown material. Secondly, the surface band bending and the interplay between competing stabilisation mechanisms on the polar and non-polar surfaces of ZnO are also investigated using x-ray photoelectron spectroscopy following different surface treatments.

To guide the interested reader through the main experimental findings and conclusions, chapter 2 will summarise the key properties of ZnO relevant to this thesis. A comprehensive introduction to the experimental methods and techniques employed,

is given in chapter 3. Chapter 4 presents the characterisation of electrically active defects in hydrothermally grown ZnO with low lithium concentrations (Low-Li HT ZnO). These measurements were carried out using thermal admittance spectroscopy (TAS) and deep level transient spectroscopy (DLTS). A wide range of trap energies were probed due to the high sensitivity of TAS to shallow levels and DLTS to deep levels. Low-Li HT ZnO, along with conventional hydrothermally grown ZnO (containing high concentrations of Li) and melt-grown ZnO (containing only trace amounts of Li) will then form the subject of a detailed study using high-resolution photoluminescence spectroscopy on bulk single crystals before and after annealing in different ambients (such as oxygen, nitrogen, and forming gas) in chapters 5 and 6 respectively. The impact of hydrogen on the photoluminescence of ZnO is investigated via hydrogen and deuterium implantation experiments in chapter 7. Chapter 8 is devoted to the effects of metal ion implantation and the deposition of thin metal and metal oxide overlayers on excitonic PL emission. The interplay between hydrogen and the surface hydroxyl coverage on different crystallographic faces of ZnO, and the associated surface band bending is investigated using synchrotron x-ray photoelectron spectroscopy (XPS) in chapter 9, which allows for the use of varying photon energies to adjust surface sensitivity. These measurements are complemented by real-time laboratory-source XPS measurements, which have the advantage of monitoring the evolution of the surface band bending directly during annealing.

2 | Properties of ZnO

This chapter gives a concise overview of selected properties of ZnO relevant to this thesis. In particular, the structure and electrostatic stabilisation of ZnO surfaces, the hydrothermal growth of ZnO bulk crystals, the role of hydrogen in ZnO and the optical properties of ZnO will be discussed.

2.1 ZnO and its surfaces

The II – VI compound semiconductor ZnO crystallises in the wurtzite structure. This is a direct result of the tetrahedrally coordinated sp^3 bonding hybridisation, with the bonding sp^3 states forming the valence band and the anti-bonding sp^3 states forming the conduction band [27]. Although the bonding can be considered as covalent, the large difference in electronegativity between oxygen and zinc atoms causes a significant bond polarity with an ionicity of 0.616 on the Phillips scale [28], which is close to the borderline between ionic and covalent bonding. The bond polarity also explains the preferential wurzite crystallisation for ZnO rather than the alternative zincblende structure [27]. The ZnO crystal is made up of alternating layers of Zn and O atoms along the c-axis direction with different interplane distances of $R_1 \approx 0.6\,\text{Å}$ and $R_2 \approx 2\,\text{Å}$ [29], as shown in Fig. 2.1. In an ionic model, each layer consists of only anions or cations (O^{2-} or Zn^{2+}) resulting in a non-zero dipole moment between the layers in the c-direction. Stacking of these dipoles leads to a monotonic increase in the electrostatic potential across the crystal, which diverges as the number of layers approaches infinity. Such "unstable" surfaces are called Tasker-type-3 surfaces, named after P. W. Tasker [30] who first discussed the stability of ionic crystals in 1979. It follows that the ZnO(0001) or Zn-polar surface and the ZnO($000\bar{1}$) or O-polar surface are theoretically unstable in this ionic picture compared to alternative surfaces for which no dipole moment is present (known as Tasker-type-1 surfaces) such as the m-plane face (ZnO($10\bar{1}0$)) and the a-plane face (ZnO($11\bar{2}0$)), which are terminated by equal numbers of Zn and O atoms.

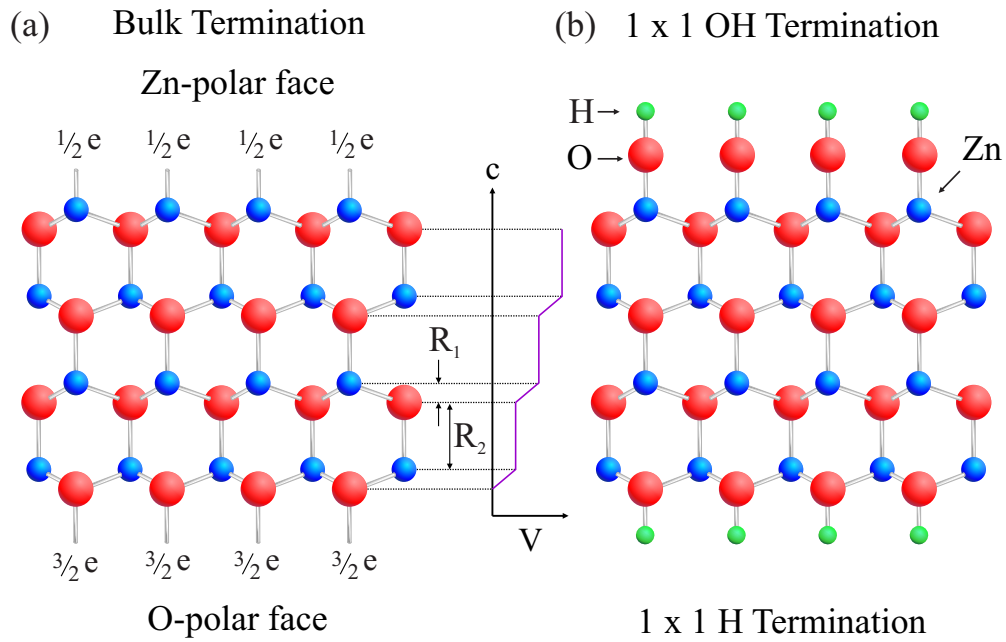

Figure 2.1.: ZnO wurzite lattice structure in the bulk (a) with number of valence electrons according to the electron counting rule. The side graph shows the divergent electric potential (V) of Zn-O doublelayers categorised as Tasker-type-3. (b) Hydroxyl and hydrogen surface termination on the ZnO(0001) polar and ZnO(000$\bar{1}$) polar face.

To compensate for the diverging electrostatic energy at the surface, three main stabilisation mechanisms have been proposed: (i) a fractional charge transfer from the O-polar to the Zn-polar surface [31], (ii) surface reconstruction and the removal of surface atoms [32, 33], and (iii) the adsorption of polar adsorbates, in particular hydroxyl groups on the Zn-polar face and hydrogen on the O-polar face [34]. Regarding mechanism (i), Meyer and Marx [35] showed via DFT modelling that although charge transfer partially compensates the internal electric field, it cannot completely neutralise it, irrespective of the size of the sampling slab in the calculation. Therefore, a second process such as mechanisms (ii) and (iii), must be involved. The predicted surface reconstructions strongly depend on the crystal face. Calculations suggest a triangular reconstruction of the Zn-polar face is favoured in the absence of terminating hydroxyl groups [34]. This is consistent with experimental findings of Dulub *et al.* [32] who observed triangular islands and pits for sputter-cleaned ZnO bulk crystals annealed in ultra-high vacuum (UHV). The removal of Zn atoms in pits, formed by single-layer step edges, and the subsequent O-termination of these edges was observed for a wide range of hydrogen and oxygen chemical potentials [36]. In the case of the O-polar face, several studies (such as Ref. [37]) have determined that the unreconstructed ZnO(000$\bar{1}$) face must be terminated by hydrogen and that a clean, unreconstructed surface is unlikely to be achieved under most experimental conditions. An adsorbed hydrogen adlayer with

a 0.5 ML coverage was proposed for hydrogen-rich conditions [34, 38]. In the absence of hydrogen, the removal of 1/4 of the surface oxygen atoms has also been predicted to stabilise the ZnO(000$\bar{1}$) face [39]. Early results suggested a (1×3) oxygen vacancy structure for the hydroxyl-free ZnO(000$\bar{1}$) surface [40, 41]. However, more recently Lauritsen *et al.* [42, 43] have experimentally observed (2×2) and (5×5) honeycomb-like structures on the ZnO(000$\bar{1}$) face under elevated measurement temperatures (450 °C) and subsequent hydrogen desorption.

As each hydrogen atom donates 0.5 e^- to the surface, hydrogen adsorption onto ZnO surfaces introduces shallow donor states in the near-surface region [44]. The increase in surface carrier concentration resulting from hydrogen adsorption was reported as early as 1969 by Heiland *et al.* [24, 45]. These authors observed downward surface band bending and electron accumulation after hydrogen exposure and upward band bending and electron depletion after oxygen exposure. Strong downward band bending, combined with an energetically high bulk Fermi level position, can lead to the quantisation of electron states in a quasi-2D potential well at the surface [46]. Interestingly, the formation of such a quantised two dimensional surface electron gas has, so far, only be observed on the ZnO(000$\bar{1}$) polar face [44]. Similar surface downward band bending and electron accumulation layers have also been reported for other metal oxides, such as In_2O_3 [47] and CdO [48].

In addition, to the electrostatic stabilisation issues discussed above, the high ionicity of the Zn-O bond also produces strong spontaneous polarisation effects in ZnO, that are explained by the following model: The lattice parameters for the hexagonal unit cell of wurtzite ZnO are $c = 5.2069$ Å and $a = 3.2496$ Å [49], leading to a c/a ratio of 1.6024, which is smaller than the ratio of 1.6333 for the ideal hexagonal close-packed (hcp) structure. This indicates a displacement of the atoms in the unit cell as each tetrahedron (ZnO_4) is distorted from the ideal T_d symmetry [50] as shown in Fig. 2.2(a). Combined with the heteropolar bonding nature of the Zn-O bond, this distortion creates a permanent net-dipole moment along the crystal c-axis [51]. These dipole moments cancel in the bulk but produce equal and opposite bound polarisation charges at the ZnO(0001) and ZnO(000$\bar{1}$) polar surfaces. The spontaneous polarity of ZnO at zero-strain is $\sigma_{SP} = -0.057\,C\,m^{-2}$, significantly larger compared to most binary semiconductors, including GaN with $\sigma_{SP} = -0.029\,C\,m^{-2}$ [52]. The net-dipole moment is equivalent to a bound negative sheet carrier concentration on the Zn-polar face and a positive sheet carrier concentration on the O-polar face. In order to screen these polarisation charges, a re-arrangement of free carriers will occur in the near-surface region. Electrons will tend to move towards the O-polar surface and form an accumulation layer, whereas a depletion region is formed on the Zn-polar surface resulting in

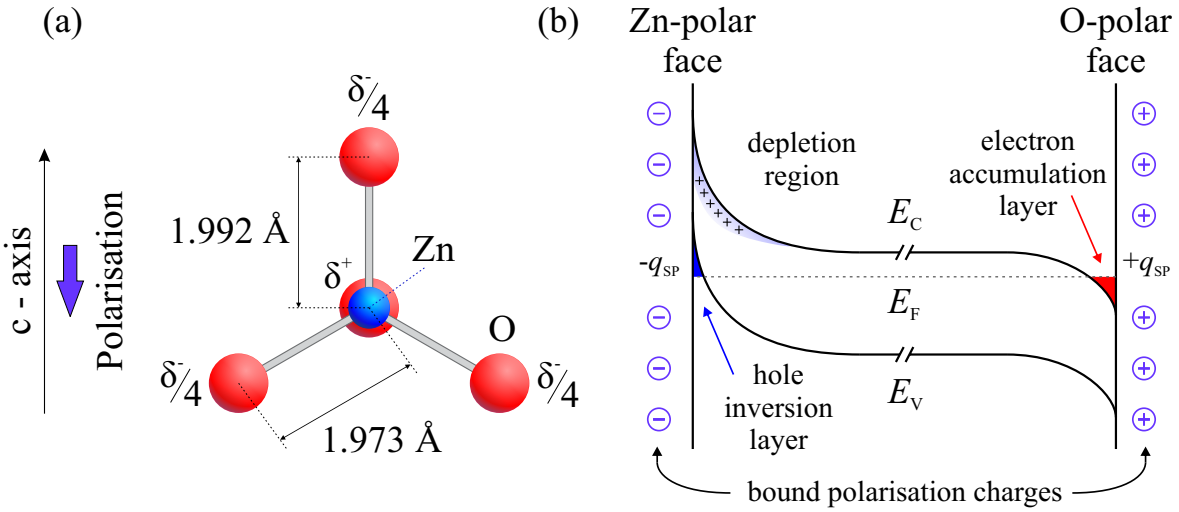

Figure 2.2.: (a) Distortion of the ZnO_4 tetrahedron and (b) surface band bending as a result of the induced polarisation charges.

upward band bending. The amount of screening and therefore the extent of the surface band bending will depend on the free carrier concentration. For example, if the free carrier concentration is low, the concentration of positively charged ionised donors in the depletion region near the Zn-polar face will be insufficient to screen the negative spontaneous polarisation charges. If the resulting upward band bending is sufficiently strong, the Fermi level can move into the valence band at the surface and an inversion layer of holes may be formed (see Fig. 2.2(b)). In contrast to the ionic model, this spontaneous model is independent of the effects of surface adsorbates, i.e. hydrogen and hydroxyl groups and with these, the introduction of donor states to the surface. As such, spontaneous polarisation effects are only likely to be independently observed on clean "hydroxyl-free" Zn-polar and O-polar surfaces.

To what extent these two models can explain the observed surface stabilisation and surface band bending effects in ZnO, will be investigated in Chapter 9.

2.2 Optical properties of ZnO

The wide bandgap of ZnO (3.36 eV at room temperature) makes it transparent in the visible spectrum. By alloying ZnO with MgO or CdO, the bandgap can be increased or decreased, respectively. As a direct-gap semiconductor, all emission and absorption processes are highly efficient as the participation of phonons is not necessary. This explains the sustained interest in ZnO for optoelectronic devices, such as light emitting devices (LED) operating in the UV spectral range. These optical properties are directly related to the band structure of ZnO, which will be discussed next.

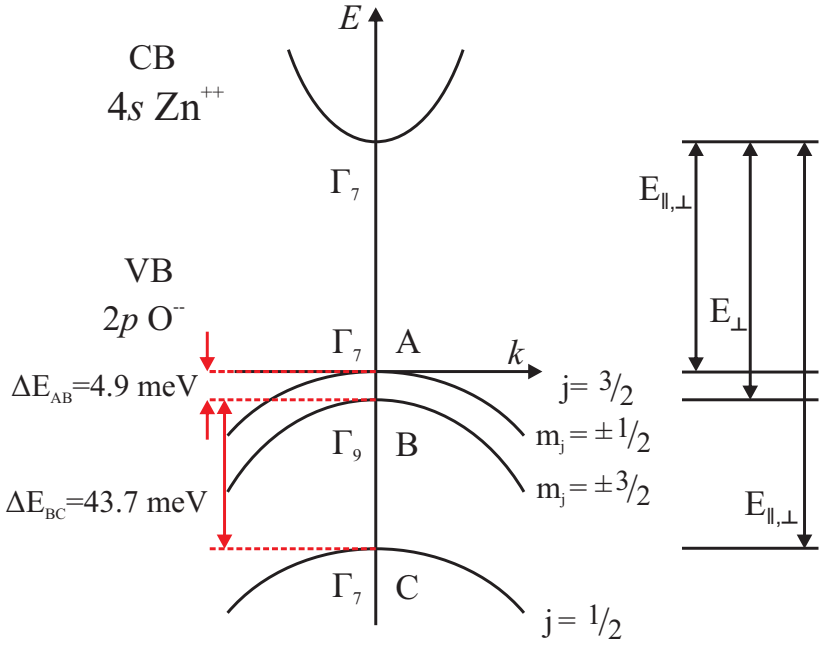

Figure 2.3.: Band structure and symmetries for ZnO. The valence bands are shown in the Γ_7 symmetry, which results in a negative spin-orbit splitting and a $j = 3/2, m_j = \pm 1/2$ top band. Also shown are the allowed transitions for an electric field vector E parallel and perpendicular to the crystal c-axis [27].

The conduction band (CB) of ZnO is formed by the empty $4s$ levels of Zn^{2+} in the ionic bonding scheme or by the lowest antibonding sp^3 hybridisation in the covalent scheme. The valence band is made from the occupied $2p$ O^{2-} states or alternatively the highest bonding sp^3 hybrid states. The spin-orbit coupling (Δ_{so}) splits the sixfold degenerate atomic p-levels of the highest valence band into a fourfold degenerated $j = 3/2$ state and a twofold degenerated $j = 1/2$ state [53]. Due to the anisotropy between the c- and a-axis in wurtzite ZnO (C_{6v} symmetry), the crystal-field splitting (Δ_{cf}), in addition to the spin-orbit splitting, results in three twofold degenerated valence bands: A, B, and C. The $j = 3/2$ state splits into heavy holes (A-valence band) with $m_j = \pm 3/2$ and light holes (B-valence band) with $m_j = \pm 1/2$ (see Fig. 2.3). These names originate from the different dispersion relations and, therefore, different effective masses. Lambrecht *et al.* [54] calculated a $\Delta_{so} = -9\,\text{meV}$ and $\Delta_{cf} = 40\,\text{meV}$.

Electrons in the conduction band and holes in the three valence bands can interact with each other due to the attractive Coulomb interaction and can form correlated pairs, known as excitons. Excitons in ZnO show a high binding energy of $\sim 60\,\text{meV}$, which makes ZnO an attractive choice for room-temperature excitonic lasing. The symmetry ordering of the three valence bands (A-B-C) has been extensively discussed over the last 50 years and is still controversial, with a disputed $\Gamma_7 - \Gamma_9 - \Gamma_7$ [55, 56] or $\Gamma_9 - \Gamma_7 - \Gamma_7$ [57, 58] ordering. In recent years, the $\Gamma_7 - \Gamma_9 - \Gamma_7$ ordering has been

accepted by a majority of authors, as it can be directly explained by the interaction of the Zn-3d bands with the closely lying valence band p-states [54]. This interaction results in a $\Delta_{so} < 0$ and, hence, a reversed ordering of $\Gamma_7 - \Gamma_9 - \Gamma_7$ ($j = 1/2$ state is energetically higher then $j = 3/2$). However, this controversy is far from settled, with recent experimental findings supporting the $\Gamma_9 - \Gamma_7 - \Gamma_7$ symmetry [59] in strain-free bulk ZnO crystals. A possible solution to this controversy would be the investigation of cubic ZnO in which Δ_{cf} must be zero. The different bands could then be easily distinguished by uniaxial stress measurements. This method has been quite successful with other semiconductors such as ZnSe and ZnTe. Unfortunately, it is currently not possible to grow cubic ZnO with the necessary crystalline quality.

The band structure explains the experimentally observed exciton recombination in photoluminescence spectroscopy as holes from the three valence bands can only participate in the light emission process for certain propagation directions with respect to the polarisation (E) of the electric field of the incoming photon and the crystal c-axis. The experimental background for photoluminescence spectroscopy will be addressed in Sec. 3.2.

2.3 Hydrothermal growth of ZnO

Since the days of A.-L. Lavoisier, who described impure ZnO as *Pompholix* or *flowers of zinc* in his seminal work *Traité Élementaire de Chimie* (1789), the growth processes and impurities incorporated in ZnO have changed tremendously. The highest crystal quality ZnO material available today, is grown via the hydrothermal technique as the growth process takes place near thermodynamic equilibrium and is well established for the mass production of quartz and GaN. In general, hydrothermal growth of ZnO is carried out in an autoclave filled with supercritical water as a solvent in a temperature range between 300 – 450 °C and 70 – 250 MPa (see Fig. 2.4(a)). Supercritical water forms under increased temperature ($T_{\mathrm{c}} = 374\,^{\circ}\mathrm{C}$) and pressure ($p_{\mathrm{c}} = 22.1\,\mathrm{MPa}$) and is characterised by an increased diffusivity and enhanced acidity that favours the dissociation of ionic compounds such as ZnO [9]. Because the solubility of ZnO is still quite limited, mineralisers such as LiOH, NaOH, and KOH as well as Li_2CO_3 and H_2O_2 are also used to increase solubility.

Changing the temperature of the solution directly changes the solubility of the solute, in this case the metastable complex of Zn^{2+} and O^{2-}. Therefore, by applying a temperature gradient between the seed crystal, in the centre of the autoclave, and the autoclave Pt lining, the solution is exclusively super-saturated at the seed crystal and growth will commence only from this point. Temperature control of $\Delta T \pm 3\,\mathrm{K}$ is

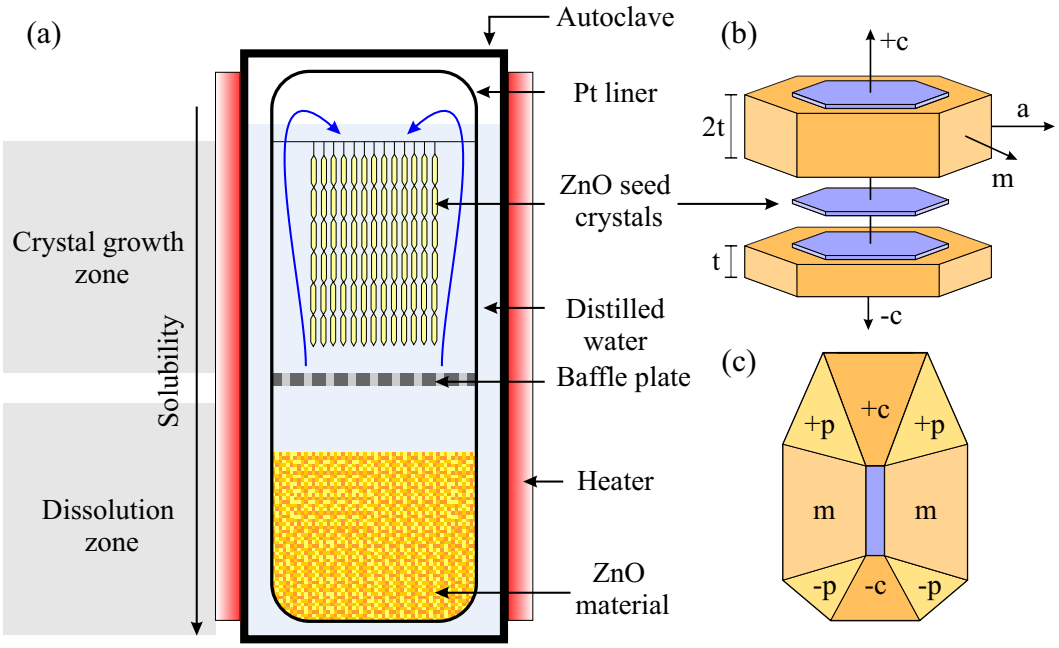

Figure 2.4.: (a) Autoclave schematic for the hydrothermal growth of ZnO bulk single crystals. ZnO crystal growth on a c-plane (b) and m-plane (c) seed.

necessary to avoid spontaneous nucleation and crystal cracking. The basic chemical reactions between the seed crystal and the metastable ZnO_2^{2-} solution are as follows [8]:

$$Zn^{+}_{Surface} + ZnO_2^{2-} \rightarrow 2\,ZnO_{Crystal} \qquad \text{on ZnO}(0001),$$

$$O^{2-}_{Surface} + ZnO_2^{2-} + 2\,H_2O \rightarrow 4\,OH^{-} + ZnO_{Crystal} \qquad \text{on ZnO}(000\bar{1}).$$

These equations also explain why the growth rate is 2 – 3 times faster in the (+c) than in the (−c) direction (see Fig. 2.4(b)) [60]. Mineralisers, especially Li, decrease the positive surface charge and, therefore, lower the incorporation of negatively charged species, limiting the growth speed to approximately 0.2 mm / day [9]. The growth rate not only depends on the face of the seed crystal, but also on the exact molar ratio of the mineralisers. The growth rate of hydrothermal ZnO is rather slow compared to the 1 mm / h rate for pressurised-melt growth and 70 µm / h for seeded chemical vapour transport (SCVT). Recently, an improved hydrothermal growth process has been proposed [61], utilising only minor amounts of mineralisers and thereby doubling the growth rate and further improving crystalline quality. This material also showed no Li, Na, or K contamination within the detection limit of the SIMS setup used.

In terms of crystalline quality, hydrothermal ZnO (HT ZnO) material shows the lowest full width at half maximum (FWHM) for the (0002) x-ray diffraction rocking

curve at approximately 18 arcsec [62], compared to 30 arcsec for melt-grown material from Cermet Inc. [63]. The FWHM increases up to 30 arcsec after chemical-mechanical polishing of the HT ZnO material. Earlier studies found that the FWHM for polished ZnO(0001) faces is slightly larger, 43 arcsec, than for polished ZnO($000\bar{1}$) faces, at 37 arcsec [8].

Impurity incorporation strongly depends on the crystallographic plane, the growth direction and the distance from the seed crystal. Ehrentraut *et al.* [8] found up to 12 ppm of Li in crystals cut from ($000\bar{1}$) or (−c) direction close to the seed crystal compared with <1 ppm for greater distances from the seed. For crystals cut from the (0001) or (+c) direction, the lithium concentration was roughly constant at 2 ppm. This trend was reproduced for Fe, with <11 ppm and <1 ppm, and Al, with <8 ppm and <0.5 ppm in the (−c) and the (+c) direction, respectively. The K concentration was determined to be <0.3 ppm for both growth directions. In general, the main impurities introduced in the growth process are: Li (1.3 ppm wt) and Na (0.11 ppm wt) from the mineralisers, Pt (7.1 ppm wt) from the autoclave lining, as well as Si (0.18 ppm wt), Ca (0.1 ppm wt), and Al (0.02 ppm wt). A more recent study, comparing only the ZnO(0001) and ZnO($000\bar{1}$) faces of (+c) wafers yielded comparable impurity concentrations [64] and found that the elements Na, Si, K, and Ga are present in smaller concentrations on the a-plane compared to the polar planes. In homoepitaxial films grown by chemical vapour deposition [65], the ZnO($000\bar{1}$) face showed significantly higher elemental impurity concentrations than the ZnO(0001) face, with factors of up to 100 for Na and 40 for Li. Group VII elements, such as F, Cl, and I were also significantly more concentrated, by at least one order of magnitude for the ZnO($000\bar{1}$) face. The only exception was N, which seems to preferentially incorporate on the ZnO(0001) polar face [66].

A special kind of hydrothermal grown ZnO bulk crystal with low lithium and other group I impurity concentrations has recently become available from Tokyo Denpa Co. Ltd. (Japan). This Low-Li HT ZnO material is essentially grown in the same manner as conventional HT ZnO but is subjected to high-temperature (1100–1400 °C) post-growth annealing followed by a subsequent re-grinding and re-polishing process. Its electrical and optical properties will be addressed in chapter 4 and 5, respectively. Epi-ready HT ZnO wafers with low lithium concentration that were additionally mirror-polished in an undisclosed way, were obtained from the Mitsubishi Chemical Corporation.

2.4 Hydrogen in ZnO

ZnO shows a prevailing n-type conductivity in almost all situations. The origin of this conductivity is still quite controversial. Traditionally, the n-type conductivity has been

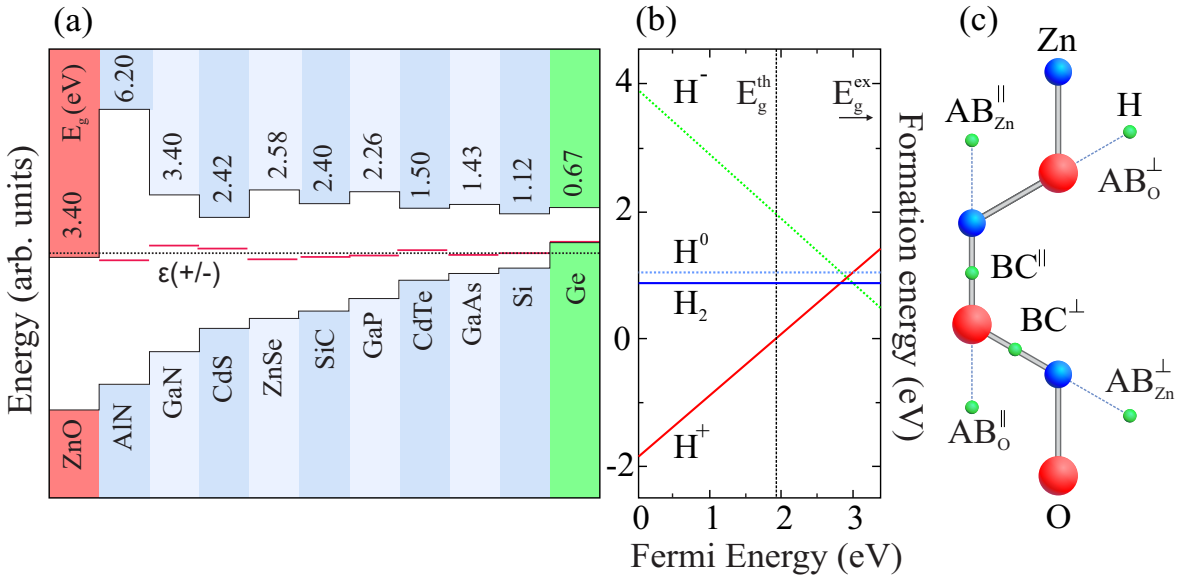

Figure 2.5.: The average transition level $\varepsilon(+/-)$ is shown in (a) as a dashed line with regard to different semiconductors and their respective bandgaps (E_g from [70]). Red lines indicate DFT calculations of $\varepsilon(+/-)$ carried out by van de Walle *et al.* [12]. (b) Reproduction of formation energy graph from Ref. [13]. For all E_F positions up to the theoretical bandgap E_g^{th}, H^+ has the lowest formation energy. The possible positions of interstitial hydrogen in the ZnO lattice with anti-bonding (AB) and bond-centred (BC) positions as well as their orientations, $\parallel$ and $\perp$, are shown in (c).

attributed to native point defects such as Zn interstitials (Zn_i) or oxygen vacancies (V_O) [67]. Zn_i are shallow donors, but possess relatively high formation energies and low diffusion barriers, making them highly unstable and unlikely to be the main source of the observed n-type conductivity [68]. V_O can also be excluded as they have been shown to form rather deep donor states [11]. In addition, V_{Zn}, O_i and zinc and oxygen antisite defects have been proposed, however, they also have high formation energies and, in the case of V_{Zn}, act as compensating acceptor-like defects [11, 69]. Therefore, unintentionally incorporated hydrogen has been proposed as an alternative source for n-type conduction, as it is unavoidably introduced in almost all growth processes.

In the 1950s, Mollwo [71] and Thomas and Lander [72] found that the conductivity of ZnO crystals could be increased by the incorporation of hydrogen through diffusion, and reported an ionisation energy of 40 meV for the associated donor. Interstitial hydrogen (H_i) in semiconductors usually acts as an amphoteric impurity, which means that it tends to counteract the prevailing conductivity by incorporating as a donor (H^+) in p-type material and as an acceptor (H^-) in n-type material. Unusually, the Fermi level energetic position, at which the character of H changes from donor-like to acceptor-like, is actually above the conduction band minimum for ZnO. This is in contrast

to most semiconductors where this transition level, $\varepsilon(+/-)$, lies within the bandgap. Figure 2.5(a) shows the calculated $\varepsilon(+/-)$ values for different semiconductors taken from Ref. [12]. The dashed line indicates the position of the average transition level. For ZnO, the transition level lies in the conduction band; interestingly for Ge, it lies in valence band. Therefore in non-degenerate n-type ZnO, with a Fermi level in the bandgap close to the conduction band minimum, hydrogen will incorporate exclusively as a donor.

Van de Walle [13] illustrated this behaviour by calculating the formation energies of different H species with respect to the Fermi energy. As shown in Fig. 2.5(b), H^+ exhibits the lowest formation energy across the entire bandgap (in this case the theoretical bandgap $E_g^{th} = 1.91\,\text{eV}$, as density functional theory (DFT) calculations tend to underestimate E_g). The reason for the high lying $\varepsilon(+/-)$ transition level, according to van de Walle [13], is the strong O-H bond which significantly decreases the formation energy of H^+. During p-type doping, the formation energy of H^+ decreases even further as the Fermi energy shifts deeper into the bandgap, providing an explanation for the well-known difficulty in producing stable, high quality p-type ZnO material.

Apart from the interstitial site, hydrogen can also substitute at the oxygen site by occupying oxygen vacancies. The removal of an oxygen atom leaves two electrons from the surrounding zinc dangling bonds in addition to the electron from the hydrogen atom in the oxygen vacancy. Two of these three electrons occupy states in the valence band and stabilise a multi-centre bond. The remaining electron is transferred to the conduction band minimum (CBM) and consequently substitutional H_O forms a shallow donor with the help of the surrounding Zn atoms. These hydrogen tetrahedrally-coordinated multi-centre bonds were described only recently in ZnO [14] and are rare compared to centres with fewer bonds, e.g. hydrogen in Si forms a three-centre bond (H-Si-H). With increasing oxygen chemical potential or higher oxygen partial pressure, the formation energy of H_O increases rapidly as the oxygen vacancies are filled. As a result, the conductivity of ZnO tends to decrease with oxygen annealing. However, H_O has a significantly higher dissociation energy than H_i. Wardle *et al.* [73] showed that interstitial hydrogen in ZnO has a low migration barrier of 0.5 eV and should, therefore, be mobile at temperatures as low as 200 K. On the other hand, n-type conductivity is observed in ZnO even after annealing at high temperatures ($\geq 600\,^\circ\text{C}$). This indicates that hydrogen must be bound to other defects, such as H_O, to explain the high temperature stability.

In addition to these two shallow donors, a third hydrogen-related donor state is commonly observed in IR absorption spectroscopy at a local vibrational mode (LVM) frequency of $3611\,\text{cm}^{-1}$. This absorption line is attributed to isolated hydrogen on a

Table 2.1.: Overview of hydrogen-related lines observed in IR absorption, Raman spectroscopy and and photoconductivity measurements.

Label	Frequency (cm^{-1})	Chemical Identity	Ref.
V_{Zn}-H_2	3312.2	V_{Zn}-H_2 ($OH_{\parallel}$)	[76]
XH (H_{AB})	3326.0	V_{Zn}-H^- or CaH/MgH	[77–79]
V_{Zn}-H_2*	3329.0	metastable V_{Zn}-H_2 ($OH_{\perp}$)	[80]
V_{Zn}-H_2*	3348.4	metastable V_{Zn}-H_2 ($OH_{\perp}$)	[80]
V_{Zn}-H_2	3349.6	V_{Zn}-H_2 ($OH_{\perp}$)	[76]
$XH^{(n+1)}$	3358.0	excited state of XH	[77]
H-I*	3577.3	O_{Zn} or Li-H or $Li\text{-}OH^-$	[81–83]
H_{BC}	3611.0	H_{BC}	[75]
H_2	4145.0	H_2 or V_O^{2+}-H_2	[84, 85]

bond-centred position (H_{BC}) [74, 75] between the Zn and O atoms in the ZnO lattice. The hydrogen atom forms a covalent bond with the oxygen atom resulting in a LVM line in IR absorption [76].

Apart from isolated hydrogen, the formation of hydrogen complexes is commonly reported (see Table 2.1). Zn vacancies as double acceptors and H_{BC} as a single shallow donor in ZnO are attracted to each other by their Coulomb interaction. Due to the high mobility of H_{BC}, a V_{Zn}-H_n complex is formed, where V_{Zn}-H acts as a deep acceptor and V_{Zn}-H_2 is neutral. The latter consists of two non-equivalent O-H bonds; one aligned perpendicular to and the other parallel to the c-axis. Both result in unique transitions in IR absorption spectroscopy. In the case of the metastable V_{Zn}-H_2 complex, both bonds are oriented perpendicular to the c-axis. For a summary of all lines see Table 2.1. However, V_{Zn}-H_2 complexes were only observed after deliberate hydrogenation of samples, excluding their origin as the main source of n-type conductivity in ZnO.

A further unusually stable IR absorption line was reported by Lavrov *et al.* [81] exclusively in hydrothermally grown ZnO, labelled H-I*. Remarkably, Lavrov *et al.* found that H-I* disappears only after annealing above 1200 °C. As previously mentioned, Li is a common impurity in HT ZnO material and strongly (out-)diffuses to the surface at elevated temperatures (typically 1100–1400 °C). Consequently, Li is likely to be involved in the H-I* complex in some sort of thermally stable substitutional defect complex. The same line was observed by Halliburton *et al.* [82] in HT ZnO and assigned to a $Li\text{-}OH^-$ complex, similar to complexes observed in MgO. Shi *et al.* [83] showed that the deuterium counterpart of H-I* has a line splitting that fits well with

the natural abundance of the Li isotopes, ^{6}Li and ^{7}Li. DFT calculations by the same authors favoured bond-centred hydrogen between O and Li, with the Li atom on the Zn site (Li_{Zn}-H-O). This is consistent with Wardle *et al.* [86] who found Li_{Zn}-H to be the most soluble defect in ZnO. Bond-centred hydrogen has a low thermal stability annealing out between 150 – 190 °C, compared to hydrogen bound on the O site which is stable up to temperatures of 550 – 650 °C.

However, one hydrogen-related IR absorption line, XH [79], in melt- and vapour-phase-grown ZnO material was observed to increase in intensity with annealing up to 450 – 500 °C and then decrease at higher temperatures without any external source of hydrogen. This indicates that hydrogen must be present in a form that is invisible to IR absorption measurements, so called *hidden hydrogen*. Hidden hydrogen is believed to be the major sink for H_{BC} above 190 °C as this temperature is too low to permit hydrogen out-diffusion from the crystal. Shi *et al.* [79] linked hidden hydrogen to the presence of electrically inactive H_2. Experimental evidence for this assumption was provided by Lavrov *et al.*, who observed a LVM line at 4145 cm^{-1}, close to the frequency of free H_2 at 4161 cm^{-1}, although it is not completely clear if this line belongs to interstitial H_2 or V_O^{2+}-H_2 [85].

Apart from the various hydrogen-related lines presented above, several additional complexes have been proposed in doped ZnO material. Substitutional nitrogen on the O site is an acceptor and a possible candidate for p-type doping. In ZnO:N, neutral nitrogen-hydrogen complexes have been observed that anneal out at temperatures above 700 °C [87]. Acceptor incorporation in ZnO is, in general, limited by the formation of compensating donor defects. Therefore, the observation of neutral N-H complexes may provide the opportunity to incorporate these neutral complexes without triggering the formation of compensating defects. After incorporation, an annealing cycle could then remove the hydrogen, leaving the exposed p-dopant behind, as was demonstrated in GaN:Mg [88] where the centre could be repeatedly passivated and activated by annealing in N_2 or N_2+H_2, respectively. A recent theoretical study by Matsubara *et al.* [89] suggests that interstitial hydrogen may also bond with other shallow donors such as Al, In, or Ga in n-type ZnO, creating a neutral complex that forms a new donor level deep in the bandgap.

Table 2.1 gives an overview of the principal, hydrogen-related lines observed in IR absorption, Raman spectroscopy, and photoconductivity measurements. In contrast to IR and Raman spectroscopy where many hydrogen-related features have been reported, only one line, I_4 at 3.3628 eV, has been consistently assigned to hydrogen in ZnO photoluminescence spectroscopy. Correlation of I_4 with electron nuclear double resonance spectroscopy (ENDOR) [90] and electron paramagnetic resonance (EPR) studies [17]

showed a reduction in hydrogen signal amplitude with annealing that matches the quenching of I_4. Based on its temperature stability, I_4 is believed to originate from H_O. Lavrov *et al.* [75] reported a PL emission line which was attributed to H_{BC} at 3.3601 eV in vapour-phase-grown ZnO after hydrogenation in a DC plasma or H_2 gas. These authors showed via photoluminescence spectroscopy that the concentration of H_{BC} increases with sample depth and is inversely correlated to H_O (I_4) which, in turn, shows its highest concentration close to the sample surface. This may be explained by the fact that the concentration of oxygen vacancies, which form the basis for H_O, increases significantly near the ZnO surface. Lavrov *et al.* also estimated a donor binding energy for H_{BC} of 53 meV, compared to 47 meV for H_O.

3 | Experimental Techniques

This chapter provides an overview of the experimental techniques used in this thesis and relevant associated theoretical concepts. The sample processing and *a priori* assumptions for the data evaluation are also discussed.

3.1 Capacitance Spectroscopic Methods

The intrinsic properties of a semiconductor can be greatly altered by the introduction of impurity elements and the formation of defects. This can be advantageous, for instance in the case of doping, allowing the tuning of free carrier concentration and conductivity. However, it can also be undesirable as defects can potentially form non-radiating centres in optoelectronic devices and so limit device efficiency. Defects exist in different spacial configurations, such as three dimensional, planar, linear or one-dimensional point defects, each distorting the periodic crystal structure and introducing defect states into the bandgap.

The electrically-active defect levels in semiconductors can be distinguished by their energetic position in the bandgap. Defects close to the conduction or valence bands are called shallow defects as they are ionised at room temperature. In contrast, deep defects lie close to the centre of the bandgap and act as generation or recombination centres. Shallow defects can be modelled as an effective-mass hydrogenic impurity with an electron weakly bound by a long range Coulomb potential [91]. In this case, the Bohr radius describes the extension of the wavefunction. In contrast, deep defects have a strongly localised wavefunction, with a spacial extension similar to the lattice constant, and cannot be described using an effective-mass approximation. Due to the large energetic distance to the band edges, deep defects are more likely to capture free electrons or holes [70]. In general, the concentration of shallow defects is much higher than the concentration of deep defects. Therefore, the position of the Fermi level and the free carrier concentration are determined by shallow impurities, which renders it difficult to investigate the nature of deep defects by means of temperature-dependent

Hall measurements.

Frequency-dependent and transient capacitance measurement techniques, such as thermal admittance spectroscopy (TAS) and deep level transient spectroscopy (DLTS), can be used to determine the concentrations of shallow and deep defects and also the rate of emission and capture cross-section for electrons and holes. The calculation of capture and emission rates for band-impurity recombinations is generally described by Shockley-Read-Hall statistics [92] and is extensively presented in Ref. [91]. The total concentration of deep centres is N_t of which n_t are already occupied by electrons and $(N_\mathrm{t} - n_\mathrm{t})$ are unoccupied. The exact number of occupied states depends on the interplay between the capture $(c_\mathrm{n,p})$ and emission $(e_\mathrm{n,p})$ rates for electrons and holes. Keeping in mind that electrons are emitted and holes are captured by occupied states, the net rate of electron occupancy can be written as:

$$\frac{\mathrm{d}n_\mathrm{t}}{\mathrm{d}t} = (c_\mathrm{n} + e_\mathrm{p})\,(N_\mathrm{t} - n_\mathrm{t}) - (e_\mathrm{n} + c_\mathrm{p})\,n_\mathrm{t}. \tag{3.1}$$

Emission and capture follow a Fermi-Dirac distribution:

$$e_\mathrm{n} = \sigma_\mathrm{n}\langle v_\mathrm{n}\rangle N_\mathrm{c} \exp\left(-\frac{E_\mathrm{c} - E_\mathrm{t}}{k_\mathrm{B}T}\right), \tag{3.2}$$

$$c_\mathrm{n} = \sigma_\mathrm{n}\langle v_\mathrm{n}\rangle N_\mathrm{c} \exp\left(-\frac{E_\mathrm{c} - E_\mathrm{F}}{k_\mathrm{B}T}\right), \tag{3.3}$$

with $\sigma_\mathrm{n,p}$ being the defect level capture cross-section. Referring to Ref. [93], the thermal velocity $\langle v_\mathrm{n}\rangle$ and the conduction band density of states N_c can be written as:

$$\langle v_\mathrm{n}\rangle = \left(\frac{3k_\mathrm{B}T}{m_\mathrm{e}^*}\right)^{\frac{1}{2}}, \tag{3.4}$$

$$N_\mathrm{c} = 2\left(\frac{m_\mathrm{e}^* k_\mathrm{B}T}{2\pi\hbar^2}\right)^{\frac{3}{2}}. \tag{3.5}$$

Here, $\hbar$ denotes the reduced Planck constant and m_e^* denotes the effective mass of the band to which the electron is emitted. Interestingly, the Fermi level, E_F, of the semiconductor only appears in the equation for the emission rate, Eq. 3.2, but not in the equation for the capture rate. Therefore, $c_\mathrm{n,p}$, generally depends on the doping level of a given semiconductor, whereas $e_\mathrm{n,p}$ and the trap cross-section $\sigma_\mathrm{n,p}$ are inherent properties of the defect level or trap itself. From a temperature-dependent measurement

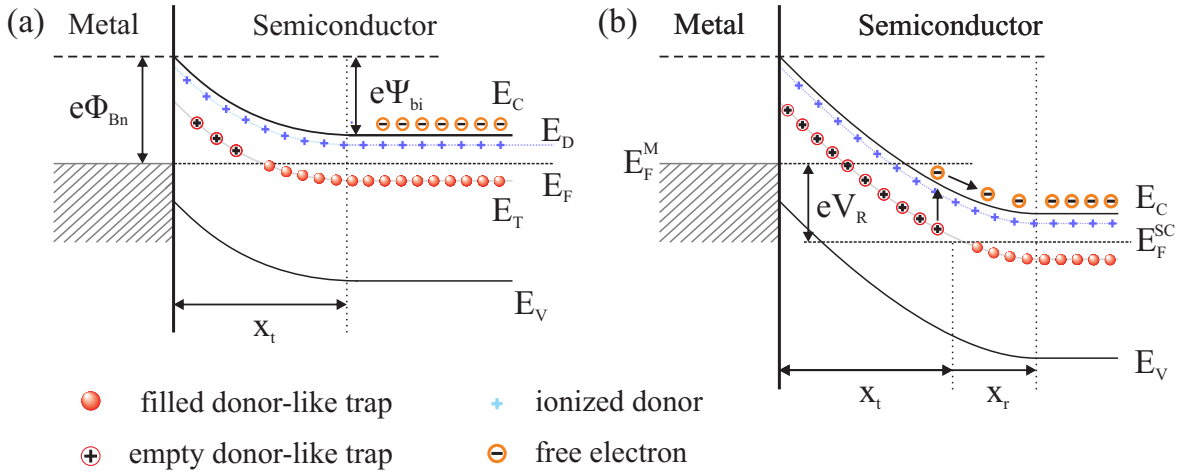

Figure 3.1.: Schottky contact (a) without and (b) with applied reverse bias V_R and the corresponding depletion widths x_t and x_r.

of the emission rate, one can construct an Arrhenius plot using:

$$\ln\left(\frac{e_n}{T^2}\right) = \ln\left(2\frac{\sqrt{3}m_e^* k_B^2}{(2\pi)^{\frac{3}{2}}\hbar^3}\sigma_n\right) - \left(\frac{E_c - E_t}{k_B}\right)\frac{1}{T}. \tag{3.6}$$

The slope of such a plot yields the activation energy and the intersection with the vertical axis gives the apparent capture cross-section of a given trap or defect level. The Arrhenius plot is therefore used in the evaluation of TAS and DLTS experiments but is strictly only valid if $E_c - E_t$ itself is temperature independent.

3.1.1 Thermal Admittance Spectroscopy (TAS)

Admittance spectroscopy measures the frequency dependence of the complex admittance (Y), which is defined as the current flow in response to a small oscillating driving voltage [91, 94] and can be written as $Y = G(\omega) + j\omega C(\omega)$ with a frequency dependent conductance $G(\omega)$ and capacitance $C(\omega)$. Oscillating the reverse voltage, V_R in Fig. 3.1, changes the band bending and the depletion region widths of the Schottky contact. The change in band bending leads to the emission of electrons from the trap states into the free-electron continuum above the conduction band minimum, as the semiconductor Fermi level E_F^{SC} shifts downward under biasing. Shallow donors with an energetic level of E_D can follow this change instantly if they are not already ionised at the measurement temperature, whereas for deeper levels, E_T, the response depends on their emission and re-capture rates. For high frequencies, the deep levels cannot follow

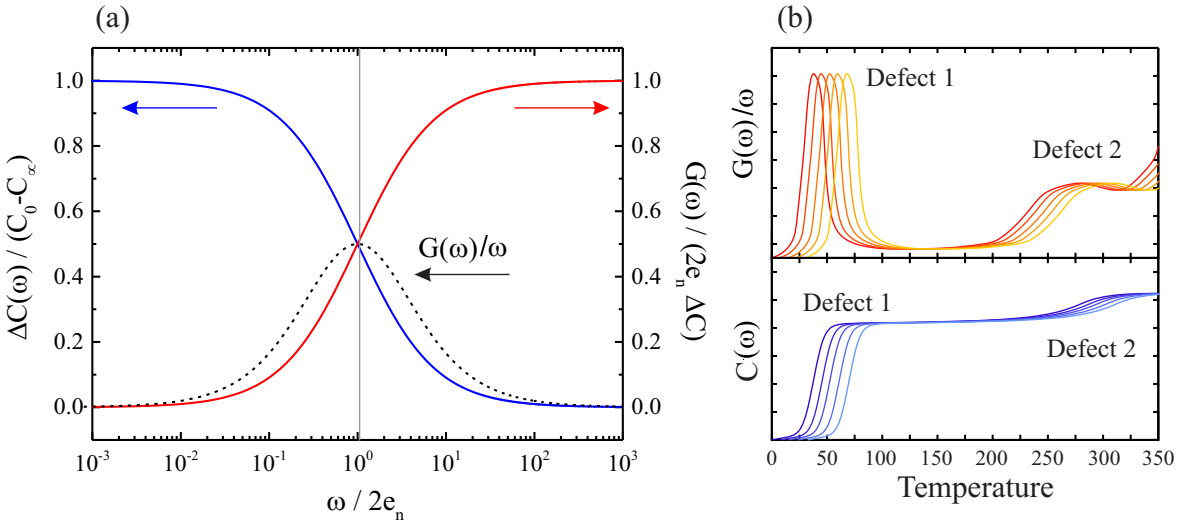

Figure 3.2.: (a) Frequency dependence of capacitance and conductivity for the Schottky contact in Fig. 3.1 and oscillating reverse bias. (b) Schematic TAS spectra for a material with two defects in G(ω)/ω and C presentation.

the sudden change in band bending and the measured capacitance is the depletion capacitance $C_\infty = \epsilon\epsilon_0/x_\mathrm{r}$. For lower frequencies, the deep level can emit electrons if the trap level crosses E_F and the subsequent capacitance increase follows $C(\omega) = C_\infty + \Delta C$. The capacitance and conductance can then be written as:

$$C(\omega) = C_\infty + \left(1 + \frac{\omega^2}{4e_n^2}\right)^{-1} \Delta C\,, \tag{3.7}$$

$$G(\omega) = \quad 2e_n \left(1 + \frac{4e_n^2}{\omega^2}\right)^{-1} \Delta C\,. \tag{3.8}$$

Both identities are plotted in Fig. 3.2(a) as a function of frequency and show an inflection point at $\omega = 2e_\mathrm{n}$. Rather than finding the inflection point in capacitance or conductivity, the maximum of $G(\omega)/\omega$ is determined by:

$$\left.\frac{G(\omega)}{\omega}\right|_\mathrm{max} = \frac{\Delta C}{2}\,, \tag{3.9}$$

and presented, for an exemplary TAS measurement, in Fig. 3.2(b). The step size of the capacitance is related to ΔC and can be used to calculate the defect concentration N_t following:

$$\frac{\Delta C}{C_\infty} = \frac{N_t}{N_D}\,. \tag{3.10}$$

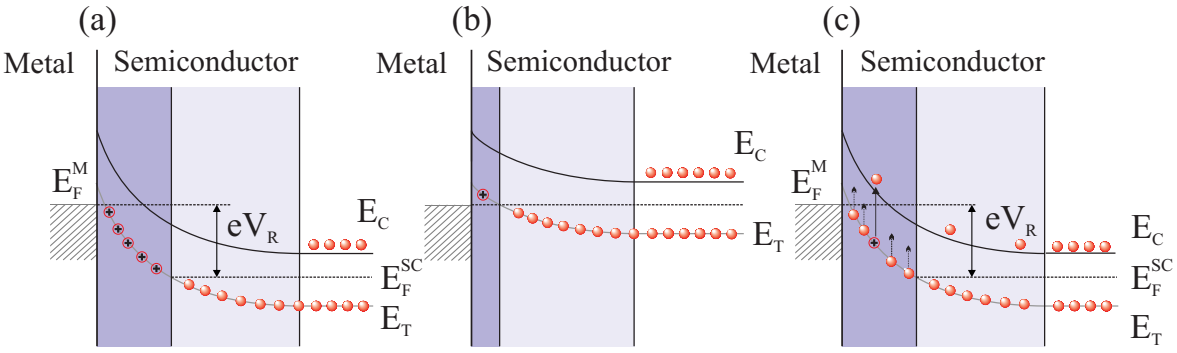

Figure 3.3.: DLTS measurement with reverse biased Schottky contact (a), filling pulse (b) and emission of electrons which results in the capacitance transient.

Figure 3.2(b) shows two different idealised defects. Defect 1 is the shallow defect level and corresponds to the freeze-out of the main donor. For lower temperatures, the semiconductor will act as an insulator and the series resistance of the material will dominate. However, the freeze-out peak can still be evaluated if one considers the approach of Pautrat *et al.* [95] who used an exponent of $T^{3/2}$ rather than T^2 in equation 3.6. The difference in temperature dependence arises due to a change in the dominant scattering mechanism, similar to the change in the exponent for the carrier mobility $\mu(T) = \mu_0 T^x$, often used in temperature-dependent Hall effect measurements.

Changing the nominal reverse bias on the Schottky diode changes the depletion width and allows for the depth-dependent measurement of defects. TAS experiments are limited by the measurement frequencies and temperature. Measurement noise will dominate the $G(\omega)/\omega$ and $C(\omega)$ spectra if the chosen measurement frequency is too low. The highest possible frequency is limited by the series resistance of the Schottky contact. TAS is preferentially used for the detection of shallow defect levels.

TAS measurements were performed at the Institute of Experimental Physics II at the University of Leipzig, Germany. All measurements were performed in dark conditions over a temperature range of 10 – 330 K using a helium flow cryostat. Signal detection was carried out by a Agilent 4294 A precision impedance analyser, operated with a test signal of 50 meV in a frequency interval between 100 Hz to 10 MHz.

3.1.2 Deep Level Transient Spectroscopy (DLTS)

Rather than applying an oscillating reverse bias as used in TAS, deep level transient spectroscopy (DLTS) [96] measures the capacitance transient of the Schottky junction as carriers are trapped at defect levels in the depletion region. Figure 3.3(a) shows the Schottky junction under a constant reverse bias (V_R). All defect levels below the semiconductor Fermi level (E_F^{SC}) are occupied whereas levels above E_F^{SC} are ionised. After

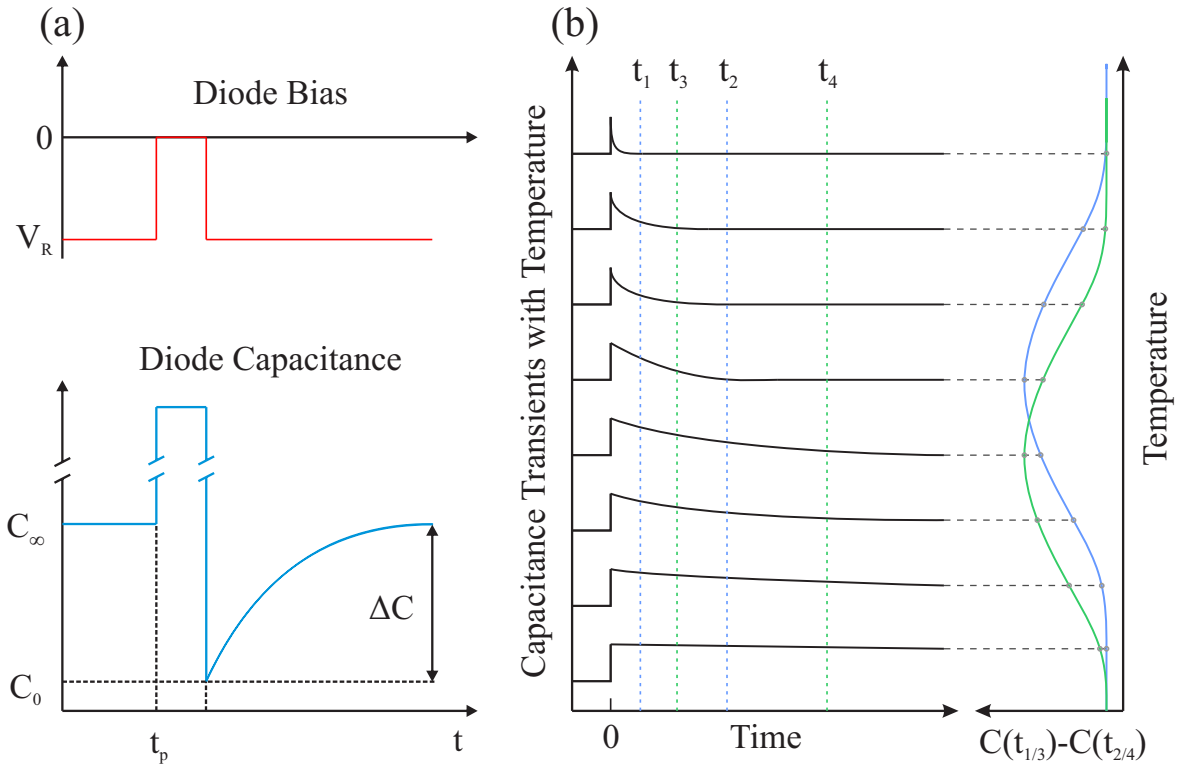

Figure 3.4.: Applied reverse bias to Schottky diode and corresponding capacitance transient (a). (b) DLTS signal $C(t_{1/3}) - C(t_{2/4})$ for two different rate windows $rw_1 = t_2 - t_1 < rw_2 = t_4 - t_3$ with increasing temperature after Lang *et al.* [96].

a short filling pulse ($0 \geqslant \mathrm{V_{Fill}} > \mathrm{V_R}$), shown in Fig. 3.3(b), the depletion width shrinks and ionised traps recapture electrons. Following the filling pulse (see Fig. 3.3(c)), the depletion width increases again and the emission of electrons from the filled traps into the conduction band is monitored as a function of junction capacitance C. The time evolution of C follows an exponential decay with $C(t) \propto \exp(-e_\mathrm{n} t)$, and is shown in Fig. 3.4(a). During a DLTS measurement, the capacitance transient is probed at two different points in time ($t_{1/2}$). The time interval $t_2 - t_1$ is called the rate window rw. As shown in Fig. 3.4(b), the time constant of the exponential capacitance transient decreases with increasing temperature. For low temperatures, the capacitance difference between t_1 and t_2 is almost zero. With increasing temperature and faster decay times, more and more of the capacitance decay lies within the rate window. The difference function (green and blue lines for two different rate windows in Fig. 3.4(b)) reaches a maximum after which the most of the capacitance decay occurs before t_1 and the difference signal drops. Choosing a larger rate window rw_2 (green lines for t_3 and t_4), shifts the capacitance difference function toward lower temperatures. The peak maximum of the difference function denotes the maximum emission rate $e_\mathrm{n}^\mathrm{max}$ at this temperature,

given by:

$$e_{\mathrm{n}}^{\max} = \frac{t_1 - t_2}{\ln(t_1/t_2)} \,. \tag{3.11}$$

Employing a multitude of different rate windows will yield a series of peaks similar to the ones obtained in TAS measurements for varying measurement frequencies. Each rate window corresponds to a specific emission rate e_{n} for a certain temperature T; keeping in mind that $e_{\mathrm{n}}(T)$ is temperature-dependent according to Eq. 3.2. The $(e_{\mathrm{n}}(T), T)$ dataset can then be used to construct an Arrhenius plot and using equation 3.6, the thermal activation energy and the capture cross-section of the defect level can be obtained. As DLTS measurements depend on rate windows rather than measurement frequencies, levels deep in the bandgap can be probed.

DLTS experiments were carried out at the University of Leipzig, Germany. The setup consisted of a Boonton 7200 capacitance bridge, a National Instruments PCIe-6251 data acquisition card, and commercial Laplace DLTS software [97]. TAS and DLTS measurements were carried out with the assistance of Dipl.-Phys. F. Schmidt.

3.2 Photoluminescence Spectroscopy

The radiative recombination of electrons and holes is called luminescence. If the excitation of the electron-hole pair is achieved by means of a photon, the emitted light is called photoemission. This process forms the basis of photoluminescence spectroscopy (PL), which is routinely used in the optical characterisation of semiconductors. In general, the photoexcitation is accomplished by means of a laser, e.g. a HeCd or excimer laser for the UV regime and Ar^+ or a HeNe laser for the visible regime. The incident photons transfer their energy to electrons in the valence band, promoting them to the conduction band. These excited electrons can now form a quasiparticle with the associated holes. These quasiparticles are known as excitons.

The formation of correlated electron-hole pairs, were first described as “excitation packets” by J. Frenkel [103] in 1930 and by G.H. Wannier [104] in 1937 for metals and insulating crystals. Photons absorbed by the crystal promote electrons into the conduction band leaving behind holes in the valence band. The Coulomb interaction between these two opposite charged particles leads to a decrease in the binding energy of the exciton-complex in comparison with the free electron and hole. In semiconductors such as ZnO ($\varepsilon_{\mathrm{ZnO}} = 6.5$) with high dielectric constants, the Coulomb interaction is screened by the valence electrons. Therefore, electrons and holes are weakly bound with typical

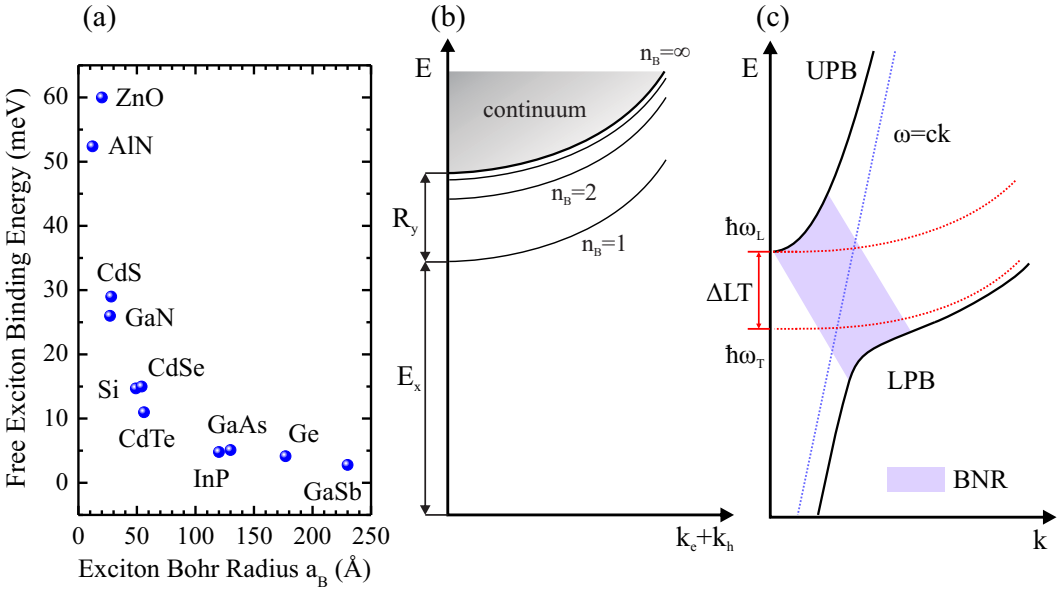

Figure 3.5.: (a) Binding energy of the free exciton $E_{\mathrm{D}}^{\mathrm{B}}$ over exciton Bohr radius a_{B} with data from [98–101]. (b) Dispersion relationship in exciton-picture for different quantum numbers $\mathrm{n_B}$. (c) Exciton-photon coupling close to the bottle neck region (BNR) [102].

exciton binding energies of the order of tens of meV. As a result, the exciton radius is commonly much larger than the lattice spacing (see Fig. 3.5a). These excitons are generally known as Wannier-Mott excitons, in contrast to Frenkel-excitons with exciton binding energies in the hundreds of meV. The former can be theoretically described by an effective-mass approximation with the electron and hole orbiting around a mutual centre of mass with a dispersion relation of:

$$E(n,\vec{K}) = E_{\mathrm{g}} - \mathrm{Ry}_{\infty}\frac{1}{n^2} + \frac{\hbar^2\vec{K}^2}{2M} \qquad \text{with} \tag{3.12a}$$

$$\mathrm{Ry}_{\infty} = 13.6\,\mathrm{eV}\frac{\mu}{m_0}\frac{1}{\varepsilon^2}, \tag{3.12b}$$

$$\mu = \frac{m_{\mathrm{e}}m_{\mathrm{h}}}{m_{\mathrm{e}}+m_{\mathrm{h}}}, \tag{3.12c}$$

$$a_{\mathrm{B}}^{\mathrm{ex}} = a_{\mathrm{B}}^{\mathrm{H}}\epsilon\frac{m_0}{\mu}, \tag{3.12d}$$

where Ry_{∞} denotes the exciton Rydberg energy, $n = 1, 2, 3\ldots$ the principal quantum number, $\vec{K}$ the wave vector, and M the translational mass of the exciton [102]. Furthermore, μ is the reduced exciton mass of the electron m_{e} and hole m_{h}, m_0 the free electron mass and $a_{\mathrm{B}}^{\mathrm{ex}}$ the exciton Bohr radius. The last term in equation 3.12a accounts for the kinetic energy of the exciton. Although the effective-mass approximation is often used

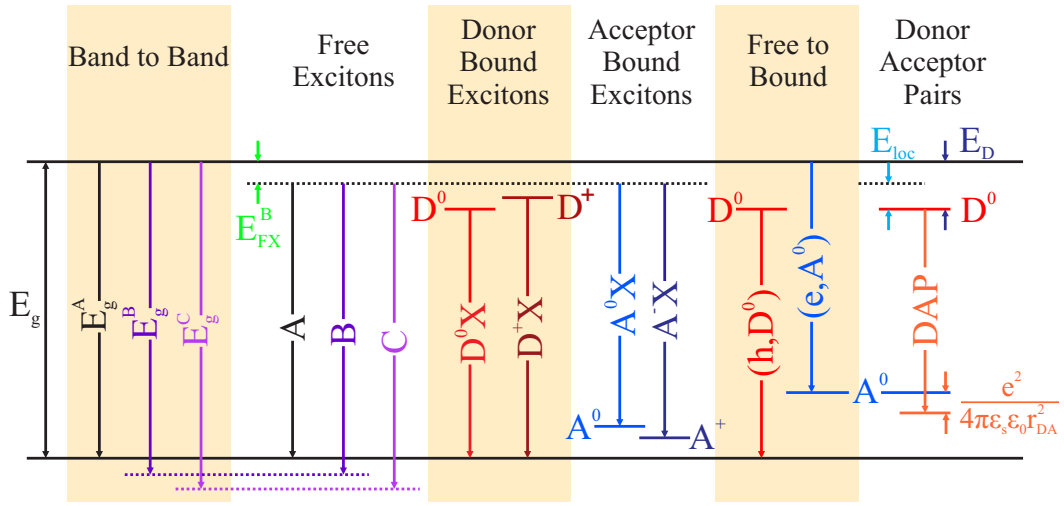

Figure 3.6.: Overview of radiative recombinations in a semiconductor [106]. Due to the Coulomb interaction, the donor-acceptor pair (DAP) transition energy is larger than the energetic distance between donor and acceptor level.

in the context of a hydrogen atom, it would be more applicable to speak of an exciton as an electron-positron pair due to their similar masses [105]. However, analogous to the hydrogen atom, the exciton exhibits excited states which converge towards E_g as $n \to \infty$ (see Fig. 3.5(b)). Although the electron and hole will be ionised for $n \to \infty$, their wave functions will still be affected by the Coulomb interaction.

The interaction of an exciton with the electromagnetic field of an incident photon leads to the formation of exciton-polaritons. The dispersion relationship of this quasi-particle consists of an upper polariton branch (UPB) and a lower polariton branch (LPB). At $\mathbf{k} = 0$, the UPB shows excitonic behaviour and becomes photon-like for values of $\mathbf{k}$ above the so called bottleneck region (see Fig. 3.5(c)). The LPB is photon-like close to $\mathbf{k} = 0$ but shows an excitonic dispersion for high $\mathbf{k}$. The energetic distance between the two branches at $\mathbf{k} = 0$ determines the splitting between longitudinal and transverse excitons. Here, the longitudinal exciton refers to the exciton-like part of the UPB and the transverse exciton to the exciton-like part on the LPB. In conclusion, for $\mathbf{k} = 0$ the UPB and the longitudinal exciton coincide in energetic position. Although, this picture is not completely valid [27], it is most appropriate for the model presented here.

Excitons can recombine radiatively or non-radiatively via different channels with typical lifetimes of 0.2 – 5 ns in bulk ZnO at low temperatures. Detecting the specific wavelength distribution of these excitons allows a determination of their bonding state and, therefore, the energetic position in the bandgap. Although impurity centres, such as donors and acceptors, form different levels or traps in the bandgap, their chemical

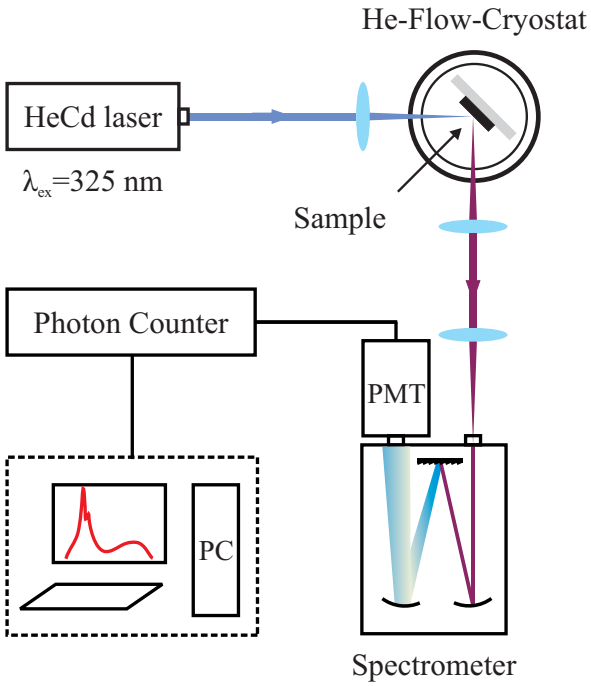

Figure 3.7.: Experimental setup for photoluminescence measurements at the University of Canterbury.

identification is far from straightforward. Figure 3.6 shows an overview of the possible recombinations in a semiconductor.

Levels close to the valence and conduction bands are referred to as shallow acceptors or donors due to their low binding energies; states deep in the bandgap are called deep defects. Excitons bound to shallow impurities will dissociate at temperatures around 80 K in ZnO. Therefore, it is necessary to carry out PL measurements at sufficiently low temperatures, usually around the temperature of liquid helium (T = 4.2 K). Due to the large exciton binding energy in ZnO (60 meV), free exciton emission can be observed at room temperature in PL measurements.

This high exciton binding energy makes ZnO an interesting candidate for room temperature excitonic lasing. Thomas [107] gave one of the first accounts of the exciton spectrum of ZnO in 1960. Since then, PL techniques have been regularly used to investigate ZnO bulk crystals, thin films, and nanostructures. Over 13 characteristic transitions were reported, of which only four have been chemically identified in the last 60 years.

In this work, a continuous wave HeCd laser, emitting at 325 nm (3.815 eV), was employed, resulting in above bandgap excitation ($E_g^{ZnO}(3\,K) = 3.44\,eV$) with an excitation power of 10.5 mW after focusing optics. Samples of interest were mounted with silver paste in an Oxford OptistatCF2 helium flow cryostat, see Fig. 3.7. A stable base

temperature between 3 K and 4 K was used for the low temperature PL measurements. Although it is possible to submerge the sample completely in liquid helium, inevitable He gas bubble formation dramatically reduces the luminescence intensity leading to reduced resolution. The emitted luminescence from the sample was then focused by lenses with UV transmissivity of $> 92\,\%$ into a 1 m Spex1400 monochromator equipped with a 1200 lines/mm holographic grating. A Hamamatsu R943-02 GaAs photomultiplier tube (PMT) at an integration time of 1 s was used for detection.

Due to the high sensitivity of the PMT and the stable low temperatures possible with the He-flow cryostat used, PL experiments could be carried out with relatively narrow slit widths of between 6/6 µm and 10/10 µm (entrance/exit slits widths of the spectrometer) for ZnO bulk single crystals. With these settings, it is possible to resolve emission lines with a FWHM of approximately 50 µeV for the lowest possible spectrometer step width of 0.001 nm (9 µeV). The resulting PL spectra were calibrated to the recorded transition lines of a Hg lamp (i.e. 365.0158 nm). Two optical density filters were used, one to block non-lasing plasma lines and spontaneous emission of the HeCd laser (90 % transmission at 325 nm) and one to block back-scattered laser light from the cryostat windows (long-pass edge filter above 327.5 nm). For conversion to photon energy units, the vacuum wavelength of 1239.84187 nm was used. All photoluminescence measurements were performed in the Rutherford Building of the Department of Physics and Astronomy at the University of Canterbury.

3.3 Ion Implantation

Ion implantation is used to introduce impurity atoms and defects, with a higher level of control over concentration and spatial propagation than possible with diffusion. In ZnO, ion implantation has been primarily used to identify the chemical origin of at least three PL transitions, namely the group III elements Al, Ga, and In. During the implantation process, the dopant atom is ionised by sputtering of the respective elemental target. The elemental vapour is then accelerated by an electric field and the resulting ion beam is guided into a bending magnet with a given curvature, R. By adjusting the magnetic field, B, and the accelerating potential, V, one can select ions with a certain charge-to-mass ratio (m/q) according to $R \cdot B = \sqrt{2\mathrm{m}V/\mathrm{q}}$. The purity of the initial target material is, therefore, of little importance. For example, a Ga-Al target was used in for Ga implantation, with Al ions rejected by the bending magnet.

Every ion impinging on the surface of the host crystal undergoes a series of collisions with the lattice atoms. As the energy of the ions is generally much higher than the lattice binding energy, elastic scattering is assumed to be the dominant scattering

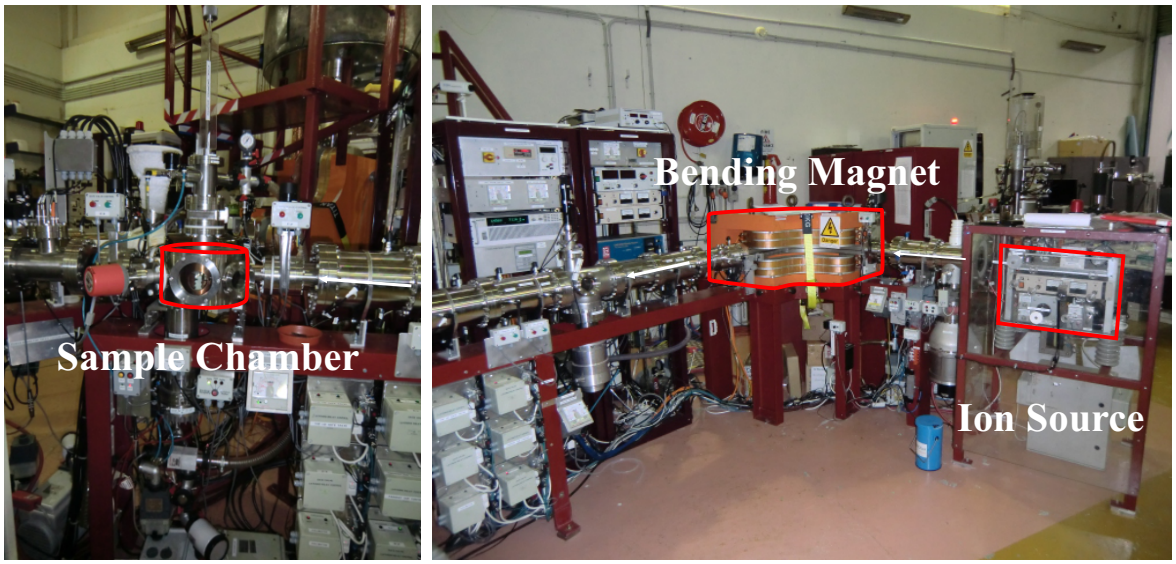

Figure 3.8.: Ion implantation facilities at GNS Science in Lower Hutt.

mechanism. In addition to elastic host atom scattering, the ions can scatter inelastically with electrons in the crystal. Both scattering processes contribute to the so called stopping power of a given material. At lower energies, the nuclear stopping power dominates; this is the case for implantation energies between $10-200\,\mathrm{keV}$, while electronic stopping power dominates at higher energies. The distance travelled by the implanted ions normal to the sample surface is commonly referred to as the average projected range R_p. As elastic scattering processes are statistical processes, they can be modelled using a Monte Carlo approach with the SRIM (Stopping and Range of Ions in Matter) package. Averaging a large number of simulated trajectories yields an approximation of R_p and helps determine the necessary implantation parameters for a desired implantation depth. In an ideal experiment, the implantation profile should exhibit a Gaussian shape. However, scattering theory shows that this is only the case when the scattering ion and host atom have identical masses. In general, the R_p peak will be displaced towards the surface for lighter ions in a heavy target (e.g. B in Si) and towards the bulk for heavier ions in a lighter target (e.g As in Si) [108].

Ion implantation of ZnO was carried out at the low-energy ion implantation facilities at GNS Science (see Fig. 3.8) in Lower Hutt with the help of Dr. Andreas Markwitz and Dr. Peter Murmu. During implantation, the ZnO samples were kept in a vacuum at $2 \times 10^{-7}\,\mathrm{mbar}$ with the ion beam rastering over the mounted samples under 'close-to-normal' incidence to ensure homogeneous lateral implantation. For Ga, Al, and Pt, the respective ions were produced by sputtering a target containing the corresponding element. For H_2^+ and D_2^+, the respective gases were used as ion sources.

Table 3.1.: Overview of the implantation parameters for various ion implantations. Target current denotes ions hitting the ZnO sample over an area of 1 cm^2. Mass separation is achieved by changing the magnetic field of the bending magnet. Note that H- and D-implantation was repeatedly performed at three different implantation depths for the same samples.

	Ion Energy (keV)	Beam Curr. (μA)	Target Curr. (μA)	Fluence (atoms cm^{-2})	Magnetic Field (G = 1×10^{-4} T)
H_2^+	4	1	0.8	$7 \times 10^{14} - 10^{15}$	304
	10	1	2.1	$7 \times 10^{14} - 10^{15}$	480
	18.3	10	5.4	$7 \times 10^{13} - 10^{14}$	480
D_2^+	4.4	10	2.14	$7 \times 10^{13} - 10^{14}$	464
	8.5	10	1.6	$7 \times 10^{13} - 10^{14}$	646
	18.3	10	0.5	$7 \times 10^{13} - 10^{14}$	950
Ga^+	41	1	0.3	$7 \times 10^{13} - 10^{14}$	5732
Al^+	20.5	1	1.52	$7 \times 10^{13} - 10^{14}$	2454
Pt^+	80	1	0.61	$7 \times 10^{13} - 10^{14}$	6676

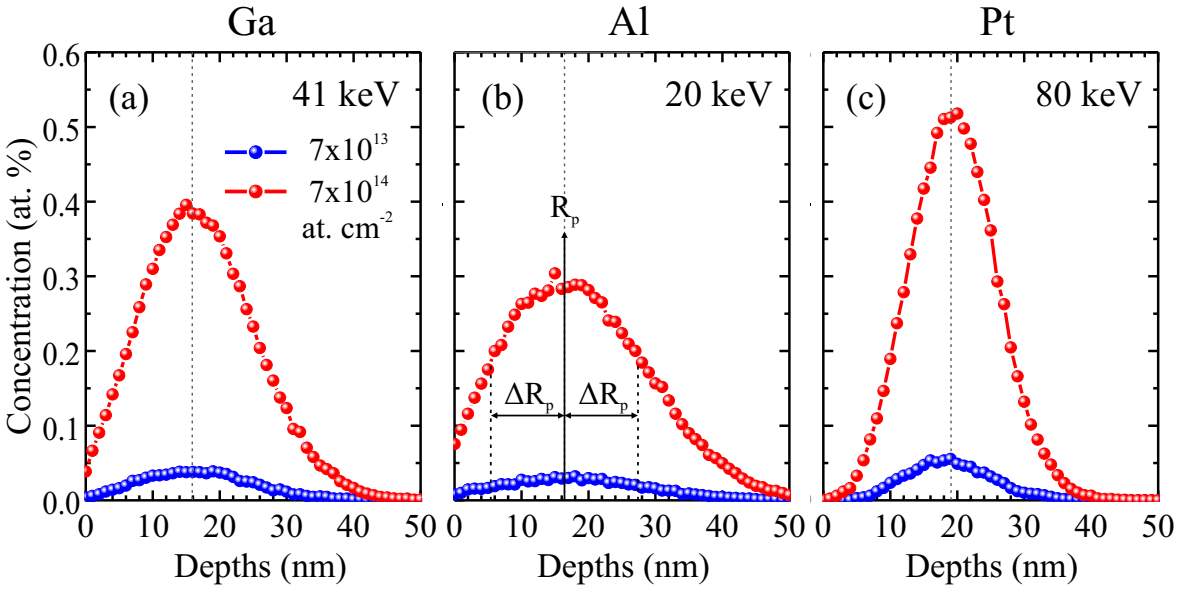

Figure 3.9.: Dynamic-TRIM calculations for (a) Ga, (b) Al, and (c) Pt implantation for two different doses. The projected range R_p is marked as a thin dashed line. ΔR_p is referred to as *straggle* and represents the variance of a Gaussian implantation profile. Calculations were carried out by Dr. P. Murmu.

In addition to the 90° bending magnet, two quadrupole lenses were employed to focus the beam onto the samples. The exact implantation dose was monitored by a charge counter.

All implantation parameters were chosen to yield an average implantation depth of $R_p = 20\,nm$ beneath the surface, with two different doses of $7 \times 10^{13}\,cm^{-2}$ and $7 \times 10^{14}\,cm^{-2}$. The implantation parameters used are summarised in Table 3.1. The necessary SRIM (Stopping and Range of Ions in Matter) or TRIM (Transport of Ions in Matter) calculations were carried out by Dr. Peter Murmu and are presented in Fig. 3.9. As the implantation was performed under 'close-to-normal' incidence, channeling cannot be neglected. Therefore, the experimental implantation profiles will likely have a lower peak concentration and deeper implantation depth compared to the calculated profiles. Channeling will predominantly be observed for lighter elements such as hydrogen and deuterium.

For hydrogen ($^1H_2^+$) and deuterium ($^2H_2^+$) implantation, three separate implantation depths, centred at 20 nm, 40 nm, and 90 nm, were chosen to create a linear doping profile from the sample surface into the bulk. This was done to ensure reasonably deep doping for any further surface sensitive Raman spectroscopy measurements. As molecular hydrogen and deuterium will dissociate into their atomic constituents after hitting the surface, the implantation concentrations given, refer to atomic species, rather than molecular ones.

3.4 X-ray Photoelectron Spectroscopy

Photoelectron spectroscopy (PES) is a surface analysis techniques that is widely used today in physics and chemistry. It is based on the principle of the photoelectric effect, observed by H. Hertz in 1887 using light arcs [109] and explained theoretically by A. Einstein in his *annus mirabilis* in 1905 [110]. The first high resolution photoemission spectrometer was developed in the 1950s, an achievement for which K. Siegbahn was awarded the Nobel Prize in physics in 1981. After this, PES was widely adopted one of the most common surface analysis tools, yielding information about electronic band structure, chemical oxidation state and atomic composition. Since the early days of Siegbahn, x-ray sources have mainly been used for excitation, hence the name x-ray photoelectron spectroscopy or XPS. Today, the most common excitation x-ray sources are Al K_α ($h\vartheta = 1486.7\,eV$) and Mg K_α ($h\vartheta = 1253.6\,eV$) sources for lab based equipment and helium gas discharge lamps for ultraviolet photoelectron spectroscopy (UPS). Furthermore, with the commissioning of third-generation synchrotron facilities and the use of insertion devices such as wigglers and undulators, it has been possible

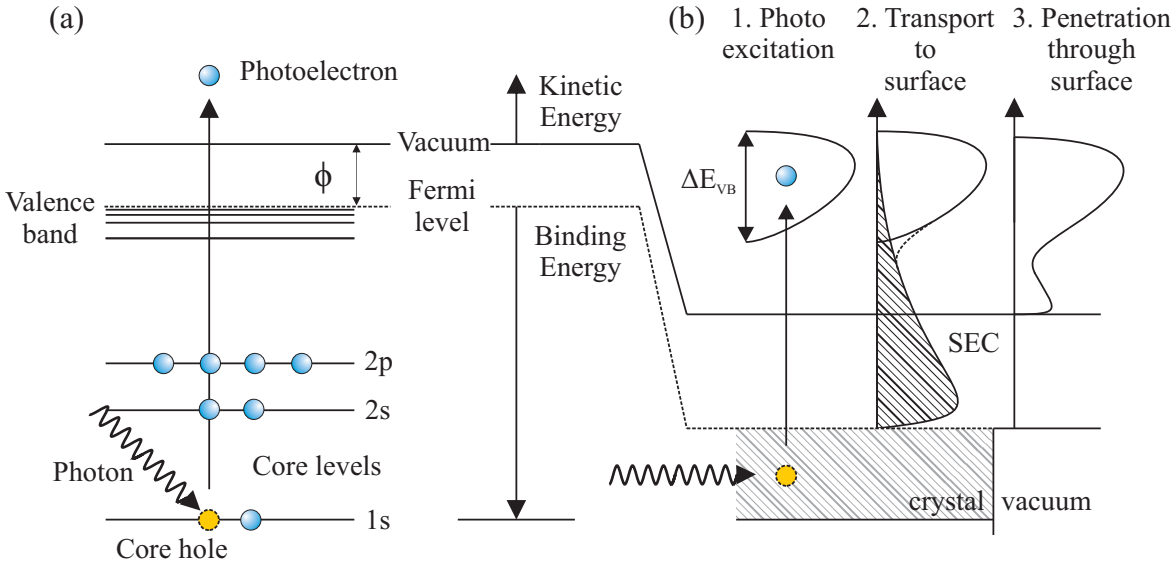

Figure 3.10.: (a) Photoexcitation of an electron by a photon. The work function ϕ is the energetic distance between the Fermi level and the vacuum level. (b) Three-step process of photoexcitation. SEC in step two represents secondary electrons which are generated by inelastic scattering events. Only photoelectrons leaving the surface can be detected and therefore the distribution in step three cuts off at the vacuum level.

to use synchrotron radiation as the x-ray source. Synchrotron radiation allows the user to freely choose a desired excitation energy from the ultraviolet (5 – 100 eV), soft x-ray (100 – 1000 eV) and standard x-ray energies (> 1000 eV).

Regardless of the excitation energy used, the fundamental physical principle remains the same. Under photon irradiation of a gas or the surface of a solid, the energy of the incident photon, $\hbar\omega$, is absorbed by a core level or valence band electron with a binding energy E_B (Fig. 3.10). The electron is released when the photon energy is large enough to overcome the binding energy. After excitation, a hole is left behind in the atomic shell. The photoelectrons leave the sample and are analysed according to their kinetic energy (E_{kin}). Considering conservation of energy, the original binding energy of the photoelectrons can be determined using Eq. 3.13 if the work function of the material (ϕ) and the energy of the incident photon are known:

$$E_{kin} = \hbar\omega - \phi - E_B \tag{3.13}$$

In practice, the sample should be carefully grounded to the spectrometer in order to align the Fermi level (E_F) of both the sample and the spectrometer. Consequently, the specific work function of the sample under investigation is not required and instead the known work function of the spectrometer can be used. A further benefit of good electrical contact, is the avoidance of sample charging, provided the samples are suffi-

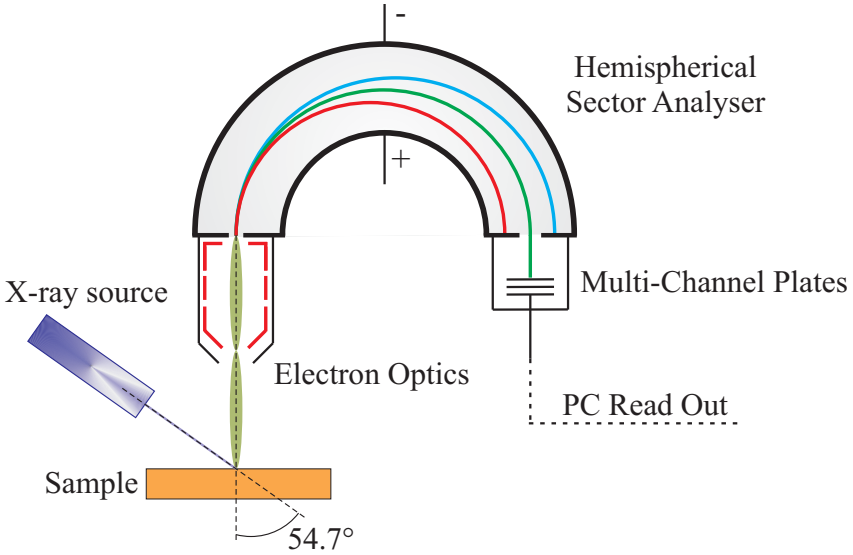

Figure 3.11.: Experimental Setup for typical XPS measurement. The angle between the x-ray source and the analyser is 54.7°, also known as the *magic angle*. The electron optics retard the incoming photon electrons to the pass energy and focus them on the entrance slit of the HSA.

ciently conducting. Where this is not the case a separate electron flood gun has to be used to avoid drifting of the XPS spectra.

Experiments based on the photoelectric effects are commonly described by the so-called three step model [111]. In the first step, see Fig. 3.10(b), a photon is absorbed and its energy excites an electron. After excitation, the electron can travel to the sample surface in the second step. As the electrons not only scatter elastically but also inelastically, a background of secondary electrons is detected. Finally, the electrons that reach the surface and leave the sample can be detected in the third step. This three step model helps to highlight some important aspects of XPS experiments:

1. The generation depth of photoelectrons depends on the incident photon energy.

2. Although x-rays have an attenuation length on the order of a few µm, the photoelectrons have a small escape depth. As only photoelectrons that reach the surface can be detected, the XPS technique is highly surface sensitive.

3. After the photoelectron leaves the surface a positive hole is left behind; therefore, the final state is distinctively different from the initial (ground) state of the system. The core hole can be filled by an Auger process ejecting a corresponding Auger electron.

To measure the kinetic energy spectrum of the ejected photoelectrons, several different techniques have been developed, such as time-of-flight methods, deceleration /

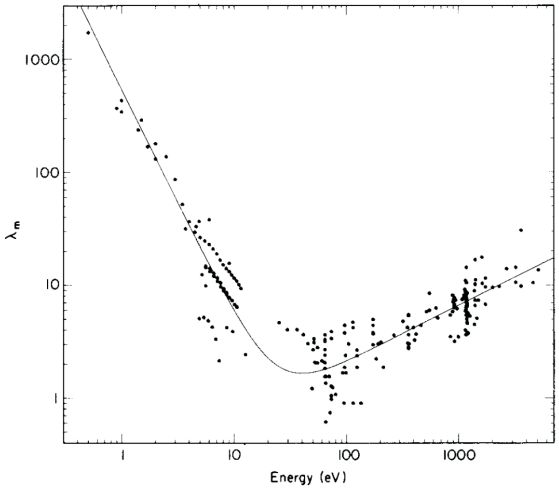

Figure 3.12.: Electron mean free path in monolayers for different elements versus kinetic energy. Reproduced from the seminal work of Seah and Dench [112].

deflection of electrons in electric fields, or change of path measurements in magnetic fields. For all XPS measurements presented in this thesis, hemispherical sector analysers (HSA) were used, as shown in Fig. 3.11. Before photoelectrons reach the HSA they are collected and focused into the entrance slit of the HSA by electron optics. The HSA itself consists of two concentric hemispheres, held at different electrical potentials. Only electrons with a specific initial kinetic energy E_{kin}, will be deflected with the right trajectory and focused onto the exit slit without any distortion. To achieve a constant absolute resolution, most instruments use a pre-retardation stage prior to the energy analyser. By retarding the electrons to a fixed kinetic energy before entering the analyser, the same resolution is achieved across the entire spectrum. This distinct energy is called the pass energy, and this particular mode of operation is known as fixed analyser transmission (FAT) mode. After leaving the HSA, the photoelectrons with a particular kinetic energy are counted either using electron multipliers or more commonly microchannel plates. The angle between the incident x-ray photons and the analyser was held at the magic angle of 54.7°, for which the photoionisation cross-section shows no anisotropy with the photoelectron emission angle. Further equipment details are given in the respective sections of this thesis. The only two elements not detectable via XPS are hydrogen and helium, due to their very small photoionisation cross-sections. Furthermore, helium does not easily form compounds that could be detected and hydrogen shares its electron in compounds via valence-like orbitals with varying energies.

The advantages of using electrons in surface spectroscopy is that they are relatively easily detected and counted. Furthermore, electrons can be focused (i.e. into an analyser

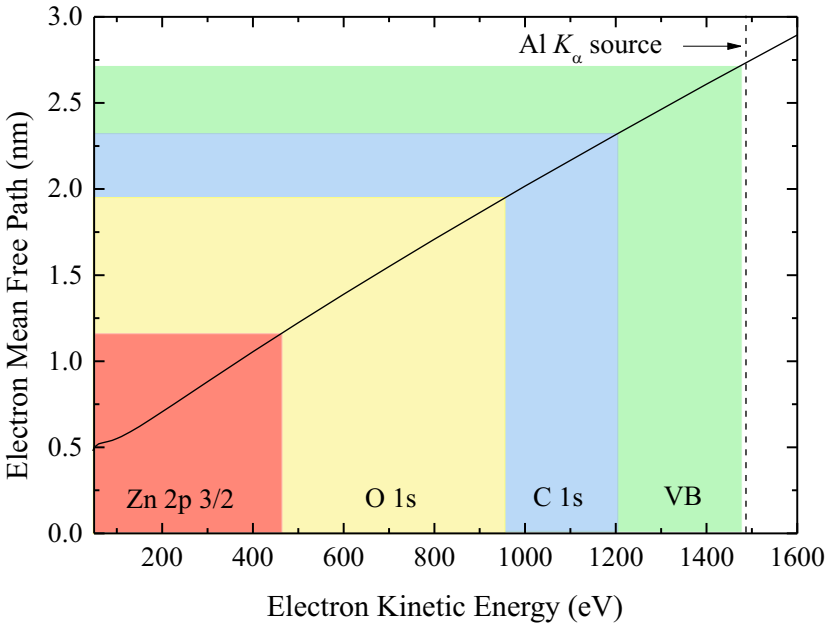

Figure 3.13.: Calculated IMFP for various kinetic energies (KE) of the photoelectron. Assuming a Zn 2p 3/2 binding energy of 1021 eV, the maximal possible kinetic energy would be 465 eV with a corresponding IMFP of 11.7 Å. The colour-shaded areas assume an x-ray excitation of 1486.7 eV.

entrance) and their kinetic energy is tunable (i.e. via the pass energy). One of the disadvantages of using electrons is the need for ultra-high vacuum conditions ($< 10^{-9}$ mbar) to achieve an electron scattering length of the order of meters corresponding to the size of the HSA and electron optics. Electron scattering in solids is described by the universal electron mean free path, which is given for different elements as a function of electron kinetic energy in Fig. 3.12.

The mean free path is given in monolayers, corresponding to only a few Å. The black curve is a rough approximation of the selected elements; therefore, the term universal is used. Furthermore, the graph shows a distinct minimum at 2 – 5 Å for a kinetic energy of 40 – 50 eV. This minimum is mainly determined by the energy dependence of the electron-electron scattering cross-section and electron-phonon scattering effects at very low energies. Due to the different scattering mechanisms involved, it is more correct to refer to the inelastic mean free path λ_{IMFP} (IMFP) as the limiting factor for surface/bulk sensitivity. It is defined according to the International Organisation for Standardisation (ISO) [113] as the distance between two inelastic scattering events or according to Hüfner [111] as the distance for which the probability of an electron escaping without significant energy loss due to inelastic scattering is e^{-1} of its original value.

Unfortunately, there are four different terms to describe the surface sensitivity of XPS measurements which are used more or less interchangeably in literature, namely the IMFP itself, the effective attenuation length, the mean escape death, and the information depth. The sampling depth, which is quite similar to the information depth, is defined as the depth from which 95 % of the electrons are scattered and is approximated as three times the IMFP. For a detailed discussion of these four terms see Ref. [114].

One method of calculating the IMFP for a certain material system is based on the TPP-2M formula (named after its authors Tanuma-Powell-Penn - 2 Modified) [115]. The TPP-2M formula takes into account the atomic weight, density, bandgap and number of valence electrons. Figure 3.13 shows the calculated energy dependence of the IMFP for ZnO using the QUASES software based on the TPP-2M algorithm by S. Tougaard [116]. For example, we would expect at a photon energy of $h\vartheta = 1486.7\,\mathrm{eV}$ to detect photoelectrons originating within a depth of $\lambda_{\mathrm{IMFP}} = 2.7\,\mathrm{nm}$ beneath the surface or approximately the first 10 Zn-O double layers, or in terms of the sampling depth $3\lambda_{\mathrm{IMFP}} = 8.1\,\mathrm{nm}$ (31 Zn-O double layers).

Finally, it should be noted, that it is quite difficult to experimentally estimate the surface sensitivity itself. Experimental methods for measuring the IMFP, such as the deposition of thin film overlayers, are affected by surface and interface roughness and surface reconstruction. Theoretical calculations on the other hand have to be corrected for surface effects because the IMFP is strictly speaking only a bulk identity and neglecting elastic scattering events introduces further uncertainties.

3.4.1 The Soft X-Ray Beamline at the Australian Synchrotron

XPS measurements using synchrotron radiation were carried out at the soft x-ray beamline (SXR) at the Australian Synchrotron (AS) in Melbourne, Australia. The advantage of using synchrotron radiation lies in the tunability of the photon energy and the high x-ray beam intensity (8×10^{11} Photons/s at SXR), low angular divergence and small bandwidth of photon frequencies. All these factors are commonly summarised as the *brilliance*. Tuning the photon energy allows the elemental sensitivity to be adjusted by choosing a regime with a high photoionisation cross-section for a specific element (see Fig. 3.14) or changing the x-ray attenuation length.

Three different photon energies were used to ensure an optimal surface sensitivity and to allow the measurement of all relevant core level binding energies. For survey spectra (BE: 0 eV to 1197 eV), a photon energy of $h\vartheta = 1486.7\,\mathrm{eV}$ was used to ensure comparability with laboratory-based Al K_α x-ray sources. For O $1s$ and C $1s$ core

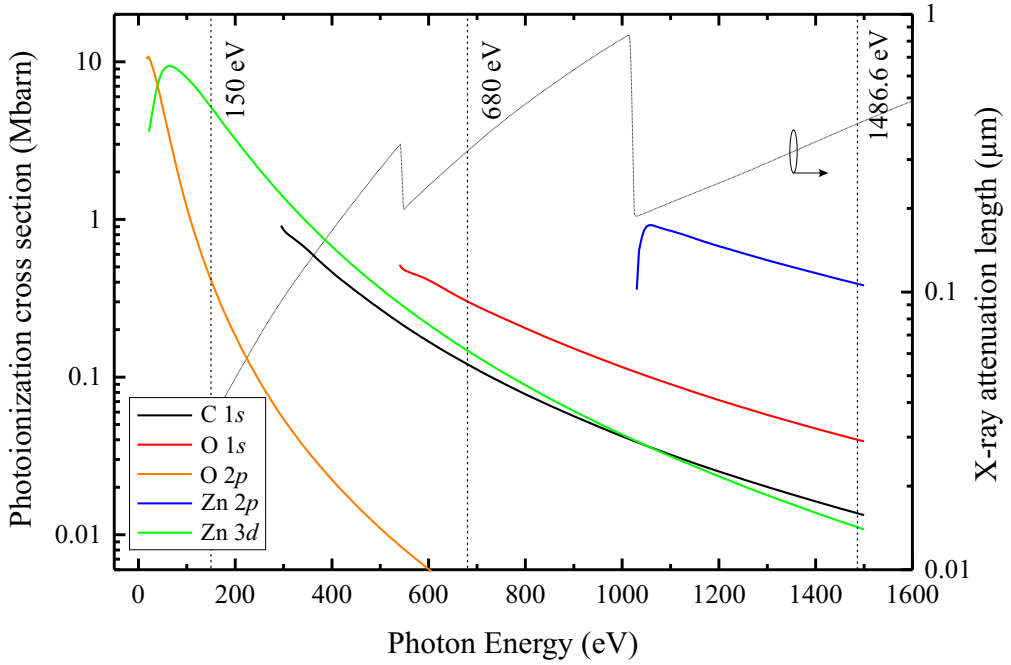

Figure 3.14.: Energy dependence of photoionisation cross-sections for different element core levels with data taken from [117]. The cross-section is given in Mbarn with $1\,\text{barn} = 10^{-24}\,\text{cm}^2$. For comparison the area of a single Zn atom is roughly 560 Mbarn. The dotted line shows the calculated energy dependence of the x-ray attenuation length in ZnO for x-ray incidence along the surface normal. Data taken from [118].

level scans, a photon energy of $h\vartheta = 680\,\text{eV}$ was chosen. For this photon energy, the resulting photoelectrons originating from the O $1s$ core level have a similar kinetic energy ($\sim 149\,\text{eV}$) compared to the photoelectrons from the valence band region (VB) scans which were measured using $h\vartheta = 150\,\text{eV}$ photons. The polarisation was always kept linear-horizontal. The binding energy scale was calibrated using the Fermi edge and the Au $4f$ doublet of a reference Au foil, with the Au $4f_{7/2}$ line at 84 eV. Generally, the shift in binding energy scale and, therefore, the calibration required was larger for higher photon energies. All XPS spectra were recorded using a SPECS Phoibos 150 hemispherical electron analyser with a pass energy of 10 eV. The typical base pressure of the analyser chamber was of the order of $\leq 1 \times 10^{-10}\,\text{mbar}$. Annealing and cleaving experiments were carried out in a separate preparation chamber with a base pressure of $\leq 5 \times 10^{-10}\,\text{mbar}$. When not stated otherwise, (−c) ZnO bulk crystal wafers were used due to their low resistivity ($\sim 0.2\,\Omega\,\text{cm}$), which prevented sample charging effects. Samples were cleaned in ultrasonic baths of acetone, methanol, and isopropyl alcohol for 5 min each and dried in a stream of dry air or nitrogen gas immediately before loading into the system. To ensure optimal thermal and electrical contact, the wafers were mounted on boron nitrite or molybdenum sample holders using tantalum foil.

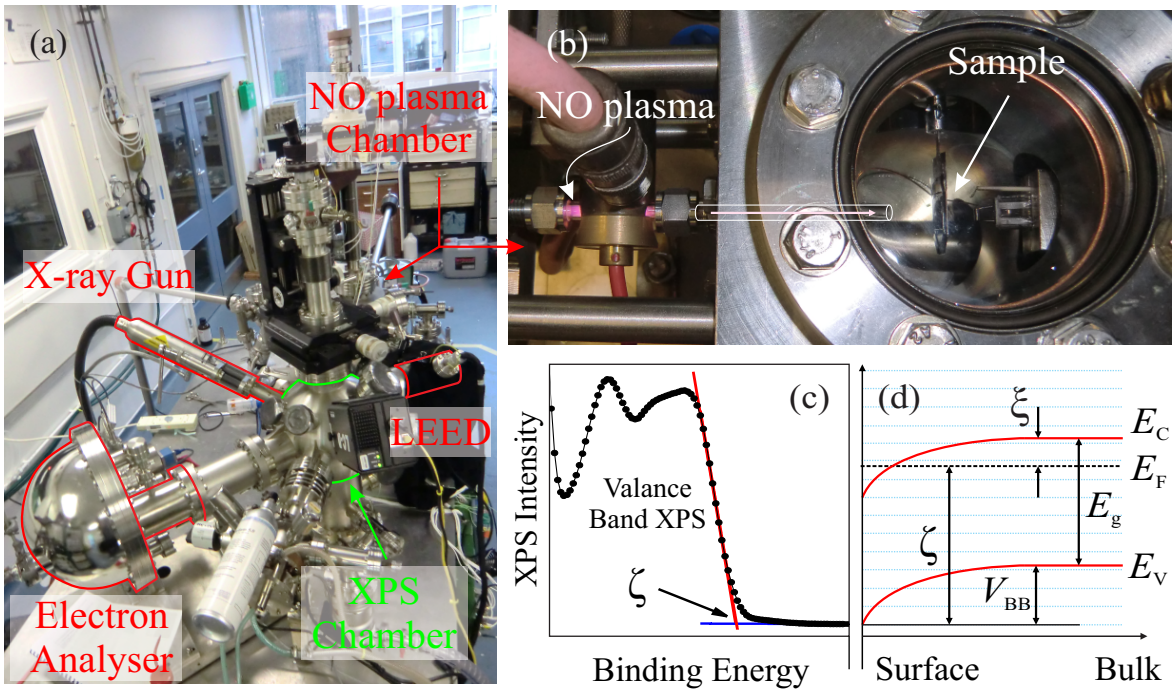

Figure 3.15.: The real-time XPS setup at Aberystwyth University is shown in (a) with equipment fitted to the UHV analyser chamber marked by red contour lines. The NO plasma and connected preparation chamber is shown in (b). (c) and (d) present an exemplary extraction of ζ from the leading valence band edge and the schematic view of the surface band bending V_{BB}.

The absence of sample charging was carefully tested by varying the incident photon flux. No charging effects were observed and all XPS spectra in this thesis were taken without the use of an electron flood gun. Atomic force microscopy carried out after XPS measurements showed no beam induced damage on the ZnO samples.

3.4.2 Real-time XPS at Aberystwyth University

XPS measurements at the SXR beamline of the Australian Synchrotron can only be performed at room temperature to avoid the possibility of sample decomposition contaminating the main synchrotron ring. Furthermore, potential re-hydroxylation of samples from residual gases in the chamber cannot completely be ruled out, even at UHV conditions. Therefore, real-time *in situ* XPS measurements during sample annealing were carried out at Aberystwyth University (United Kingdom). The Aberystwyth setup (see Fig. 3.15) consists of an UHV chamber with a base pressure of 5×10^{-10} mbar, fitted with a Mg K_α ($h\vartheta = 1253.6\,\mathrm{eV}$) x-ray source and a low-energy-electron-diffraction (LEED) unit. Photoelectrons are detected, after transversing a Specs Phoibos 100 hemispherical electron analyser, by a 40 mm double-microchannel plate, a phosphorescent screen, and a 640×480 pixel CCD (charged-coupled device) detector. Real-time data acqui-

sition was carried out in CCD snapshot mode at 1 – 2 Hz, depending on the gate time of the CCD for the Zn $2p_{3/2}$ and O $1s$ core levels, at pass energies of 20 – 60 eV with a snapshot energy window of approximately 10.5 eV. In snapshot mode, the electron analyser remains at a constant energy, and the CCD detector maps the entire XPS spectrum that is dispersed over its focal plane in a single shot [119]. Due to the data file handling limit of the CasaXPS software, five consecutive snapshots were averaged before peak quantification was carried out on the averaged core level spectra.

All samples were cleaned *ex situ* with the same organic solvents as in the previous section and mounted on a molybdenum sample holder, which was then attached to an graphite/boron nitride heater inside the UHV chamber. A thermocouple bolted on the front of the heater faceplate near the sample ensured accurate temperature monitoring. After loading, all ZnO samples were cleaned *in situ* in a stream of *activated* atomic oxygen for 20 min (see Fig. 3.15(b)). The *activated* oxygen was produced by a nitric oxide (NO) plasma, which dissociates NO into atomic nitrogen and atomic oxygen. The nitrogen combines into its molecular form, whereas the *activated* oxygen atoms readily form a chemical bond to any adventitious carbon on the sample surface and gently removes it without appearing to interact with the surface hydroxyl groups [120]. However, NO plasma treatment requires a further 130 °C annealing step to remove excess adsorbed oxygen from the sample surface.

3.4.3 Fitting procedures and monolayer coverage calculation

The CasaXPS software was extensively used in the peak fitting and quantification analysis of the measured XPS spectra, with core level spectra fitting using pseudo-Voigt functions. This software provides individual sum (SGL) and product form (GL) options for the pseudo-Voigt functions. The sum function is believed to show a certain superiority over the product function [121] in terms of fitting quality and has been widely used in this thesis. However, for some samples/core levels, the data could only be meaningfully interpreted using the product formula. In all cases, a Shirley function was used to fit the background signal.

The OH and H_2O components of the O $1s$ core level were fitted with a constrained full width at half maximum (FWHM) and a minimal energetic separation of 1.2 eV and 2.4 eV from the O $1s$ lattice oxygen peak maximum, respectively. These constraints prohibited a shift of the fitting components into the O $1s$ lattice oxygen signal and ensured comparable atomic percentages for all components across all measurements.

The monolayer coverage of surface hydroxyls and water was calculated from the extracted atomic percentages of the OH and H_2O components using a Lambert-Beer absorption law approximation [122, 123]:

$$\frac{I_{\mathrm{ads}}}{I_{\mathrm{ads}} + I_{\mathrm{sub}}} = 1 - \exp\left[-\frac{d}{l}\right] \tag{3.14}$$

with I_{ads} and I_{sub} being the peak areas for the adsorbate and substrate signal (e.g. OH and bulk-oxygen), respectively, d the adsorbate layer thickness, and l the photoelectron mean free path with $l = \lambda_{\mathrm{IMFP}} \cos\theta$. For photon energy of $h\vartheta = 680\,\mathrm{eV}$, the kinetic energy of photoelectrons originating from the O $1s$ core level will be approximately $680\,\mathrm{eV} - 531\,\mathrm{eV} = 149\,\mathrm{eV}$. At this kinetic energy, a TPP-2M calculation yields an photoelectron mean free path l of approximately 6.2 Å [116]. Following the procedure used in Ref. [123] and the references therein, the thickness of 1 ML is approximated as the Zn-OH distance (1.95 Å) plus half of the distance between Zn and O atom in a single three-fold coordinated double layer (0.56 Å) (see Fig. 2.1 in Sec. 2.1). This gives a monolayer thickness of $d = 2.3$ Å. Inserting the values for d and l into equation 3.14 yields a monolayer coverage of unity when $I_{\mathrm{ads}}/(I_{\mathrm{ads}} + I_{\mathrm{sub}}) = 0.31$, for $\theta = 0°$ (i.e. detection perpendicular to the sample surface).

The surface band bending for the various ZnO crystals was determined using the approach of Chambers *et al.* [124] by extrapolating the leading edge of the valence band XPS spectrum to the instrument background, as illustrated in Fig. 3.15(c). The intersection of both linear fits gives $\zeta = E_{\mathrm{F}} - E_{\mathrm{V}}$ from which the surface band bending $V_{\mathrm{BB}} = E_{\mathrm{g}} - \zeta - \xi$ can be calculated (see Fig. 3.15(d)). The energetic distance between conduction band minimum and Fermi level, ξ, can be calculated from $\xi = (k_{\mathrm{B}}T/q)\ln(N_{\mathrm{C}}/n)$, where N_{C} is the conduction band effective density of states ($2.94 \times 10^{18}\,\mathrm{cm}^{-3}$ for ZnO) and n is the bulk carrier concentration. If the resistivity (ρ) or conductivity (σ) of the material in question is known, n can be estimated according to $\sigma = n\,q\,\mu$. For HT ZnO bulk crystals, a carrier mobility of $\mu = 150\,\mathrm{cm}^2\,\mathrm{V}^{-1}\,\mathrm{s}^{-1}$ was typical, and where possible this was confirmed using Hall effect measurements.

4 | Hydrothermal ZnO with low lithium contamination

The conductivity of hydrothermally grown ZnO is strongly influenced by the presence of group I impurities, which compensate shallow donors, resulting in high resistivity material with carrier concentrations 3 – 4 orders of magnitude lower than single crystals grown using the melt or vapour-phase techniques. Recently, HT ZnO with much lower concentrations of lithium and other group I impurities has become available. The following chapter investigates the electrically active defects in this new Low-Li HT ZnO material using thermal admittance spectroscopy (TAS) and deep level transient spectroscopy (DLTS). The study of group I impurities in ZnO is important in the effort to produce p-type ZnO as they have proven acceptor-like properties.

4.1 Lithium in ZnO

Hydrothermally grown ZnO contains high levels of group I impurities due to the use of mineralisers, such as LiOH or NaOH, to increase the solubility of the ZnO precursor material. The dominant impurity is Li with typical concentrations of $10^{17} - 10^{18}\,\mathrm{cm}^{-3}$, followed by Na and K at concentrations typically an order of magnitude lower than Li [9, 64]. Lithium is predicted to act as a deep acceptor on the substitutional Zn site ($\mathrm{Li}_{\mathrm{Zn}}$) and as a shallow donor on interstitial site (Li_{i}) [86, 125]. Both Li configurations have been found experimentally by means of electron paramagnetic resonance [126, 127]. As a shallow acceptor, Li compensates various shallow donors, e.g. H_{i}, H_{O}, $\mathrm{Al}_{\mathrm{Zn}}$, $\mathrm{Ga}_{\mathrm{Zn}}$ or $\mathrm{In}_{\mathrm{Zn}}$, leading to highly compensated material. Consequently, hydrothermally grown ZnO wafers cut from the (+c) direction of their ZnO seed crystal show very low carrier concentrations ($10^{13} - 10^{14}\,\mathrm{cm}^{-3}$) and high resistivities ($10^{2} - 10^{3}\,\Omega\mathrm{cm}$) (see Table 4.1).

The removal of Li and other group I elements results in a less-compensated, lower-resistivity n-type material useful for improved device performance and reduced impurity

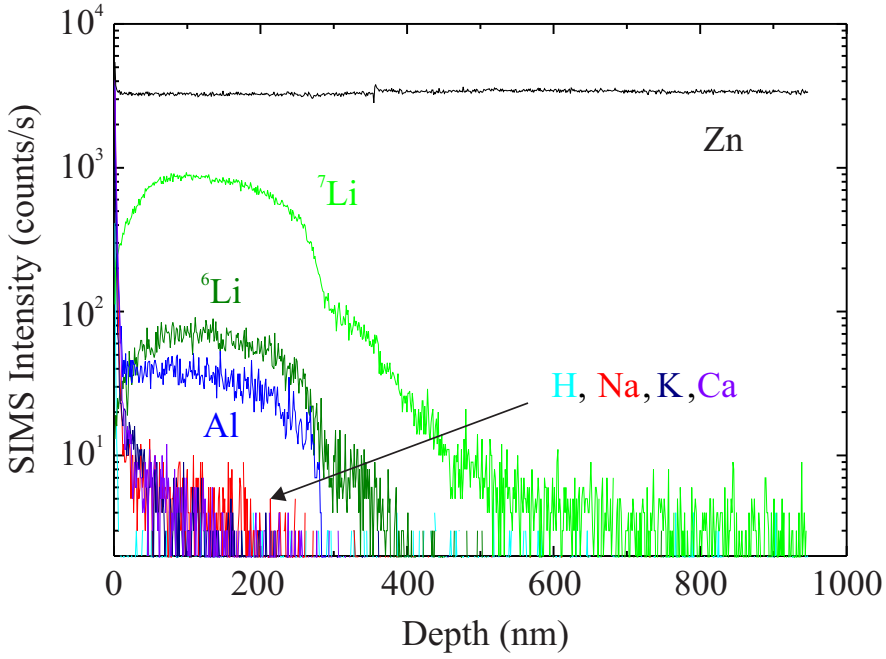

Figure 4.1.: TOF-SIMS depth profiles of conventional hydrothermal O-polar ZnO annealed at 1100 °C in oxygen atmosphere. TOF-SIMS measurements were carried out by Robyn Goacher at University of Buffalo.

interdiffusion during homoepitaxy. Recently, hydrothermally grown ZnO wafers with low Li concentrations of < 0.01 ppm have become commercially available from Tokyo Denpa Co. Ltd. (Japan). This "Low-Li" HT ZnO is prepared by the high-temperature annealing of conventional HT ZnO at 1100 – 1400 °C. Annealing drives Li and other group I impurities from the bulk to the surface where they can be removed by subsequent surface grinding and re-polishing steps.

The time-of-flight secondary ion mass spectrometry (TOF-SIMS) impurity depth profile for a conventional HT ZnO wafer annealed at 1100 °C in oxygen is shown in Fig. 4.1. The data was collected in positive ion mode using a 20 keV C 60$^+$ sputter beam at $\sim$ 0.5 nm/s and a 25 keV Bi$^+$ analyser beam. Significant accumulation of both ^{6}Li and ^{7}Li isotopes as well as Al was observed in a 300 – 400 nm wide region beneath the surface. The SIMS signal for the ^{6}Li isotope is approximately ten times smaller compared to ^{7}Li, which is consistent with their natural abundance (^{6}Li : ^{7}Li = 7.5 : 92.5) [128]. To a lesser extent, Na, K, and Ca accumulation can also been seen in the first 100 – 200 nm. The hydrogen concentration was smaller than the detection limit of the SIMS setup. Using the relative sensitivity factors (RSF) of ZnO for SIMS measurements proposed by Laufer *et al.* [64], one obtains near-surface peak concentrations of approximately 3.2×10^{18} cm^{-3} for Li, 7.6×10^{17} cm^{-3} for Al, and 1.3×10^{16} cm^{-3} for Na. The concentrations of residual group I impurities do however vary between different Low-Li wafers depending

Table 4.1.: Overview of electrical properties of different ZnO single crystal materials.

	n (cm^{-3})	μ ($\mathrm{cm}^2\,\mathrm{V}^{-1}\mathrm{s}^{-1}$)	ϱ ($\Omega\,\mathrm{cm}$)
HT (+c)	$10^{13}-10^{14}$	180 – 200	3000
HT (−c)	10^{17}	140	0.5
HT Low-Li	$10^{15}-10^{17}$	140	0.1 – 10
Melt	$10^{16}-10^{17}$	180 – 190	0.3 – 0.5

on the efficiency of the surface Li-diffusion / re-grinding process resulting in a range of carrier concentration values between $10^{15}-10^{17}\,\mathrm{cm}^{-3}$ (see Table 4.1).

4.2 Schottky diodes on Low-Li HT ZnO

Arrays of high quality Schottky diodes were fabricated on both polar faces of Low-Li HT ZnO single crystal wafers. Each diode consisted of an iridium oxide Schottky contact with a diameter of $\sim 400\,\mu\mathrm{m}$ deposited by *eclipse* pulsed laser deposition (eclipse-PLD) [129] and an electron-beam deposited Ti/Pt ohmic contact. Current density-voltage ($J-V$) characteristics for both polar surfaces are presented in Fig. 4.2. The series resistance for Schottky diodes on Low-Li HT ZnO was calculated from the forward bias region following the approach suggested by Cheung *et al.* [130]. The extracted series resistance was $\sim 200\,\Omega$ dramatically smaller compared to identical diodes fabricated on conventional HT ZnO which had a series resistance of $\sim 9\,\mathrm{M}\Omega$.

This low series resistance results in very high on/off ratios of $I(1\,\mathrm{V})/I(-1\,\mathrm{V}) \sim 10^{10}$ for diodes fabricated on the Zn-polar face to $\sim 10^6$ for diodes on O-polar face. For a set of identical diodes fabricated on both polar faces of the same Low-Li HT ZnO wafer, the ideality factors, η and the zero-bias effective barrier heights, $\Phi_{\mathrm{B}}^{\mathrm{eff}}$, were determined using standard thermionic emission theory [93] and shown in Fig. 4.2 as plots of $\Phi_{\mathrm{B}}^{\mathrm{eff}}$ versus η for each face. Also shown is the image-force-controlled ideality factor limit (i.e. the lowest possible ideality factor, η_{if}), for an ideal laterally homogeneous Schottky barrier. The individual $\Phi_{\mathrm{B}}^{\mathrm{eff}}$ values have not been corrected for image-force lowering effects which would reduce $\Phi_{\mathrm{B}}^{\mathrm{eff}}$ by approximately 70 meV on both polar faces. Fig. 4.2(b) shows that the barrier heights of diodes on the Zn-polar face are consistently higher by almost $\sim 260\,\mathrm{meV}$ than those on the O-polar face. This observation was previously reported by Allen *et al.* [22, 129], who found a similar difference in the barrier heights of Schottky diodes on conventional HT material. It was proposed that this barrier height difference

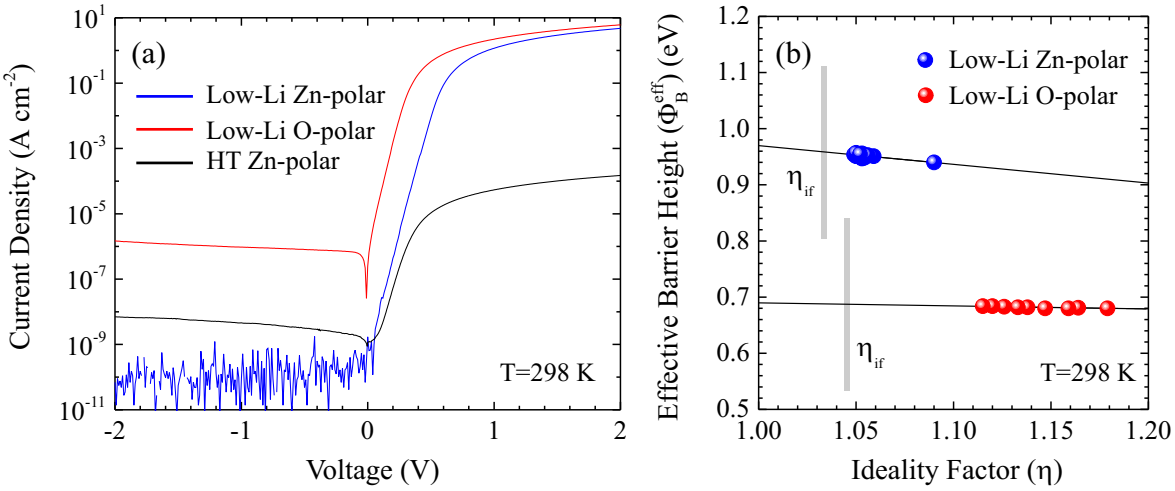

Figure 4.2.: (a) Current density-voltage characteristics of iridium oxide Schottky contacts fabricated on Low-Li HT and conventional HT ZnO. (b) Φ_B^{eff} vs η plots for multiple Schottky contacts on both polar faces of the same Low-Li HT ZnO wafer. The barrier heights are not corrected for image-force-effects which lower Φ_B^{eff} vs η by $\sim 70\,\text{meV}$ on each face.

was due to the presence of equal and opposite bound surface charges on the Zn-polar and O-polar faces produced by the large spontaneous polarisation of ZnO along the c-axis. It was also predicted that this difference may be reduced in materials with higher carrier concentration due to the screening of these polarisation charges. However, Low-Li HT ZnO, with its lower concentration of group I acceptors does have a much higher free carrier concentration ($\sim 10^{17}\,\text{cm}^{-3}$) compared to conventional HT ZnO, yet the barrier height difference between the polar faces is almost identical for both materials suggesting that the proposed screening effects are not significant.

Bias-dependent capacitance and conductance measurements were also carried out on the Schottky diodes on both polar faces and are presented in Fig. 4.3(a-b). The capacitance increases with decreasing reverse bias as the depletion region shrinks reaching a maximum value when positively biased. At this point, flat band conditions in the junction occur corresponding to the built-in voltage V_{bi} of an ideal diode. V_{bi} can also be determined from a $1/C^2$ vs V plot by extrapolation toward $1/C^2 = 0$. Figure 4.3(a – b) yields values of $V_{bi} = 0.45\,\text{V}$ and $0.18\,\text{V}$ for Zn-polar and O-polar face, respectively, which are significantly smaller than the $0.74\,\text{V}$ and $0.36\,\text{V}$ values extrapolated from the corresponding $1/C^2$ vs V plots (see Fig. 4.3(c)). However, the higher built-in potential on the Zn-polar face compared to the O-polar face is consistent with the polarity effect observed in the effective barrier heights.

The net-donor concentration $N_D - N_A$ as function of the depletion width w can be

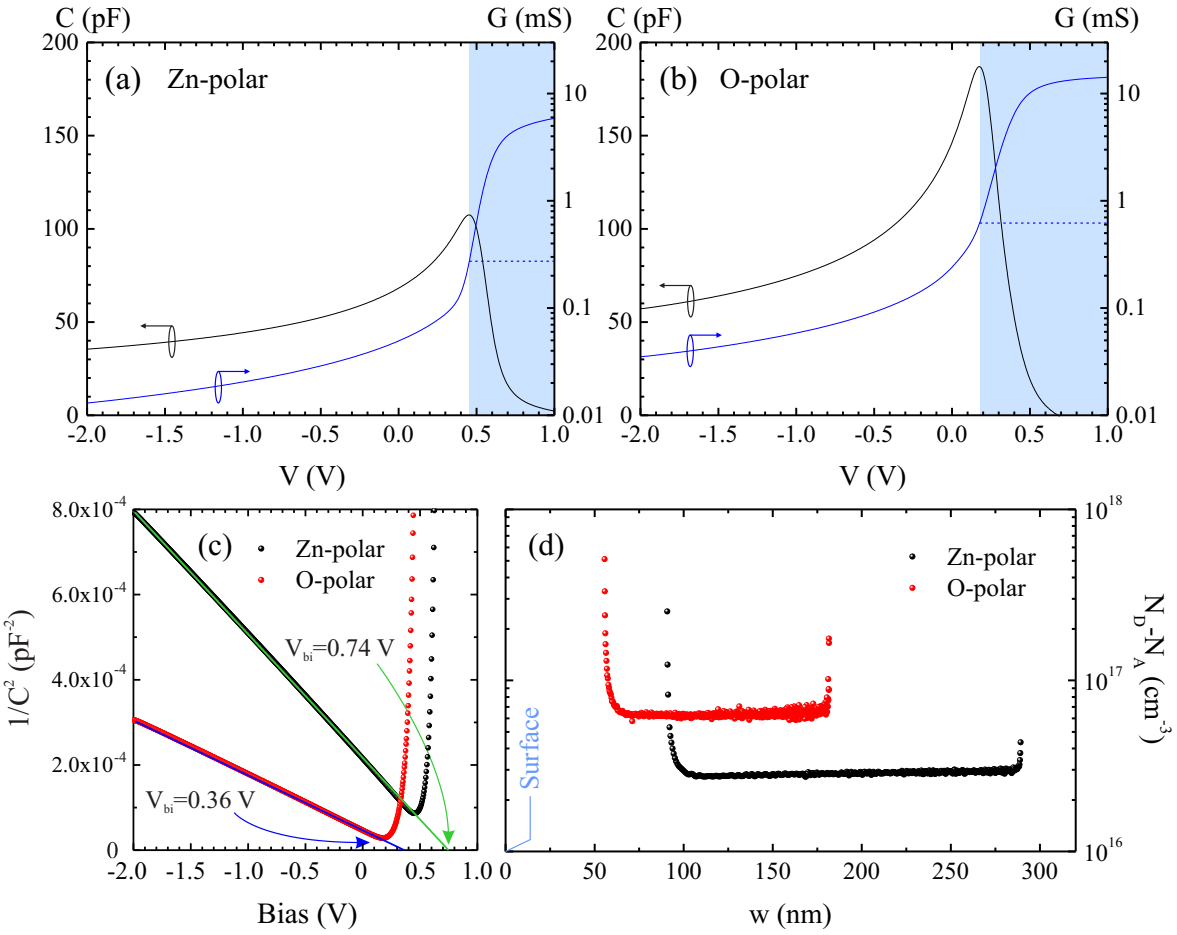

Figure 4.3.: Capacitance C and conductivity G versus diode bias for Zn-polar (a) and O-polar (b) faces Low-Li HT ZnO at 1 MHz. The extraction of the built-in voltage at $1/C^2 = 0$ is shown in (c) and the net-donor concentration for both faces as function of the depletion widths is shown in (d).

calculated from:

$$N_\mathrm{D} - N_\mathrm{A} = -\frac{2}{e\,\varepsilon\,\varepsilon_0}\left[\frac{\mathrm{d}}{\mathrm{d}V}\left(\frac{1}{C^2}\right)\right]^{-1} \qquad \text{and} \tag{4.1}$$

$$w = \frac{\varepsilon\,\varepsilon_0}{C}\,. \tag{4.2}$$

The resulting concentration profile is shown in Fig. 4.3(d). The differences in the depletion widths w can be explained by the difference in diode capacitance between the Zn-polar and O-polar faces. Both faces exhibit a constant net-donor concentration profile of $2.9\times10^{16}\,\mathrm{cm}^{-3}$ and $6.3\times10^{16}\,\mathrm{cm}^{-3}$ for Zn-polar and O-polar face respectively. The strong increase in net-donor concentration close to the surface/interface is an artefact due to the sudden increase in diode conductivity for larger forward biases, as indicated by the shaded area in Fig. 4.3(a – b).

4.3 TAS and DLTS characterisation of Low-Li HT ZnO

Electrically active defects can dramatically affect the electrical and optical performance of semiconductor devices. Temperature-dependent Hall measurements are often employed to identify such defect centres and their energy levels. However, thermal admittance spectroscopy (TAS) and deep level transient spectroscopy (DLTS) offer the opportunity to extract more quantitative parameters, such as the defect level capture cross-section, and an approximate defect concentration. Although both techniques in ZnO have always been limited by the Schottky diode quality, several works report on deep defect levels in thin films and various types of bulk ZnO crystals (i.e. [20, 21, 131]). Less attention has been paid to the role of Li. Figure 4.4(a – d) shows the temperature-dependent TAS measurements on both polar faces of Low-Li HT ZnO for test-frequencies of 20 kHz to 5 MHz and a test signal amplitude of 50 mV. Frequencies lower than 20 kHz result in a strong increase in the signal-to-noise ratio. Following the equations in Sec. 3.1.1, a maximum in $G(\omega)/\omega$ or an inflection point in C, gives the defect emission rate (e_n) at a certain temperature. With these data sets, one can construct an Arrhenius-plot, as shown in Fig. 4.6 and extract the activation energy and capture cross-section.

For low test frequencies in Fig. 4.4, the Zn-polar Low-Li HT ZnO face exhibits four distinct peaks whereas at high frequencies, only the two shallower defect centres, that ionise at low temperatures, are present. The deeper lying defects, with a larger energetic distance to the conduction band minimum, are absent because the test frequency has exceeded the emission rate of these traps. The same process can be observed in the capacitance steps in Fig. 4.4(c). On the O-polar face, only the two shallow defects are observable. For a better comparison, both TAS datasets are shown for a single test frequency of 140 kHz in Fig. 4.4(e) and (f). On the Zn-polar face, four defects with activation energies of 70 meV, 160 meV, 190 meV, and 285 meV are present. For Schottky contacts on the O-polar ZnO surface, only two defect levels with activation energies of 70 meV and 115 meV are observable. The absence of the deeper levels might be explained by the lower quality of the Schottky contacts on the O-polar face as both defect levels are observed in DLTS (see below).

The insets in Fig. 4.4(c) and (d) present the frequency dependence of the diode capacitance at room temperature for different reverse bias voltages. In each case, the capacitance is constant up to the cut-off frequency at ~ 1 MHz. This indicates that only a few defects are present which contribute to the observed capacitance. In addition, these defect centres are uniformly distributed as different bias voltages and, hence, depletion region widths produce similar constant capacitance behaviour.

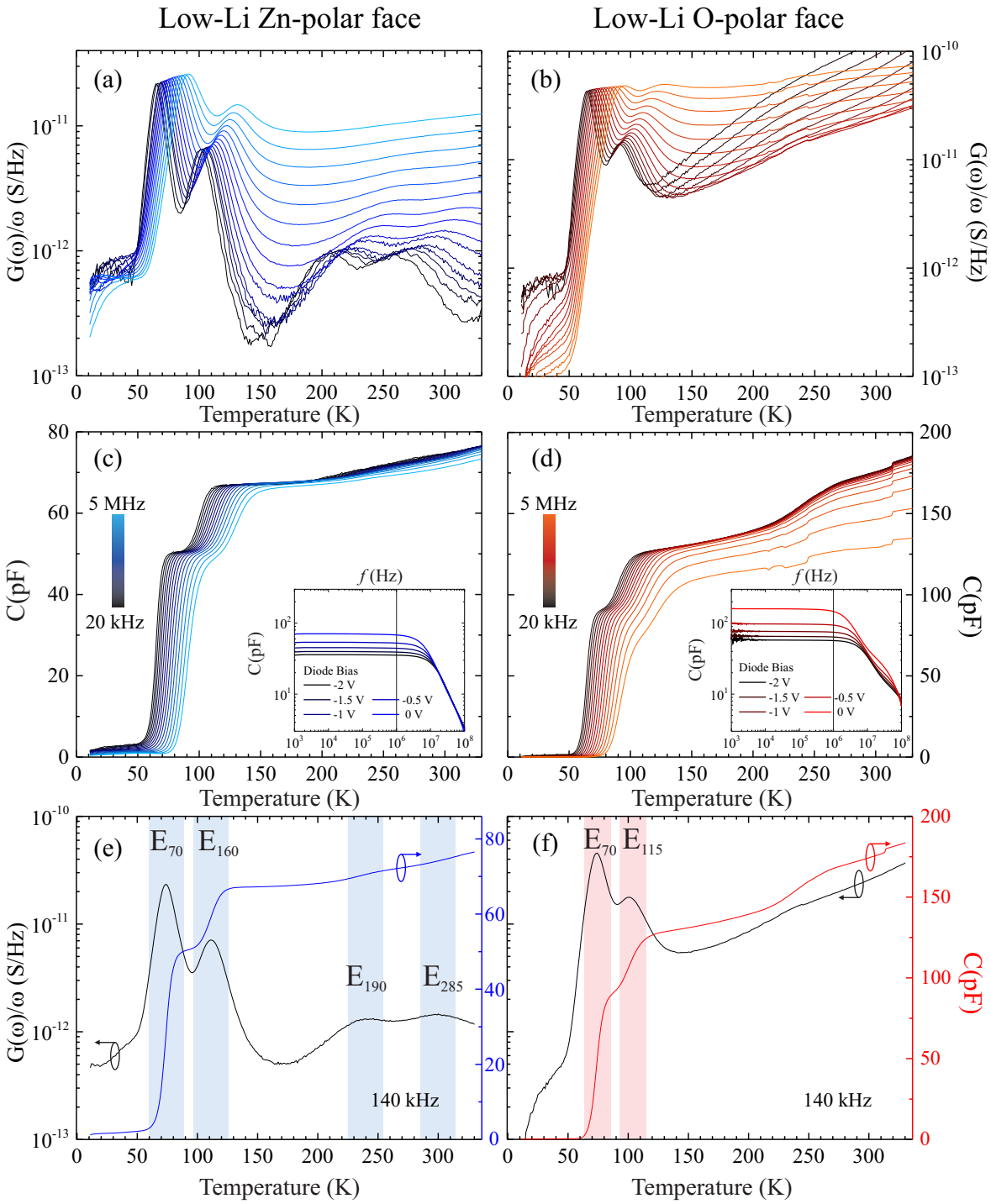

Figure 4.4.: TAS measurements for unbiased Schottky diodes on the Zn-polar (a,c,e) and O-polar (b,d,f) faces of Low-Li HT ZnO. $G(\omega)/\omega$ (a – b) and C (c – d) were obtained as a function of temperature for test frequencies of 20 kHz to 5 MHz between 10 K and 325 K. Individual defect levels are shown for a test frequency of 140 kHz in (e – f) as maxima in $G(\omega)/\omega$ or inflection points in C. Insets in (c) and (d) present the frequency dependence of C for various reverse bias voltages at room temperature.

Using conventional HT ZnO material obtained from the same supplier (i.e. Tokyo Denpa Co. Ltd.), v. Wenckstern *et al.* [20] observed a shallow level at approximately 15 meV which they attributed to hydrogen. The absence of E_{15} in our work is not surprising, as Low-Li HT ZnO is annealed above 1100 °C where H_i and H_O are highly mobile and easily diffuse out of the crystal. The main shallow donor defect, E_{50}, observed by v. Wenckstern *et al.* , is commonly assigned to substitutional Al and is replaced in Low-Li HT ZnO by a slightly deeper defect level, E_{70}. Although SIMS measurements indicate that the Al concentration has been significantly reduced due to the high temperature / re-grinding procedure, we still observe a strong Al-related I_6 transmission in photoluminescence spectroscopy (see chapter 5 for PL results). Evidence for an Al_{Zn}-related defect level comes from Auret *et al.* [21], who observed a E_{64} defect in pulsed laser deposited ZnO thin films on sapphire substrates with a heavily doped Al-buffer layer after annealing at 750 °C. Other effective-mass donors In, Fe or Pt are possible alternatives for E_{70}, as they are major impurities in HT ZnO [9, 62] and are less likely to segregate to the surface due to their larger atomic size. Of all these, In is perhaps the most likely candidate, as an In-related I_9 PL emission line is consistently observed in Low-Li HT ZnO.

Interestingly, Vines *et al.* [132] reported a defect level with an activation energy of 55 meV, which was present in as-received hydrothermally grown ZnO but absent after annealing at $\geq$ 1100 °C with subsequent surface regrinding. The hydrogen-related donor-bound exciton recombination I_{6-H} observed in this work (see Sec. 5.2) for conventional HT ZnO has a donor binding energy of $\sim$ 52 meV (extracted from PL spectroscopy). I_{6-H} is not present in Low-Li HT ZnO or conventional HT ZnO after annealing at 600 °C. This provides further evidence towards a Li-related assignment for both I_{6-H} in PL and the E_{50} defect level in TAS/DLTS for conventional HT ZnO material. The observed Low-Li HT ZnO defect level with an activation energy of 65 – 70 meV is then assigned to either Al_{Zn}, Ga_{Zn} or In_{Zn}. In addition, two defects deeper in the bandgap, i.e. E_{115} and E_{160}, were observed in Low-Li HT ZnO. Both have similar activation energies and capture cross-sections to levels reported by Auret *et al.* [21] in PLD grown ZnO thin films annealed up to 750 °C. These authors observed E_{160} regardless of the annealing conditions, however, E_{115} could only be observed in unannealed films. Auret *et al.* attributed E_{115} to a metastable oxygen-related defect. For E_{160} they found an increased emission rate with applied reverse bias, which indicates a strong Poole-Frenkel effect, commonly observed for donor-like defects. Schifano *et al.* [133] reported on a negative-U centre donor-type defect with an activation energy of 80 – 100 meV and tentatively assigned it to oxygen vacancies.

Figure 4.5 shows DLTS spectra for Schottky diodes fabricated on the Zn-polar and

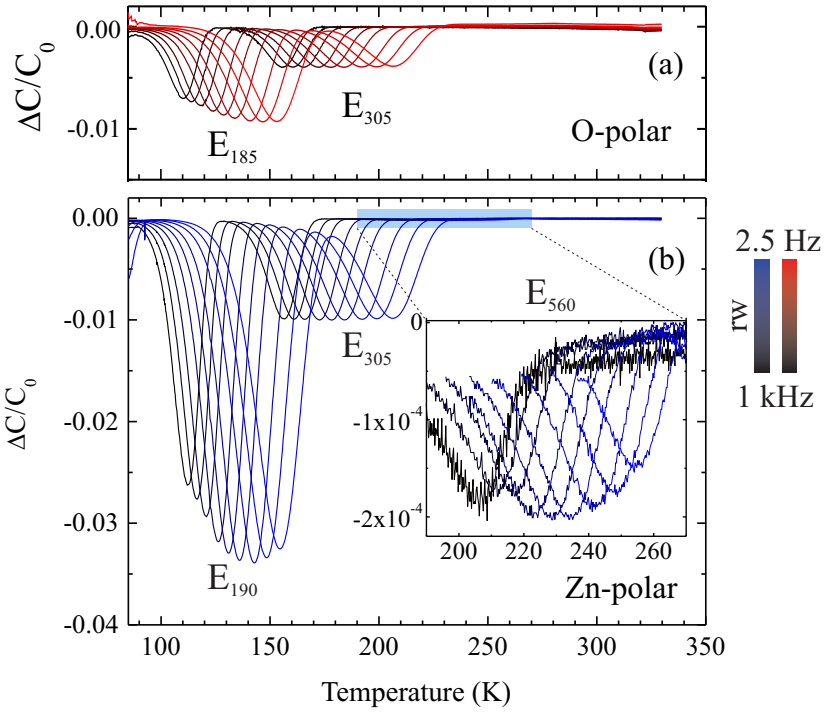

Figure 4.5.: Low-Li HT ZnO DLTS spectra for rate windows rw between 2.5 Hz and 1 kHz measurend on (a) O-polar and (b) Zn-polar faces. The inset is a magnification of the blue shaded area and reveals E_{560}.

O-polar faces of Low-Li HT ZnO with rate windows $rw = 2.5 - 1000$ Hz. Regardless of surface polarity, two deep defects, $E_{185/190}$ and E_{305}, are observed. They are the same defects observed in the TAS measurements on the Zn-polar face. E_{305} has been repeatedly observed regardless of growth method in thin-films, microwires, and bulk ZnO [134, 135] and is generally refered to as E3. Although commonly observed, its origin is uncertain. So far, oxygen vacancy complexes, Zn interstitials [134], Fe- and Ni-related impurities [136] have been proposed. Although, E_{305} in Fig. 4.5 seems to form one broad feature, this peak usually consists of two closely lying levels, E3 and E3' [137], which can only be resolved with enhanced DLTS techniques, such as Laplace-DLTS [97].

Compared to E3, E_{190} is present in Low-Li HT ZnO on both faces in significantly higher concentrations but was not observed in conventional HT ZnO material [20]. In the literature this level is commonly referred to as T2. Recently, Schmidt *et al.* [138] showed that the concentration of T2 strongly depends on the heat treatment of the ZnO crystal, with increasing T2 concentrations observed for higher annealing temperatures. This explains why Low-Li HT ZnO, with its heat treatment up to 1400 °C shows a significantly larger T2 signal than microwires grown at 950 °C or PLD films deposited at 650 °C, as well as the absence of T2 in conventional HT ZnO which is grown at only

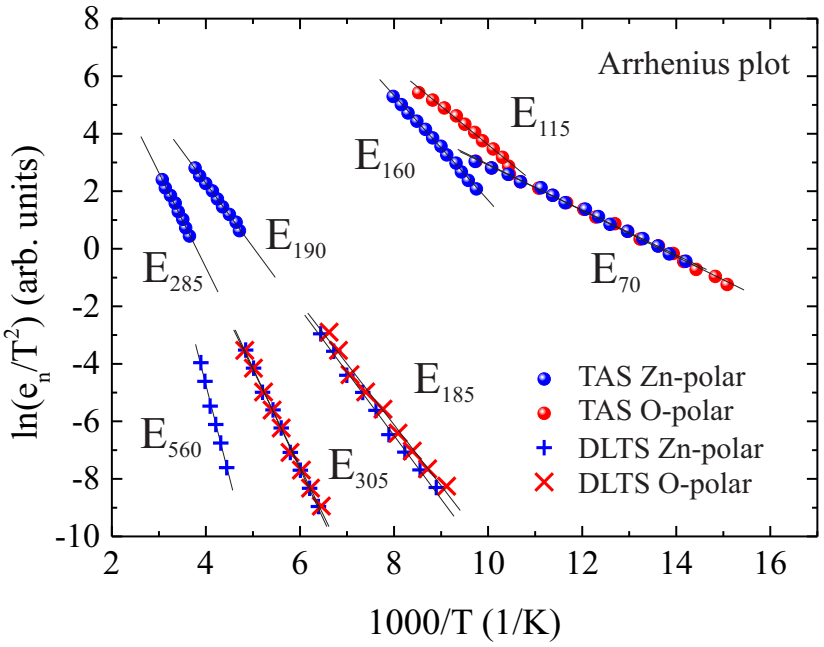

Figure 4.6.: Arrhenius plot of defect levels obtained from TAS and DLTS. Solid lines indicate linear fits to the data from which activation energy and apparent cross-section were obtained.

300 – 400 °C. In addition to the temperature dependence of T2, Schmidt *et al.* [138] showed that its activation energy and apparent cross-section depend on its concentration and, therefore, on the position of E_F. They proposed a complex involving a donor and a zinc vacancy (V_{Zn}) acceptor. Calculations show that V_{Zn} has a smaller formation energy for higher lying Fermi levels [16, 135, 139]. If the participating donor is abundantly present, then the concentration of T2 would only depend on the concentration of V_{Zn}, which are preferentially formed at higher temperatures.

A third defect, E_{560} or E4 in the literature, with a signal intensity 50 times lower than that of E3 can be observed but only on the Zn-polar face, possibly due to the better Schottky contact characteristics on this face and is shown in the inset in Fig. 4.5(b). Similar levels have been reported in vapour-phase-grown ZnO [140] and oxygen-implanted ZnO thin films [141]. Furthermore, irradiation with He^+ and H^+ ions introduced E4 into bulk ZnO, which led to the assumption that E4 is related to V_O [142, 143]. However, Zn- and O-ion implantation [144] did not produce any sign of E4. Recently, Quemener *et al.* observed that annealing in a Zn-rich ambient induced an E4 signal, whereas annealing in an O-rich ambient quenched the signal, independent of the background impurity level or growth conditions [145]. In conclusion, E4, like T2, seems to be introduced during the high temperature annealing process involved in the production of Low-Li HT ZnO rather than being linked to group I impurities.

Table 4.2.: Electronic properties of defects detected by TAS and DLTS in Low-Li HT ZnO compared to conventional HT ZnO.

		Low-Li HT ZnO						Conventional HT ZnO (Ref. [20])		
		Zn-polar			O-polar			Zn-polar		
		E_t (meV)	σ (cm^{-2})	N_t (cm^{-3})	E_t (meV)	σ (cm^{-2})	N_t (cm^{-3})	E_t (meV)	σ (cm^{-2})	N_t (cm^{-3})
TAS		70	–	6×10^{16}	70	–	1×10^{16}	13	–	–
TAS		160	4×10^{-13}	9×10^{15}	115	2×10^{-14}	3×10^{15}	52	6×10^{-17}	–
TAS	T2	190	6×10^{-17}	2×10^{15}	–	–	–	–	–	–
TAS	E3/E3	285	2×10^{-16}	2×10^{15}	–	–	–	–	–	–
DLTS	T2	190	7×10^{-17}	2×10^{15}	185	6×10^{-17}	1×10^{15}	318	–	8×10^{14}
DLTS	E3/E3’	305	7×10^{-16}	6×10^{14}	305	5×10^{-16}	5×10^{14}	321	–	4×10^{14}
DLTS	E4	560	2×10^{-12}	1×10^{13}	–	–	–	–	–	–

4.4 Summary

The electrical properties of hydrothermally grown ZnO single crystals with low lithium concentrations (Low-Li HT ZnO) were studied. The fabrication of high quality Schottky contacts on both polar faces of Low-Li HT ZnO enabled the use of the capacitance-based defect spectroscopy techniques TAS and DLTS to investigate the electrically active defects present in this material. The key findings were:

- Annealing in an oxygen ambient at $T \geq 1100\,^{\circ}C$ leads to the segregation of Li and Al in the first $\sim 300\,nm$ beneath the crystal surface. An additional re-grinding and polishing step can significantly reduce the Li and other group I concentration to $< 0.01\,ppm$.

- Low-Li HT ZnO wafers exhibit free carrier concentrations $1-4$ orders of magnitude higher than for conventional HT ZnO wafers. This is due to the removal of shallow Li acceptors which efficiently compensate the shallow donors in HT ZnO.

- Iridium oxide Schottky contacts fabricated on the Zn-polar face of Low-Li HT ZnO samples exhibit extremely high rectification ratios, of up to 10 orders of magnitude with ideality factors of 1.05, close to the image-force-controlled limit for ideal contacts. Schottky contacts fabricated on the Zn-polar face exhibit higher effective barrier heights than on the O-polar face, with the barrier height difference ($\sim 260\,meV$) similar to that observed for conventional HT ZnO.

- TAS and DLTS revealed six different trap levels in Low-Li HT ZnO: E4/E_{560}, E3/E_{305}, T2/E_{190}, E_{160}, E_{115}, and E_{70}. Of these, T2/E_{190} appears to be introduced by the high temperature heat treatment process and is thought to be due to the creation of V_{Zn}. The E_{50} defect commonly observed in conventional HT ZnO was absent in Low-Li HT ZnO. Significantly, both E_{50} and the hydrogen-related PL emission line I_{6-H} are only observed in ZnO wafers that contain high concentrations of Li and hydrogen. The PL measurements, carried out later in this work, suggest that a complex of Al, Li and H is responsible for I_{6-H}. In the post-growth annealing and regrinding process involved in the production of Low-Li HT ZnO, this Li_{Zn}-H_O-Al_{Zn} complex dissociates as Li and H are removed from the crystal. The remaining substitutional Al_{Zn} may then form the E_{70} defect level, exclusively observed in the Low-Li HT ZnO material.

5 Photoluminescence Spectroscopy of ZnO

Low temperature photoluminescence spectroscopy (PL) provides valuable insights into the impurity and defect nature of semiconductor materials. PL spectroscopy has been widely used in the last 50 years to characterise ZnO bulk crystals, thin films, and nanostructures. However, relatively few of the observed exciton features have been conclusively assigned to the responsible impurity or native defect. In this section, high-resolution PL is carried out on ZnO bulk single crystal wafers of different growth techniques and post-growth treatments. A comparison of the PL emission of these materials in association with their different impurity concentrations is used to identify the origin of a number of new features. Conventional hydrothermally grown ZnO bulk crystals will be abbreviated as *HT ZnO* in this work and hydrothermally grown ZnO with low lithium concentrations will be referred to as *Low-Li HT ZnO*. Both HT ZnO and Low-Li HT ZnO single crystals were obtained from Tokyo Denpa Co. Ltd. (Japan). In addition, mirror-polished epi-ready HT ZnO bulk crystals, also with reduced lithium concentrations, were supplied by the Mitsubishi Chemical Corporation and are abbreviated as *Mitsubishi/Mitsu. ZnO*. *Melt-grown* ZnO single crystals were obtained from Cermet Inc. (USA).

5.1 Free Exciton Recombination in ZnO

Investigations into the nature of free excitons in ZnO, are usually done by means of reflectivity rather than PL measurements as shown in Fig. 5.1(a) (see also PhD thesis of M. Henseler [146]). This is due to the very wide dynamic range required in PL measurements to separate emission from the longitudinal and transverse free excitons A_{L} and A_{T} (factor of 10^3 lower intensity than donor-bound excitons) from their B- and C-equivalents and their excited states (factor of $10^2 - 10^3$ lower intensity than A_{T}). Figure 5.1(a) is a reproduction of the work of Chichibu *et al.* [147] which identifies the

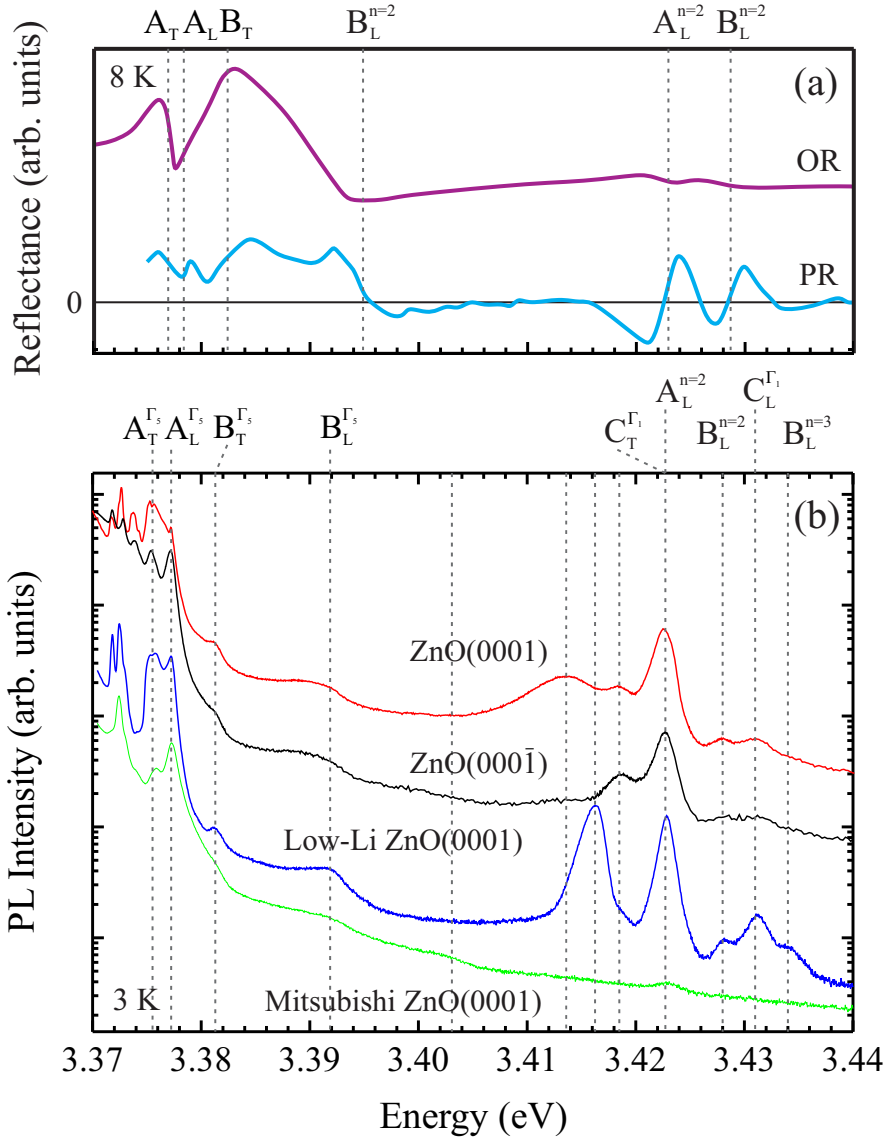

Figure 5.1.: Free exciton states in bulk ZnO. The upper panel is a reproduction of the work of Chichibu *et al.* [147] using low temperature (8 K) polarised optical reflectance (OR) and photoreflectance (PR) with their line assignment shown above. The lower panel shows PL measurements carried out at the University of Canterbury with alternate line assignment. The energy scale is the same for both graphs. For a comparison of the line positions with literature see Table 5.1.

free excitons as well as their excited states. Due to the high dynamic range of the current PL setup it was possible to resolve these features via low temperature PL spectroscopy as well as several, previously unreported lines on various types of ZnO bulk single crystals.

Emission from longitudinal and transverse free A-excitons (A_L, A_T), as shown in the lower panel of Fig. 5.1(b), exhibits the highest intensity, followed by emission from free

excitons involving holes from the B-valence band, B_T (3.3813 eV) and B_L (3.3920 eV). At even higher energies, the excited states $A_L^{n=2}$ (3.4227 eV) and $B_L^{n=2}$ (3.4280 eV) can be resolved. The assignment of free excitons from the C-valence band, especially C_T is not straightforward. Chichibu *et al.* [147] assigned the line at 3.4187 eV as C_T. Other authors report values with slightly higher energies, with C_T overlapping with $A_L^{n=2}$.

For a literature comparison see Table 5.1. Two additional peaks are resolved for the conventional HT ZnO material at 3.4136 eV and 3.4187 eV, with the former significantly stronger on the Zn-polar face. Chichibu *et al.* [148] observed a broad peak in this energetic region in ZnO epilayers and attributed it to the excited states of bound excitons. No excited states with energies above A_L were reported in the work of Meyer *et al.* [149] and it is questionable why excitons should be bound to donors with energies above the free exciton energy [150]. Furthermore, as both polar faces of HT ZnO (+c) crystals show the same intensity in the respective donor bound exciton transitions but not in the peaks in question, this excited state assignment seems unlikely.

The Low-Li HT ZnO material exclusively exhibits an intense feature at 3.416 eV as well as superior resolution for the higher excited states. These Low-Li HT ZnO wafers are annealed up to 1100–1400 °C and subsequently re-ground and re-polished. The intense transition could therefore be linked to a polishing defect or the removal of light impurities such as H or Li which would otherwise mask the transition in conventional HT ZnO.

The epi-ready Mitsubishi material has been mirror-polished in an undisclosed way. Only the free A and B excitons and $A_L^{n=2}$ can be observed. However, a small shoulder at approximately 3.4031 eV, which is not present in the other wafers, is observable. Considering the high absorption coefficient for free excitons and the resulting small escape depth beneath the surface [27], the absence/low intensity of free exciton features on the Mitsubishi sample was attributed to the surface modifications introduced by different polishing mechanisms. Hamby *et al.* [151] reported on decreased luminescence intensity as well as line broadening for ZnO bulk crystals that were mechanically polished compared to chemo-mechanically polished. They also reported on an emerging donor-acceptor pair (DAP) transition with prolonged mechanical polishing. However, as will be shown in the following sections, the D^0X region exhibits very narrow line widths and no DAP transitions.

In this work (see Table 5.1), the $A - B$ free exciton splitting was calculated as $\Delta(A_T^{\Gamma_5} - B_T^{\Gamma_5}) = 5.9$ meV and $\Delta(A_L^{\Gamma_5} - B_L^{\Gamma_5}) = 14.3$ meV, which is in close agreement with literature values reported for HT ZnO wafers from Tokyo Denpa, e.g. 5.93 meV and 12.33 meV [150]. Gruber *et al.* [154] performed calculations on the change in $A -$

Table 5.1.: Overview of the free exciton positions observed in this work compared to literature values. All values in eV.

Ref.	$A_T^{\Gamma_5}$ n=1	$A_L^{\Gamma_5}$ n=1	$A_L^{\Gamma_5}$ n=2	$B_T^{\Gamma_5}$ n=1	$B_L^{\Gamma_5}$ n=1	$B_L^{\Gamma_5}$ n=2	$B_L^{\Gamma_5}$ n=3	$C_T^{\Gamma_1}$ n=1	$C_L^{\Gamma_1}$ n=1
This work[1]	3.3754	3.3773	3.4227	3.3813	3.3916	3.4281	3.4340	3.4227	3.4311
[146][2]	3.3746	3.3765	–	3.383	3.394	–	–	3.421	3.434
[147, 148][1,2]	3.3767	3.3785	3.4214	3.3821	–	3.3932	3.4274	–	–
[152][1,2]	3.3757	3.3771	3.4220	3.3898	–	–	–	3.4360	–
[150][1,3]	3.3755	3.3775	3.4228	3.3815	3.3899	3.4283	3.4348	3.4228	3.4312
[153][2]	3.3757	3.3785	3.4260	3.3835	3.3996	–	–	3.4219	3.4338
[153][1]	3.3747	3.3765	–	3.3834	3.3925	–	–	–	–

[1] Photoluminescence
[2] Photoreflectivity
[3] All given values were obtained from (+c) Tokyo Denpa wafers.

B splitting under compressive and tensile strain and showed that for a c-axis strain between $\varepsilon_{cc} = \Delta c/c = -4 \times 10^{-3}$ and 4×10^{-3} the splitting is close to the bulk value of 5 – 6 meV. Furthermore, Schleife *et al.* [155] found that the $A-B$ splitting compared to the $A-C$ splitting is largely uninfluenced by biaxial strain in wurzite ZnO. The measured $A-B$ and $A-C$ splittings are similar for all investigated materials. Minor deviations might be introduced by the relatively broad transitions of the B and C excitons but the same degree of strain can be assumed. On the other hand, the $\Delta A_{LT}^{\Gamma_5}$ splitting, given in Table 5.2, changes under different annealing conditions as well as for different wafer types. For the conventional (+c) HT ZnO material, the extracted values are in close agreement with literature. Although the Zn-polar face yields higher splittings than the O-polar face this is attributed to the fact, that A_L and A_T are more distinct on this face as opposed to a polarity-related difference. In addition, the broad peak formed by A_L and A_T on the O-polar face has approximately the same width as the fully resolved peaks on the Zn-polar face. The only deviation is the Cermet wafers with relatively small splitting compared to the literature. However, this splitting increases after annealing in oxygen and forming gas.

The energetic distance between the ground state $A_L^{n=1}$ and the excited state $A_L^{n=2}$ of the A exciton can be used to calculate the free exciton binding energy. Under the assumption of hydrogen-like energy levels and an energy separation of 45.3 meV, a free exciton binding energy of 60.4 meV is obtained, which is in very good agreement with literature [153]. Furthermore, it is possible to approximate the bandgap at the measurement temperature of 3 K, which yields 3.4377 eV.

Table 5.2.: $\Delta A_{\mathrm{LT}}^{\Gamma_5}$ splitting for different wafers and processing conditions. All values in meV.

	as-received ...-face					O_2 ann.		N_2 ann.		FG ann.	
	Zn	O	a	m	r	Zn	O	Zn	O	Zn	O
HT (+c)	1.91	1.89	1.98	2.07	1.89	1.89	1.61	1.74	1.47	1.84	1.24
HT (−c)	1.93	1.89	–	–	–	–	–	–	–	–	–
Low-Li HT	1.98	1.98	–	–	–	–	–	–	–	1.75	1.52
Mitsubishi	2.11	1.73	–	–	–	–	–	–	–	–	–
Mitsu. offcut	2.07	1.75	–	–	–	–	–	–	–	–	–
Cermet	1.66	1.43	–	–	–	1.89	1.52	–	–	1.89	1.25
HT [27]	2.07	1.96	–	–	–	–	–	–	–	–	–
Cermet [27]	1.96	2.03	–	–	–	–	–	–	–	–	–

As the free excitons are less resolved on the ZnO$(000\bar{1})$ polar face, the uncertainty for the given values is higher.

5.2 Bound exciton recombination in ZnO

Excitons can readily bind to neutral and ionised donors and acceptors leading to further recombination lines in the PL spectra at emission energies lower than for the free excitons. In the following, we denote excitons bound to neutral donors (acceptors) as D^0X (A^0X) and ionised donors (acceptors) as D^+X (A^+X). Rather than giving the peak position for every observed transition, usually the localisation energy E_{loc} defined as energy difference between A_{T} and the respective line in question, is usually reported in the literature. The energetic position of the various bound excitons and, therefore, their E_{loc} depends on the ratio of the effective electron to hole mass $\sigma = m_{\mathrm{e}}^*/m_{\mathrm{h}}^*$ in the semiconductor. Therefore, the ordering in ZnO is thought to be $E_{\mathrm{loc}}(D^+X) < E_{\mathrm{loc}}(D^0X) < E_{\mathrm{loc}}(A^0X)$ [18], although D^0X and A^0X might partially overlap. Theoretical calculations [156] show that the binding of excitons to ionised acceptors should be unstable in ZnO as a free electron and neutral acceptor is energetically favourable.

Thomas [107] first reported bound exciton transitions in ZnO in 1960, addressing them as "impurity excitons". Five years later, Reynolds *et al.* [57] introduced the labelling system of $I_1 - I_{10}$ for the ten unidentified peaks they observed, which is universally used today. A significant amount of insight into the photoluminescence properties of ZnO was provided by the group of Meyer *et al.* whose work [17] is by far the most cited reference in the field.

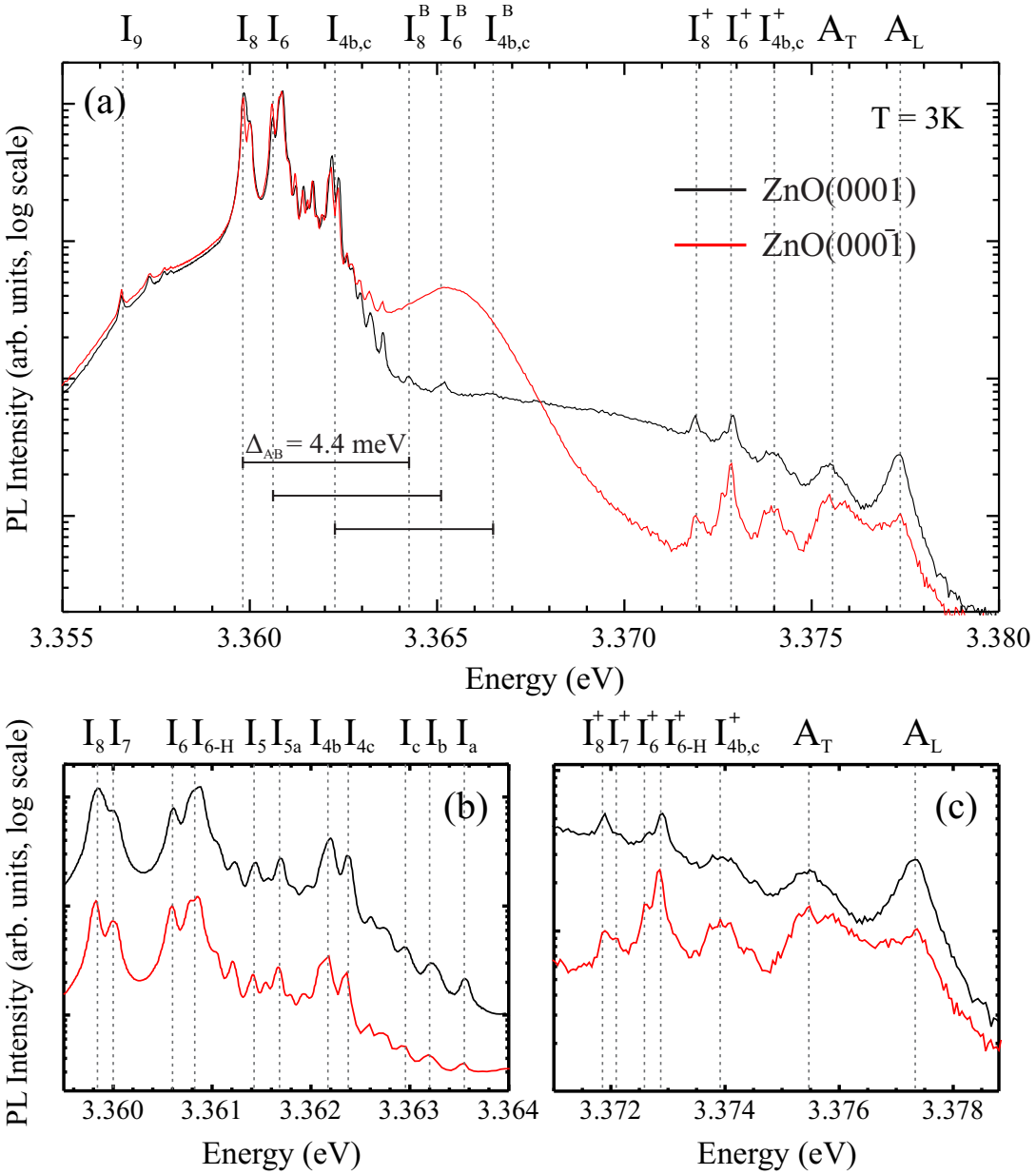

Figure 5.2.: Photoluminescence spectra of the near-band-edge region of hydrothermally grown ZnO bulk single crystals (a) at 3 K. The dominant D^0X region is enlarged in (b) and the D^+X region in (c). The Zn-polar face (ZnO(0001)) is shown in black and the O-polar face (ZnO(000$\bar{1}$)) in red. All PL spectra in (b) are vertically offset.

Figure 5.2(a–c) shows the near-band-edge PL recorded at 3 K in this work from the Zn-polar ZnO(0001) and O-polar ZnO(000$\bar{1}$) faces of a HT ZnO bulk single crystal obtained by Tokyo Denpa Co. Ltd. (Japan). For the near-band-edge region, a sampling step size of 46 μeV (0.005 nm) was chosen while for the dominant donor-bound excitons in Figure 5.2(b) a scanning step size of 9 μeV (0.001 nm) was used, which allowed the resolution of transition lines with a full width at half maximum (FWHM) as low as

50 µeV, above their respective backgrounds. All lines were labelled in accordance with Reynolds *et al.* [57] and Meyer *et al.* [17]. An overview of all PL emission lines observed in this work can be found in Table A.1.

To date, the physical identity of the responsible donor has only been established for a few of the D^0X lines. For example, Strassburg *et al.* [157] observed a strong I_9 line at 3.35657 eV in In-doped films after annealing. Subsequent secondary ion mass spectroscopy (SIMS) revealed In aggregation at the sample surface leading to the assignment of I_9 to indium. The identification of I_8 (3.35984 eV) was achieved mainly by radiotracer methods [158], implanting ZnO with the different Ga and Zn isotopes. Furthermore, Ga readily incorporates into ZnO thin films from GaN substrates or templates [159, 160] and subsequently leads to intense I_8 lines. See Sec. 8.1 for the findings of Ga implantation studies carried out in this work.

The most commonly reported recombination line is I_6, which is attributed to Al. Evidence comes from Al implantation experiments [161] as well as SIMS [17]. Al is routinely found in films grown on an Al_2O_3 substrate due to substrate diffusion. In our high resolution PL spectra shown in Fig. 5.2 two distinct transitions, I_6 (3.36055 eV) and I_{6-H} (3.36081 eV) can be observed. It will be shown later that only I_6 is related to substitutional Al, whereas I_{6-H} is related to an aluminium/lithium/hydrogen complex.

Hydrogen is also commonly associated with I_4 at 3.3628 eV, which was not observed in any of the hydrothermal ZnO material. Instead a close lying doublet transition occurs at 3.36214 eV and 3.36233 eV, labelled I_{4b} and I_{4c}. As Meyer *et al.* [149] labelled an unknown transition at 3.3620 eV as I_{4a}, the notation naturally follows with the subscripts b and c. Lines I_{4b} and I_{4c} have not been previously reported in the literature. The reason for that may be the relatively small distance from the conventional I_4 line, which is commonly observed in melt and vapour-phase grown material. The purpose of the next chapters is to link $I_{4b,c}$ as well as I_{6-H} to hydrogen. For the remaining transitions I_5, I_{5a} and I_7 the chemical nature of the donor has not yet been established.

Excitons bound to ionised donors (D^+X) can be observed (Fig. 5.2(c)) at higher energies compared to their neutral donor-bound counterparts. In general, the D^+X intensity scales roughly with the intensity of their D^0X counterparts. Therefore, several authors have reported on correlated pairs of emission lines e.g. I_0 and I_6, I_1 and I_8, as well as I_2 and I_9 [17, 162]. Magneto-PL measurements [18, 163] provided proof of the ionised nature of the hitherto unidentified I_0, I_1, and I_2. In this work, D^+X transitions are marked as I_x^+. Although, D^+X transitions have been previously reported, the resolution obtained in this work is unparalleled for PL studies of ZnO. For the closely lying I_7 and I_8 lines, the corresponding ionised versions (I_7^+ and I_8^+) can be

resolved at 3.37217 eV and 3.37189 eV, respectively. The same holds for I_6^+ (3.37260 eV) and $I_{6-\mathrm{H}}^+$ (3.37286 eV). Only $I_{4\mathrm{b,c}}^+$ merges to a single broad transition (3.37392 eV). The I_9^+ transition (3.36771 eV) is not observed in as-received HT ZnO, however it does appear after annealing in an oxygen atmosphere (see Sec. 6.1).

The dominant $\mathrm{D^0X}$ lines exhibit another set of related lines, spaced ~ 4.4 meV toward higher energies. These lines result from donor-bound excitons involving a hole from the B-valence band. The splitting between the A and B valence bands has been calculated to be 4.7 – 4.9 meV [54] with experimentally reported values closer to 4.5 meV [149]. This is in good agreement with the value obtained from the spectra in Fig. 5.2(a). Excited state transitions, such as excitons involving holes from the B-valence band and rotational-vibrational states (e.g. I_a) can be identified by their unique luminescence temperature dependence which is presented in the next section.

A direct comparison of the PL spectra taken on the Zn-atom-terminated ZnO(0001) face and the O-atom-terminated ZnO($000\bar{1}$) face reveals a broad Gaussian-shaped peak on the latter face centred at about 3.3653 eV. This feature was constantly observed on all O-polar face samples investigated in this work and can even be used to determine the polarity of the crystal surface. In contrast, an almost linear background emission is consistently observed on the Zn-polar face, which extends from the B-valence band replicas to the $\mathrm{D^+X}$ region. At higher energies, the background intensity on the O-polar face decreases dramatically and is significantly lower in the $\mathrm{D^+X}$ region compared to the Zn-polar face. Due to the lower background intensity, the individual $\mathrm{D^+X}$ transitions can be more easily distinguished on the O-polar face.

A similar broad feature at the same energetic position is often reported for ZnO and GaN nanostructures [164, 165] and occasionally in bulk crystals [166]. The origin is thought to be a surface-related donor-bound exciton (SX) recombination which is strongly influenced by adsorbates on the surface. For ZnO, an exciton bound to a surface terminated by OH-species is a likely candidate [167]. An alternative explanation is given by Sann *et al.* [168], who observed an emission line at $I_{3\mathrm{s}} = 3.366$ eV after annealing ZnO powder in an $\mathrm{NH_3}$ atmosphere. Using electron paramagnetic resonance (EPR), this transition was assigned to Zn interstitials (Zn_i).

Apart from I_4, I_6 and I_8, the chemical origins of the remaining transitions are unknown. Shallow donors should be formed by group III elements on the Zn lattice site or by group VII elements on an O lattice site. Meyer *et al.* [149] argued that the group III element boron could be a candidate for $I_{4\mathrm{a}}$, $I_{5\mathrm{a}}$ or I_5 as it is lighter than Al and should, therefore, have a smaller localisation energy. However, SIMS measurements performed in this work could not detect any traces of boron. The group VII elements F, Cl, Br, and I were also not detected.

5.2.1 Temperature-dependent PL

With increasing temperatures, most recombination lines generally decrease in intensity as the underlying excitonic complexes thermally dissociate and bound excitons become free excitons. Certain transitions, however, show an initial increase in intensity with increasing temperature. These lines can be assigned to excited states, such as excitons involving holes from the B-valence band or rotational-vibrational states [18]. A third group of excited states, electronic-excited states, are only resolvable in PL excitation experiments. To distinguish between the first two types and to identify the nature of the lines observed in Fig. 5.2, temperature-dependent PL measurements were carried out between 3 K and 120 K. The temperature evolution for both polar faces is shown in Fig. 5.3.

The peak intensities of the dominant transitions are shown in Fig. 5.4 as a function of inverse temperature. The underlying temperature dependence was fitted using a model proposed by Bimberg *et al.* [169]. In addition, a second term was introduced into Eq. 5.1 to account for the temperature-dependent activation of the luminescence, similar to the one proposed by Shibata in Ref. [170]. The constants A_i yield no directly accessible information, but can be best described in the context of Boltzmann statistics as the ratio of the number of degeneracies for different energy levels.

$$I(T) = \frac{A_0}{1 + \sum_{i=1}^{n} A_i \exp\left(\frac{-E_i}{k_\mathrm{B}T}\right)} \cdot \left[1 + A_{n+1} \exp\left(\frac{-E_\mathrm{A}}{k_\mathrm{B}T}\right)\right] \tag{5.1}$$

E_i are the different decay energies and E_A the activation energy. For emission lines with a monotonic decrease in luminescence intensity with increasing temperature, two decay energies (n=2) were used in the fitting process while only one (n=1) was required when an intensity increase was present. Intensity refers to the peak intensity of the respective line due to the fact that the close spacing of peaks prohibited meaningful peak integration. In general, the temperature-intensity relationship could not be sufficiently fitted by a single level model ($n = 1$). However, because extracted decay and activation energies depend somewhat on the fitting procedure and/or weighting of the data, the values are not exact. The obtained decay and activation energies are summarised in Table 5.3.

Lines with a monotonic decrease in intensity with increasing temperature belong to donor-bound exciton transitions and the extracted decay energies should, in general, approximately scale with their localisation energy. This relationship is only partially observed for the extracted energies. In addition, decay energies obtained from the O-polar face tend to be lower than those from the Zn-polar face. Interestingly, the

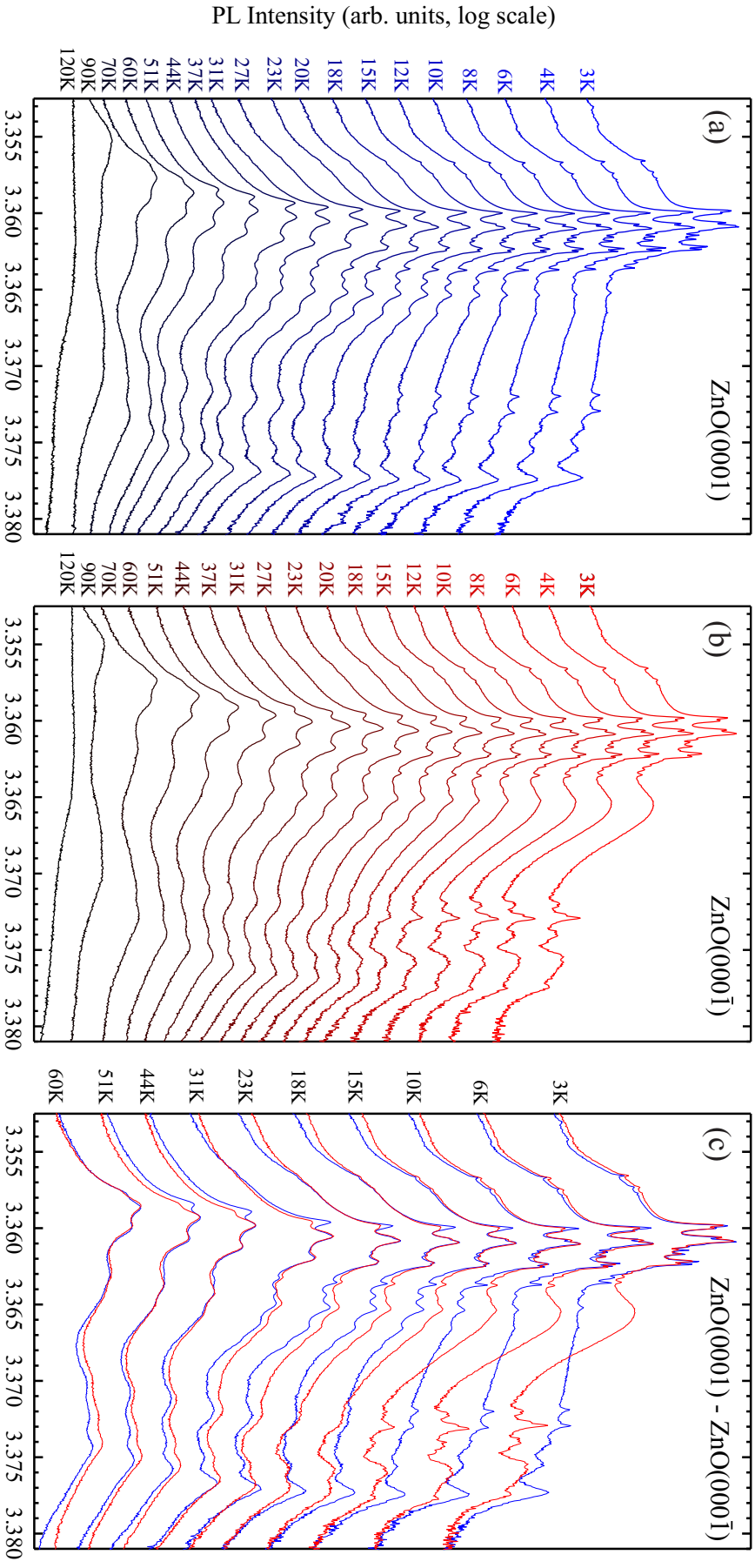

Figure 5.3.: Temperature-dependent PL measurements of the (a) Zn-polar and (b) O-polar faces between 3 K and 120 K. (c) shows the direct comparison between both faces for selected temperatures.

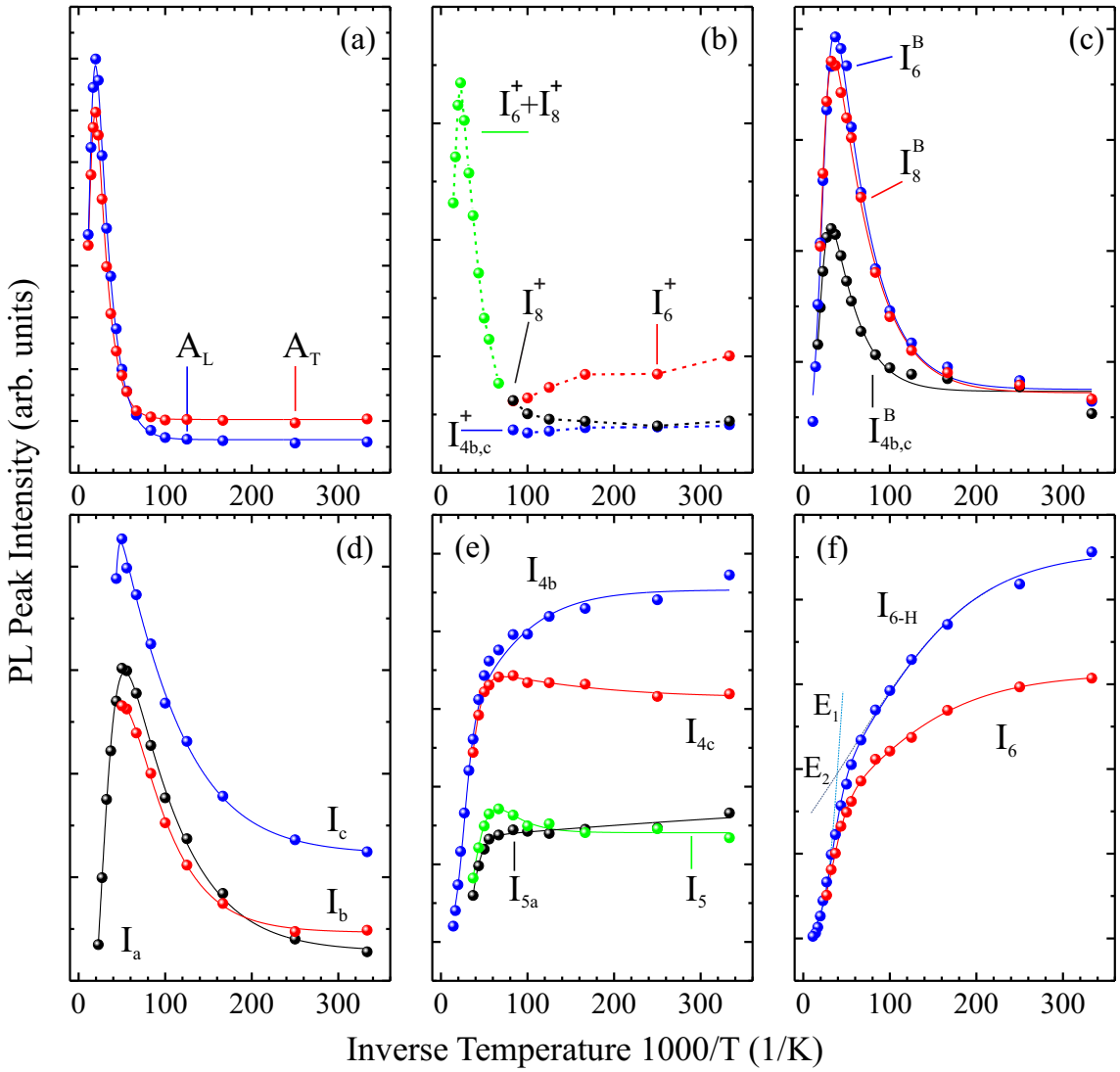

Figure 5.4.: Peak intensities of all dominant near-band-edge transitions at various temperatures (spheres) and least-square fit lines (straight line). All data was obtained on the O-polar face, except for the I^{B} transitions in (c). The $\mathrm{D}^{+}\mathrm{X}$ transitions in (b) merge at 18 K, hence, the sum signal is shown for higher temperatures. The dashed lines in (f) show exemplary single-level fits with E_1 and E_2 for $I_{6-\mathrm{H}}$.

extracted decay energies seem to increase if the underlying PL data exhibits a higher degree of noise, such as the data for the ZnO(0001) polar face. Generally, decay energies of 10 – 20 meV are reported for bulk ZnO [19, 156, 171] with lower energies of 5 – 13 meV reported for ZnO nanostructures [165]. Most of these reports involve the extraction of decay energies from very broad transitions due to a lack of resolution, and do so for only a small number of temperature points which introduces even larger fitting errors. A complete list of the decay and activation energies for the dominant lines observed in this work is given in Table 5.3.

Figure 5.4(a) shows the peak intensities of the free excitons A_{L} and A_{T} versus inverse

Table 5.3.: Summary of extracted decay and activation energies from the temperature-dependent PL measurements. All values are given in meV.

	Zn-polar face			O-polar face		
	E_1	E_2	E_A	E_1	E_2	E_A
A_L	44.9*	–	4.5	23.4	–	6.0
A_T	36.1*	–	7.8	21.7	–	7.1
I_4^B	16.0	–	3.1	18.5	–	4.6
I_6^B	14.6	–	2.5	15.0	–	1.7
I_8^B	15.6	–	2.3	4.0*	–	3.2
I_c	*	–	2.2	30.0*	–	1.5
I_b	*	–	2.8	6.0*	–	2.0
I_a	11.6	–	1.7	8.9	–	1.6
I_{4c}	22.8	0.4	–	10.8	–	0.9
I_{4b}	15.6	1.4	–	14.6	1.8	–
I_{5a}	*	–	–	11.9	0.1	–
I_5	*	–	–	7.6	–	3.4
I_{6-H}	12.1	1.0	–	11.5	1.2	–
I_6	14.5	2.0	–	10.0	1.2	–
I_7	16.0	1.3	–	7.2	0.9	–
I_8	15.9	2.3	–	8.4	1.0	–
I_9	16.9	2.3	–	14.2	1.2	–

* For these PL emission lines not enough data points could be recorded to obtain a meaningful result. For example I_c on the O-polar face (see Fig. 5.4) exhibits only one temperature point with decreasing luminescence intensity, therefore the estimated E_1 is highly inaccurate.

temperature. Initially, at low temperatures, their intensities are constant and significantly increase above 12 K reaching a maximum at 51 K. With increasing temperature the donor-bound excitons dissociate into free excitons and neutral donors, therefore, a luminescence increase in free exciton emission is commonly observed. The decrease in intensity for temperatures higher than 51 K is consistent with Hamby *et al.* [171], who observed the same effect starting at 60 K. Ionised donor transitions in Fig. 5.4(b) show a slight initial decrease in intensity. Above 12 K, I_4^+ is no longer observed, and I_6^+ and I_8^+ merge to a broad peak which reaches a maximum at 44 K. No activation energies were extracted for the broad Gaussian-shaped feature that was only observed on the O-polar face, as it was superimposed on the B-excitons. However, if the in-

creasing B-exciton luminescence is discarded, one could argue that the broad polarity feature quenches between 23 K and 31 K, as shown in the direct comparison between both polar faces in Fig. 5.3(c). Grabowska *et al.* [165] found that their SX emission in nanostructured materials vanished faster than the bound exciton recombinations with an decay energy of 5 – 6 meV [172] and is completely quenched at 20 K. A similar quenching region is observed in our data which adds evidence to this Gaussian-shaped feature being surface related.

Temperature-dependent PL measurements can also be used to distinguish between ground state and excited state transitions. The I_{6-H} to I_9 emission lines belong to ground states of donor-bound excitons. However, I_4^B to I_8^B are associated with excited states. As already observed in Fig. 5.2, these transitions occur at an energetic spacing of 4.4 meV above their respective ground state equivalents. The activation energies, E_A, obtained for the same transitions are between 1.7 – 4.6 meV, which is in reasonable agreement with the A-B valence band splitting. Consequently, I_4^B to I_8^B are confidently assigned to donor-bound excitons involving a hole from the B-valence band.

Another class of excited states are rotational-vibrational states with activation energies of 1 – 4 meV, as observed in excitation magneto-PL studies [173]. The transitions I_{a-c} in Fig. 5.2(b) are 0.8 – 1.4 meV higher in energy than $I_{4b,c}$ and have an E_A of 1.5 – 2.8 eV. Meyer *et al.* [149] reported the same set of lines at 0.8 – 1.4 meV above their I_4 transition and tentatively attributed them to rotational-vibrational states of I_4. Hydrothermal ZnO material investigated here does not exhibit I_4, but instead $I_{4b,c}$ and as all the I_{a-c} transitions show the same energetic spacing as the ones reported by Meyer *et al.* , they are assigned to rotational-vibrational states of $I_{4b,c}$. For I_{4c} on the O-polar face (see Fig. 5.4(e)) a weak luminescence increase with temperature can be observed. Although I_{4c} could potentially be an excited state, it is conceivable that an additional underlying transition causes this behaviour, potentially an I_x^B transition from one of the unidentified lines at the higher energy side of I_9 or a rotational-vibrational state of I_{6-H}/I_6. This could also be a valid origin for I_5. Interestingly, for all investigated hydrothermally grown ZnO wafers the intensity ratio between I_{4b} and I_{4c} is roughly 0.7. This makes a different chemical origin somewhat unlikely.

Lautenschläger *et al.* [65] reported four unidentified lines in homoepitaxially grown O-polar films, of which two could be found at 3.3619 eV (called X_1) and 3.3622 eV (called X_2). Their energetic separation (0.3 eV) is reasonably close to the 0.18 eV separation between I_{4b} (3.36219 eV) and I_{4c} (3.36237 eV). However, they found that the intensity ratio of both lines stayed constant with increasing temperature, whereas in our case the ratio approaches unity. The transition at I_{4c} shall therefore tentatively be assigned to an excited state of I_{4b}, but magneto-optical measurements would be necessary to confirm this assignment.

5.3 PL on different crystal planes of HT ZnO

As a consequence of the wurtzite structure of ZnO, large spontaneous polarisation and piezoelectric fields along the c-axis are likely to be present (up to 0.9 MV cm^{-1} [174]). These intrinsic fields are usually detrimental in device applications, e.g. limiting the quantum efficiency in quantum wells due to the quantum-confined Stark effect. This has led to increased research into the growth of non-polar ZnO films and substrates. Heteroepitaxy of non-polar ZnO thin films commonly employs r- and m-plane sapphire, to achieve a- and m-plane ZnO films, respectively, as well as cubic substrates such as MgO. For homoepitaxy, the corresponding face of a bulk ZnO substrate is used.

PL investigations into non-polar and semi-polar ZnO thin films are fairly common [175–178], but these show only modest PL quality and resolution. On the other hand, PL reports concerning different crystallographic faces of bulk ZnO single crystals are limited. In this section, the Zn-polar and O-polar faces of HT ZnO crystals cut from both the (+c) and (−c) growth directions from the seed crystal, the non-polar a- $(11\bar{2}0)$ and m-plane $(10\bar{1}0)$ faces and the semi-polar r-plane $(1\bar{1}02)$ face are investigated. Figure 5.5 shows the 3 K PL spectra for all these planes. In comparison, the polar faces of the (−c) material show an inferior PL quality, with only a few features being resolved above the underlying background. For both (−c) polar faces I_6, I_7, I_8 and I_9 and the free excitons are observed. In contrast to the (+c) growth direction, $I_{6-\mathrm{H}}$ seems to be absent and $I_{4\mathrm{b,c}}$ cannot be resolved; instead only a weak line close to the conventional I_4 position is present. This is also the case for the non-polar m-plane face, which in addition shows only a weak I_6 line.

The overall quality of the PL spectrum obtained for the m-plane face, compared to the a-plane face, suggests that the former was cut from the (−c) direction. Both the a- and r-plane faces show a greater number of resolvable features, similar to the (+c) polar faces. The a-plane spectrum is very similar to the (+c) ZnO$(000\bar{1})$ polar face. Interestingly, the a-plane face shows a doublet line at the position of the transverse free exciton A_{L}. This feature is also observed for the semi-polar r-plane face. In addition, the broad surface related I_{SX} peak, which is observed at the same energy ($\sim$ 3.3653 eV) for the O-polar faces of (+c) and (−c) material is also present on a-plane and r-plane faces but is shifted to higher energies ($\sim$ 3.3665 eV and $\sim$ 3.3671 eV, respectively).

As mentioned in Sec. 2.3, impurity incorporation depends not only on the crystallographic face but also on the growth direction. The concentrations of impurities, which form non-radiative centres, are much higher in the (−c) growth direction. Sekiguchi *et al.* [179] investigated hydrothermally grown ZnO crystals grown on different basal planes of the seed crystal and observed a reduced intensity in room temperature

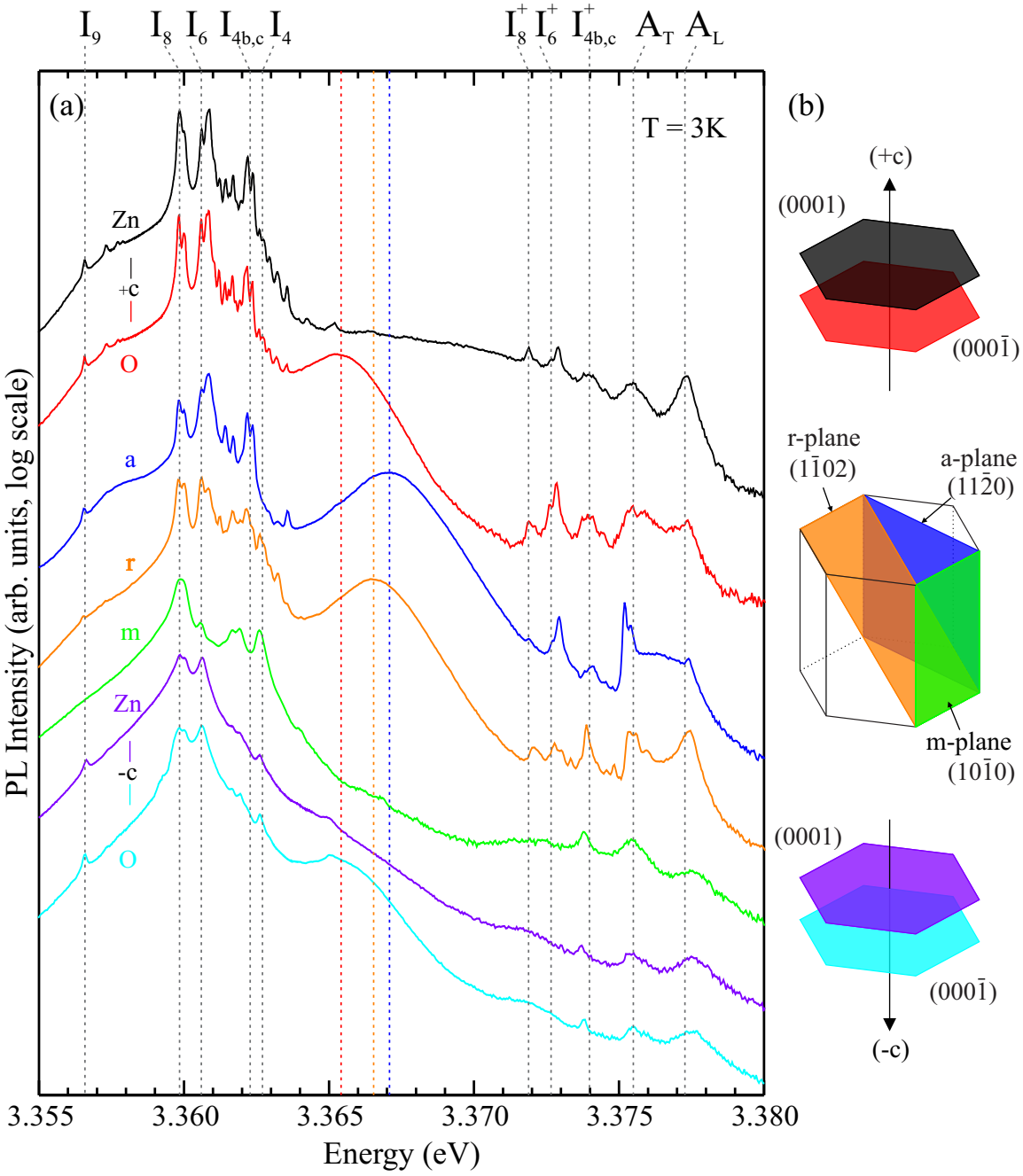

Figure 5.5.: (a) 3 K PL spectra of the Zn-polar and O-polar faces of hydrothermal ZnO crystals cut from the (+c) and (−c) growth direction from the seed crystal as well as the non-polar a- and m-plane and the semi-polar r-plane faces. The spectra are colour coded with the respective planes in (b). All spectra are vertically offset for clarity.

cathodoluminescence (CL) for the (−c) direction. They argued that the different polarisation of Zn-terminating atoms in the (+c) and O-terminating atoms in the (−c) direction resulted in a greater incorporation of non-radiative deep defects in (−c) direction. On the other hand, Mass *et al.* [180] argued that the non-radiative centres will

be introduced in higher concentrations into the faster growth axis which is in the (+c) direction and subsequently found lower PL intensities on the (+c) Zn-polar face.

The most complete account of PL measurements on the different ZnO faces and different substrate growth directions was given by Sasaki *et al.* [181]. They observed significantly more PL features for crystals grown in the (+c) direction and assigned this to a higher overall crystalline quality. In addition, the O-polar face showed I_{SX}, which was incorrectly assigned to ionised donor-bound transitions. For the a-, m-, and r-plane faces, PL data on ZnO bulk crystals is rare. There are a multitude of reports on ZnO epilayers with different polarities, but due to the high residual anisotropic strain in heteroepitaxial non-polar films the transition energies are significantly blueshifted and only one broad D^0X feature is usually present. However, Lautenschläger *et al.* [177] observed a broad feature similar to I_{SX} at 3.3665 eV on a-plane ZnO epilayers grown on a-plane ZnO-bulk substrates.

A few recent works [182–184] on ZnO bulk crystals report that the absolute PL intensities of free excitons are larger on the O-polar face compared to the Zn-polar face and state that this may be caused by the opposite band bending on each polar face. However, as shown in this work (see 9.1), both faces actually exhibit downward band bending under most laboratory conditions. Furthermore, the O-polar PL intensity in the free exciton and D^+X region was, in general, lower than on the Zn-polar face, and the small intensity difference in the D^0X region is more likely due to slight optical misalignment. The PL data presented here is the first to resolve the multitude of transition lines on the different planes of hydrothermal ZnO as well as the polarity-dependent I_{SX} feature. The crystals cut from the (+c) seed direction consistently show superior PL quality compared to those cut from the (−c) direction. Interestingly, the PL spectra from the a-plane $(11\bar{2}0)$, r-plane $(1\bar{1}02)$ and O-polar faces is rather similar in nature and significantly different from the Zn-polar face for which I_{SX} is absent and replaced by a very broad background emission.

5.4 Influence of growth process and post-treatment

Due to the limited escape depths of the photons involved (≤ 40 nm), photoluminescence spectroscopy is a surface sensitive technique. Hence, the resulting PL spectra are sensitive to surface impurities and lattice imperfections. Naturally, the quantity and type of impurities in the sub-surface region depends on the growth technique as well as post-growth treatments such as annealing cycles and/or chemo-mechanical polishing. Figure 5.6 shows the 3 K PL measurements of the near-band-edge (NBE) region for hydrothermally grown ZnO bulk crystals from Tokyo Denpa Co. Ltd. and melt-grown

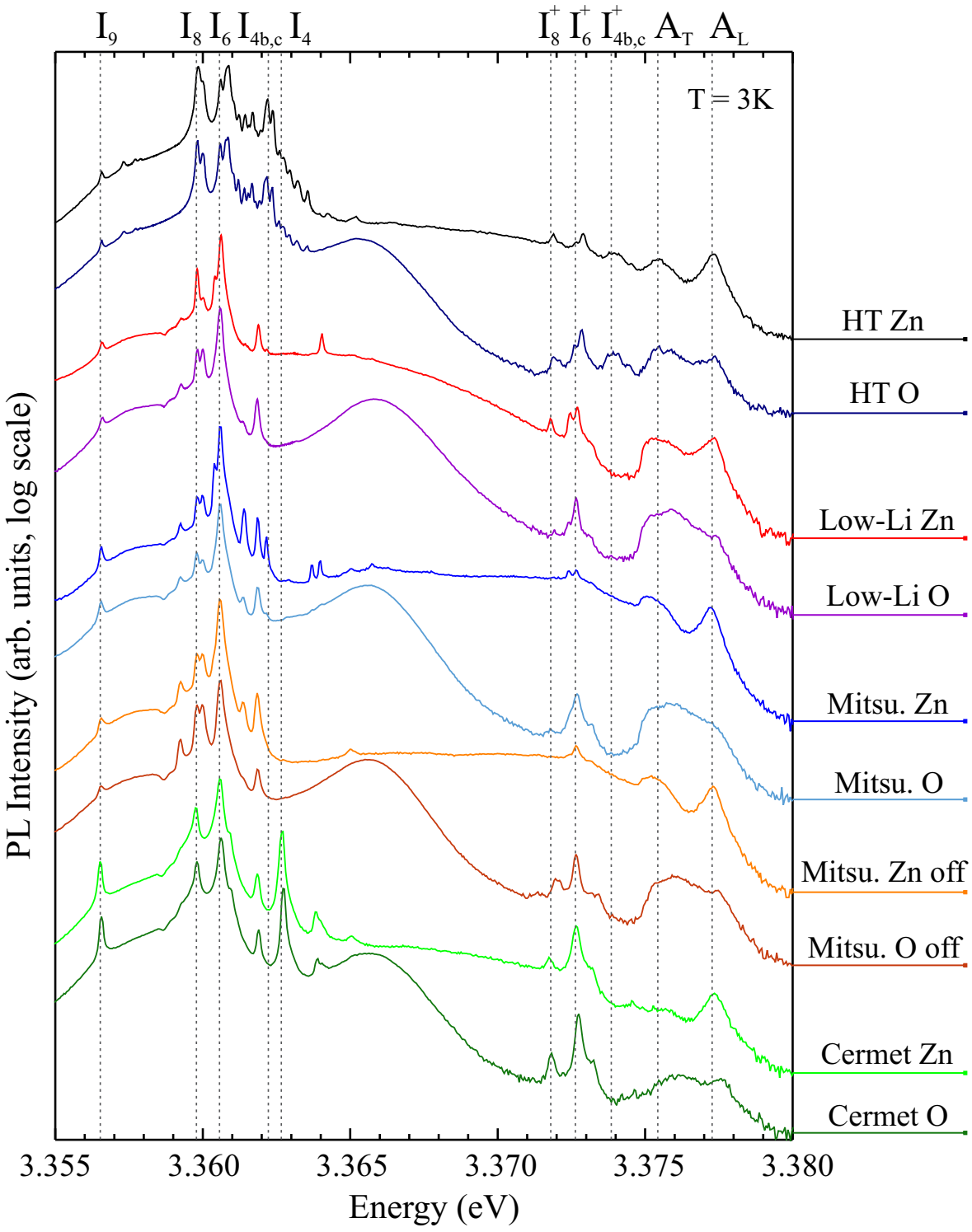

Figure 5.6.: Comparison between hydrothermally grown ZnO bulk crystals with different post-growth treatments (conventional HT, Low-Li HT, Mitsubishi HT) and melt-grown ZnO crystals (Cermet) at 3 K. *Mitsu. off* denotes a regular Mitsubishi wafer with a 0.5° offcut. Spectra are vertically offset for clarity.

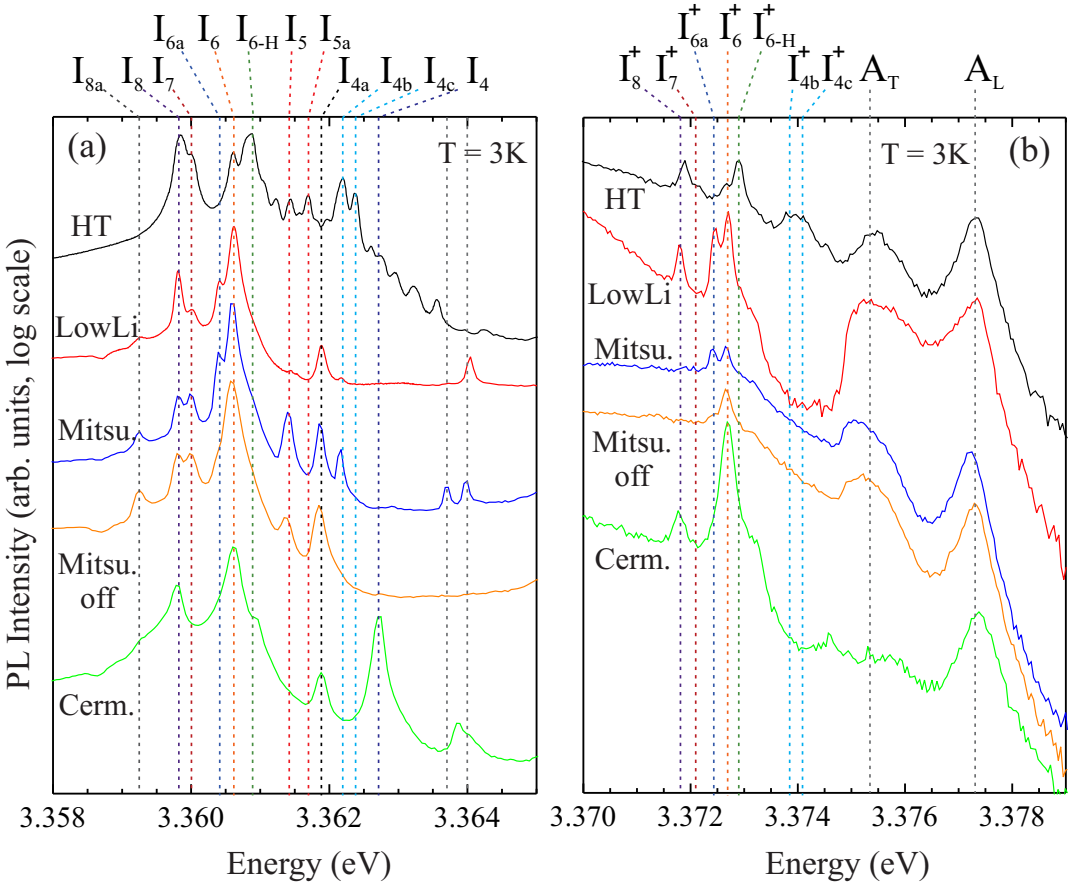

Figure 5.7.: (a) Neutral donor-bound exciton and (b) ionised donor-bound exciton regions for all investigated crystals presented in Fig. 5.6. Only Zn-polar faces are shown. Spectra are vertically offset for clarity.

ZnO bulk crystals purchased from Cermet Inc. Furthermore, spectra for HT ZnO with relatively low lithium concentration, referred to as Low-Li HT ZnO in the following, are presented as well as spectra for special mirror-polished HT ZnO supplied by the Mitsubishi Chemical Corporation (labelled as *Mitsubishi* or *Mitsu.*) which has been subjected to an undisclosed annealing re-polishing procedure to achieve a very low surface roughness, suitable for homoepitaxial growth. Some of the Mitsubishi ZnO bulk crystals have been cut with an offset angle of up to 0.5° to achieve a step-terrace surface morphology and are labelled as *Mitsu. off*.

The broad I_{SX} peak is present on all O-polar polar faces and is not influenced by post-growth treatment. If I_{SX} has an impurity-related origin, one can conclude that the relevant impurity must be introduced by both hydrothermal and melt growth techniques and must be preferentially incorporated on the ZnO$(000\bar{1})$ face. The D^0X and D^+X regions of all Zn-polar faces are enlarged in Fig. 5.7(a) and (b), respectively.

Of all ZnO single crystals, the conventional HT ZnO material exhibits the highest

number of resolvable D^0X features. The Low-Li HT ZnO and Mitsubishi HT ZnO wafers exhibit, I_6, I_7, and I_8, similar to the HT ZnO wafer. The hydrogen-related $I_{4b,c}$ lines are not observed as these wafers have been annealed at temperatures up to 1400 °C, resulting in the out-diffusion of hydrogen. Interestingly, I_{6-H} is also not present, indicating that the origin of this transition line lies in an impurity which must have been removed by the annealing and re-polishing process. It will be shown later in Sec. 6.1 that hydrogen is also the most likely candidate for the origin of this emission line.

Both the Low-Li HT and the Mitsubishi HT ZnO material show several new lines: I_{4a} (3.36188 eV), I_{6a} (3.36041 eV), and I_{8a} (3.35925 eV). The I_{4a} transition, which has been previously reported by Meyer *et al.* [149] and I_{8a} are also present on melt-grown ZnO. It could be argued that the different strain fields in the various materials result in shifted line positions so that the I_{6-H} and I_6 lines in the conventional HT ZnO material are simply redshifted in the Low-Li HT ZnO and Mitsubishi HT ZnO wafers. However, all other recombination lines on either side of these particular lines in the spectra match up, and these three newly observed lines behave differently under annealing, as will be shown later. Therefore, the case that I_{4a}, I_{6a} and I_{8a} are three independent lines can be made with some certainty. The Mitsubishi wafer exhibits two additional lines at 3.36371 eV and 3.36397 eV. The latter is also observed in Low-Li HT ZnO material. Based on their energetic spacing of 4.5 – 4.7 meV from I_{8a} they could potentially be replicas involving B-excitons. Alternatively, excited states of I_{4a} and I_5 provide another possible explanation since the Mitsubishi wafer exhibits both I_{4a} and I_5 and the two unidentified peaks while the Low-Li HT ZnO material only exhibits I_{4a} and one of these higher energy lines. Several lines observed on the conventional HT ZnO wafer on both energetic sides of I_{5a} and I_5 are believed to be due to excited states. Their absence in the Low-Li HT ZnO and Mitsubishi HT ZnO material, combined with the absence of I_{6-H} suggests that they may be excited states of I_{6-H}. A comparison of Low-Li HT ZnO and conventional HT ZnO spectra does not reveal any obvious lithium related recombination lines in the near-band-edge emission.

In comparison to hydrothermally grown ZnO material, melt-grown material consistently has larger PL line widths. Only the conventional I_4 (3.36272 eV), I_{4a}, I_6 and I_8 lines are observed as well as a weak intensity I_{8a} shoulder at 3.35928 eV. In addition, a shoulder at 3.36092 eV is present in HT, Low-Li HT and both Mitsu. ZnO samples and is assigned to I_9^B. Interestingly, hydrothermally and melt-grown ZnO do not have the same hydrogen-related I_4 emission line. However, it will be shown in the following chapters that both transitions are hydrogen-related. On the higher energy side of I_4, a broad feature is observed at 3.36388 eV, which Meyer *et al.* [149] tentatively attributed

to excited states of I_4 similar to the ones labelled $I_{\mathrm{a-c}}$ in conventional HT ZnO.

Figure 5.7(b) shows the expanded D^+X region for the same Zn-polar face spectra presented in Fig 5.6. All wafers types exhibit a well-defined A_L line which is typical for Zn-polar faces. Annealing and re-grinding does not appear to alter this characteristic. On all crystals, the dominant D^+X feature is I_6^+ or I_{6-H}^+ consistent with the dominant D^0X transitions. Although, the initial assignment of these features to ionised donor-bound excitons was achieved by correlating their PL intensity with that of the neutral donor-bound transitions, the intensity relationship can depend on the specific probing position on the sample surface itself. For conventional HT ZnO wafers, all ionised features (I_{6-H}^+ (3.37286 eV), I_6^+ (3.37260 eV), I_7^+ (3.37217 eV) and I_8^+ (3.37189 eV)), can be resolved as well as a broader feature assigned to $I_{4b,c}^+$ (3.3739 eV). The Low-Li HT ZnO and Mitsubishi HT ZnO show no I_{6-H}^+ but exhibit I_{6a}^+ (3.37230 eV) consistent with their D^0X transitions. As both wafers were annealed at high temperatures which results in significant hydrogen out-diffusion, no emission that could be linked to $I_{4b,c}^+$ was found. This is especially noticeable for the Low-Li HT ZnO, which shows a significant decrease in intensity between I_{6a}^+ and A_T.

In melt-grown ZnO, broad I_6^+ and I_8^+ transitions are present. Interestingly, no I_4^+ could be observed although I_4 itself shows intense luminescence. Meyer *et al.* [18] deduced from Haynes rule, that, for donor binding energies < 47 meV, the excitons cannot bind to the corresponding ionised donor. Assuming a donor binding energy of approximately 46.1 meV for hydrogen (extracted from the position of I_4 in Fig. 5.6(a)), one would not expect an exciton bound to an ionised hydrogen donor (I_4^+) to be stable. In the case of HT ZnO wafer, $I_{4b,c}$ instead of I_4 is observed. This is assumed to be due to hydrogen in a different bonding configuration that has a higher donor binding energy of 47.3 eV. Therefore, following the Haynes rule argument employed by Meyer *et al.*, it should be possible to observe the respective ionised transition $I_{4b,c}^+$. Further evidence will be provided in the following chapters that out-diffusion of hydrogen leads to a simultaneous quenching of $I_{4b,c}$ and the broad $I_{4b,c}^+$ emission.

5.5 Two-Electron-Satellites and Y-Lines

The recombination of an exciton bound to a neutral donor can leave the donor in the ground $1s$ state or an excited $2s$ or $2p$ state. The donor $1s$ state represents the normal D^0X line whereas the $2s$ and $2p$ final states give rise to the two-electron-satellites (TES) [185]. Such TES transitions are shown for different ZnO bulk single crystals in Fig. 5.8. No difference was observed in the TES transitions for different polar faces and, therefore, only spectra for the Zn-polar faces are shown. The non-polar and semi-polar

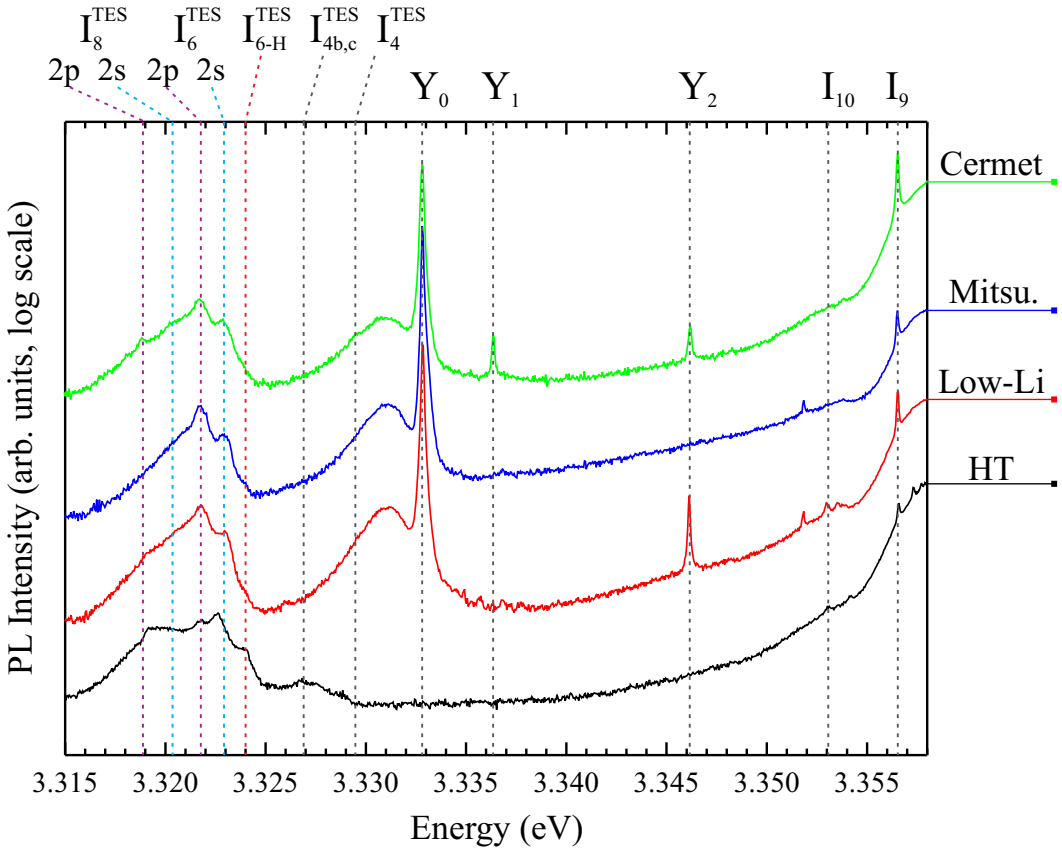

Figure 5.8.: TES and Y-line region for the Zn-polar faces of different ZnO wafers. The spectra are vertically offset for clarity.

faces of hydrothermal ZnO exhibit only blurred TES transitions and are also not shown. Higher electron excitations ($n = 3, 4, \dots$) are not observed. Considering a hydrogenic model in the effective-mass approach (EMA), the energetic difference between the $1s$ ground state and the $2p$ final state gives the donor binding energy E_D [27, 186], where $E_\mathrm{D} = \frac{1}{4} E_\mathrm{D,EMA} + (E_{2p} - E_{1s})$. However, the short range chemical potential of an individual impurity (e.g. hydrogen or aluminium) leads to a chemical shift of the donor binding energy E_D from the effective-mass donor with $E_\mathrm{D,EMA} \sim 55\,\mathrm{meV}$. This is the reason why not all donor-related PL lines occur at the same photon energy. This chemical shift, predominantly influences states of s-symmetry, such as $1s$ and $2s$. For hydrogen, with a binding energy ($E_\mathrm{D} = 46.1\,\mathrm{meV}$ according to [187]) lower than the effective mass donor, the $1s$ state is shifted to higher energies which leads to the observed I_4 line.

Meyer *et al.* [17] showed, using perturbation theory, that for the $2s$ state of I_4 the chemical splitting is negative. Therefore, $I_4^\mathrm{TES}(2p)$ is, in general, observed at higher PL energies than $I_4^\mathrm{TES}(2s)$ in PL spectra. For all other transitions (i.e. $I_5 - I_9$) the $2s$ state is the deepest (occurs at higher PL energy). This is clearly shown for I_6^TES and I_8^TES in

Table 5.4.: Summary of TES transitions.

Line	$E(1s)$ (eV)	E_{Loc} (meV)	E_{D} (meV)	$E(2p)$ (eV)	$E(2s)$ (eV)	$E(1s-2p)$ (meV)	$E(1s-2s)$ (meV)
I_4	3.36272	12.68	47.2	3.3295	–	33.2	–
$I_{4\mathrm{b}}$	3.36219	13.21	49.1	3.3270	–	35.1	–
$I_{6-\mathrm{H}}$	3.36081	14.59	51.6	3.3239	–	36.9	–
I_6	3.36055	14.85	52.8	3.3218	3.3229	38.8	37.7
I_8	3.35984	15.56	55.0	3.3188	3.3204	41.0	39.4
$I_{8-\mathrm{Ga}}$	3.35961	15.92	55.4	3.3183	3.3196	41.4	40.0
I_9	3.35657	18.87	64.9	3.3057	–	50.7	–
I_{10}	3.35303	22.37	73.5	3.2935	–	59.5	–
Y_0	3.33286	42.54	*	3.2693	3.2698	63.6	63.1

For TES lines which could not clearly be identified, the $2p$ state was assumed.
* Y_0 cannot be described as an effective-mass donor.

Fig. 5.8. I_4^{TES} is only observed on the melt-grown Cermet material as a small feature at 3.3295 eV, but any $2s-2p$ splitting could not be resolved. As mentioned earlier, hydrothermally grown ZnO does not exhibit the conventional I_4 line and, therefore, I_4^{TES} is not present. However, the conventional HT ZnO does show a broad and diffuse feature at approximately 3.3270 eV. As $I_{4\mathrm{b,c}}$ is shifted to lower energies compared to the conventional I_4 line, the same is expected for the respective TES transitions. It is therefore likely that this feature is $I_{4\mathrm{b,c}}^{\mathrm{TES}}$. For the Low-Li HT and Mitsubishi materials, both of which have been annealed at high temperatures, $I_{4\mathrm{b,c}}$ was not observed and similarly no broad $I_{4\mathrm{b,c}}^{\mathrm{TES}}$ is present. The conventional HT ZnO wafer, shows an additional shoulder on the higher energy side of I_6^{TES} at 3.3239 eV that is not present in the other wafers. As only the conventional HT ZnO material, shows $I_{6-\mathrm{H}}$ and the TES shoulder in question, it is assigned to the TES of $I_{6-\mathrm{H}}$. As Sec. 6.4 will show, $I_{6-\mathrm{H}}^{\mathrm{TES}}$ quenches at the same time as $I_{6-\mathrm{H}}$ after annealing of the conventional HT ZnO material in oxygen at 600°C.

Table 5.4 gives a summary of the extracted TES parameters. The donor binding energy is calculated using the equation given previously for the $2p-1s$ splitting. All values are in good agreement with those published by Wagner *et al.* [187]. The only significant deviation is I_4^{TES} with an $E(2p) = 3.3295$ eV, higher than the 3.3287 eV value given in Ref. [187]. The reason for the difference is mainly due to the poor resolution of $I_4^{\mathrm{TES}}(2p)$ and $I_4^{\mathrm{TES}}(2s)$. This also introduces a small error in the calculation of $E_{\mathrm{D}}(I_4)$. The $2p-1s$ spacing versus localisation energy is plotted in Fig. 5.9(a). For I_4 to I_9, a

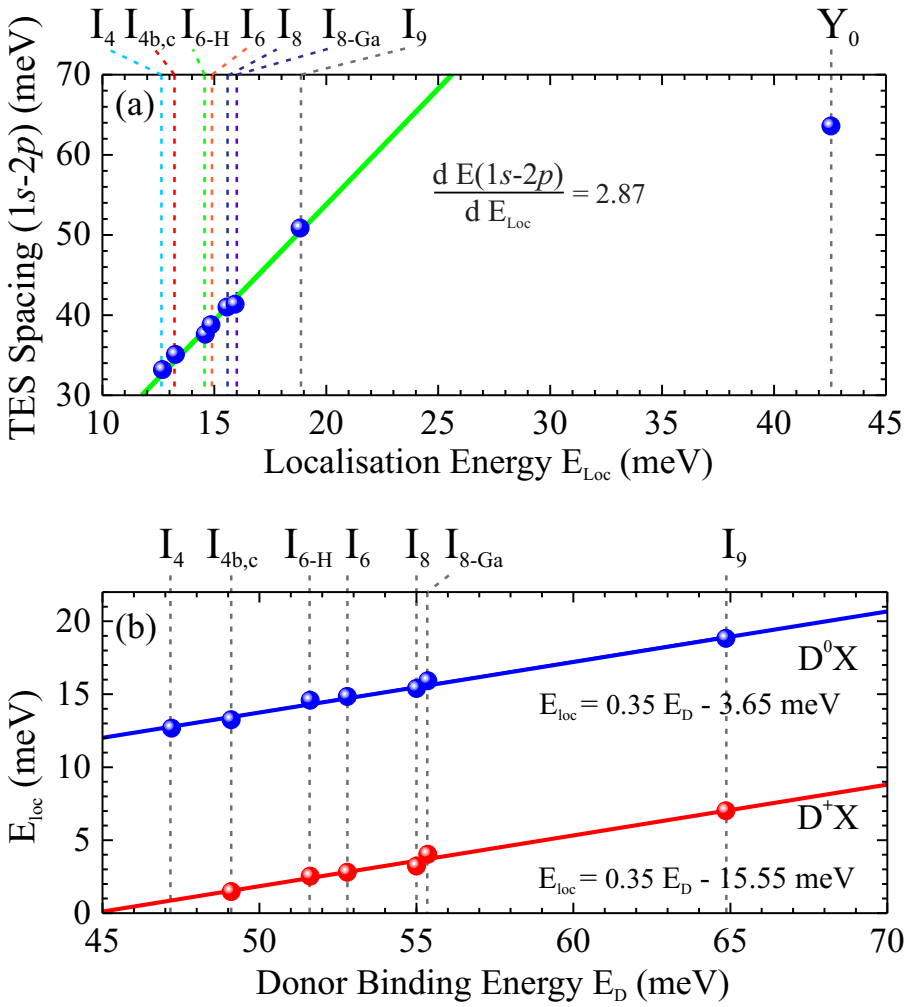

Figure 5.9.: (a) TES ($1s-2p$) spacing and localisation energies for neutral donor-bound excitons $I_4 - I_9$ with a linear fit. (b) Haynes plot for D^0X (blue) and D^+X (red) transitions.

linear relationship between the TES spacing and E_{loc} is observed, and a linear fit yields a slope of 2.87. The extracted energies of $I^{\mathrm{TES}}_{\mathrm{4b,c}}$ and $I^{\mathrm{TES}}_{\mathrm{6-H}}$ seem to fit well with the data of the other bound exciton transitions.

The binding energy of an exciton to a neutral donor, or localisation energy (E_{loc}) shows a linear dependence with the donor binding energy itself. This relationship is known as Haynes rule after J.R. Haynes, who investigated acceptor- and donor-bound excitons in silicon as early as 1960 [188]. Interestingly, this relationship not only holds for neutral donors but also for ionised donor-bound excitons as seen by comparing the respective linear fits in Fig. 5.9(b). For both lines the respective linear equation yields a slope of 0.35 for D^0X and D^+X. Meyer *et al.* [18, 150] obtained slope values of 0.37 and 0.5, respectively, and attributed the difference between the slopes to the varying influence of central cell effects on neutral and ionised donors. However, if the three

newly found transitions ($I_{4b,c}$, I_{6-H} and I_{8-Ga}) as well as the corrected peak energies for the ionised donor I_9^+ are included, the D^+X and D^0X slopes obtained in this work are identical. I_{8-Ga} and I_9^+ will be introduced in the following chapters.

The red line fit in Fig. 5.9(b) for D^+X reaches a zero localisation energy around 44.7 meV. For donor binding energies below this threshold an exciton cannot bind to the ionised donor. This explains why I_4^+ is not observed but I_{4b}^+ is present as I_4 has an E_D close to this threshold. Meyer *et al.* [18] found this critical value for E_D to be 47 meV. In their work an I_4 donor binding energy of 46.1 meV is given. Although, the exact energies might be slightly shifted in this work, the findings here are in qualitative agreement with their work.

The dominant narrow transition in Fig. 5.8 is labelled Y_0 and is only present in melt-grown Cermet material or in hydrothermally grown material that has been annealed (i.e. Low-Li HT and Mitsubishi HT), but not in unannealed conventional HT ZnO. Although its FWHM is comparable on all wafers where Y_0 is present, the line intensity is stronger on the Low-Li HT and Mitsubishi HT material. Two similar recombination lines at higher energies, Y_1 (3.33643 eV) and Y_2 (3.34623 eV), are observed in the melt-grown ZnO. Whereas, Y_1 is exclusively observed in the melt-grown ZnO crystals, Y_2 is also present in the Mitsubishi material but not the Low-Li HT wafer. This indicates that Y_2 is not introduced by the annealing process like Y_0, but rather by the different subsequent grinding and re-polishing steps. This suggests that Y_2 is linked to structural defects in the surface region.

Brandt *et al.* [189] observed Y_2 (labelled in their work as I_{12}) in ZnO thin films grown on Al_2O_3 with a MgO or heavily Al-doped ZnO buffer, but not in films grown without a buffer layer. A neutral donor-bound exciton origin was suggested, possibly due to a distorted lattice. Returning to Fig. 5.9(a), the Y_0 TES splitting with regard to its E_{loc} significantly deviates from the linear relationship of the neutral donor-bound exciton transitions. Obviously, it cannot be described by the same linear fit obtained for the D^0X transitions. Y_0, sometimes labelled as *DBX* or *DD*, was reported as early as 1976 in Li- and Na-doped single crystals [190] and has since been observed in undoped bulk single crystals [191], in homo- [192] and heteroepitaxy [193], as well as in nanostructures [194] and powders [195]. In ZnO nanowires, Y_0 was only observed in wires above a certain critical diameter [194]. Robin *et al.* [196] reported Y_0 emission for nanowires of 300 nm diameter, but not for 150 nm diameter wires. However, their PL resolution seems to decrease rapidly with the diameter of the specimen. Therefore it is possible that Y_0 was present but not resolved.

Until the comprehensive work of Wagner *et al.* [187] was recently published, various

origins of Y_0 were reported, e.g. deep neutral donor-bound or shallow acceptor-bound excitons [197], point defects (V_O, Zn_i) [191], structural effects [198] and because of its energetic position - a TES transition [199]. Wagner *et al.* showed that Y_0, as well as Y_1 and Y_2, originate from the recombination of excitons bound to extended structural defects which act as additional donor states. Based on the small activation energy ($E_A = 12\,\text{meV}$) of the Y transitions, compared to their large localisation energy, they argued that the defect model consists of deeply bound excitons with one additional weakly bound charge carrier that cannot be described in the EMA model. As already mentioned, Y_0 is only observed in hydrothermally grown material after annealing in oxygen and after ion-implantation. This fact will be addressed in the following chapters.

5.6 Summary

In this chapter, the free exciton and near-band-edge emission spectra of ZnO single crystals of different crystal polarities and growth methods were investigated by 3 K photoluminescence spectroscopy. The unparalleled resolution of the current PL setup and the high crystalline quality of the ZnO crystals studied, made it possible to resolve various new PL lines, not yet reported in the literature. Temperature-dependent PL measurements allowed ground and excited state transitions to be distinguished. From the respective two-electron-satellites, a Haynes rule relationship for both D^0X and D^+X transitions could be determined. The most significant findings were in particular:

- Free excitons involving holes from the *A*, *B*, and *C* valence bands as well as their excited states can be observed in PL spectroscopy. The presence of excitons from different valence bands strongly depends on the crystal face polarity and post-growth processes such as annealing and re-grinding.

- The O-polar face generally exhibits a broad Gaussian-shaped feature at approximately 3.3655 eV, that is absent on the Zn-polar face. This polarity related effect is consistently observed independent of the type of ZnO material. A similar broad feature is observed on the a-plane $(11\bar{2}0)$ and r-plane $(1\bar{1}02)$ faces.

- For hydrothermally grown bulk ZnO, the normal hydrogen-related I_4 line is not observed. Instead a new transition at lower energies, $I_{4b,c}$ is present. As all other spectral lines match up with literature values, a strain effect can be excluded. In contrast to I_4, it is possible to identify a D^+X replica of $I_{4b,c}$. The $I_{4b,c}$ emission lines are only observed for conventional HT ZnO which contains significant amounts of group I elements. Therefore, a possible complex involving H and Li

is likely to be involved.

- A higher energetic line $I_{6-\mathrm{H}}$ can be resolved in the commonly observed I_6 transition for conventional HT ZnO and usually represents the dominant component. The D^+X transitions of both components can be separately resolved. $I_{6-\mathrm{H}}$ is only present in conventional HT ZnO but is absent in Low-Li HT ZnO or melt-grown material. This makes an involvement of the abundant group I elements in conventional HT ZnO very likely. Due to its close proximity to the Al-related I_6 transition, some form of Al-Li-related complex is a likely origin.

- Several excited states, including *B*-exciton replicas, of the dominant D^0X transitions can be identified using temperature-dependent PL.

- The PL resolution is significantly higher for hydrothermal ZnO material grown in the (+c) direction than for material grown in the (−c) direction. R-plane and a-plane ZnO material shows similar quality PL emission to the (+c) material including a broad feature observed on the O-polar face. M-plane wafers exhibit inferior PL emission similar to that for (−c) material.

- TES transitions can be observed for the newly identified $I_{4\mathrm{b,c}}$ and $I_{6-\mathrm{H}}$ lines at 3.3270 eV and 3.3239 eV, allowing their respective donor binding energies to be calculated.

6 | Photoluminescence of annealed ZnO single crystals

Several previously unreported bound exciton recombinations and polarity-related differences in ZnO PL were observed in chapter 5. In order to gain further insight into the origin and the temperature stability of those new features, ZnO bulk single crystals of different growth techniques and post-growth treatments were annealed in oxygen, nitrogen, and forming gas mixtures. The evolution of the PL emission after annealing is investigated in this chapter.

6.1 ZnO annealed in oxygen gas

One of the most common substrate preparation and post-growth semiconductor processes involves annealing in various chemical atmospheres. During the annealing process, lattice atoms gain kinetic energy, enabling them to rearrange, resulting in a reduction in lattice stress. In addition, annealing in an oxygen atmosphere can improve the stoichiometry of oxide semiconductors. Furthermore, the grain size of thin films usually increases with annealing temperatures thereby decreasing the surface roughness. Annealing treatments of ZnO bulk crystals and substrates are commonly carried out at very high temperatures, usually above 1000 °C, in order to create surfaces containing atomic steps and terraces [200]. PL measurements can be used to monitor improvements in crystalline quality on annealing, usually through the evolution of higher transition intensities and narrower peak widths.

The majority of reports on the PL properties of ZnO under annealing have focused on the broad emission of deep centres. For example, a broad, green band centred at 2.5 eV in HT ZnO material [201] is believed to be related to oxygen vacancies (V_O). Furthermore, a structured Cu-related band at 2.5 eV [202] is generally only present after annealing above 600 °C in oxygen ambients. However, due to the narrow line widths and close proximity of the various excitonic features in the NBE region, a complete account

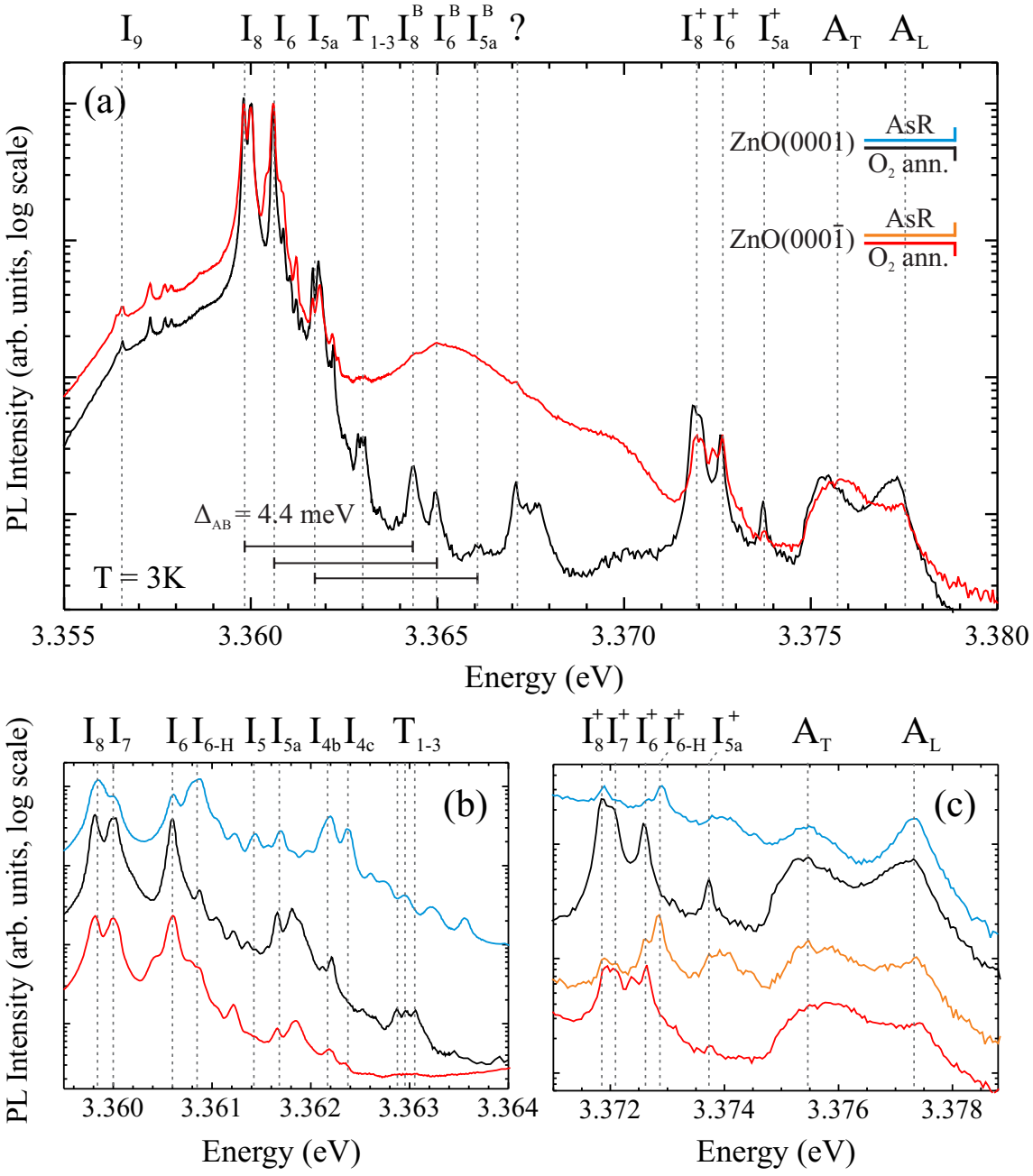

Figure 6.1.: PL spectra at 3 K for both polar faces of hydrothermal ZnO bulk single-crystals after annealing in O_2 atmosphere for 90 min at 600 °C.

of the effect of annealing on PL emission has not yet been produced. Historically, PL spectroscopy following heat treatments has been used to study diffusion processes e.g. the incorporation of Al in ZnO thin films from sapphire (Al_2O_3) substrates and the out-diffusion of hydrogen by monitoring the intensity of the respective donor-bound exciton transitions. Obviously, this approach is limited to the chemically identified transitions such as the hydrogen-related I_4 or Al-related I_6 emission line. In this chapter, the PL

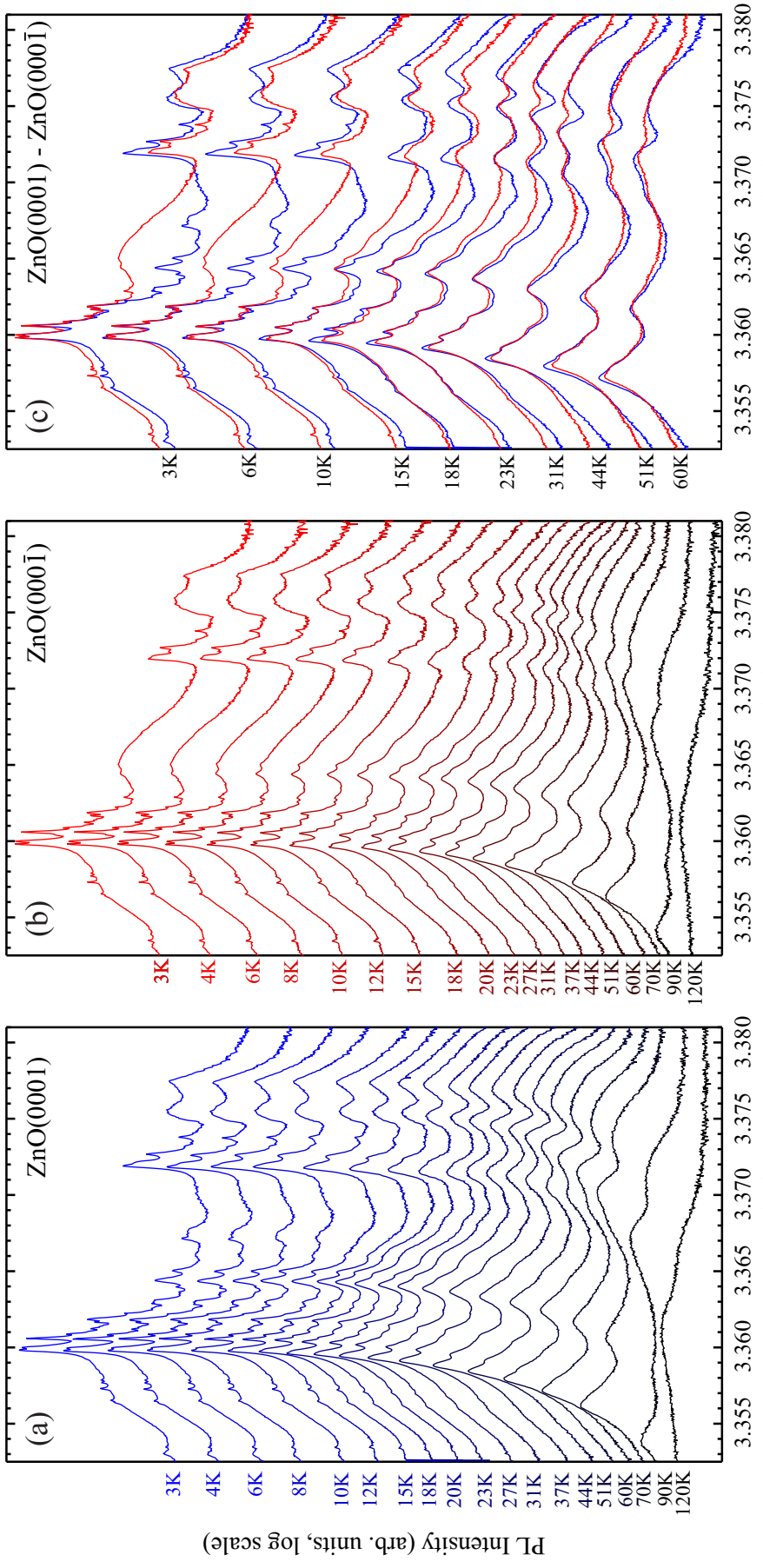

Figure 6.2.: Temperature-dependent PL measurements of 90 min O_2-annealed Zn-polar (a) and O-polar (b) surfaces between 3 K and 120 K. (c) shows the direct comparison between both faces for selected temperatures.

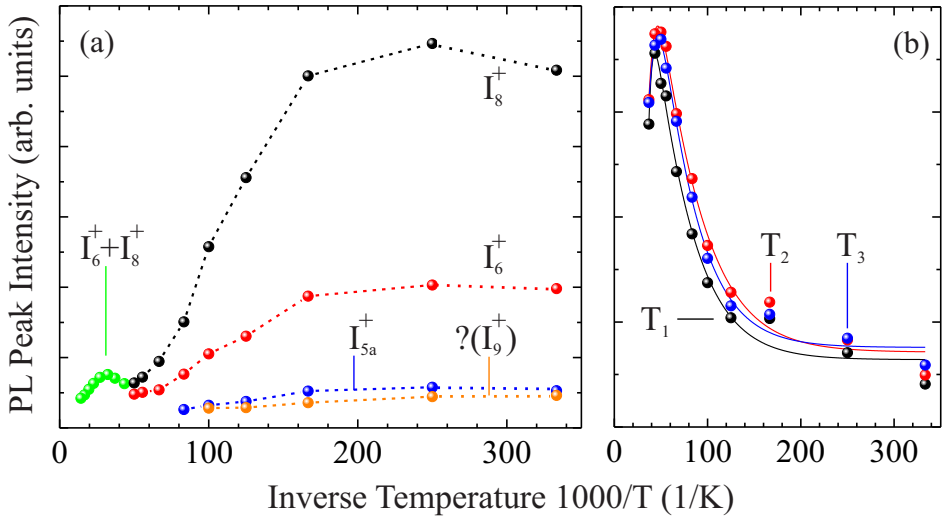

Figure 6.3.: Temperature-dependent PL peak intensities for observed D^+X transitions in (a) and for the unidentified triplet in (b). The intensity maximum at 31 K for the $I_6^+ + I_8^+$ combined signal is caused by the broadening of the A_L free exciton and, hence, an increase in background intensity. The solid lines in (b) represent a two layer fit of the activation energies for the triplet states.

emission of bulk ZnO crystals has been investigated following different post-treatments, such as annealing in oxygen, nitrogen, and forming gas. Annealing was carried out in a quartz tube furnace in a steady flow of the respective instrument grade (99.99%) gas. High-resolution PL spectroscopy at a temperature of 3 K, presented in Fig 6.1, unveiled at least two new hydrogen-related transitions in addition to I_4 and numerous new and as yet unidentified transition lines.

Zn-polar and O-polar face samples from the same hydrothermally grown ZnO bulk crystal material as used in Sec. 5.2 were annealed at 600 °C for 90 min in a stream of O_2 gas. Immediately after removal from the furnace, the hydrothermal ZnO crystals exhibit a yellow-green fluorescence under normal room lighting that fades within 30 s as the crystals were allowed to cool to room temperature without assistance. In dark conditions no visible luminescence is observed by the naked eye. The 3 K PL spectra for both polar faces after O_2 annealing is shown in Fig. 6.1. The striking difference between the annealed and unannealed samples is the dramatic decrease in background intensity on the Zn-polar face between 3.362 eV and the ionised donor-bound exciton region at 3.372 eV. The O-polar face shows a smaller decrease in background intensity in the same region. Although the emission on the O-polar face still exhibits the broad feature at 3.365 eV, a new broad shoulder at 3.3698 eV is visible. For both polar faces the dominant D^0X transitions are I_6, I_7 and I_8. Annealing in O_2 does not seem to have any influence on these D^0X lines. In contrast, $I_{4b,c}$ and I_{6-H} have been completely

quenched. Due to the quenching of $I_{4b,c}$ and the lower background intensity, two closely spaced lines are visible at 3.36166 eV, possibly I_{5a}, and at 3.36182 eV, attributed to I_{4a}. The temperature dependence of these peaks suggests that both are ground state rather than excited state transitions (see also Fig. 6.2). The excited states $I_{a,b,c}$ are absent after heat treatment, which provides further evidence that they are linked to $I_{4b,c}$ which is also absent.

At slightly higher energies, a close lying triplet (T: 3.36306 eV, 3.36296 eV, 3.36287 eV) is present (see also Fig. 6.3(b)). A similar peak at 3.3630 eV was reported by Meyer *et al.* [18] in Li-doped ZnO bulk crystals grown in the vapour phase, labelled as I^*. The I^* transition showed an intensity correlation with I_{10} and was tentatively assigned as I_{10}^+. However, the intensity of I_{10} in these annealed hydrothermal ZnO bulk crystals (not shown) is only approximately half the intensity of this triplet, making an ionised donor transition unlikely. In addition, temperature-dependent PL measurements (Fig. 6.2 and 6.3(b)) showed an increase in the triplet intensity with temperature with an intensity maximum reached at around 20 K. A similar behaviour was observed earlier for excited states with intensities peaking at the same temperature. An increase in intensity is also found for the combined signal of ionised donor-related lines $I_6^+ + I_8^+$, shown in Fig. 5.4(b) for the unannealed wafer and Fig. 6.3(a) for the annealed wafer. With increasing measurement temperature the I_6^+ and I_8^+ lines merge and, hence, their combined signal is shown. In contrast to rotational-vibration states, the increase in intensity of $I_6^+ + I_8^+$ for increasing temperatures is caused by the broadening of A_L (see Fig. 6.2) and the intensity maximum is reached at 44 K. For the triplet in Fig. 6.3(b) the intensity maximum is reached at a temperature of 20 K, similar to the intensity maximum for excited states (e.g. I_a). This favours an rotational-vibrational excited state assignment for the triplet over a ionised donor transition. In addition, their activation energies (T_1: $E_1 = 26.0$ eV and $E_A = 2.4$ eV, T_2: $E_1 = 15.6$ eV and $E_A = 2.1$ eV, T_3: $E_1 = 13.2$ eV and $E_A = 2.5$ eV) are similar to the excited states given in Table 5.3. On the other hand, if one assumes the localisation energy of the triplet to be that of the ionised donor transition for I_{10}, taken from the Haynes plot in Fig. 5.9(b), its position would be in agreement with a linear fit of the other ionised donor-bound transitions. Therefore, it is possible that the excited states and the ionised donor-transitions superimpose each other.

At energies of 4.3 – 4.6 meV above I_{5a}, I_6, and I_8 the respective B-excitonic transitions (I_{5a}^B: 3.36606 eV, I_6^B: 3.36496 eV and I_8^B: 3.36437 eV) are resolved in great detail, as the background intensity is reduced by the annealing process. This assignment is also supported by their increasing intensity with temperature up to 20 – 23 K. A broad feature containing a narrower maximum at 3.36712 eV is consistently observed after

O_2 annealing. Its localisation energy of 8.27 meV agrees well with that of I_2 reported by Meyer *et al.* [18], who assigned it to the ionised donor transition of I_9 after observing an intensity correlation between the two. In this work, however, I_9^+ will be assigned to a different peak (discussed in Sec. 7.1.2) that fits perfectly into the Haynes plot in Fig. 5.9.

Figure 6.1(c) shows the D^+X region in greater detail. For comparison, the PL spectrum for an unannealed bare ZnO crystal is included in the same figure. As the background intensity decreases, all lines become well-resolved. I_6, I_7, and I_8 are not affected by annealing in an O_2 atmosphere and their ionised replicas are all present. In contrast, I_{6-H} quenches dramatically, as does I_{6-H}^+. On the lower energy side of I_6^+, an additional small peak is resolved, similar to the low energy shoulder of I_6. This shows that the peak shape of the neutral donor-bound transitions can be replicated quite accurately in the ionised donor-bound region. The broad $I_{4b,c}^+$ hump-like feature is no longer present after annealing, leaving a sharp peak at 3.37373 eV, possibly linked to one of the peaks near I_{5a}. Finally, it is interesting to note that on the high energy side of I_9, three new lines appear that are only vaguely perceptible on the Zn-polar face of the unannealed wafer (see Fig. 5.2(a)). Their intensity-temperature dependence suggests a ground state behaviour. All effects reported in this section were consistently observed in a number of other hydrothermal ZnO wafers after O_2 annealing. Low-Li HT and Mitsubishi HT ZnO crystals had already been annealed in their post-growth processing and, therefore, no further O_2 annealing was carried out.

For comparison, a melt-grown Cermet wafer was annealed under identical conditions (600 °C for 90 min in a flowing O_2 ambient) and the resulting PL is presented in Fig. 6.4. Once again, a decrease in background intensity occurs, similar to that observed for the hydrothermal ZnO. On the O-polar face, the broad SX peak is quenched. The hydrogen-related I_4 and its associated excited states at $\sim$ 3.3639 eV were also quenched on annealing. The remaining D^0X transitions, including I_{4a} and the D^+X transitions, were unaffected and no additional peaks (such as I_{5a} and its higher energetic neighbour) were revealed. Neither the unannealed nor annealed melt-grown material showed any sign of I_{6-H}. In general, the quenching of $I_{4b,c}$ and I_4 seems to indicate a similar chemical or impurity origin. Given the close proximity of the recombination lines, they may involve different atomic configurations of hydrogen. A conventional HT ZnO wafer was stepwise annealed in oxygen gas in 50 °C steps up to 600 °C, with each step having a duration of 30 mins. The respective 3 K PL spectra taken by A. Neiman of University of Canterbury (not shown) indicated that $I_{4b,c}$ quenches between 350 °C and 400 °C, suggesting a lower thermal stability than I_4 which quenches between 550 – 600 °C.

Interestingly, with the quenching of $I_{4b,c}$, a weak donor-acceptor pair transition ap-

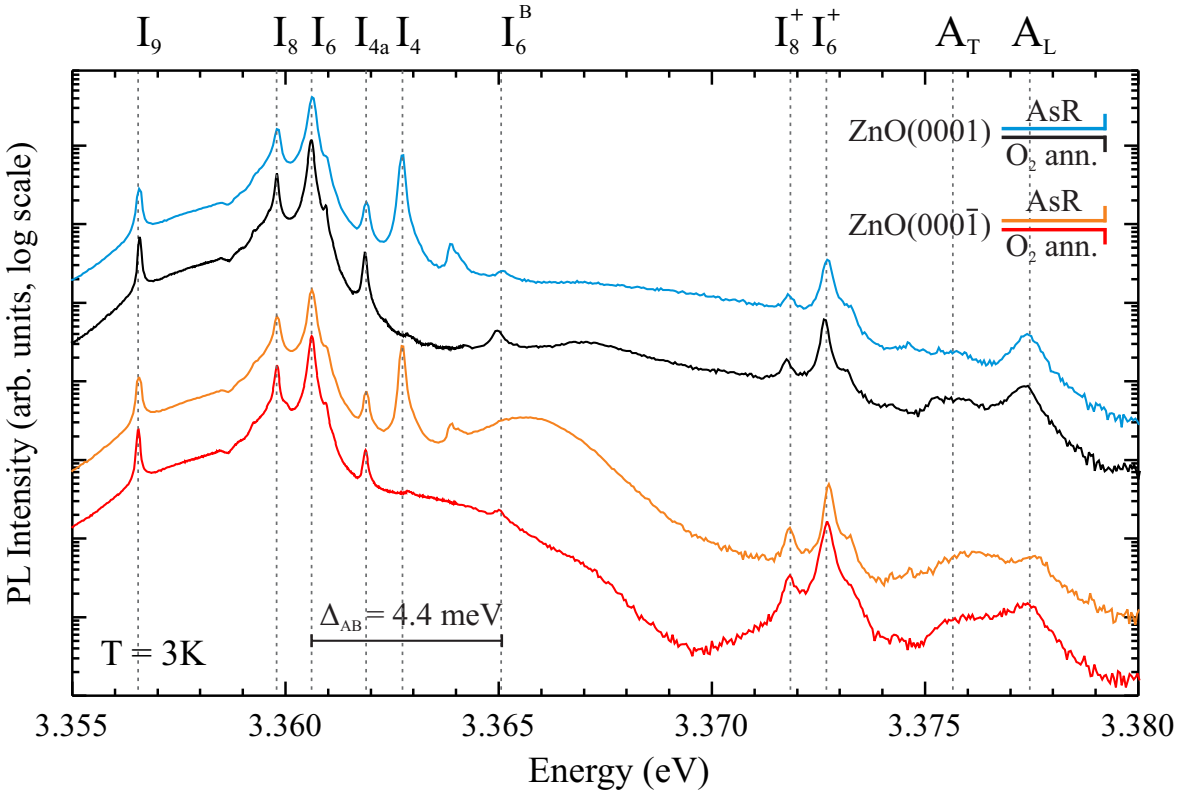

Figure 6.4.: Comparison of as-received melt-grown Cermet ZnO crystals and the same wafer annealed in O_2 atmosphere for 90 min at 600 °C.

pears after the 450°C annealing step with a zero-phonon line centred at ∼3.029 eV, followed by one or two longitudinal optical phonon replicas (LO) shifted by 70 – 71 meV towards lower energies. This DAP region is shown in Fig. 6.5 for various ZnO crystals. Assuming a photon originating from a DAP transition has an energy of:

$$\hbar\omega = E_g - E_D - E_A + \frac{e^2}{4\pi\varepsilon_0\varepsilon_s R}, \tag{6.1}$$

then the acceptor binding energy E_A can be estimated. The last term represents the Coulomb interaction between the acceptor and donor for their respective separation R. For the bandgap energy E_g, the free exciton energy plus the exciton binding energy is used, i.e. $E_g = A_L + 60\,\text{meV} = 3.4373\,\text{eV}$. Therefore, a donor binding energy of 52.8 meV (I_6) and an infinite separation (R) yields an acceptor binding energy of $E_A \approx 355\,\text{meV}$.

Similar DAP transitions were observed in Li- and Na-doped HT ZnO by Meyer and Sann *et al.* [203, 204]. They reported the strongest DAP intensity for annealing temperatures between 450°C and 650°C. Although the DAP band reported by Meyer *et al.* may be a result of the diffusion doping with group I elements, annealing in general can introduce a DAP band in HT ZnO as can be seen in Fig. 6.5. In addition, the same

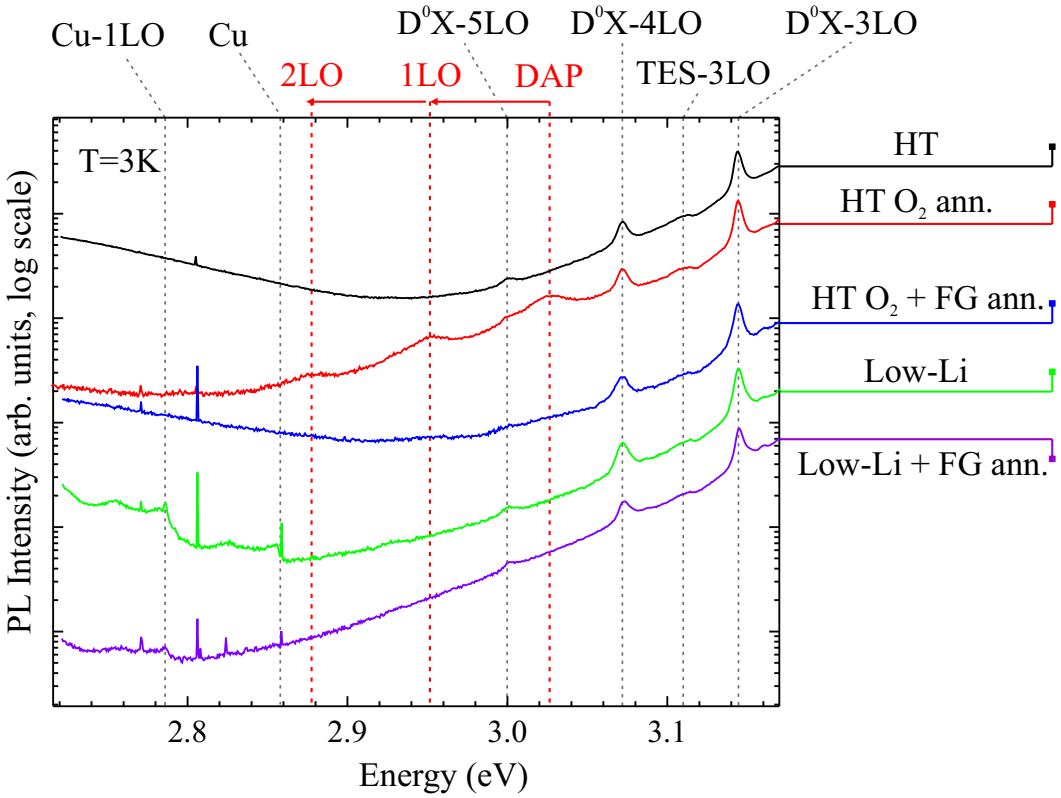

Figure 6.5.: 3 K PL spectra of ZnO single-crystals. After 30 min of O_2 annealing at 600 °C a donor-acceptor pair transition (DAP) and its phonon replicas are observable in conventional HT material but not in Low-Li HT ZnO. The copper related transitions are marked as Cu and are in perfect agreement with the energy position found by Dingle [202].

authors observed a shallow donor in EPR after H_2 diffusion into Li-doped samples at temperatures of 400°C and above. The EPR signal from the hydrogen-related shallow donor and the signal from the Li acceptor slowly decreased with annealing temperature with the initial conditions restored by annealing in air for 5 min at 600 °C [204]. This observation led to the suggestion of a hydrogen and Li complex, possibly Li_{Zn}-H-Li_{Zn}. It seems likely that with annealing the acceptor-donor complex is de-passivated by out-diffusion of hydrogen leaving the Li_{Zn} acceptor behind. Interestingly, this happens close to the temperature where the $I_{4b,c}$ signal quenches and, therefore, the $I_{4b,c}$ line may originate in the vicinity of Li atoms. This would also explain the energetic shift in $I_{4b,c}$ compared to the more commonly observed I_4, which is believed to be due to hydrogen trapped in an oxygen vacancy (H_O). Neither Low-Li HT ZnO nor Mitsubishi HT ZnO exhibit DAP transitions in as-received or O_2-annealed samples as Li was largely removed in the re-grinding/re-polishing process. A similar DAP transition is observed following ion-implantation, as discussed in chapter 7.

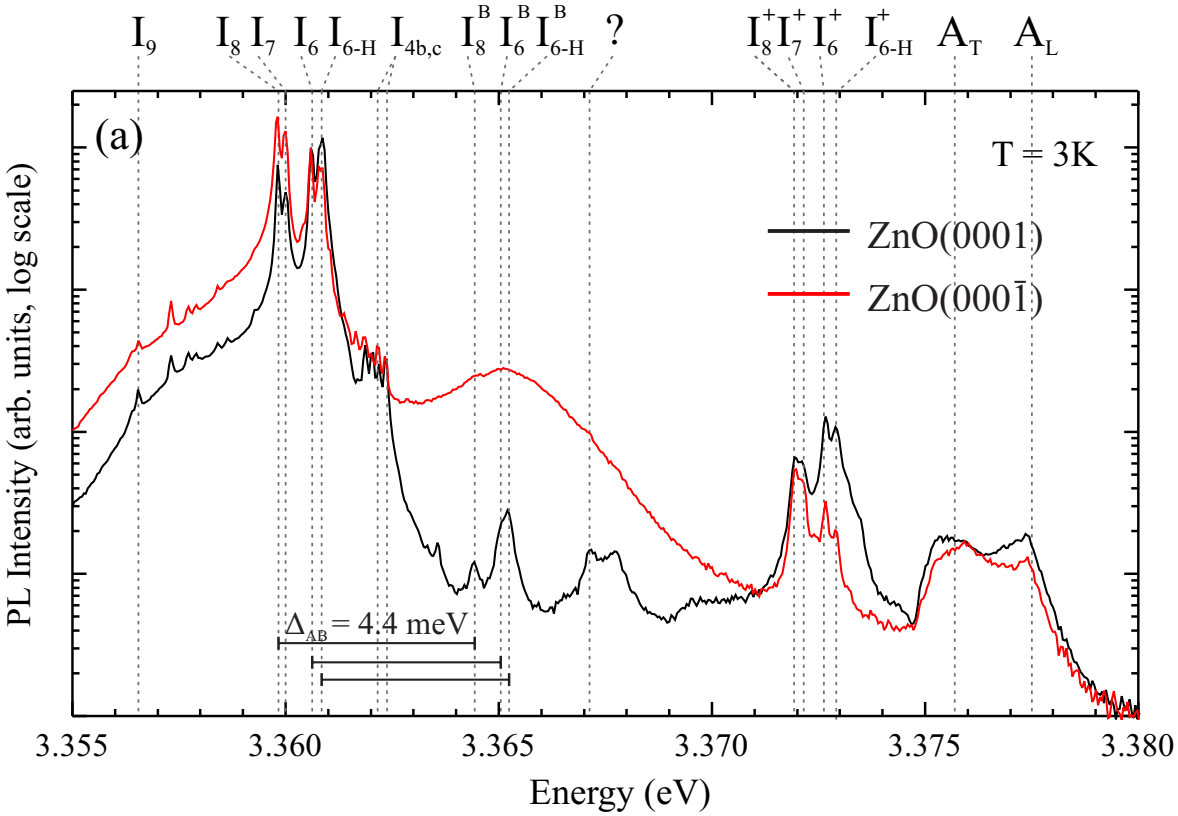

Figure 6.6.: PL spectra at 3 K for both polar faces of hydrothermally grown ZnO after annealing in N_2 atmosphere for 90 min at 600°C.

6.2 ZnO annealed in nitrogen gas

When the hydrothermally grown bulk ZnO material is annealed in oxygen-poor conditions e.g. in a stream of N_2 gas rather than O_2 gas, I_{6-H} is largely unaffected by heat treatment even though $I_{4b,c}$ quenches completely. In Fig. 6.6, both I_{6-H} and its ionised counterpart I^+_{6-H} are still present after annealing for 90 min at 600 °C in N_2. Furthermore, the corresponding B-excitonic replica is broadened compared to that observed after O_2 annealing, indicating the presence of both I^B_6 and I^B_{6-H}. The pronounced I_{5a} doublet, present after O_2 annealing, is not observed. There is a significant decrease in background emission, especially in the broad SX feature at approximately 3.365 eV similar to the background decrease after O_2 annealing, indicating that this effect is temperature-related and not due to the annealing atmosphere. First-principles calculations [139] predict that under oxygen-poor conditions the deep donor V_O and the shallow donors H_i and H_O are preferentially formed. Hydrogen bonded in an oxygen vacancy (V_O) can be regarded as H_O and has already been identified as the origin for the I_4 line. Therefore, the possibility that I_{6-H} is related to hydrogen occupying a simple oxygen vacancy seems unlikely due to its higher thermal stability compared to

I_4. However, the fact that I_{6-H} is quenched after O_2 annealing but not N_2 annealing suggests that either some form of oxygen vacancy complex is involved or that the presence of oxygen lowers the thermal dissociation barrier of hydrogen from some other donor or donor complex.

The direct incorporation of nitrogen from N_2 gas is unlikely as molecular nitrogen has a high dissociation energy of 9.76 eV [205]. Because of this, nitrogen doping is often carried out in an anhydrous NH_3 stream during the growth process or post-growth annealing. Some authors assign the shallow acceptor level, that can subsequently be observed as a DAP PL transition with a binding energy of 165 meV, to N_2 on a Zn site. However, calculations show, that this defect only forms under Zn-poor and O-rich conditions [206], which is clearly not the case for N_2 annealing [87].

6.3 ZnO annealed in forming gas

Oxygen gas annealed hydrothermal ZnO wafers were subsequently re-annealed in forming gas (95 % N_2 + 5 % H_2) for 30 min at 500 °C and then twice at 600 °C in an attempt to reintroduce hydrogen. All samples were cooled down under atmospheric conditions after removal from the furnace and reached room temperature within 5 minutes. No quenching in water took place. All samples were measured within 36 hours following annealing.

The resulting PL spectra are shown in Fig. 6.7. For both polar faces the dramatic decrease in background intensity observed after O_2 annealing was reversed. After the first forming gas (FG) anneal at 500 °C, the characteristic broad SX feature on the O-polar face is restored. Its energetic position, shifts by 1.3 meV towards higher energies after a first 30 min/600 °C anneal then shifts back to its initial position after a second 30 min/600 °C FG anneal. Surprisingly, the Zn-polar face also develops a broad Gaussian-shaped SX feature with FG annealing.

The characteristic PL spectrum of the as-received Zn-polar HT ZnO is not completely restored: After the 500 °C FG anneal, $I_{4b,c}$ is still quenched and only I_{5a} is present. Following the second 600 °C FG anneal, the hydrogen-related $I_{4b,c}$ marginally recovers on both faces. Due to its thermal stability of approximately 400 °C for O_2 and N_2 annealing, it is not surprising that $I_{4b,c}$ cannot be reintroduced in significant quantities via FG annealing at 600 °C. Annealing at 500 °C only causes a very small increase in I_{6-H} intensity. However, after a subsequent 600 °C FG annealing step, I_{6-H} recovers to its full intensity. Surprisingly, the I^{+}_{6-H} replica can only be resolved on the Zn-polar face which may be due to the significant changes in surface morphology caused by the

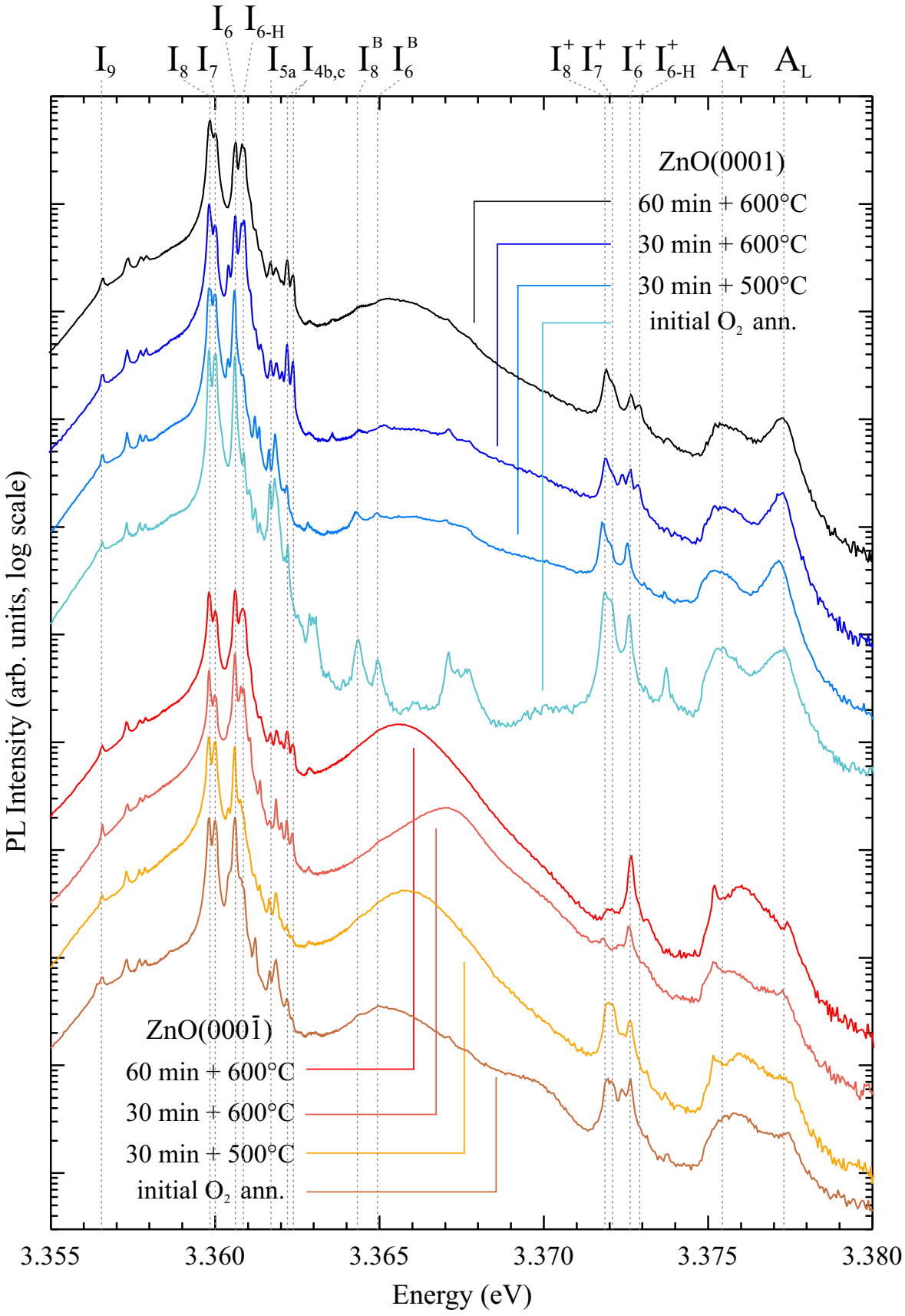

Figure 6.7.: Forming gas (95 % $N_2 + 5$ % H_2) annealing for different annealing temperatures and durations for an initially O_2-annealed hydrothermally grown ZnO wafer.

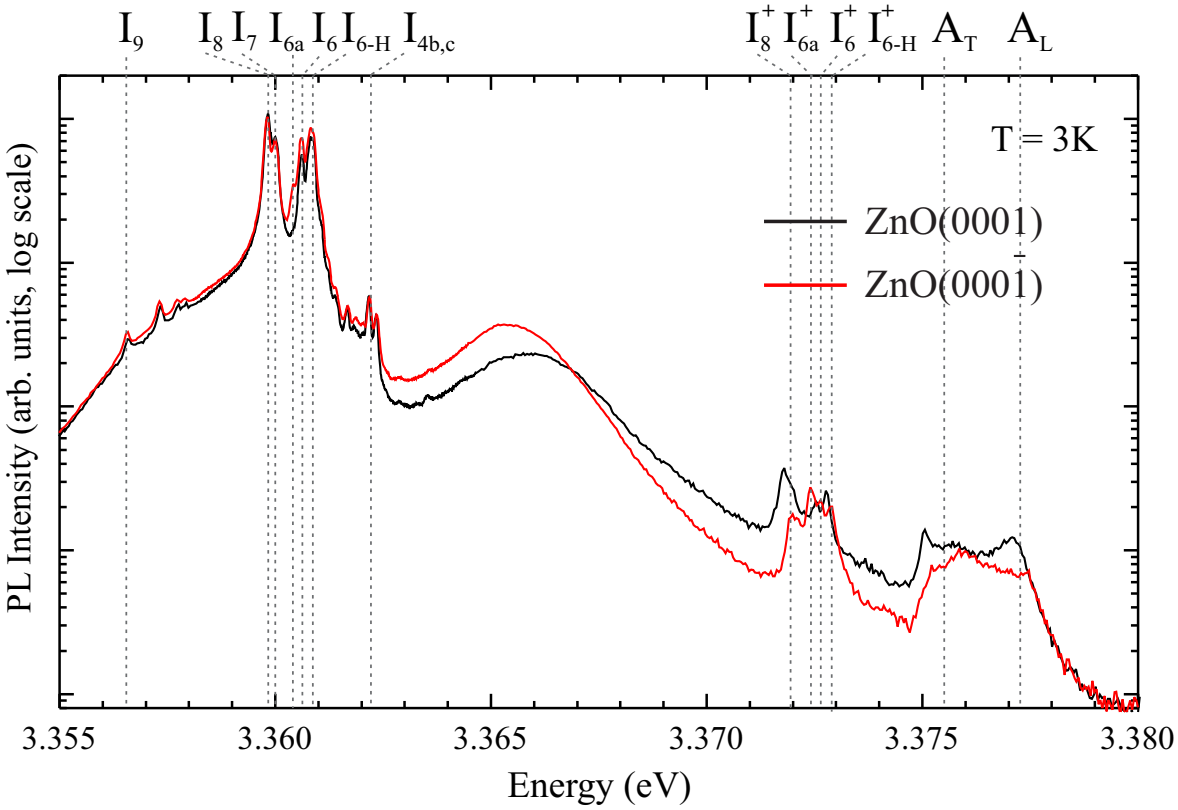

Figure 6.8.: PL spectra after annealing in 95 % Ar + 5 % H_2 gas for an initially O_2-annealed, hydrothermally grown ZnO wafer.

forming gas treatment (see below). The D^+X lines have been observed to vary significantly in intensity with probing position on the sample surface. Interestingly, the free exciton emission thought to be surface sensitive due to the large absorption coefficient of exciton-polaritons and therefore short escape depth [27], shows no change in intensity or shape. The A_L emission on the Zn-polar face still maintains its characteristic Lorentzian peak shape throughout the FG annealing process.

In addition to the forming gas (N_2-H_2) annealing, O_2-annealed HT ZnO material was re-annealed in 95 % Ar + 5 % H_2 gas (Ar-H_2) for 30 min at 600 °C. The 3 K PL spectra, presented in Fig. 6.8, is very similar to the spectra for conventional FG annealing. Once again, $I_{4b,c}$ is not re-established, but I_{6-H} recovers to its initial intensity. The I_{6a} line and its ionised donor transition I^+_{6a} at 3.37241 eV are present on the O-polar face. After the Ar-H_2 annealing, both faces exhibit the broad Gaussian SX peak, centred at 3.3659 eV on the Zn-polar face and at 3.3654 on the O-polar face.

Whereas annealing in an O_2 atmosphere at intermediate temperatures (i.e. 600 °C) does not result in a significant change of surface morphology, this is not the case for FG or Ar-H_2 annealing. Figure 6.9 shows optical and scanning electron microscopy images after FG and Ar-H_2 annealing. Optical images are only shown for the Zn-

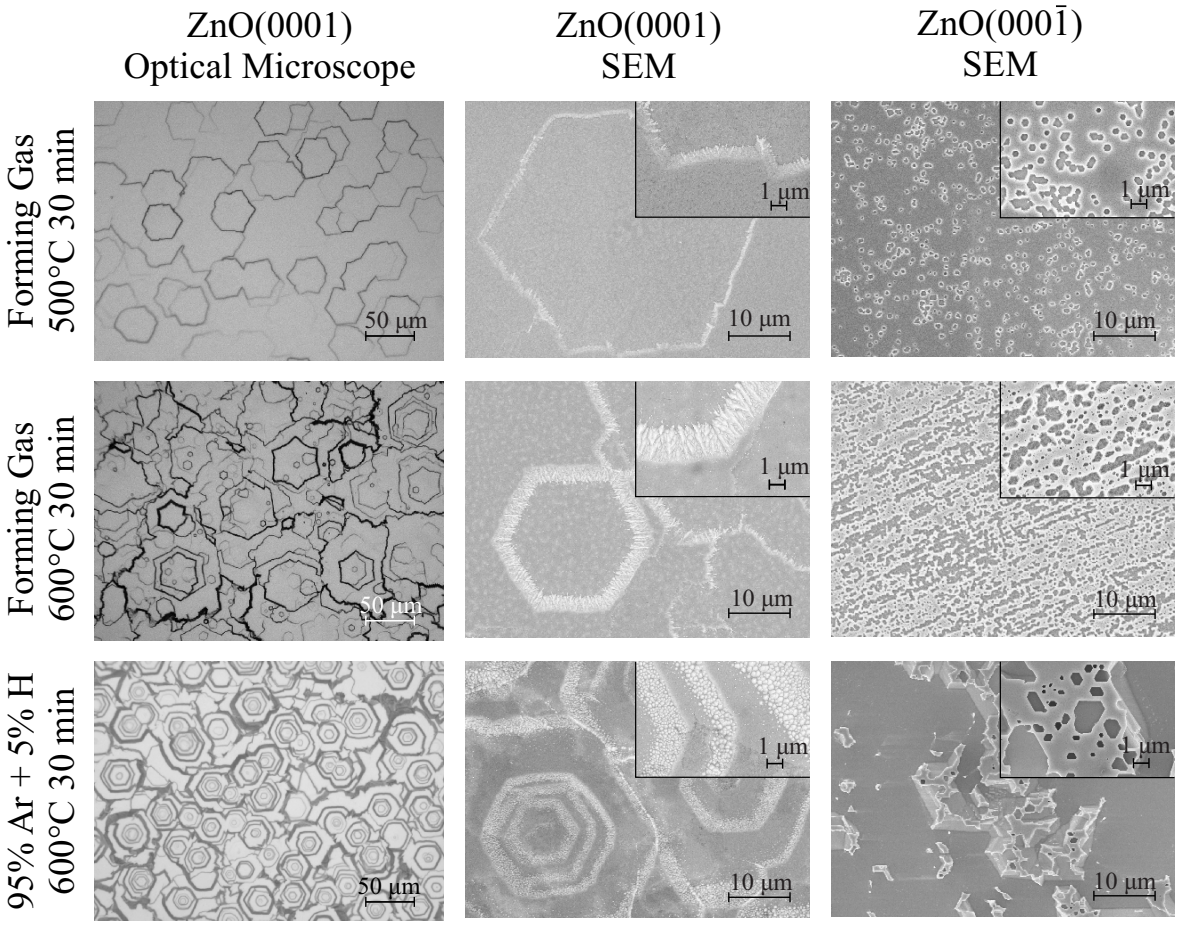

Figure 6.9.: Optical and scanning electron microscopy images for HT ZnO crystals annealed in forming gas (95 % N_2 + 5 % H_2) and 95 % Ar + 5 % H_2 (Ar-H_2) gas after initial O_2 annealing.

polar face, as the O-polar polar face was very diffuse at this magnification. The effect of FG or Ar-H_2 annealing on ZnO surfaces is comparable to that produced by wet-chemical etching [207]. The Zn-polar polar face exhibits hexagonal planar hills, not dissimilar to hexagonal (wet-)etching pits, whereas the O-polar face exhibits a rather diffuse defect structure. At higher FG annealing temperatures (i.e. 600 °C), the surface defect density on the O-polar face increased significantly. Interestingly, FG and Ar-H_2 annealing results in somewhat different surface structures. After Ar-H_2 annealing under identical conditions, a significantly higher hexagonal terrace density is observed with high vertical stacking. This change in surface structure however, has no discernable influence on the PL spectra e.g. in terms of line widths or overall intensity yield.

Low-Li HT ZnO and melt-grown Cermet ZnO wafers were also subjected to O_2 and subsequent FG annealing at 600 °C for 90 min and 60 min respectively, with the resulting PL spectra presented in Fig. 6.10. The melt-grown material shows a small recovery of the conventional I_4 line after FG annealing. As I_4 is reported to be thermally stable

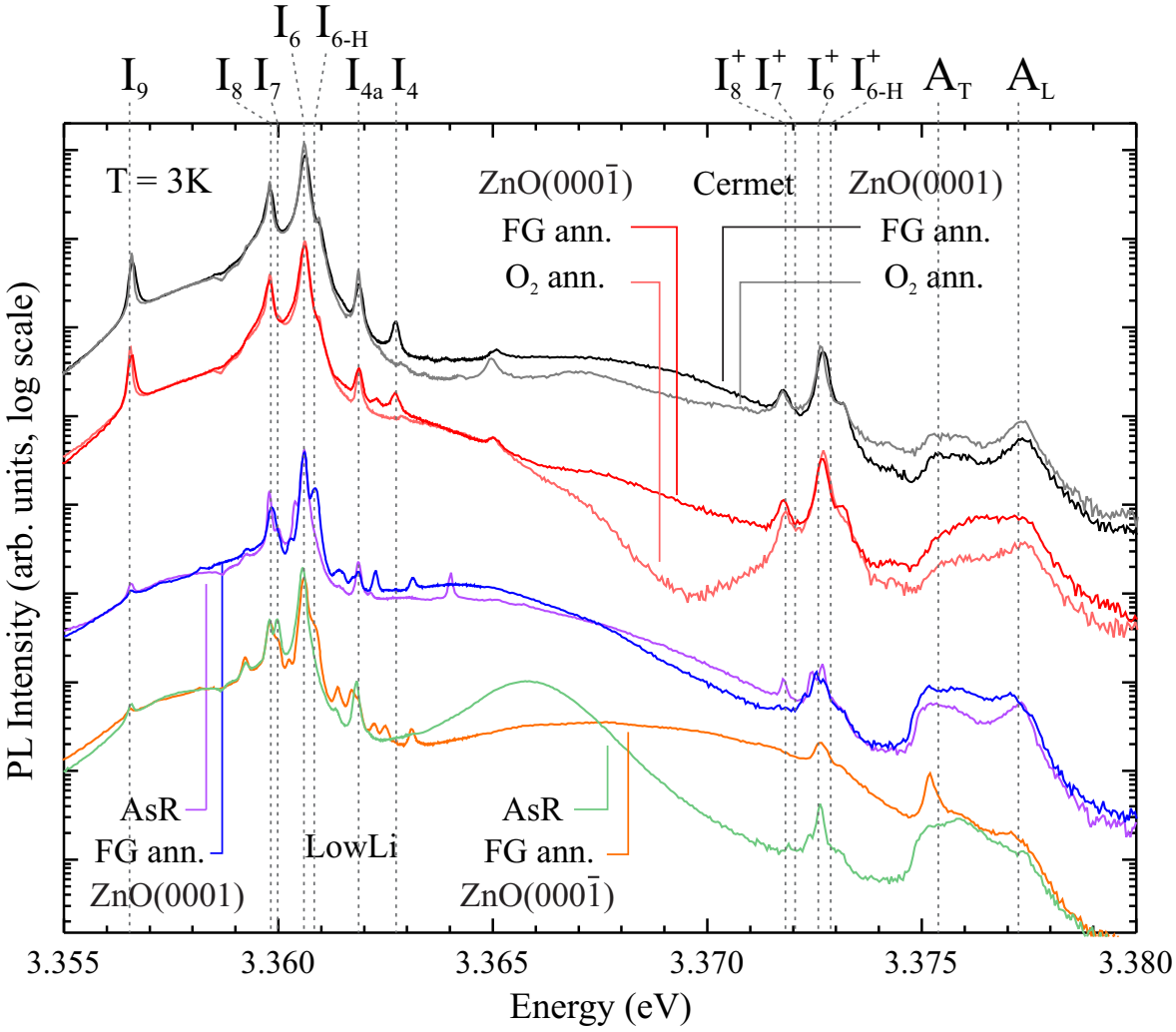

Figure 6.10.: PL spectra of melt-grown ZnO material annealed in O_2 atmosphere and after subsequent FG annealing at 600 °C for 60 min. For Low-Li HT ZnO, the FG-annealed sample is compared to an as-received (AsR) wafer because the as-received wafer was already subjected to a post-growth annealing cycle. The D^0X region is shown in greater detail in Fig. 6.11.

to higher temperatures (∼600 °C), than $I_{4b,c}$ (∼400 °C), it is possible to re-introduce it more effectively via FG annealing. This was not possible for $I_{4b,c}$, which appears to immediately re-dissociate for FG annealing at temperatures of 500 – 600 °C. For the Low-Li HT material, neither I_4 nor $I_{4b,c}$ are present after FG annealing. Significantly, I_{6-H} was introduced in the Low-Li HT material via forming gas annealing but not in the Cermet melt-grown ZnO. This exclusively links the presence of I_{6-H} to hydrothermally grown ZnO and so its origin is likely to be due to impurities or defects unique to hydrothermal material.

To investigate this effect further, the dominant neutral donor-bound emission region for different ZnO materials, before and after FG annealing, is shown in Fig. 6.11. As

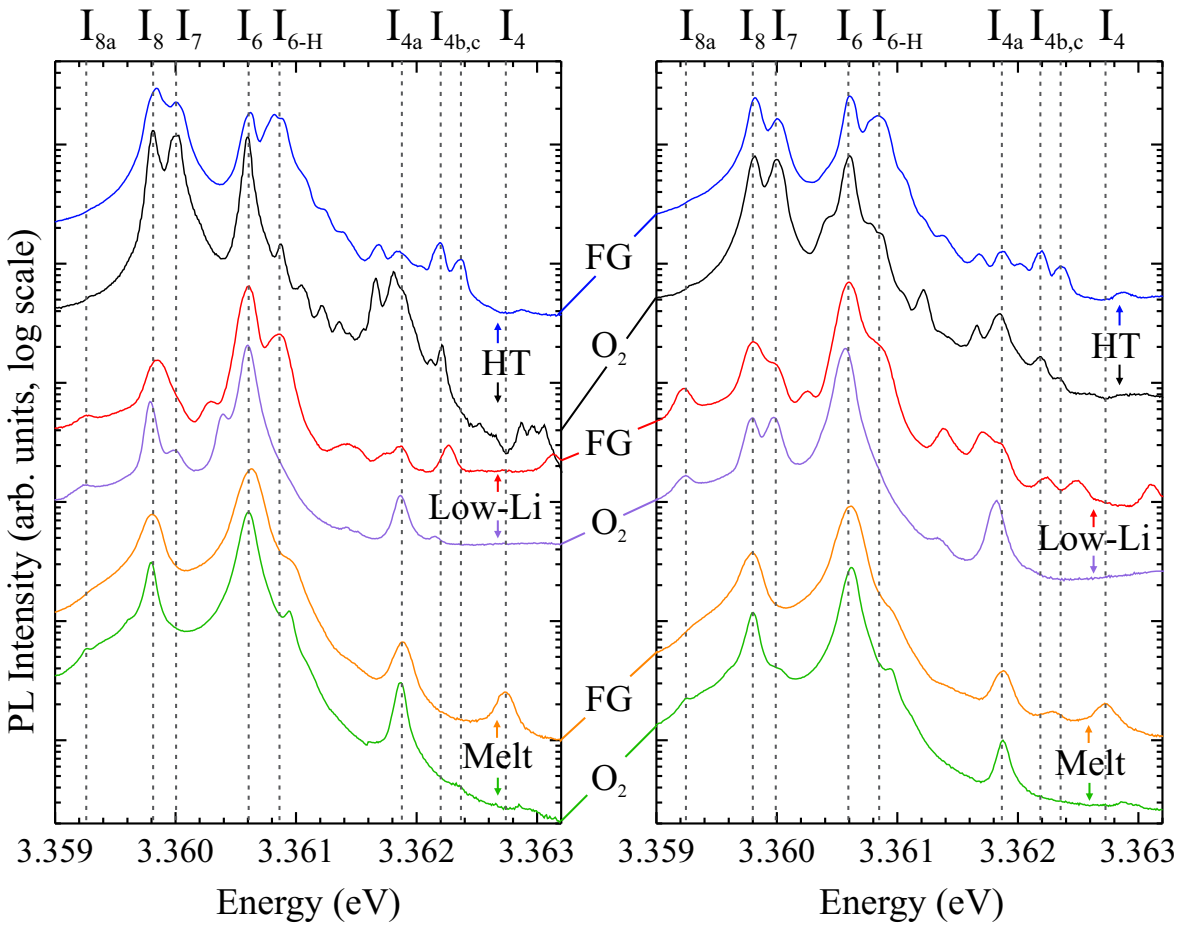

Figure 6.11.: Dominant D^0X region for different ZnO materials after initial O_2 and subsequent FG heat treatment.

already mentioned, I_{6-H} can be reintroduced into O_2-annealed HT ZnO by FG annealing. In Low-Li material, which shows no initial I_{6-H}, it can also be introduced by FG annealing, although with a significantly lower intensity compared to HT ZnO. Interestingly, I_{6-H} cannot be introduced by FG annealing into melt-grown ZnO. Therefore, it seems likely that the underlying hydrogen complex of I_{6-H} is not formed in melt-grown ZnO due to the absence of one binding partner, most probably lithium. Unlike HT ZnO, melt-grown material shows only trace amounts of Li or Na. Significant concentrations (in the 10^{16} to $10^{17}\,cm^{-3}$ range) of Li are present in conventional HT ZnO via the alkaline mineralisers used in the hydrothermal growth process. The concentration of Li is significantly reduced in Low-Li HT ZnO by high temperature (1100 – 1400 °C) annealing and subsequent re-grinding/re-polishing of the surface, however residual amounts of Li will still be present.

Substitutional Li on the Zn-site is supposed to form a complex with hydrogen [81, 83] and could potentially provide the recombination centre for I_{6-H}. This would explain why Low-Li HT ZnO with its lower lithium concentration compared to conventional

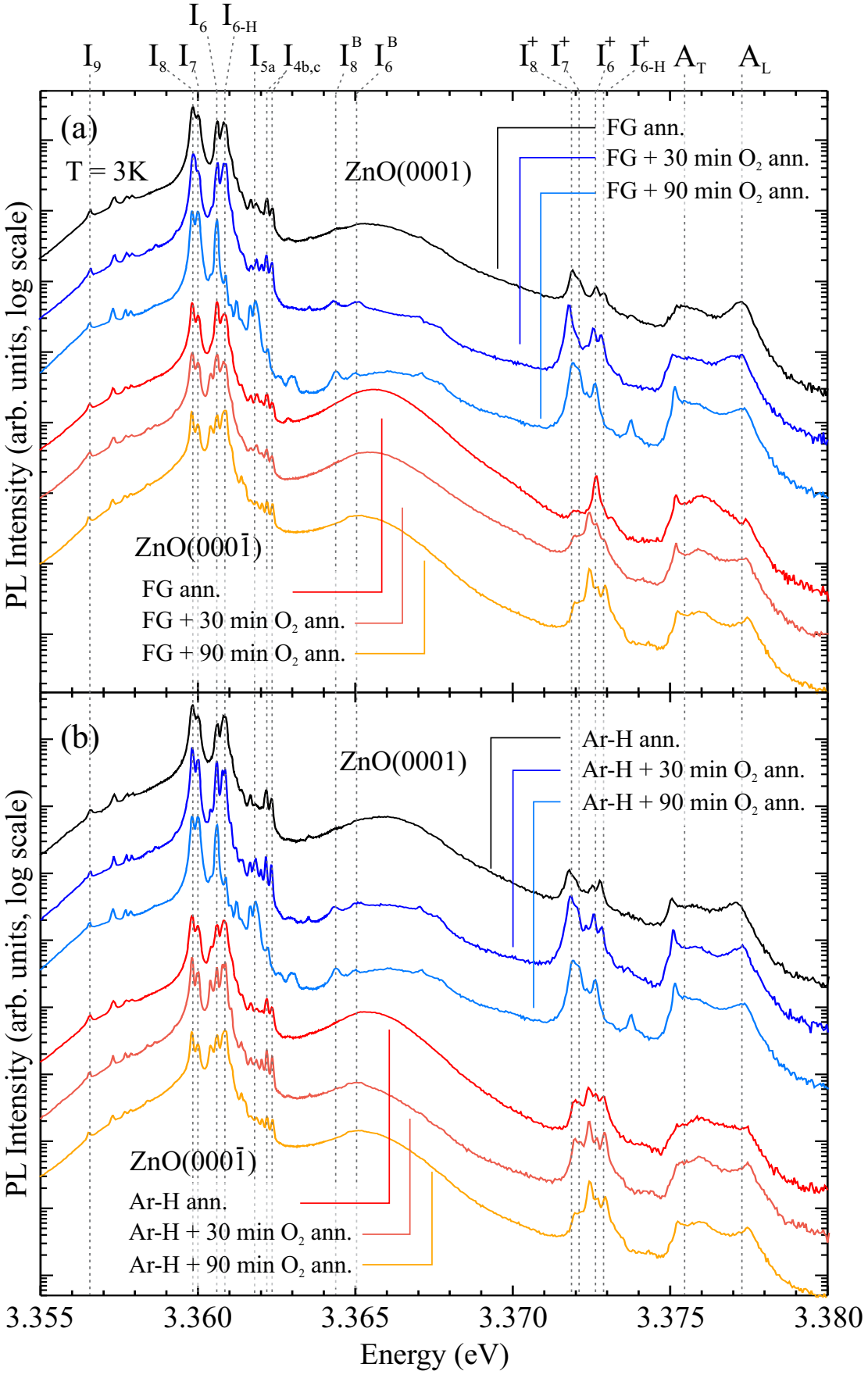

Figure 6.12.: 3 K PL spectra after re-annealing in O_2 atmosphere for 30 min after initial O_2 plus (a) FG or (b) Ar-H_2 annealing of a conventional HT ZnO wafer).

HT ZnO, shows a much weaker I_{6-H} emission after FG treatment. Furthermore, O_2 annealing reveals the I_{4a} line on conventional HT ZnO, possibly superimposed by excited rotational-vibrational states of I_6 that is not commonly observed in as-grown HT material. After FG annealing, I_{4a} is only vaguely resolved as the diffuse background intensity increases. The same behaviour is observed for Low-Li HT and melt-grown ZnO, where I_{4a} decreases in intensity and broadens. Teke *et al.* [152] stated that FG annealing at 600 °C for 10 min improved the luminescence yield of the excitonic transitions of melt-grown material (also obtained from Cermet Inc.) due to improved crystal quality. Although, FG annealing seems to introduce new peaks in the PL spectra (in Fig. 6.10) no appreciable change in PL intensity was observed and the line widths tended to increase slightly, as can be seen in Fig. 6.11. To ensure the reproducibility of the observed PL changes, a final O_2-annealing cycle was carried out on the same (FG-annealed) samples and the resulting PL spectra are presented in Fig. 6.12. Apart from a smaller decrease in background intensity, all PL features are in close agreement with those obtained after the first O_2-annealing step. However, this time, quenching of I_{6-H} was only observed on the Zn-polar face regardless of the composition of forming gas previously used. After 90 min of O_2 annealing, $I_{4b,c}$ is no longer present on both Zn-polar faces, revealing the I_{5a} line and its ionised donor replica at 3.37378 eV. Following the final O_2 annealing step, the broad Gaussian-shaped SX peak at 3.3655 eV again decreases in intensity on the Zn-polar face but is almost unchanged on the O-polar face.

The fact that I_{6-H} is present in HT ZnO but not in melt-grown ZnO leads to the conclusion that a complex formed between H and the abundant group I elements in HT material is involved. As mentioned in Sec. 2.4, substitutional Li on the Zn site is likely to form a complex with interstitial hydrogen. Using temperature-dependent Hall effect measurements (TDH), Look [208] found in HT ZnO annealed in FG at $T \geq 600$ °C a new shallow donor with a binding energy of 48 meV. This donor was not observed when a N_2 atmosphere was used. The new donor was found to be stable to at least 400 °C when subsequently re-annealed in N_2. Only a minor I_4 line was observed after annealing, leading to the conclusion that the donor must be unrelated to I_4 itself with a stable hydrogen complex being proposed, e.g. Al_{Zn}-Li_{Zn} which dissociates under high temperatures in the presence of hydrogen to $Al_{Zn} + Li_{Zn}$-H. However, $I_{4b,c}$ and I_{6-H} are observed in as-received HT ZnO material, which is grown in thermodynamic equilibrium, making a complex dissociation unlikely. Furthermore, IR measurements [209] showed that the 3577 cm^{-1} line, associated with the Li_{Zn}-H or Li_{Zn}-OH complex, is stable up to 1200 °C for several hours. None of the ZnO crystals investigated in this thesis showed any change in their post-annealed PL spectra with time as confirmed by subsequent measurements conducted several months later.

6.4 Y-lines and TES region of annealed ZnO

Annealing in different atmospheres not only has a profound impact on the D^0X transitions, but also on the appearance of Y-lines and on the TES region in general. Figure 6.13 shows both these regions for different ZnO materials under various annealing conditions. For conventional HT ZnO (Fig. 6.13(a)), annealing in O_2 or N_2 atmosphere introduces Y_0 and its broad low-energy shoulder. Although, several new peaks appear, the previously reported Y_1 and Y_2 [187, 189] were not identified. Remarkably, the N_2-annealed HT ZnO material shows as many as seven new, unidentified features near the Y_1 position (see inset). Broader transitions, in the same region, are found for O_2-annealed Mitsubishi ZnO in Fig. 6.13(c). Interestingly, after FG annealing of HT ZnO, both Y_0 and its accompanying shoulder shows a significant decrease in intensity.

Wagner *et al.* [187] provided convincing evidence for Y lines being excitons bound to extended structural defects and suggested a complex involving one singly ionised and one neutral donor. The bound exciton would then donate its electron to the complex and leave a weakly bound hole. It is conceivable that hydrogen would simply passivate the ionised donor and, therefore, quench Y_0. However, the process must be more complex as no quenching is observed after FG annealing for Low-Li HT ZnO or melt-grown ZnO, shown in Fig. 6.13(b) and 6.13(d). The structural defects are believed to be bulk-like rather than surface-related, as shown by confocal micro-PL [187], and similar to basal plan stacking faults, that result in the 3.31 eV emission line reported by Schirra *et al.* [210]. The SEM scans presented in Fig. 6.9 show that all materials exhibit the same hexagonal layered structure after FG annealing, however, the intensity of Y_0 varies strongly, making a purely surface-related origin of Y_0 unlikely. The Low-Li HT ZnO and Mitsubishi HT ZnO crystals were both annealed in their post-growth processing and exhibit Y_0 in their as-received forms. In contrast to HT ZnO, melt-grown material is grown at high temperatures, up to 1900 °C [9]. The rapid cooling of the melt-grown ZnO immediately after crystallisation introduces significantly more structural defects than HT ZnO growth at low temperatures (300 – 400 °C) close to thermodynamic equilibrium and, therefore, this promotes the characteristic Y_0 line. Furthermore, Y_1 and Y_2 are only observed in melt-grown ZnO but annealing in different atmospheres seems to have no significant effect on these lines apart from a small increase in intensity after O_2 annealing. The presence of Y_1 and Y_2 also depends on the individual sample, i.e. the Low-Li HT ZnO crystal in Fig. 5.8 on p. 75 exhibits Y_2 whereas a different crystal from the same batch, used for the annealing experiments in Fig. 6.13, shows no indication of Y_2. Y_0 is always accompanied by a broad shoulder on its lower energy side, centred at 3.3311 eV. For samples with a strong I_4 emission, this

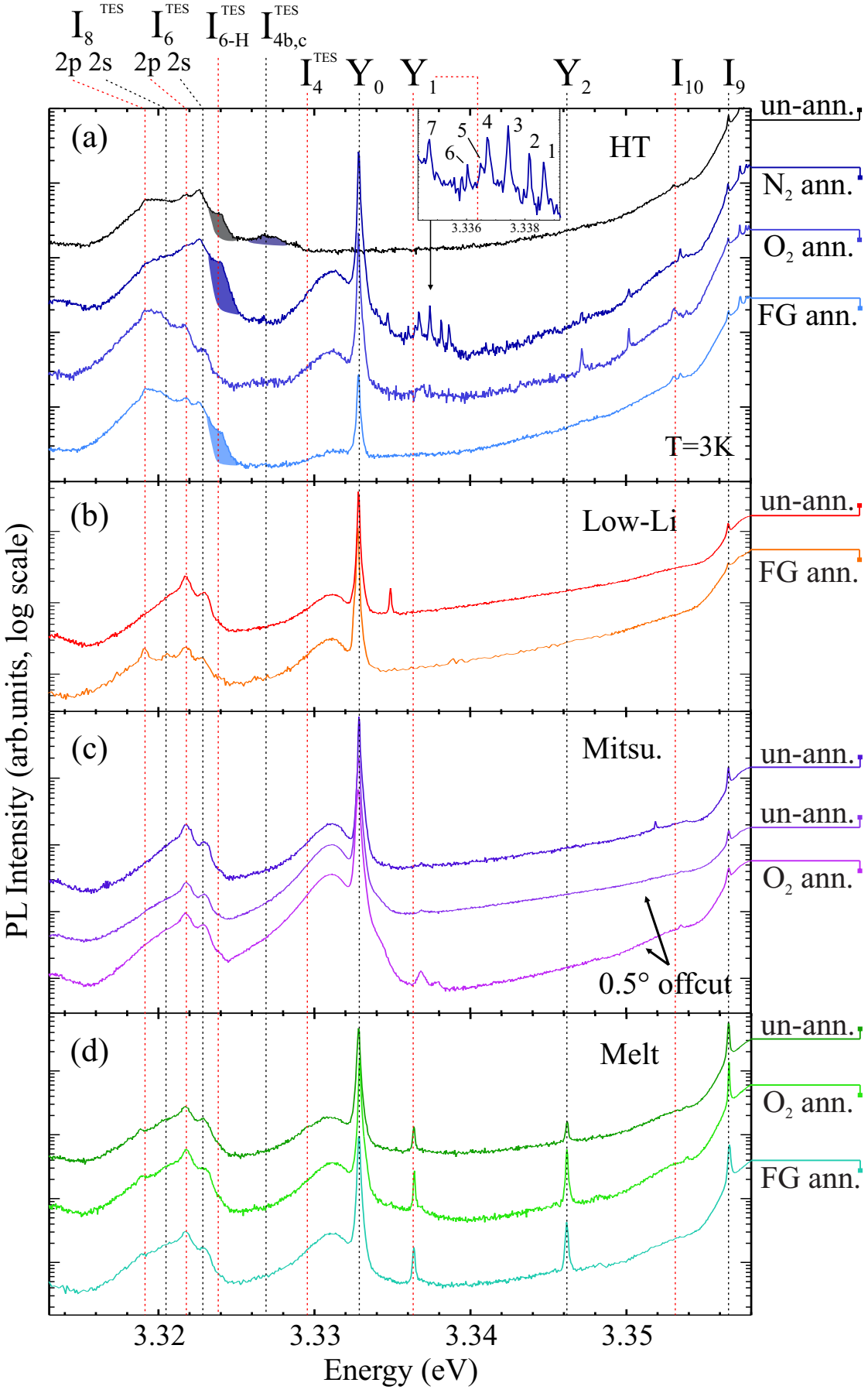

Figure 6.13.: Y-lines and TES region for different materials and annealing conditions. The $I_{4b,c}^{TES}$ and I_{6-H}^{TES} are marked as shaded areas.

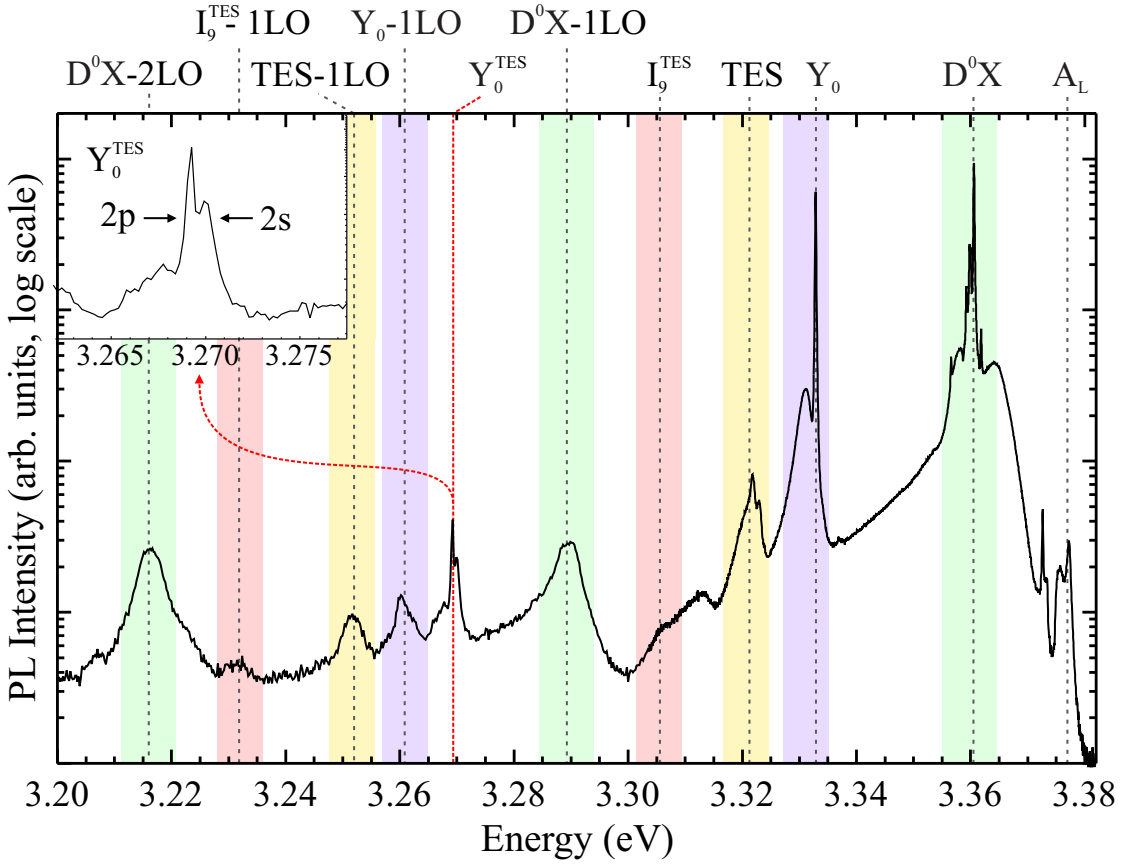

Figure 6.14.: 3 K PL spectrum of the O-polar face of Mitsubishi 0.5° offcut wafer after O_2 annealing. The fine splitting of the TES transition for the Y_0 line is resolved (see inset) as well as its longitudinal-optical phonon replicas labelled as LO.

peak is superimposed by the I_4^{TES} transitions. However, it is also present when no I_4 is observed, as in O_2-annealed material.

Certain TES spectra in Fig. 6.13(a), exhibit an distinct shoulder (shown as shaded areas) on the high energy side of the TES peak. For the conventional HT ZnO this shoulder is always observed when $I_{6-\mathrm{H}}$ is present and is likely to be its respective TES line. As all TES transitions, except for I_4, exhibit an orbital splitting of $E(2s) > E(2p)$, the high energy edge of the $I_{6-\mathrm{H}}^{\mathrm{TES}}$ shoulder is assigned to $I_{6-\mathrm{H}}^{\mathrm{TES}}(2s)$ with $I_{6-\mathrm{H}}^{\mathrm{TES}}(2p)$ being partially overlapped by $I_6^{\mathrm{TES}}(2s)$. This overlapping can be seen after O_2 annealing of HT ZnO, where the intensity of $I_6^{\mathrm{TES}}(2s)$ suddenly decreases as the underlying $I_{6-\mathrm{H}}^{\mathrm{TES}}(2p)$ transition quenches. In Low-Li HT, Mitsubishi HT, and melt-grown ZnO, which all show no indication of $I_{6-\mathrm{H}}$, this shoulder is absent. After FG annealing, a relatively weak $I_{6-\mathrm{H}}$ could be observed in Low-Li HT ZnO with an intensity approximately 40% that of I_6. Taking this low intensity ratio and the high background intensity in the TES region into account, it is not surprising that $I_{6-\mathrm{H}}^{\mathrm{TES}}$ is not observed in this case.

The PL spectrum of the Mitsubishi O-polar sample after O_2 annealing is shown in Fig. 6.14. Longitudinal optical phonon-replicas (LO) of the dominant D^0X transitions, the Y_0 line, and the D^0X - TES region are shown and colour coded. As expected, the energetic distance between individual phonon-replicas and the zero-phonon line is 71.4 – 72.6 meV, close to the average reported value for LO phonons in ZnO of 72 meV. Due to the exceptionally strong Y_0 line in this material, the Y_0^{TES} and its orbital splitting can be resolved (see inset). The extracted TES splitting parameters are summarised in Table 5.4. Furthermore, the weak TES transition of I_9 is present at 3.3057 eV, followed by a second peak at 3.3130 eV. The latter was assigned by Schirra *et al.* [210] as a free to bound acceptor transition (e,A^0). Spatially resolved cathodoluminesence and tunnelling electron microscopy revealed that these acceptor-like defects appear preferentially on basal plane stacking faults. The combined phonon-replica of these two D^0X transitions produces a weak feature at 3.23315 eV. The second phonon replica at 3.2164 eV exhibits a asymmetric shoulder on its higher energy side. With an assumed LO phonon spacing of 72 meV, one could anticipate I_{10}^{TES} as a possible origin, as it is expected in this region. However, I_{10}^{TES} itself falls into the so called Fano-resonance [102] region, characterised by a strong decrease in intensity at 3.30 eV and, consequently, is seldom observed in bulk HT ZnO material.

6.5 Summary

This chapter addressed the changes in PL emission of bulk ZnO single crystals after annealing in oxygen, nitrogen, N_2-H_2 forming gas and argon-hydrogen gas. The findings are summarised as follows:

- Annealing in oxygen significantly decreases the background PL intensity in the region between 3.374 eV to 3.362 eV. In this region, the *B*-exciton transitions and further unidentified transitions are now clearly resolved.

- The decrease in background intensity is more pronounced on the Zn-polar face for which the broad Gaussian-shaped SX feature characteristic of the O-polar face is not observed. With re-annealing in forming gas or Ar-H_2 gas, the broad SX feature is introduced on both polar faces making a involvement of near-surface hydrogen likely.

- $I_{4b,c}$ and I_{6-H} quench on annealing in oxygen and so do their D^+X replicas. However, I_6, which is usually the dominant line in ZnO, is not affected by annealing. Annealing in nitrogen atmosphere quenches $I_{4b,c}$ but not I_{6-H}.

- After $I_{6-\mathrm{H}}$ is quenched by annealing in oxygen, it can be reintroduced by subsequent annealing in forming gas or Ar-H_2 gas. To a lesser extent, this can also be achieved for Low-Li HT ZnO material, which does not show any sign of $I_{6-\mathrm{H}}$ in its as-received state. However, it is not observed in as-received or FG-annealed melt-grown ZnO material. In contrast to melt-grown ZnO, hydrothermal ZnO contains large amounts of group I impurities introduced in the growth process via alkaline mineralisers. A Li- and H-related defect is, therefore, a likely origin for $I_{6-\mathrm{H}}$.

- The quenching and reintroduction of certain D^0X transitions can also be observed in their respective TES-lines.

- Oxygen annealing introduces a DAP-transition in conventional HT ZnO, which is missing in Low-Li HT ZnO material. Similar DAP-transitions were reported for Li-doped ZnO thin films.

7 | Hydrogen and Deuterium Implantation in ZnO

Initial investigations into the PL properties of hydrothermally and melt-grown ZnO single crystals revealed that various recombination lines in ZnO are related to hydrogen. Some of these PL lines could be quenched by annealing in oxygen atmosphere and re-introduced by forming gas annealing. In this chapter, hydrogen and deuterium were deliberately introduced into conventional HT ZnO and Low-Li HT ZnO by ion implantation. Following implantation, the evolution of the PL spectra after annealing in oxygen gas at different temperatures was investigated.

7.1 Hydrogen and Deuterium Implantation

Incorporation of hydrogen into ZnO is usually accomplished via diffusion, e.g. heat treatment in forming gas, H_2 gas-filled ampoules, or hydrogen plasma treatments. However, hydrogen and deuterium can also be introduced by ion implantation. Compared to diffusion mechanisms; ion implantation allows a higher degree of control over the implantation dose and implantation depth and can be carried out close to room temperature. Although ion implantation may introduce significant structural damage into the crystal, this can be advantageous in investigating the defect nature of certain impurities and complexes.

Regarding the general optical properties of implanted ZnO bulk crystals, Ip *et al.* [211] reported a considerable reduction in PL intensity and broadening of transition lines after deuterium implantation. Only a fraction of the pre-implantation luminescence intensity was recoverable after annealing up to 700 °C. This may be due to the high implantation energy used, i.e. 100 keV compared to the 4 – 18 keV energies in this work. The resulting implantation, with a projected range maximum of 1 µm, was much deeper than typical PL probing depths of approximately 90 nm. Although implantation appeared to almost completely suppress the PL emission, they found almost no change

in the structural properties of the implanted ZnO crystals in Rutherford backscattering experiments.

Lee *et al.* [212] implanted ZnO single crystals with hydrogen doses ($2 \times 10^{13} - 5 \times 10^{15}$ atoms cm^{-2}) and implantation energies (6 keV) comparable to the work presented here. They observed two dominant PL lines at 3.364 eV and 3.361 eV, and upon implantation, the latter increased in intensity and was dominant for the highest implantation dose. After vacuum annealing at 300 °C for 15 min the unimplanted PL spectrum was recovered, although with a decreased intensity.

7.1.1 D^0X transitions

Implantation was carried out at GNS Science, Wellington, NZ on the ZnO(0001) polar face of samples from conventional HT ZnO and Low-Li HT ZnO single crystal wafers supplied by Tokyo Denpa Co. Ltd (Japan). For a summary of implantation parameters see Table 3.1 in Sec. 3.3. PL spectra were measured at 4 K on as-received and implanted samples. To investigate the effect of implantation damage and the role of hydrogen and deuterium, the same samples were subjected to a series of annealing steps at temperatures between 200 – 600 °C for 30 min in a flowing O_2 atmosphere.

Figure 7.1 and 7.2 show the dominant D^0X transitions in the near-band-edge region for conventional HT and Low-Li HT ZnO crystals implanted with H and D after each annealing temperature. Note the different implantation doses for the two different isotopes. In each case, the corresponding spectra from an unimplanted and unannealed Zn-polar face reference sample is included for comparison.

We first consider Fig. 7.1(a) which shows PL spectra for HT ZnO implanted with an H dose of 7×10^{14} atoms cm^{-2}. Implantation leads to suppression of the majority of PL lines in the as-implanted, unannealed material. Most of the transitions observed in the reference sample (uppermost graph) now appear merged (lowest graph) with an intensity maximum at 3.3608 eV, the energetic position of $I_{6-\mathrm{H}}$. Considering that $I_{6-\mathrm{H}}$ is the strongest emission line in the unimplanted material, this is not surprising. Furthermore, peaks at the energetic positions of I_7, I_8, and I_9 can still be resolved. Two other peaks can be identified: one at 3.3615 eV, possibly I_5, and an unidentified peak at 3.3602 eV. Interestingly, $I_{4\mathrm{b,c}}$ has been completely quenched and only a minor peak at the position of conventional I_4 is present. Assuming the same intensity ratio of $I_{6-\mathrm{H}}$ to $I_{4\mathrm{b,c}}$ for bare and implanted crystals, one would expect $I_{4\mathrm{b,c}}$ to still be present. As implantation was carried out close to room temperature, the absence of $I_{4\mathrm{b,c}}$ may suggest that implantation damage may remove the $I_{4\mathrm{b,c}}$ binding site.

After annealing at 200 °C, all peaks become sharper and a new peak emerges at

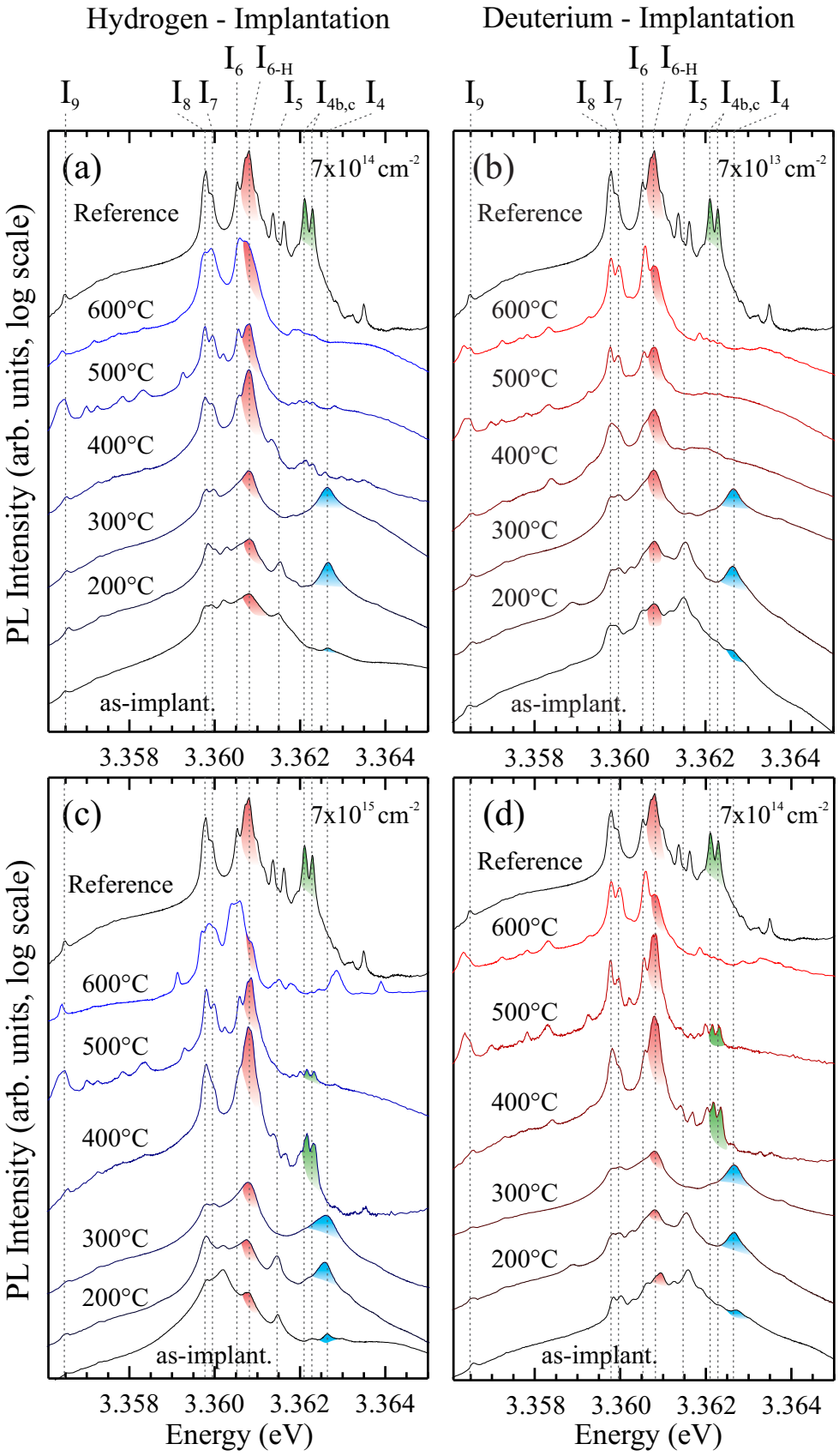

Figure 7.1.: 4 K PL spectra of hydrogen (a),(c) and deuterium (b),(d) implanted Zn-polar HT ZnO for two different implantation doses and subsequent annealing in O_2 atmosphere. PL emission from an unimplanted ZnO crystal of the same wafer is labelled as *Reference*. Hydrogen-related peaks shaded in color.

3.3626 eV. This is the characteristic position of the conventional, hydrogen-related I_4, which is not usually observed in HT ZnO material. This I_4 transition is still present after 300 °C annealing, but quenches completely after the 400 °C annealing step. Experimental studies concerning the thermal stability of I_4 usually report quenching at 500 – 600 °C. Remarkably, following 400 °C annealing, the PL spectrum closely resembles that of the unimplanted reference sample, with a distinctively strong I_{6-H} and a lower intensity I_6. Both, I_7 and I_8, show a similar relative strength after implantation and 400 °C annealing compared to the reference. Note that the peak close to the I_5 position (addressed as I_5 in the following) was thermally quenched at 300 °C.

For H implantation into HT ZnO with a dose of 7×10^{15} atoms cm^{-2}, shown in Fig. 7.1(c), the as-implanted and annealed spectra show similar trends to those observed for the 7×10^{14} atoms cm^{-2} dose. $I_{4b,c}$ is better resolved and quenches for both implantation doses after 500 °C annealing. The same thermal stability was observed in annealing experiments of unimplanted HT ZnO material. Further annealing, at 500 °C decreases the intensity ratio between I_{6-H} and I_6 from a factor of 2 for 400 °C to 1.16 at 500 °C for a dose of 7×10^{14} atoms cm^{-2}, similar to the annealing experiments of unimplanted ZnO presented in Sec. 6.1. The five new transitions between I_8 and the significantly broadened I_9 are addressed in Sec. 7.1.2. After annealing at 600 °C a visible degradation was observed on the crystal surface which is reflected in the PL quality. The individual peaks, e.g. I_7 and I_8, are no longer distinguishable and the intensity of the new transitions has significantly decreased as well. At 600 °C, crystals implanted with the lower H dose exhibit a I_{6-H}:I_6 intensity ratio of less than one while for the higher implantation dose, I_{6-H} is reduced to a mere shoulder. At the same time, I_6 seems to broaden and a I_{6a} line develops, which is commonly observed in Low-Li HT ZnO. Deuterium implantation resulted in almost identical spectral changes as those observed for hydrogen (Fig. 7.1(b,d)), suggesting that both isotopes produced a similar amount of crystal damage and that any isotopic shifts in the hydrogen-related PL lines were below the available resolution. As with hydrogen implantation, the I_4 and $I_{4b,c}$ lines are observed and exhibit the same thermal stability with annealing. The partial loss in I_{6-H} intensity is also reproduced. The only noticeable differences are the stronger I_5 transition and the better PL resolution obtained at higher annealing temperatures.

Implantation of hydrogen and deuterium was also carried out on Low-Li HT ZnO crystals with the resulting PL spectra presented in Fig. 7.2. For as-implanted Low-Li HT ZnO crystals, the dominating feature is a broad peak containing I_7 and I_8, even though the unimplanted material is dominated by I_{6a} and I_6. Annealing at 300 – 400 °C allows both lines to be separately resolved. The higher hydrogen implantation dose leads to a decrease in crystalline quality and broader PL transitions after anneal-

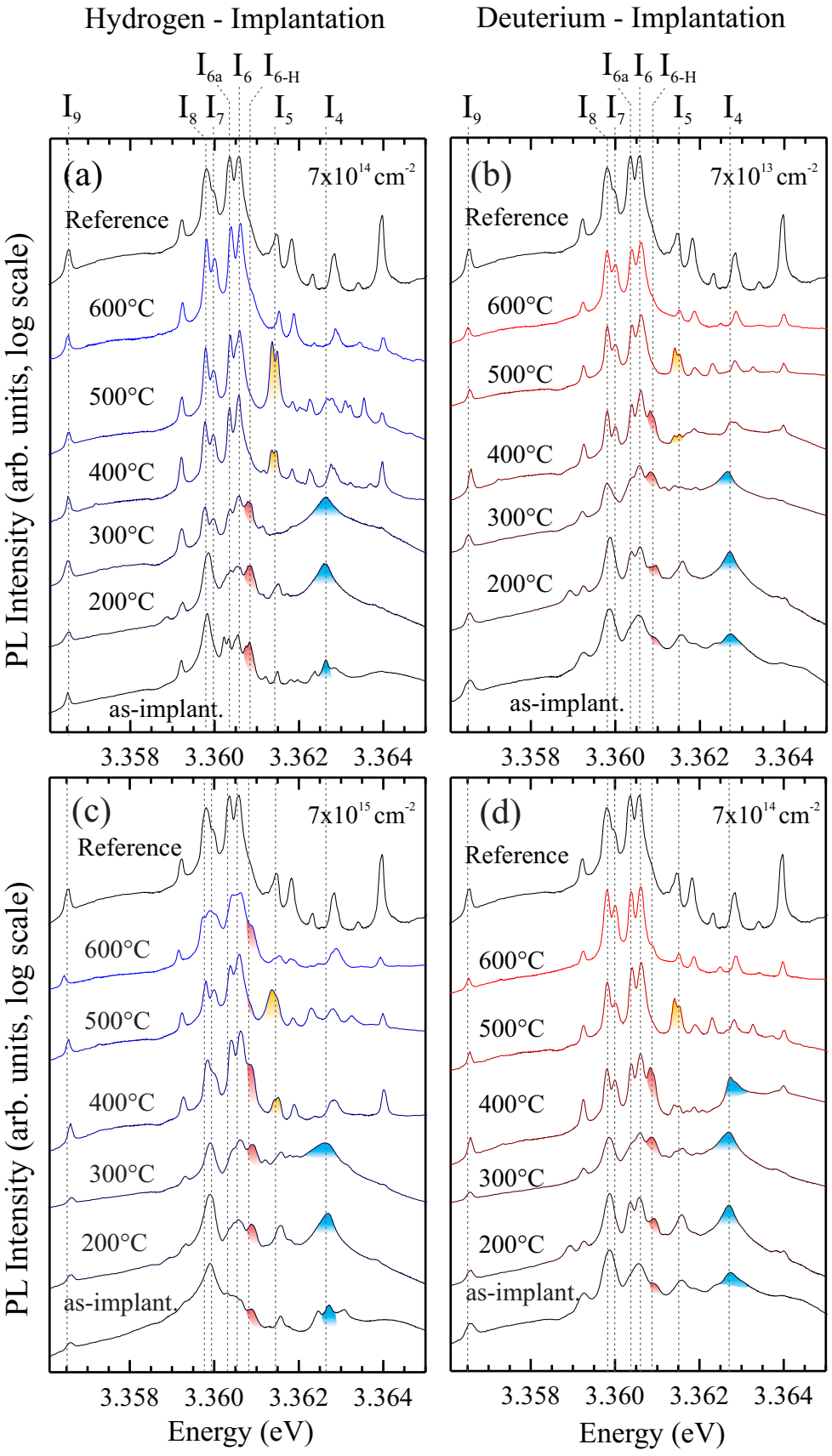

Figure 7.2.: 4 K PL spectra of hydrogen (a),(c) and deuterium (b),(d) implanted Zn-polar Low-Li HT ZnO for two different implantation doses and subsequent annealing in O_2 atmosphere. PL emission from an unimplanted ZnO crystal of the same wafer is labelled as *Reference*. Hydrogen-related peaks shaded in color.

ing at 600 °C (note: the same behaviour was observed for the H-implanted conventional HT ZnO crystals). For H implantation and low annealing temperatures, a broad feature is present around 3.3605 eV, consisting of I_{6a}, I_6 and I_{6-H}, where I_{6-H} seems to quench completely at 400 °C for Low-Li HT ZnO crystals implanted with a dose of 7×10^{14} atoms cm^{-2}. In crystals implanted with an order of magnitude higher hydrogen dose, I_{6-H} is present even after 600 °C heat treatment. As before, I_4 emerges again after annealing between 200 – 300 °C. A double peak close to the energy of I_5 at 3.3614 eV, which was not initially present, is observed upon annealing to 400 °C. Interestingly, this feature increases significantly in intensity after 500 °C annealing, to an intensity greater than that of I_8, before it rapidly quenches again after 600 °C. This effect is also observed for D implantation, but appears exclusive to Low-Li HT ZnO crystals.

Regarding overall crystalline quality, Low-Li HT ZnO implanted with a lower dose of hydrogen yields a PL spectrum almost identical to the unimplanted reference after heat treatment at 600 °C. On the other hand, crystals implanted with a dose of 7×10^{15} atoms cm^{-2} and annealed at 600 °C exhibit an overall decrease in resolution and more line broadening. One unidentified transition at 3.3640 eV seems to have been partially quenched after annealing above 400 °C. This emission line generally quenches with annealing regardless of whether implanted or unimplanted crystals are used. However, a PL comparison of different as-received Low-Li HT ZnO wafers showed that this feature is not always present. The PL spectra on D-implanted Low-Li HT material is remarkably similar to that from H-implanted crystals.

Apart from obvious changes in crystal and PL spectral quality, the key findings in H/D-implanted ZnO are: (i) the absence of $I_{4b,c}$ for the as-implanted material and the presence of I_4 after low temperature annealing, (ii) the introduction of I_{6-H} into Low-Li HT material by H and D implantation, and (iii) the emergence and subsequent quenching of I_5 for annealing temperatures around 500 °C. We now consider the implications of these findings in more detail.

(i) I_4 and $I_{4b,c}$

Following H/D implantation and annealing at 200 °C, I_4 is present in conventional HT ZnO and Low-Li HT ZnO crystals where it quenches after annealing at 400 °C. This is unusual as as-received HT and Low-Li HT ZnO crystals do not exhibit I_4. In addition, in melt-grown ZnO crystals where I_4 is commonly present, it shows a higher thermal stability of up to 600 °C. Implanted hydrogen or deuterium is likely to be readily trapped in oxygen vacancies (V_O) created by the implantation process. This would result in a strong I_4 signal, as it is believed to originate from hydrogen trapped in oxygen

vacancies. Interestingly, I_4 is present after annealing at 200 °C but not necessarily for the as-implanted ZnO crystals. This is in line with Zhang *et al.* [213] who investigated the cathodoluminescence of the V_O-related deep band emission (at 2.3 – 2.5 eV) in H-implanted HT ZnO crystals with annealing temperature. They observed a decrease in deep level CL intensity with higher H implantation doses due to the passivation of V_O by hydrogen. The lowest V_O CL intensity was reported for annealing at 200 °C for one hour. Similar conditions were used in this work. It seems therefore likely, that the 200 °C annealing step allows hydrogen to overcome the migration barrier in implantation-damaged ZnO crystals and occupy oxygen vacancies, leading to a decrease in V_O deep band emission and an increase in I_4.

The I_4 signal is completely absent after annealing at 400 °C for H/D-implanted HT and Low-Li HT ZnO crystals. This unusually low thermal stability for I_4 suggests that implantation damage may influence the hydrogen binding process. Several studies have shown that implanted hydrogen does not show the typical broadening in its SIMS profile with annealing, as would be expected due to a diffusion process. Instead, the peak position tends to be stable at its initial implantation depth or average projected range R_p [211, 214], although the peak concentration of H may decrease significantly. This implies that hydrogen is bound to structural defects introduced by the implantation process and annealing dissociates these structural defects, which leads to the fast out-diffusion of H. This trap-controlled release mechanism seems to take effect between 200 – 400 °C [214]. With the disappearance of I_4, $I_{4b,c}$ re-emerges after being absent in as-implanted ZnO. This suggests that the $I_{4b,c}$ binding site is strongly affected by implantation damage. As the overall PL quality after 400 °C annealing is relatively close to the unimplanted reference, it can be assumed that most of the implantation damage has been removed and, hence, $I_{4b,c}$ is once again observable. Hydrogen freed from V_O can now potentially bond in the $I_{4b,c}$ configuration. For annealing at 500 °C, $I_{4b,c}$ quenches irretrievably due to out-diffusion of hydrogen from the ZnO crystal, which is consistent with the annealing studies in the previous chapter.

(ii) Low-Li HT ZnO and I_{6-H}

Hydrothermally grown Low-Li HT ZnO material contains not only relatively low concentrations of lithium, but also low concentrations of hydrogen due to the high temperature (1100 – 1400 °C) post-growth Li-removal treatment. With the introduction of H and D by implantation, I_{6-H} is observable in Low-Li HT ZnO, similar its observation after annealing in forming gas. Interestingly, in the case of Low-Li HT ZnO, the I_{6-H} emission is always less intense than the neighbouring I_6. Assuming Li involve-

ment in the nature of I_{6-H} (remembering that I_{6-H} only appears in hydrothermally grown ZnO), this lower intensity ratio can be explained by the significantly lower Li concentration. In addition, I_{6-H} anneals out at high temperatures, except for a higher H implantation dose of 7×10^{15} atoms cm^{-2}. This is in contrast to conventional HT ZnO, where I_{6-H} decreases in intensity with annealing temperature but does not fully quench. Implantation experiments with various metal ions carried out as part of this work generally showed a higher thermal stability for I_{6-H} when implantation damage was present.

Chan *et al.* [215] found, using SIMS measurements, that after H implantation the residual Li present in HT ZnO material rearranged to an identical depth profile as the implanted hydrogen. This effect was even more pronounced after annealing at 600 °C in vacuum and was still observable after 800 °C annealing. They suggested hydrogen bound to an oxygen vacancy or a Li_{Zn}-OH complex as the cause of this unusually high thermal stability. The former seems unlikely given that H_O should not be stable above 600 °C. The implantation process generates defects at a certain depth, which clearly limit hydrogen diffusion. Similarly, the residual Li atoms will rearrange around the implantation damage and a Li-OH type defect complex is formed. From the higher thermal stability observed for Li and H atoms in the SIMS experiments presented by Chan *et al.*, a higher thermal stability for the Li-OH complex is expected.

Zinc vacancies introduced in the implantation process are likely to be filled by Li atoms in conventional HT ZnO. Together with the residual and implanted hydrogen, Li-H complexes can be formed which are thought to be involved in the I_{6-H} line. The higher temperature stability of I_{6-H} in ion-implanted material could then be explained by increased Li trapping in zinc vacancies. In Low-Li HT ZnO, the zinc vacancies are more likely to be occupied by hydrogen, leading to the observation of the so-called XH complex.

(iii) XH defect complex and hidden hydrogen

A new PL line, with an energetic position coinciding with I_5, appears only in implanted Low-Li HT ZnO material after annealing at 400 °C, increases in intensity at 500 °C and then disappears at 600 °C. Similar thermal behaviour was found in IR spectroscopy for the 3326.3 cm^{-1} line, first observed by McClusky *et al.* [216] and initially assigned to hydrogen in an anti-bonding lattice site (H_{AB}) perpendicular to the c-axis. However, this assignment was dismissed [217, 218] and, more recently, calcium-hydrogen complexes (CaH) [78] or Zn vacancies passivated by hydrogen (V_{Zn}-H_n) [76] have been proposed as possible chemical origins. The defect complex giving rise to the 3326.3 cm^{-1} IR line

will be referred to as XH. Interestingly, this IR line is also observed in melt-, SCVD-, and vapour-phase-grown material after subsequent annealing in H_2 gas. However, it is not present in conventional HT ZnO [81, 82], treated in the same way. Shi *et al.* [219] reported on the XH IR line and showed that it anneals out at around 150 °C and re-emerges at around 400 °C. A maximum line intensity was observed after 450 – 500 °C annealing followed by a subsequent decrease in intensity for any additional heat treatment thereafter.

This new PL line is not present in implanted conventional HT ZnO, but can be observed in implanted Low-Li HT material which has a much smaller residual Li concentration. The introduction of H and D via implantation produces a PL line with similar thermal characteristics as XH after annealing between 400 – 500 °C. Shi *et al.* [219] reported on a PL transition positioned close to I_6 in H_2 gas-annealed melt- and vapour-phase-grown crystals which showed the same annealing behaviour. Melt- and vapour-phase-grown crystals contain only trace amounts of Li. The same thermal stability was also observed for the H_{BC}-related IR line at 3611 cm^{-1}. Although, H_{BC} was reported to give rise to a PL transition at 3.3601 eV [75], apart from I_7, no lines were observed at 3.3601 eV in this work. One possible explanation was provided by Herklotz *et al.* [77]. They introduced H_{BC} and XH into melt-grown ZnO by annealing in an H_2 atmosphere. As a model: H_{BC} and XH will combine for annealing temperatures above 105 °C according to H^+_{BC}+XH $\leftrightharpoons$ X+H_2 and form molecular hydrogen, which is not detectable by IR measurements (the so-called hidden hydrogen [79]). On the other hand, H_2 will dissociate at higher annealing temperatures around 500 °C, again favouring the formation of isolated H_{BC} and XH. Annealing above this temperature leads to diffusion of unbound hydrogen out of the sample and a quenching of the XH-related IR line. Whether H_{BC} is required for this process has still not been conclusively proven. Raman spectroscopy on H-implanted ZnO crystals yielded unique features [220] on melt- and SCVD-grown ZnO substrates, which have not yet been identified as structural or hydrogen-related. Therefore, a combined Raman / IR absorption / high resolution PL study on implanted ZnO might provide deeper insight into the nature of the various hydrogen-related peaks.

7.1.2 Unique D^+0 transitions, Y-lines and DAP band

For annealing at 500 °C, several new transitions appear for both H- and D-implanted conventional HT ZnO material (see Fig. 7.3 (a)) between the energetic positions of I_8 and I_9. None of these lines were observed in the as-received or implanted Low-Li HT ZnO material and, hence, a chemical impurity origin seems likely. In addition, several

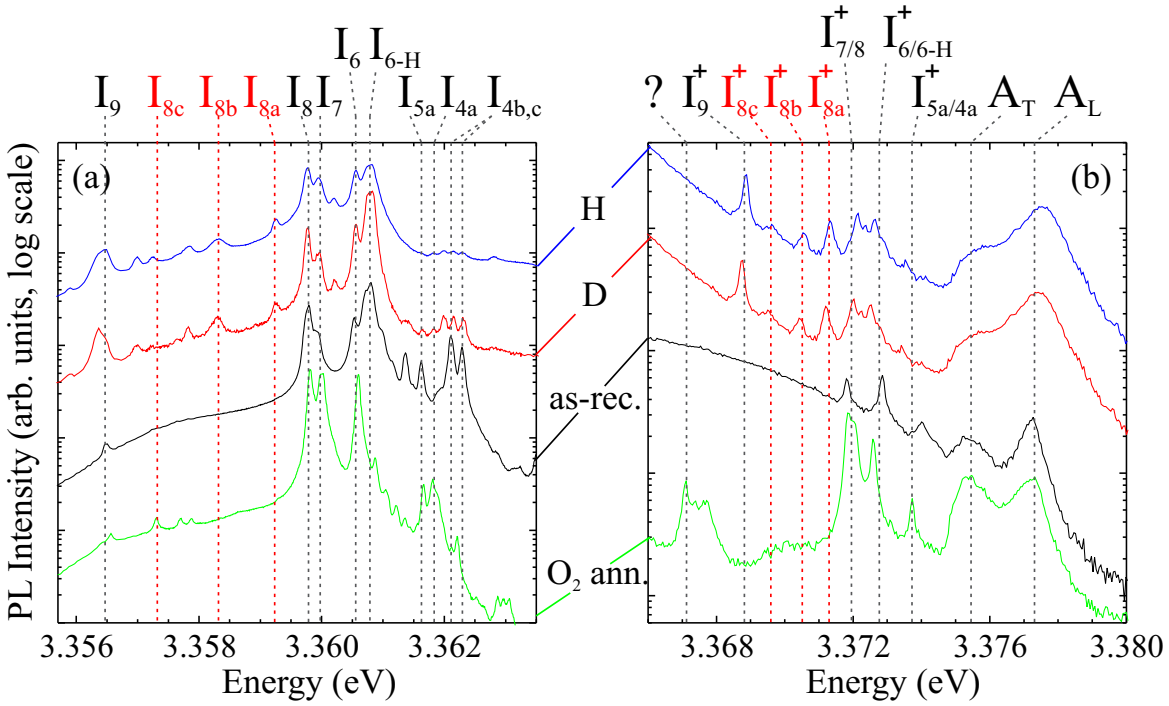

Figure 7.3.: 4 K PL spectra of as-received HT ZnO as well as hydrogen and deuterium implanted HT ZnO after 500 °C annealing. For comparison an unimplanted but 600 °C annealed HT ZnO wafer is also shown.

new D^+X transitions are observed and marked by red dashed lines in Fig. 7.3(b). By assuming a Haynes rule relationship between D^+X and D^0X for these newly observed lines, similar to that for known transitions (e.g. $I_6, \ldots$), the D^+X line positions for $I_{8a,b,c}$ were calculated and match well with the peaks present in Fig. 7.3(b). This suggests that this new transitions are likely to be due to effective mass donors and may be related to other known impurities in hydrothermally grown ZnO, such as Mg, Ca, Si or Fe, which were observed in SIMS measurements.

Interestingly, the ionised donor-bound I_9^+ is observed at 3.36874 eV for the first time. Its energetic position was also used in Sec. 5.5 to calculate the linear relationship between E_{Loc} and E_{D}. As the observed I_9^+ position scales perfectly with all other transitions, the unknown feature at 3.36713 eV is effectively ruled out as a possible candidate for I_9^+. Note, that the I_9^+ identified in this work is not the same as the one assigned by Meyer *et al.* [18]. However, the I_9^+ assignment in this work leads to almost identical slopes in the Haynes plot presented in Fig. 5.9 for both D^0X and D^+X transitions.

With heat treatment at 500 – 600 °C, various new lines emerge close to the Y-lines in Fig. 7.4. Interestingly, this occurs preferentially on H-implanted samples. Similar lines are observed after D implantation but with a reduced intensity. The only exception

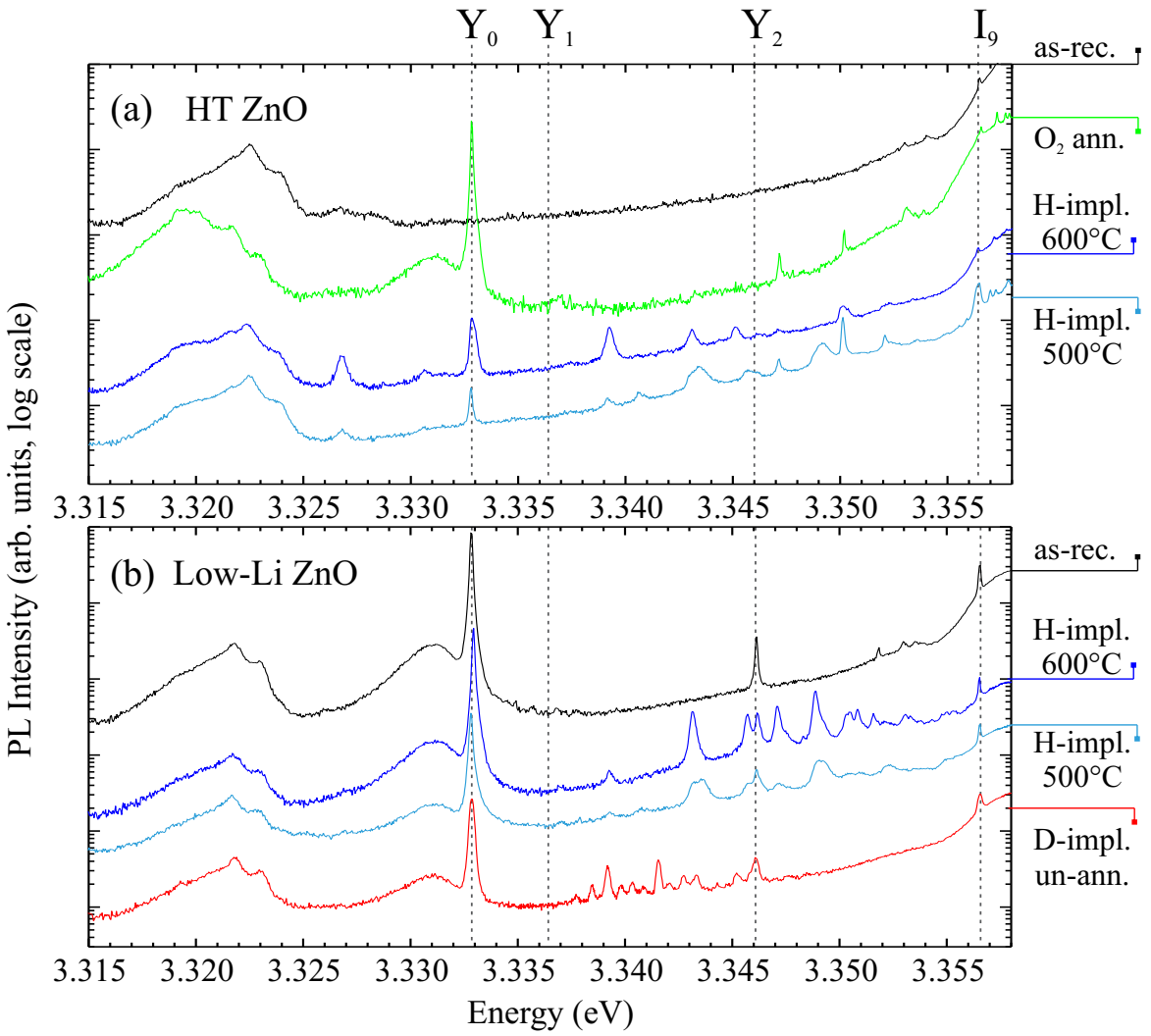

Figure 7.4.: Unique PL transition lines after hydrogen and deuterium implantation and annealing for (a) conventional HT and (b) Low-Li HT ZnO.

is Low-Li HT ZnO directly after D implantation (see Fig. 7.4(b)). No transitions are present in this region for implanted HT ZnO crystals prior to 500 °C annealing. This suggests that the origin of these transitions lies not with the structural defects themselves, but rather in other impurity centres that diffuse at higher temperatures and then are captured on extended structural defects. However, the nature of these lines remains rather uncertain.

After heat treatment at 500 °C, an unusually high DAP transition is present in almost all samples, as shown in Fig. 7.5. In particular, Low-Li HT ZnO with high doses of implanted hydrogen and deuterium exhibit an intense DAP at 3.10 eV for D and at 3.11 eV for H implantation. Excitation power-dependent PL measurements presented in Fig. 7.5(c) confirm these DAP assignments. A decrease in excitation power leads to a decrease in photo-excited donor-acceptor pairs. Therefore, the average distance

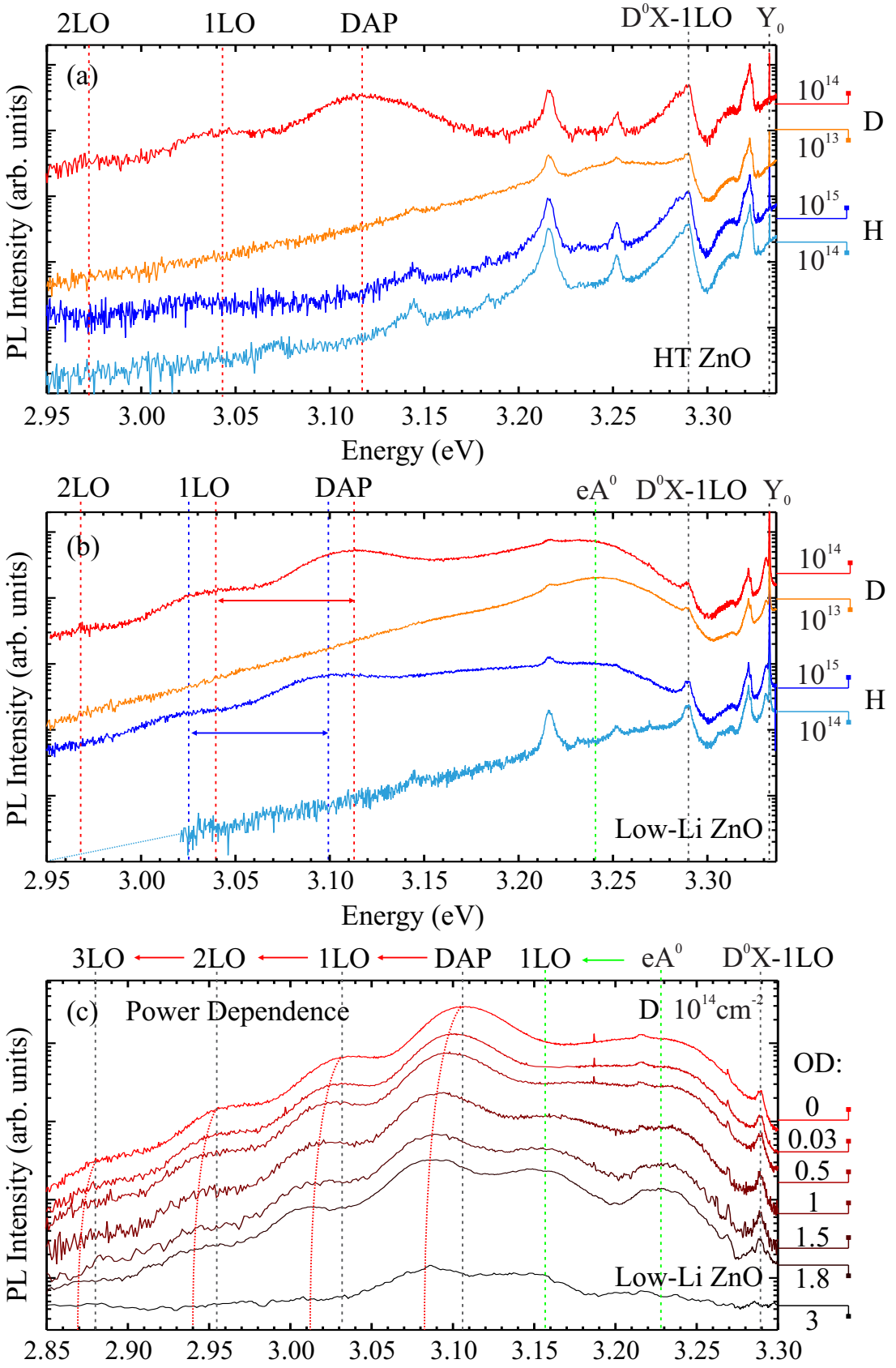

Figure 7.5.: DAP transition after implantation in conventional HT (a) and Low-Li HT (b) ZnO after 500 °C annealing. Power dependence of implanted Low-Li HT ZnO is shown in (c). PL spectra for optical densities (OD) of 1.8 and 3 are smoothed by a 3-point averaging process due low signal to noise ratio.

between the DA-pairs will increase and the Coulomb term in Eq. 6.1 will decrease [221], leading to a redshift in spectral position as clearly observed in Fig. 7.5(c).

With decreasing excitation power (i.e. higher optical densities (OD) of the in-line filters), two further peaks are resolved at 3.227 eV and 3.153 eV that do not redshift. The former is likely to be a free electron to bound acceptor transition (eA^0) and the latter its first longitudinal optical phonon replica. Similar eA^0 transitions have been observed in ZnO substrates at identical positions [199]. Interestingly, the DAP and eA^0 peaks have higher intensities in Low-Li HT ZnO samples. The strong DAP feature observed in this low-impurity material, makes a purely impurity-related acceptor origin, such as N or Li unlikely. In addition, in the unimplanted but annealed ZnO crystals shown in Fig. 6.5, the DAP band was significantly less intense and had a zero-phonon line at 3.029 eV, indicating a different underlying acceptor.

Schirra *et al.* [210] found that certain eA^0 transitions, preferentially found in epilayers, originate from acceptor-like defects located on basal plane stacking faults. A possible scenario is that implantation damage is reduced by thermal annealing until a certain stable defect formation is reached. This defect formation could potentially have an acceptor-like characteristic. This model is in line with the behaviour of as-received HT ZnO, which exhibits a structural defect-related Y line only after O_2 annealing, showing that the annealing process itself can introduce structural damage or un-passivate existing defect complexes. It is, however, noteworthy that after an additional 600 °C annealing cycle, the DAP transition, as well as eA^0, were almost completely quenched. Based on the significant line broadening and reduction in the number of observed features for higher temperatures, the optimal annealing temperature appears to be around 500 °C. Therefore, it seems unlikely that the DAP and eA^0 quench due to a sudden reduction in structural defects.

7.2 Summary

The role of hydrogen and deuterium in the photoluminescence spectrum of bulk ZnO has been investigated in this chapter. Both isotopes were introduced by ion implantation and subsequent annealing steps were used to monitor the diffusion of H and D. The findings can be summarised as follows:

- Hydrogen and deuterium implantation produced almost identical spectral changes.

- The conventional I_4 line is present in H- and D-implanted Low-Li HT ZnO and conventional HT ZnO crystals after annealing at 200 – 300 °C. It is absent for higher annealing temperatures. Oxygen vacancies, introduced by the implantation process can trap H/D which results in the observed I_4 line. Annealing in oxygen atmosphere, refills the oxygen vacancies and the freed H/D diffuses out or participates in the formation of the $I_{4b,c}$ hydrogen complex. This trap-limited diffusion process explains the lower thermal stability of I_4 in implanted HT ZnO compared to unimplanted melt-grown ZnO crystals.

- With the disappearance of I_4 after annealing at 400 °C, $I_{4b,c}$ appears exclusively in the H/D-implanted conventional HT ZnO. The $I_{4b,c}$ intensity decreases with further annealing before it disappears after annealing at 600 °C. The fact, that it is not observed in Low-Li HT ZnO, indicates a Li involvement in the $I_{4b,c}$ complex.

- H/D implantation introduces I_{6-H} into Low-Li HT ZnO which quenches after annealing at 500 °C. Due to their high temperature processing at 1100 – 1400 °C, Low-Li HT ZnO crystals exhibit not only low concentrations of Li but very low concentrations of H. This is consistent the fact that I_{6-H} can be partially introduced by FG annealing. Furthermore, I_{6-H} is always strongly observed in as-received conventional HT ZnO which indicates a Li involvement. In conclusion, I_{6-H} can be introduced into Low-Li HT ZnO, which still contains some Li, by providing the necessary hydrogen either by H/D implantation or FG annealing.

- In implanted conventional HT ZnO, the thermal stability of I_{6-H} is significantly increased and is still observed after annealing at 600 °C. It is likely that structural defects or zinc vacancies introduced by the implantation process trap hydrogen and lithium and, therefore, increase the thermal stability of potential Li-H complexes which are likely to form I_{6-H}.

- After implantation and annealing at 400 °C, the Low-Li HT ZnO material exhibits a I_5 transition which subsequently quenches at 600 °C. A similar thermal stability was reported for the XH complex observed in IR spectroscopy. In the literature, zinc vacancies passivated by hydrogen are reported as a possible origin for XH. In conventional HT ZnO, zinc vacancies created in the implantation process are likely to be filled by Li, which, in conjunction with hydrogen, may form $I_{6-\mathrm{H}}$. This may also explain the observed higher thermal stability of $I_{6-\mathrm{H}}$ in H/D-implanted HT ZnO crystals.

- The ionised donor-bound I_9^+ transition was observed after implantation and its localisation and binding energy are consisted with the experimentally obtained Haynes rule. However, I_9^+ is not identical to the commonly reported I_2 line, which is sometimes reported as the $\mathrm{D}^+\mathrm{X}$ transition of I_9.

- Several new PL transitions between I_9 and Y_0 as well as DAP transitions and free-to-bound transitions were observed, preferentially on Low-Li HT ZnO, following implantation.

8 | Metal Ion Implantation and Metal Coating of ZnO

In addition to ZnO crystals implanted with hydrogen and deuterium, hydrothermally grown ZnO wafers were implanted with Ga, Al, and Pt ions. Ga and Al are believed to be the origin of the dominant PL I_8 and I_6 lines and are, therefore, used to validate the correct peak assignment and to shed further light on the difference between $I_{6-\mathrm{H}}$ and I_6. In addition, the incorporation of Pt was studied as it is used as an autoclave lining in the hydrothermal growth process of ZnO. The second part of this chapter studies the influence of thin metal (-oxides) films, deposited on ZnO single crystals, on the PL spectra. Typical ohmic and Schottky contact metals were used for this investigation.

8.1 Metal ion Implantation

Ion implantation is commonly used for the selective doping of semiconductors. In the case of ZnO, the group III elements Al, Ga, and In are used, all of which are believed to strongly increase the bulk n-type conductivity. Among these elements, Ga seems to be the most suitable as its covalent bonding length of 1.92 Å for Ga-O is more closely matched to ZnO (Zn-O: 1.97 Å) than In-O (2.17 Å) or Al-O (2.70 Å) [222, 223]. In addition, Al, Ga, and In seem to play a crucial role in the formation of a highly conductive surface layer in ZnO after heat treatment [15]. In this work, conventional hydrothermal ZnO and Low-Li HT ZnO crystals were implanted with Ga, Al and Pt. For Ga and Al, the respective PL lines have been already identified. This assignment will be re-examined using high-resolution PL. Furthermore, the possible involvement of Al in the $I_{6-\mathrm{H}}$ line will be investigated, as suggested by its proximity to the Al-related I_6. Pt implantation was carried out in order to study the possible incorporation of Pt impurities from the autoclave lining during the growth process. The PL spectra of Pt-implanted ZnO presented in this work are the first of its kind. As outlined in Sec. 3.3, the implantation depths or projected range was chosen to be 15 – 20 nm beneath the crystal

surface and is, therefore, well within the PL detection depth. All implanted ZnO crystals were annealed in oxygen atmosphere for 90 min at 600 °C following implantation to recover the implantation damage.

8.1.1 Gallium implantation

Ga-related PL transitions have been investigated by several groups, with a significant spread in the reported spectroscopic position of associated lines. Ko *et al.* [159] observed a new line at 3.358 eV in Ga-doped ZnO films grown ontop of GaN buffer layers on sapphire substrates. Reuss *et al.* [224] investigated Ga-implanted ZnO crystals from Eagle-Picher and reported a Ga-related line at 3.359 eV. They also observed a band of phonon states in Raman spectroscopy, which they assigned to implantation damage. On annealing at 800 °C, this band was completely quenched. Ga-related PL lines are always observed when ZnO is epitaxially grown on GaN substrates due to interdiffusion from the substrate. This was shown by PL and SIMS experiments carried out by Strassburg *et al.* [157] and Meyer *et al.* [17] who found a Ga-line at 3.3598 eV. A final and unambiguous assignment was made by Johnston *et al.* [158] employing ^{73}Ga isotopes that decay into stable ^{73}Ge with a half-life of 4.87 h. Over the course of 26 h, the Ga-related PL signal at 3.3600 eV decayed in intensity in line with its isotope half-life. As all of the aforementioned lines roughly coincide with the I_8 transition at 3.3601 eV, first reported by Reynolds *et al.* [57] in 1965, I_8 has become synonymous with Ga impurities.

Although there is enough evidence for this Ga-related I_8 assignment, most implantation studies result in very broad transitions due to implantation damage. In addition, epitaxial films do not usually have the necessary structural quality to effectively resolve fine recombination lines. Therefore, Ga implantation experiments were carried out in this work, with modest implantation doses of 7×10^{13} atoms cm^{-2} and 7×10^{14} atoms cm^{-2} at an energy of 41 keV in single crystalline HT ZnO and Low-Li HT ZnO. An overview of all implantation parameters can be found in Table 3.1. To recover implantation damage, the ZnO crystals were annealed in O_2 atmosphere at 600 °C for 90 min before PL measurements were carried out.

The PL spectra of the reference HT ZnO crystal and the Ga-implanted samples from the same wafer after annealing are shown in Fig. 8.1. Due to the post-implantation heat treatment no $I_{4b,c}$ is present and an overall drop in background intensity is observed. Interestingly, the dominant transition after implantation is not I_8, as repeatedly assigned to Ga for ZnO single crystals obtained from Tokyo Denpa. Instead, a new peak labelled I_{8-Ga}, shifted 0.23 meV to the lower energy side of I_8 at 3.35961 eV, is the new dominant feature. As both the conventional I_8 and I_7 lines are still observed for the

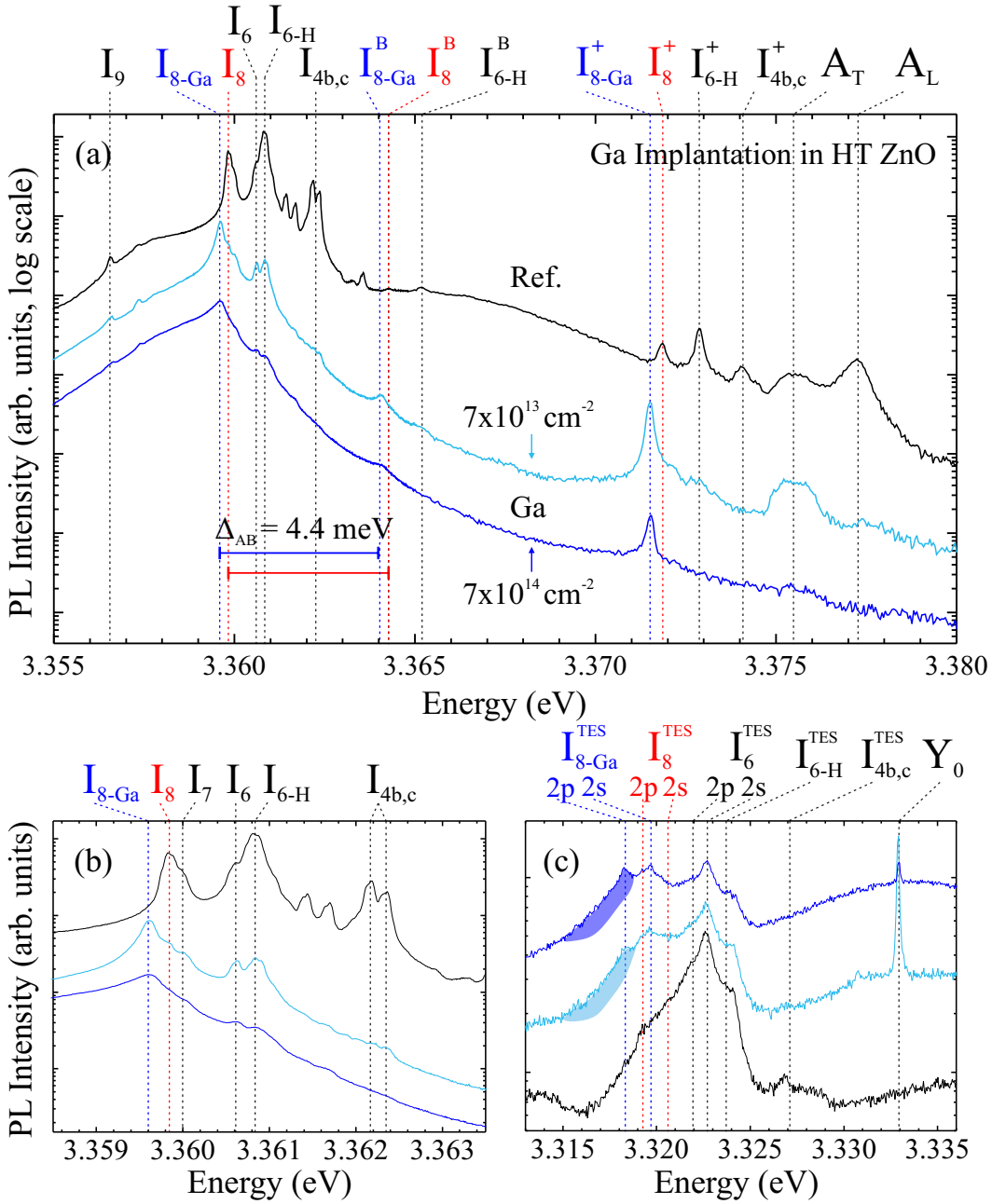

Figure 8.1.: 4 K PL spectra of a reference unimplanted HT ZnO crystal and the same wafer after Ga implantation with doses of 7×10^{13} atoms cm^{-2} and 7×10^{14} atoms cm^{-2}. Both implanted crystals were annealed in O_2 atmosphere for 90 min at 600 °C.

lower implantation dose of 7×10^{13} atoms cm^{-2}, a purely stress-induced shift can be discounted. With the emergence of $I_{8-\mathrm{Ga}}$, a B-excitonic transition $I^B_{8-\mathrm{Ga}}$ also appears, shifted slightly compared to the I^B_8 line in the reference sample. At 3.37150 eV, a second feature emerges after implantation and is assigned as the D^+X replica of $I_{8-\mathrm{Ga}}$. Note that $I^+_{8-\mathrm{Ga}}$ is also shifted compared to I^+_8. For the unimplanted ZnO crystal an intense A_L and a less intense A_T free exciton recombination is observed. After implantation,

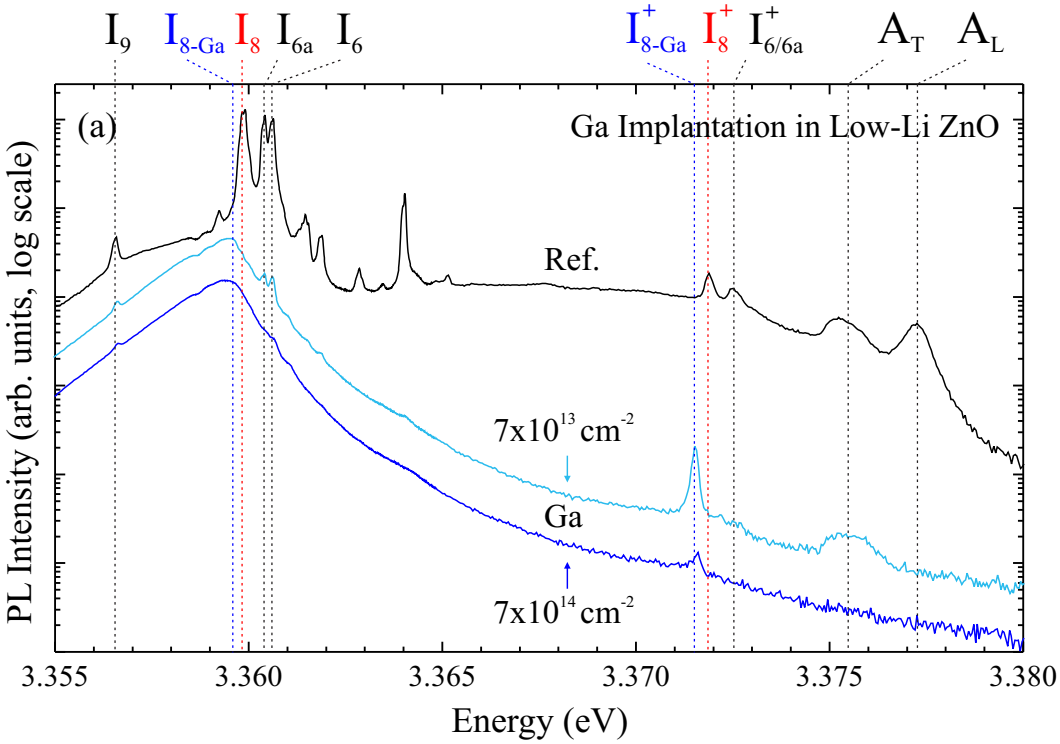

Figure 8.2.: 4 K PL spectra of a reference unimplanted Low-Li HT ZnO crystal and the same wafer after Ga implantation with doses of 7×10^{13} atoms cm^{-2} and 7×10^{14} atoms cm^{-2}. Both implanted crystals were annealed in O_2 atmosphere for 90 min at 600 °C.

A_L is completely quenched but A_T is still clearly resolved for the lower Ga dose.

Although the implanted crystals were annealed for 90 min in oxygen (i.e. the same conditions as the unimplanted ZnO crystals in Sec. 6.1), I_{6-H} is still present and can be resolved for both implantation doses. This again suggests a higher thermal stability of I_{6-H} after ion implantation and in the presence of structural defects. This is in line with the earlier finding in this work for H and D-implanted ZnO. Evidence for a new transition can also be found in the TES region presented in Fig. 8.1(c). On the lower energy side of the broad TES band, a new shoulder at 3.31825 eV (blue shaded area) can be observed which is not present for unimplanted material and is associated with the $2p$ transition of I^{TES}_{8-Ga}. From this, a donor binding energy of 55.36 eV for I_{8-Ga} is calculated. The Y_0 line appears next to the TES band and is introduced by the post-implantation heat treatment. Considering that Y_0 is thought to be related to structural defects, it is surprisingly significantly larger for the smaller implantation dose. For a higher dose of 7×10^{14} atoms cm^{-2}, a broader feature, centred under Y_0, emerges.

The same Ga implantation process was carried out for Low-Li HT ZnO crystals, and the resulting PL spectra are shown in Fig. 8.2. Although I_7 and I_8 are not resolved after implantation for either implantation dose, no deviations from the conventional

HT ZnO PL spectrum were observed. However, $I_{8-\mathrm{Ga}}$ forms a relatively broad peak in Low-Li HT ZnO.

One explanation for the Ga-related emission, shifted from the I_8 line, could be isotopic splitting. Two Ga isotopes, ^{69}Ga and ^{71}Ga, are known to be stable with a natural abundance of approximately 2:3. As the mass difference between the two Ga isotopes is relatively small, their trajectories through the bending magnet of the implanter are so close that no sufficient separation is achieved. Hence, the ZnO material discussed here was implanted with both Ga isotopes. If one assumes a negative isotope shift similar to the one observed for the $^{63/65}$Cu isotopes reported by Dingle [202], I_8 could be related to ^{69}Ga and $I_{8-\mathrm{Ga}}$ to ^{71}Ga. The energetic distance between the two PL lines (230 µeV) is similar to that reported for the Cu isotopes, which are 110 – 150 µeV [202, 225] apart. In addition, both isotope pairs have a combined width of 230 µeV [226]. Byrne *et al.* [226] very recently showed for the case of Cu, that they could control which of the two isotope peaks was dominant by doping HT ZnO single crystals (TD) with the respective isotope. They also reported that a thermal annealing step between 700 – 900 °C was necessary to activate the Cu emission. A similar heat treatment at 600 °C was carried out in this work to remove implantation damage. However, even if ion implantation introduced a significant amount of ^{71}Ga leading to the presence of $I_{8-\mathrm{Ga}}$, it is surprising that no $I_{8-\mathrm{Ga}}$ is observed in unimplanted ZnO material due to the natural abundance of Ga isotopes.

8.1.2 Aluminium implantation

Aluminium is the main impurity in all types of single crystalline ZnO. Its initial identification as I_6 was made by Schilling *et al.* [161], who Al-implanted vapour-phase-grown bulk ZnO and observed a strong emission in the I_5 / I_6 region after annealing in an O_2 atmosphere at 800 °C. This finding was later correlated with SIMS measurements [17], that showed that Al is omnipresent in the substrate and thin film material. Furthermore, Chen *et al.* [227] showed, using positron lifetime and Doppler broadening measurements, that Al implantation introduces significant concentrations of vacancy clusters (V_{Zn}-V_O). For annealing between 200 – 600 °C, these vacancy clusters combine to form large voids, with a void diameter of 0.8 nm, which are recoverable for heat treatments above 600 °C. They reported a critical implantation dose of 10^{15} atoms cm^{-2} for the creation of these voids. However, their cathodoluminescence measurements showed only a broad transition at 3.36 eV and an increase in CL intensity with annealing temperature. In general, most studies on Al in ZnO adopt the comparably simple introduction of Al by diffusion. In this work, Al implantation was carried out to gain further insight into the three closely lying I_{6a}, I_6 and $I_{6-\mathrm{H}}$ transitions.

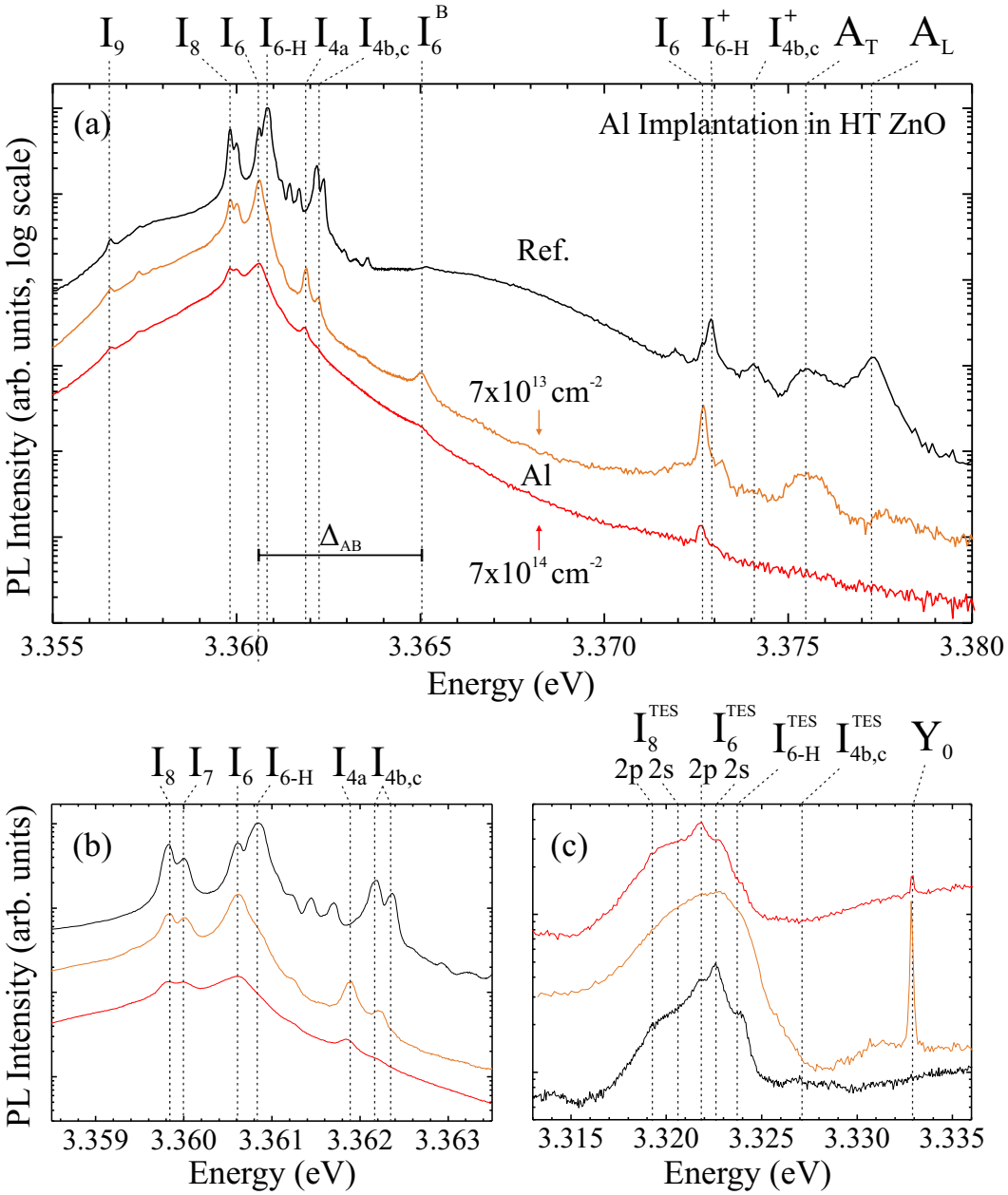

Figure 8.3.: 4 K PL spectra of a reference unimplanted HT ZnO crystal and the same wafer after Al implantation with doses of 7×10^{13} atoms cm^{-2} and 7×10^{14} atoms cm^{-2}. Both implanted crystals were annealed in O_2 atmosphere for 90 min at 600 °C.

Figure 8.3 shows PL spectra for conventional HT ZnO before and after Al implantation and subsequent 600 °C heat treatment. For the lower implantation dose of 7×10^{13} atoms cm^{-2}, I_6 increases by approximately a factor of two relative to $I_{7/8}$. At the same time I_{6-H} decreases in intensity and only a small shoulder remains. Although, I_{6-H} was observed to anneal out in unimplanted HT ZnO material at 600 °C in Sec. 6.1, it generally showed a higher thermal stability in ion-implanted ZnO, regardless of the

element used. If one considers that both Al and Li compete for the substitutional Zn-site position, a higher Al concentration in conjunction with the implantation induced displacement of Zn-atoms could lead to an exchange from Li_{Zn} to Al_{Zn}. As a result the I_{6-H}-related Li_{Zn}-H complex would dissociate and the resulting Li interstitials and unbound hydrogen could diffuse to the crystal surface in the post-implantation heat treatment. Similar observations were made by Børseth *et al.* [228], who reported on a "Li-lean" region after Al-implantation and subsequent annealing at 800 °C.

With the quenching of I_{6-H}, a shift in the D^+X lines in Fig. 8.3(a) occurs with I_6^+ replacing I_{6-H}^+ as the dominant ionised donor transition. After implantation, I_{4a} at 3.36185 eV is clearly resolved in Fig. 8.3(a – b) and could potentially be Al-related. For the lower implantation dose, the TES band broadens and no fine structure can be resolved in Fig. 8.3(c). This observation is exclusive to Al implantation. The higher implantation dose results in a somewhat sharper TES emission but the background intensity is greatly increased. This can be seen from the low intensity of the Y_0 line above the background. Similar to Ga implantation, Y_0 is better resolved for lower implantation doses and, therefore, less implantation damage.

8.1.3 Platinum implantation

Due to its high corrosion resistivity, Pt is used as a lining for the stainless steel crucible used in the growth of hydrothermal ZnO and in the holder for the ZnO seed crystals. Therefore, the presence of certain amounts of Pt in HT ZnO is unavoidable. Ehrentraut *et al.* [8] found up to 7 ppm (wt) of Pt in their HT ZnO material. To investigate the potential influence of Pt on the HT ZnO PL, Pt implantation experiments were carried out with the resulting PL spectra shown in Fig. 8.4. These represent the only reported PL measurements on Pt-implanted ZnO. Interestingly, the PL spectra for both implantation doses appear very similar to annealed unimplanted HT ZnO. Noticeable differences are an overall decrease in PL intensity and the poorly resolved free exciton peaks. I_{6-H} is still observable and its higher thermal stability suggests the presence of implantation damage, similar to that observed for Ga- or H- and D-implanted material. Both B-excitons of I_8 and $I_{6/6-H}$ are clearly visible, and I_{4a} is also present. The TES region contains a strong Y_0 line, centred on top of the underlying broad transition. A further, narrow peak is present on top of this broad emission at 3.33066 eV, on the lower energy side of Y_0. The TES line of the conventional I_4 would be expected at this position. However, the I_4 line is generally absent in annealed HT ZnO. The high PL-quality observed in Pt-implanted crystals suggests that implantation damage is almost negligible for Pt implantation. The ion beam was rastered over the sample as in the Ga and Al implantation and, hence, channelling effects can be discounted.

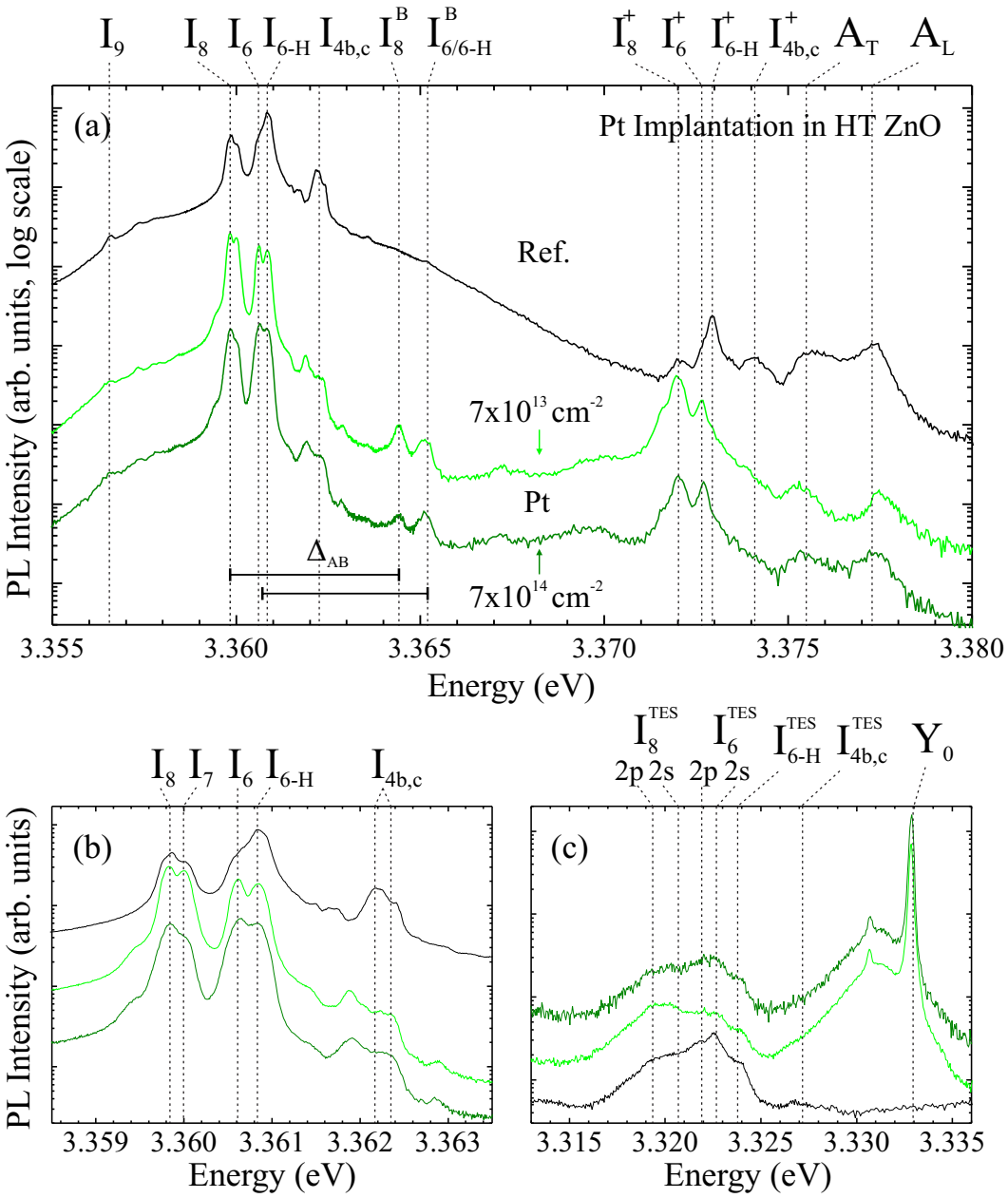

Figure 8.4.: 4 K PL spectra of a reference unimplanted HT ZnO crystal and the same wafer after Pt implantation with doses of 7×10^{13} atoms cm^{-2} and 7×10^{14} atoms cm^{-2}. Both implanted crystals were annealed in O_2 atmosphere for 90 min at 600 °C.

8.2 Metal and metal oxide-coated ZnO

In their seminal work, Okamoto *et al.* [229] showed that light emission in InGaN/GaN could be increased by several orders of magnitude by the deposition of a thin metal film on the semiconductor surface due to surface-plasmon-mediated emission. Since then, a large number of studies have been published concerning the "giant enhancement" of PL emission intensity in nanostructures after coverage with metal nanoparticles [230, 231]. The high surface-to-bulk ratio of nanostructures seems to be one explanation for the exceptionally strong surface-plasmon resonances observed. Although the increase in NBE emission seems genuine and a drastic decrease in exciton lifetime is often reported after metal deposition, the underlying reasons are still controversial. Dev *et al.* [232] observed the same strong increase in luminescence and decrease in exciton lifetime after just Ar-plasma treatment instead of metal deposition via the Ar-plasma-induced sputtering of a metallic target. Compared to the plethora of work on nanostructures, little work has been done on single crystal bulk material. Comparable work on ZnO thin films has been carried out both with laser excitation from the substrate side (back geometry) of the metal covered thin films and from the metal side (front geometry). For bulk crystals of a thickness of 500 µm the front geometry is used in this work due to the low exciton escape depth.

Here, HT ZnO single crystals were covered with 10 – 15 nm thick metal and metal oxide films by means of electron beam evaporation (Ti, Au), DC sputtering (Al), and *Eclipse*-pulsed laser deposition (PLD) [233] (IrO_x). PL measurements were carried out directly after deposition without any additional annealing step. None of the samples, regardless of the metal coverage, showed any signs of increased luminescence intensity. This is in contrast to the findings of Liu *et al.* [234] who observed an intensity increase by a factor of two in front emission geometry on ZnO thin films covered with a 30 nm thick Pt layer.

8.2.1 Titanium coverage

Figure 8.5 shows the 3 K PL spectra from the Zn-polar and O-polar faces of Ti-covered and bare HT ZnO samples from the same wafer. On both polar faces a distinct reduction in background intensity was observed between 3.373 eV and 3.363 eV for Ti-covered samples. This is very similar to the behaviour observed on samples annealed at 600 °C. On the O-polar face, the earlier established surface-related broad emission at 3.367 eV has disappeared after Ti coverage. Due to the reduced background luminescence, the B-excitons of $I^{\mathrm{B}}_{4\mathrm{b,c}}$ and $I^{\mathrm{B}}_{6/6-\mathrm{H}}$ can now be clearly distinguished. There appears to be a

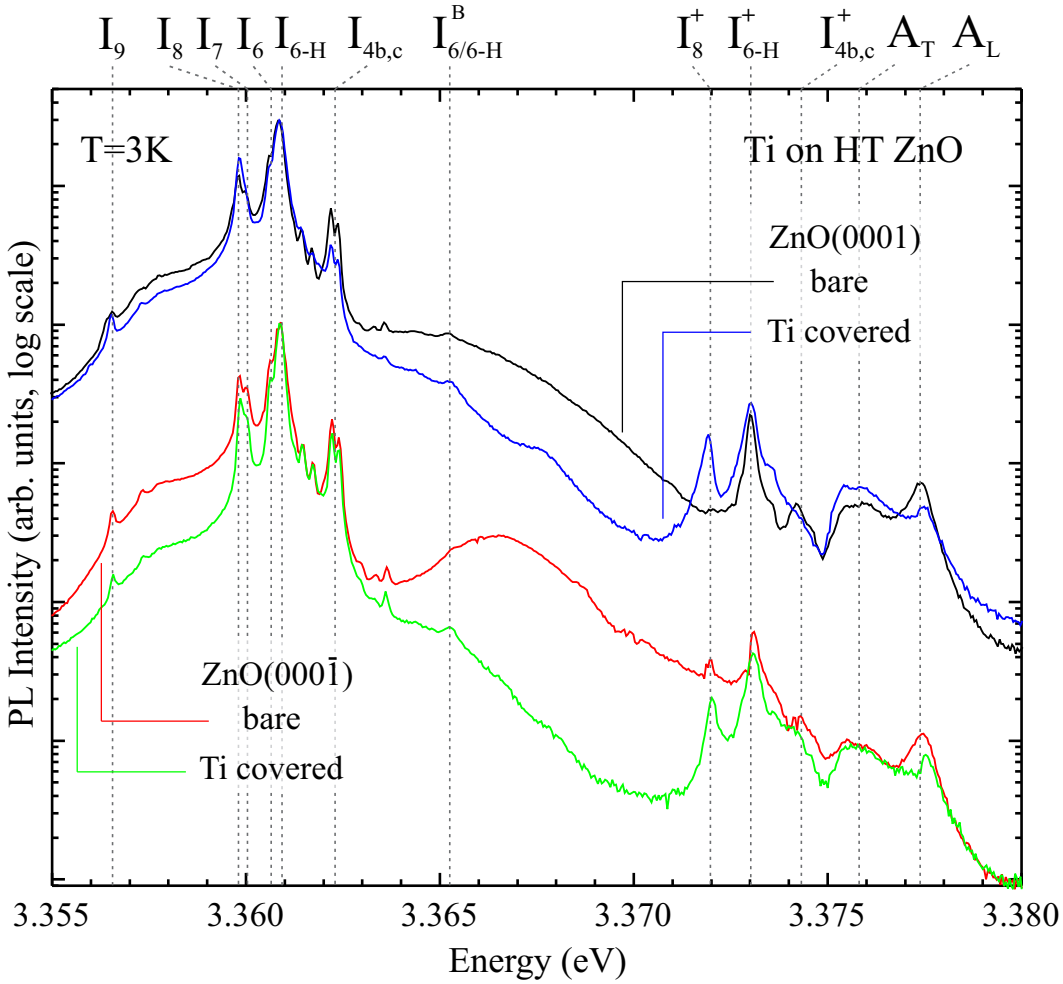

Figure 8.5.: 3 K PL spectra of Ti-covered and bare HT ZnO of the same wafer.

notable reduction in the $I_{4b,c}$ emission on the Ti-covered Zn-polar face. However, it is the only dominant transition that decreased in intensity. After deposition, I_8^+ appears on the Zn-polar face, although the intensity increase in I_8 is only marginal.

8.2.2 Gold coverage

Similar to Ti, a decrease in background intensity was observed for Au-covered ZnO samples. The broad Gaussian-like feature on the O-polar face, however, remains almost constant in intensity and shifts by 1 meV toward lower energies. On the Zn-polar face, the background intensity decreases significantly between 3.37 eV and 3.364 eV. As a consequence, $I^B_{6/6-H}$ is uncovered. The Au coverage was significantly thicker than the Ti-covered samples which accounts for the lower intensity yield and lower resolution in Fig. 8.6. Consequently, an increased spectrometer entrance and exit slit size was necessary to achieve reasonable count rates.

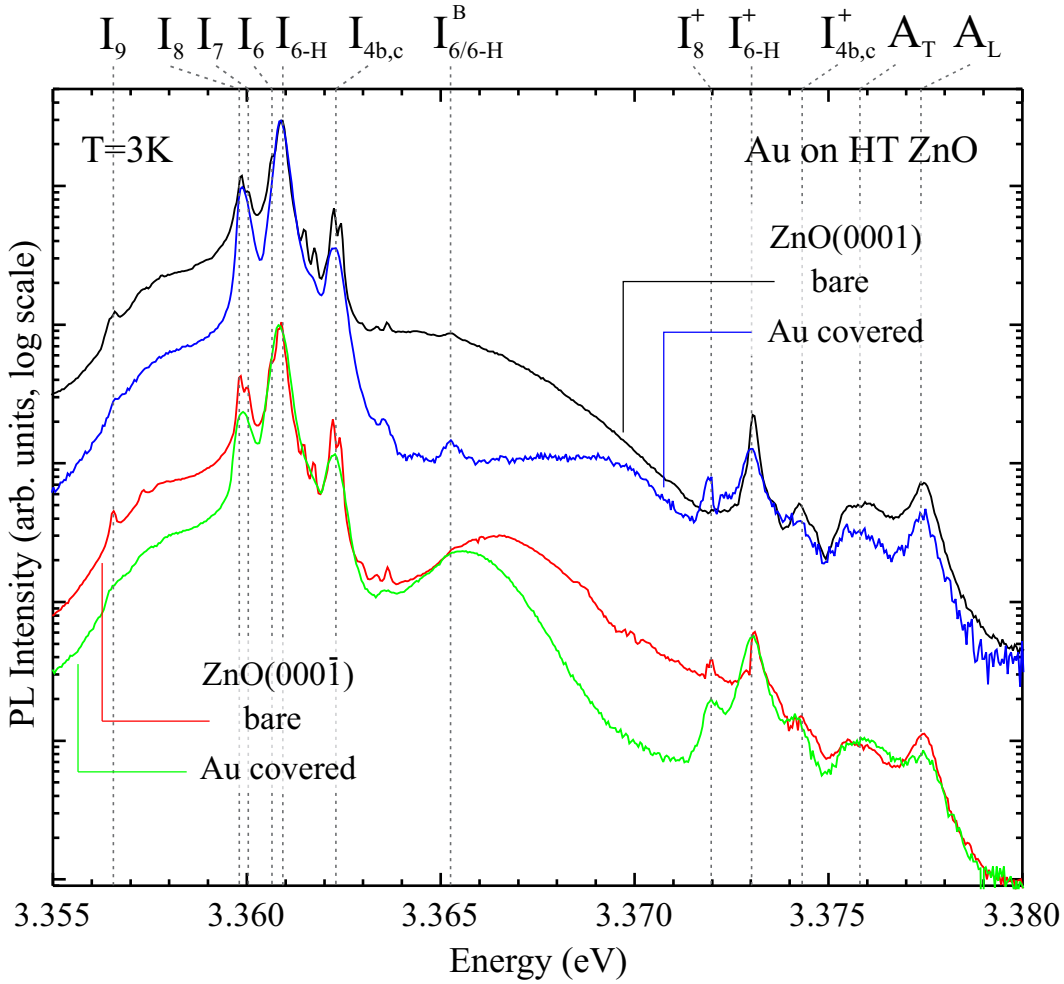

Figure 8.6.: 3 K PL spectra of Au covered and bare HT ZnO of the same wafer.

8.2.3 IrO_x coverage

PL spectra taken on IrO_x-covered HT ZnO polar surfaces are shown in Fig. 8.7. A decrease in background intensity occurs on both faces, but the Gaussian-like emission is still partially observed on the O-polar face. Interestingly, I_7 and I_8 decrease considerably in intensity as do their D^+X replicas whereas $I_{4b,c}$ remains remarkably constant. After IrO_x coverage, the shape of the free exciton emission peaks, A_L and A_T, also changes. On the bare Zn-polar face two clearly separated A_L and A_T emission peaks are observed. This separation is generally observed for all as-received Zn-polar surfaces of HT ZnO single crystals studied in this work. In addition, the FWHM of A_L is in general significantly smaller than that of A_T on this face. In contrast, the free exciton emission peaks can not usually be separated on the bare O-polar face and an almost flat feature is observed. Although this may depend on the specific ZnO wafer, it can be used as a quick method to differentiate the polar faces. After IrO_x coverage, both free exciton emissions merge into a featureless flat peak similar to the free exciton emission

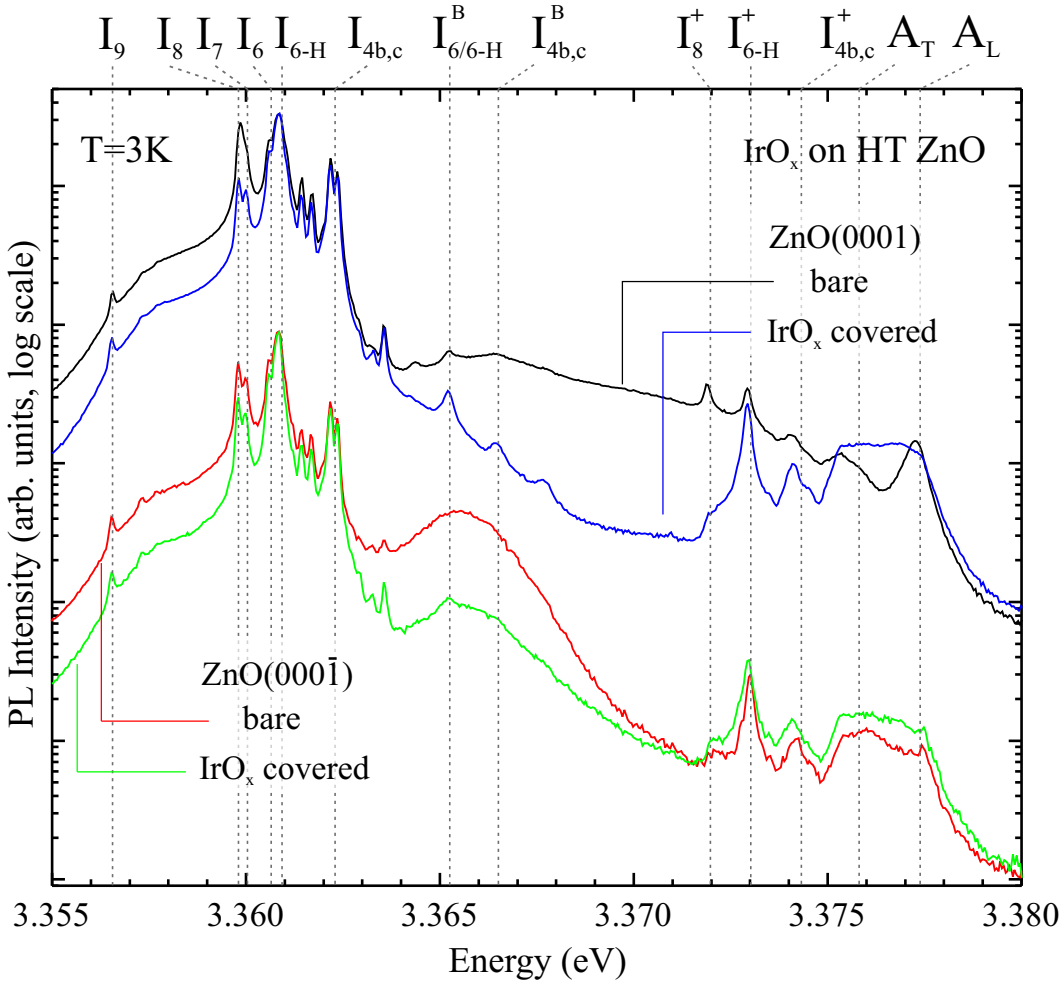

Figure 8.7.: 3 K PL spectra of IrO_x covered and bare conventional HT ZnO.

expected for uncovered O-polar faces. The same effect was observed for Ti-covered ZnO.

8.2.4 Aluminium coverage

Al metal coating was used to investigate the behaviour of the Al-related I_6 and I_{6-H} emission lines. The respective PL measurements are shown in Fig. 8.8. The reduction in the background intensity is not as dramatic as for the other metal / metal oxide overlayers. Furthermore, it is the only deposited film that results in distinct A_L and A_T emission peaks on both polar faces rather than one broad feature. In contrast to all other metal / metal oxide overlayers, where almost no change in the dominant D^0X emissions was observed, Al coverage led to the disappearance of $I_{4b,c}$ and its D^+X line without any heat treatment. I_{6-H} is still the dominant transition, followed by a new emission peak emerging between I_6 and I_7 at 3.36026 eV. This peak is found at a slightly lower spectral energy (0.15 meV) than expected for I_{6a}, which is present in Low-Li HT material. Neither face, exhibits I_8^+ after Al coverage.

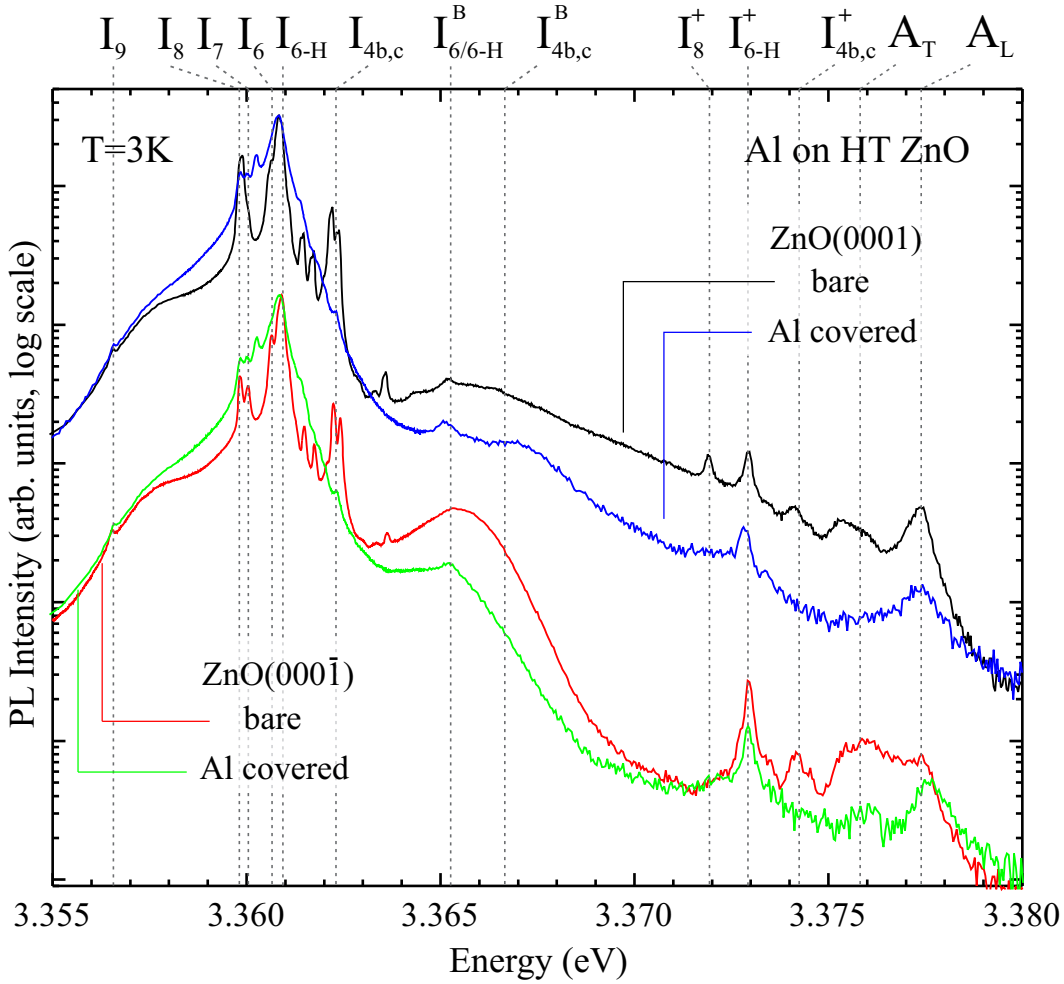

Figure 8.8.: 3 K PL spectra of Al covered and bare HT ZnO of the same wafer.

As Al deposition did not noticeably increase the luminescence intensity of I_6, a further annealing step in an inert N_2 atmosphere at 600 °C for 30 min was carried out to diffuse Al into the subsurface region of the HT ZnO crystals. The resulting PL spectra are shown in Fig. 8.9. After heat treatment, I_{6-H} dominates the neutral donor-bound exciton region on both polar faces while $I_{7/8}$ decreases significantly as most excitons are now in the vicinity of diffused Al atoms and bind to them before recombining. At the previous $I_{4b,c}$ position, several new features appear that are unrelated to $I_{4b,c}$. For all these features an (initial) increase in PL intensity with temperature was observed during temperature-dependent PL measurements, making a rotational-vibrational excited state assignment likely. Meyer *et al.* calculated a theoretical energy splitting of 1.32 meV between I_6 and its first excited state, which is in reasonable agreement with a value of 1.23 meV found in this work. On the Zn-polar face, a broad peak at 3.367 eV appears while on the O-polar face, the same peak also appears but with a much larger peak width.

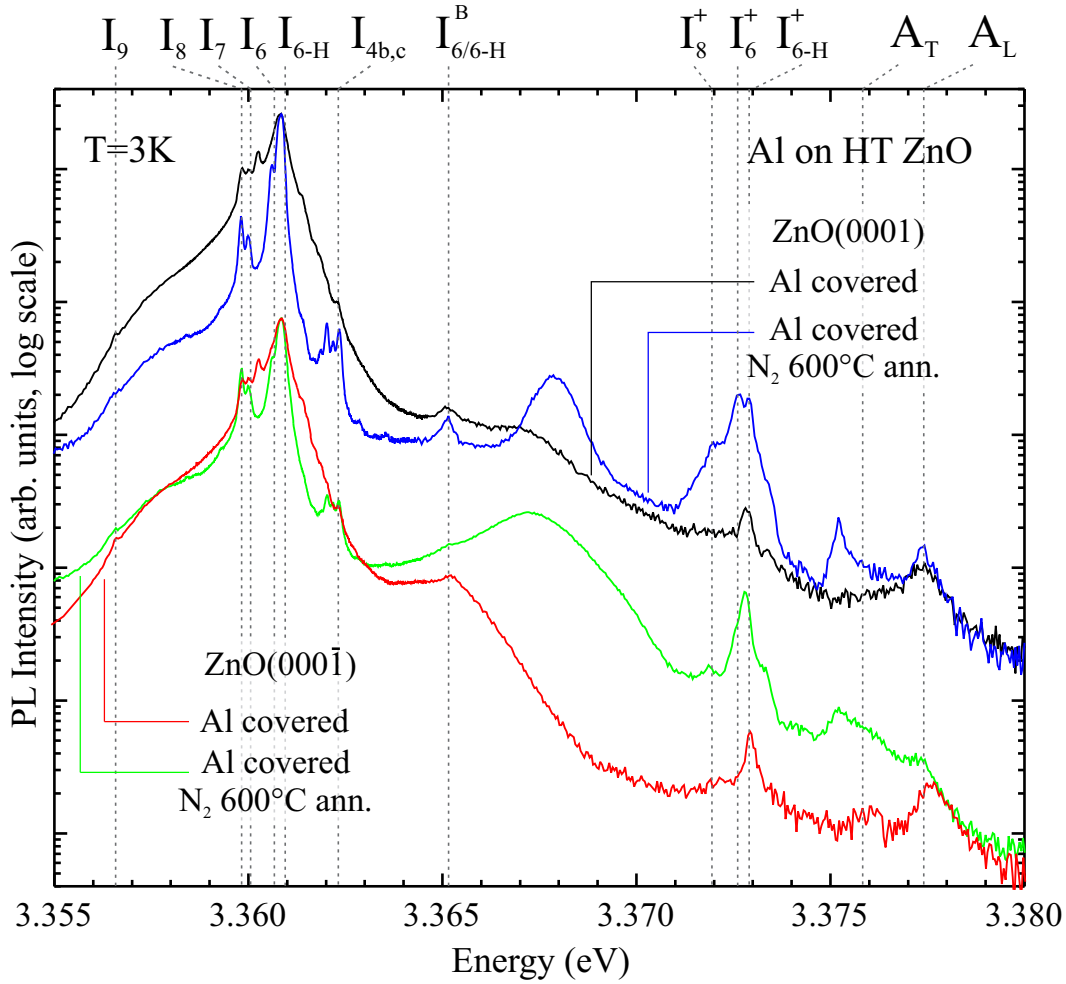

Figure 8.9.: 3 K PL spectra of Al-covered HT ZnO before and after 600 °C annealing in N_2 atmosphere for 30 min.

After annealing, D^+X transitions on the Zn-polar face were strongly enhanced with similar intensities for I_6^+ and I_{6-H}^+, in contrast to the different relative peak intensities of the corresponding D^0X emissions lines. This suggests that the assignment of unknown D^+X lines to their corresponding D^0X transitions cannot necessarily be made on the basis of intensity ratios. For Al-coated wafers, I_{6-H} is the dominant transition for both unannealed and post-annealed wafers. In comparison, I_{6-H} quenches after Al implantation followed by subsequent heat treatment. This indicates that the Al-coating and heat treatment process does not remove substitutional Li which competes with Al for available Zn lattice positions. Al atoms are likely to occupy remaining available zinc vacancies (or even replace zinc atoms in the lattice) rather than replace substitutional Li_{Zn} which is stabilised by hydrogen. Neighbouring Al_{Zn} and Li_{Zn}-H could potentially provide the origin of the I_{6-H} complex. This would explain why $I_{4b,c}$, which is related to a Li_{Zn}-H complex, disappeared after Al deposition while at the same time I_{6-H} increases significantly in intensity.

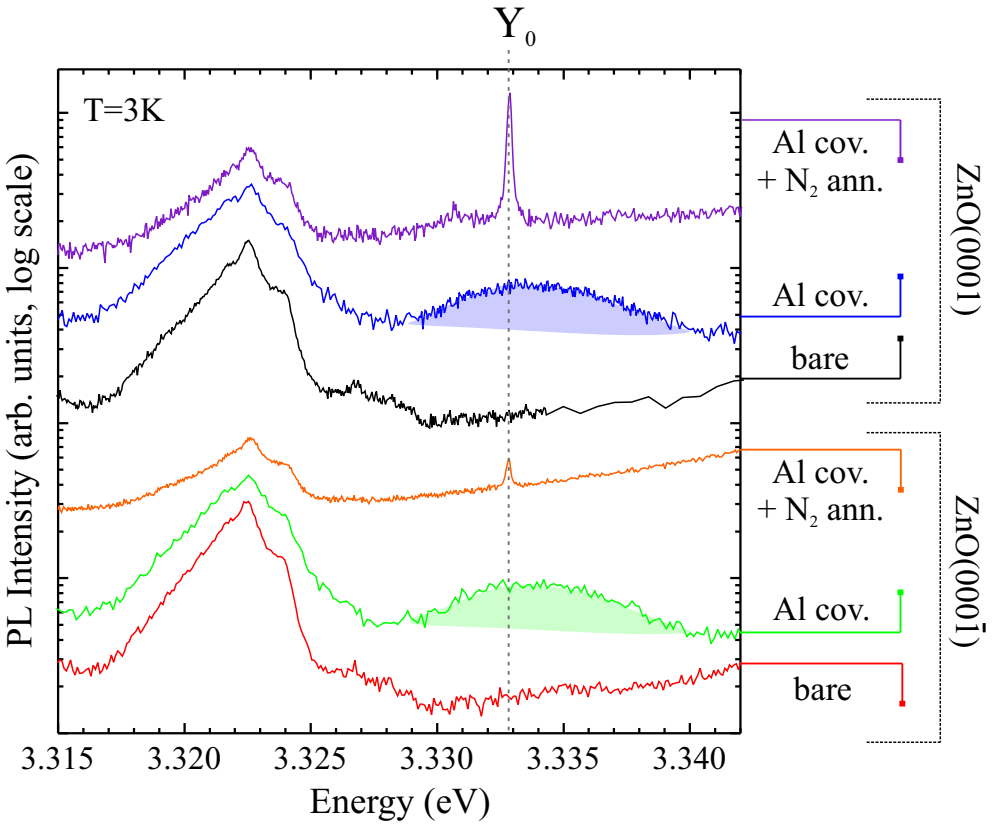

Figure 8.10.: TES region of bare and Al-covered HT ZnO before and after 600 °C heat treatment.

Al-coating also affects the TES region, as can be seen in Fig. 8.10. When HT ZnO was coated with Al, a broad peak centred at approximately 3.334 eV appeared, but no Y_0 line was observed. After heat treatment, this broad peak disappeared and Y_0 started to emerge. The same broad feature was observed after Al and Ga implantation. However, as the implantation process was always followed by an annealing step, the broad feature was relatively vague.

8.3 The role of the surface/interface in ZnO PL

In conclusion, covering ZnO single crystals with a metal or metal oxide film changes the NBE-PL rather dramatically. It is well known that when the metal has a lower work function than ZnO, an ohmic contact will be formed at the metal-semiconductor interface (e.g. Al, Ti). An ohmic contact will necessarily have a low contact barrier height or a thin depletion region (for highly doped contacts). In both cases, an electron-hole pair, generated by an incident photon, should be able to form an exciton as the built in electric field is negligible. As a result, a high surface sensitivity would be expected. In the case of metal work functions larger than that of ZnO (e.g. IrO_x), the conduc-

tion and valence bands bend significantly upwards and a Schottky barrier is formed. In the resulting depletion region, electrons and holes will be effectively separated by the strong built-in electric field, producing a so-called "optical dead layer" [235]. This recombination-free dead layer cannot be probed by photoluminescence spectroscopy and a more bulk-like PL sensitivity would be expected.

However, for all metals and metal oxides used in this study a similar decrease in PL intensity and a reduction in background intensity between the D^+X and D^0X emission regions was observed. The broad Gaussian-shaped emission on the O-polar face lies in this region and significantly decreases in intensity with metal/metal oxide coverage. According to the theory of metal-induced gap states (MIGS) [236], a metal coating will introduce additional interface states in the bandgap due to the decay of metal wave function tails. The capture of electrons in these states may decrease the recombination efficiency and lower the PL intensity yield in the near-surface region. Although, the nature of this Gaussian-shaped emission, observed on the O-polar face, is not yet understood, these findings are in line with the reduction of the SX peak on metal-coated nanowires [230].

As both ohmic and Schottky-contact metals/-oxides produced a strong reduction in the Gaussian-shaped feature, surface band bending can be ruled out as an origin. This in line with Kuehn *et al.* [237] who observed identical surface exciton decay transients under different band bending conditions. As an alternative origin for the observed surface exciton in nanomaterials, adsorbates such as hydrogen and hydroxyls, have been proposed. Following this logic, the metal/-oxide coverage must remove these surface species in order to explain the observed decrease in the SX intensity. However, annealing in oxygen and nitrogen atmospheres (see chapter 6) significantly decreased the intensity of the Gaussian-shaped feature, although all samples were exposed to atmosphere after annealing. In chapter 9 we will show that exposure to atmosphere is sufficient to completely re-hydroxylate both polar ZnO surfaces within seconds. In conclusion, defects in the (sub-)surface region are more likely to be responsible for the observed Gaussian feature. One possible defect could be oxygen vacancies as they are known to be present in significantly larger quantities on the O-polar face compared to the Zn-polar face [238].

Still puzzling, however, is the unusual enhancement of the D^+X intensity and the change in free exciton peak shape and intensity. Interestingly, no degradation of PL resolution was observed with film coverage. It would be useful to fabricate Schottky diodes on HT ZnO which would enable PL spectroscopy under different biasing regimes. With varying depletion region widths, different depths could be probed by PL spectroscopy. This could provide valuable insight into the influence of the intrinsic surface band bending in ZnO on its optical properties.

8.4 Summary

Conventional HT ZnO material was implanted with Ga, Al, and Pt and investigated by means of photoluminescence spectroscopy. Thin metal and metal oxide films were deposited on the ZnO crystal surface and PL emission was recorded through these overlayers. The findings can be summarised as follows:

- Ga implantation introduces a new emission line $I_{8-\mathrm{Ga}}$ with a 0.2 meV lower spectral energy than I_8. The B-exciton and D^+X replicas of this new Ga-related line were also observed, along with its TES transitions. This casts some doubt on an exclusive Ga assignment for I_8. Isotope splitting between $^{69/71}$Ga may provide a possible explanation as the energetic distance between I_8 / $I_{8-\mathrm{Ga}}$ is similar to that observed between the PL emission lines of the $^{63/65}$Cu isotopes.

- No significant differences in the PL spectra of Pt-implanted ZnO crystals compared to unimplanted ZnO can be observed apart from changes caused by post-implantation annealing.

- Al implantation increases the intensity of I_6 and quenches $I_{6-\mathrm{H}}$. During implantation, Al ions displace zinc atoms from their lattice positions and at the same time displace substitutional $\mathrm{Li_{Zn}}$ atoms with Al then preferentially refilling the resulting zinc vacancies. This leads to a decrease in the $\mathrm{Al_{Zn}}$-$\mathrm{Li_{Zn}}$-H-related $I_{6-\mathrm{H}}$ emission line due to the reduced number of substitutional Li and at the same time increases the purely $\mathrm{Al_{Zn}}$-related I_6 emission.

- In contrast to Al implantation, coating ZnO with Al overlayers increases the intensity of $I_{6-\mathrm{H}}$, particularly after post-deposition heat treatment at 600 °C. Interestingly, the $I_{4\mathrm{b,c}}$ emission is completely quenched by as-deposited Al overlayers (un-annealed). Al atoms thermally diffusing into the ZnO crystal will have insufficient kinetic energy to remove Li from its substitutional zinc site. However, when Al occupies zinc vacancies (or substitutional zinc sites close to $\mathrm{Li_{Zn}}$), the $I_{4\mathrm{b,c}}$-related $\mathrm{Li_{Zn}}$-H complex will become a $\mathrm{Al_{Zn}}$-$\mathrm{Li_{Zn}}$-H complex which gives rise to $I_{6-\mathrm{H}}$ at the expense of $I_{4\mathrm{b,c}}$. This explains the sudden decrease in $I_{4\mathrm{b,c}}$ with Al coating and the strong increase in $I_{6-\mathrm{H}}$.

- Deposition of metal and metal oxide films on ZnO dramatically reduces the background intensity of the PL emission between the D^+X and D^0X emission regions which on the O-polar face is dominated by a broad Gaussian-shaped feature. A similar reduction was observed after annealing in oxygen or nitrogen atmospheres

and could be subsequently reversed by annealing in forming gas. Therefore, involvement of (sub-)surface hydrogen in this PL background seems likely. The underlying cause of the Gaussian-shaped feature is still not fully understood. However, as both ohmic and Schottky contact metals produce a decrease in its intensity, surface band bending can be discounted as an origin.

9 X-ray Photoelectron Spectroscopy of ZnO

ZnO surfaces are characterised by electron accumulation layers. This is a direct result of the downward bending of the near-surface conduction and valence bands in response to donor-like surface states. These surface states can be introduced by adatoms such as hydrogen or hydroxyl groups. X-ray photoelectron spectroscopy (XPS) experiments were carried out on the polar and non-polar faces of ZnO bulk single crystals after (and during) annealing in UHV and on subsequent exposure to water or molecular hydrogen. The relationship between the surface band bending and the surface hydroxyl coverage was explored. Synchrotron-radiation and laboratory-based Al K_α sources were employed for conventional and real-time XPS measurements and potential changes in the surface reconstruction were monitored using low energy electron diffraction.

9.1 Synchrotron Radiation XPS

9.1.1 Polar faces of ZnO

Synchrotron radiation XPS was carried out on both polar faces of (−c) HT ZnO bulk single crystals to investigate the influence of hydroxyl coverage on surface band bending. O 1s core level and valence band spectra were taken at $h\vartheta = 680\,\text{eV}$ and 150 eV, followed by *in situ* annealing in an UHV environment. Zn-polar and O-polar face samples from the same wafer were mounted on the same sample holder and, therefore, underwent an identical annealing process. The annealing time was 10 min plus a ramping time of up to 20 min for the higher annealing temperatures. The O 1s core level spectra are presented in Fig. 9.1. All spectra show a dominant peak at approximately 531 eV, which represents the bulk lattice oxygen O 1s core level. A shoulder on the higher binding energy side represents the convolution of two further peaks, namely hydroxyl groups at $\sim 532.6\,\text{eV}$ and molecular water at $\sim 533.8\,\text{eV}$ on the sample surface [239]. The exact peak positions will vary with the amount of surface band bending.

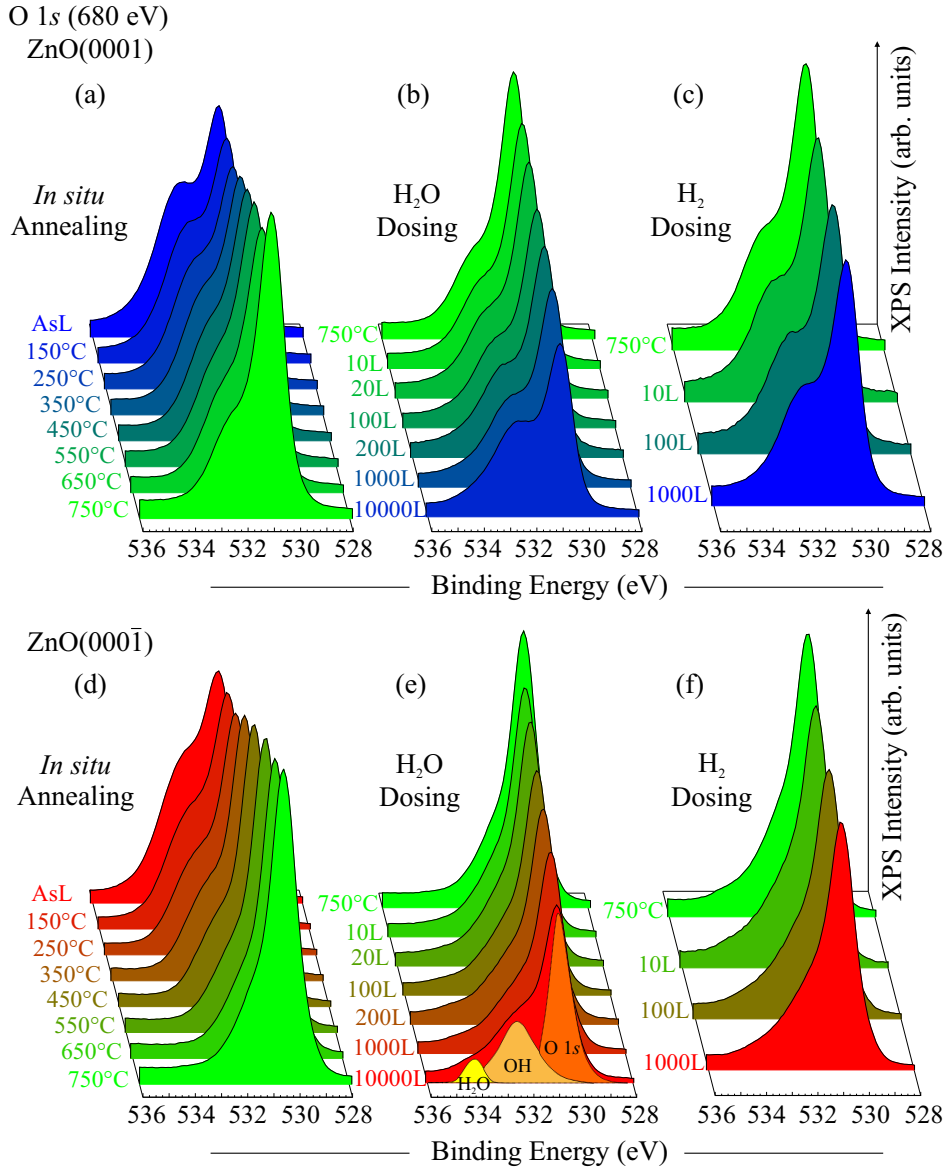

Figure 9.1.: XPS O 1*s* core level spectra taken at $h\vartheta = 680\,\mathrm{eV}$ on the Zn-polar (a – c) and O-polar (d – f) face for *in situ* annealing up to 750 °C and subsequent H_2O and H_2 dosing.

As shown in Sec. 2.1, the nature of the hydroxyl coverage is different on the two polar faces. The Zn-polar face is generally terminated by hydroxyl groups, while the O-polar face is terminated by atomic hydrogen, forming hydroxyl groups by bonding with the O atoms on the surface. H_2O is believed to adsorb onto ZnO surfaces, whereas atomic hydrogen can also diffuse into the bulk and form OH groups in the subsurface region [44, 240]. Therefore, the OH signal is likely to contain contributions from both adsorbed surface-OH (or dissociatively adsorbed H_2O) and subsurface-OH.

We first consider the as-loaded ZnO crystals. The hydroxyl/water shoulder in Figs. 9.1(a) and 9.1(d) decreases significantly on annealing, leaving only a small OH con-

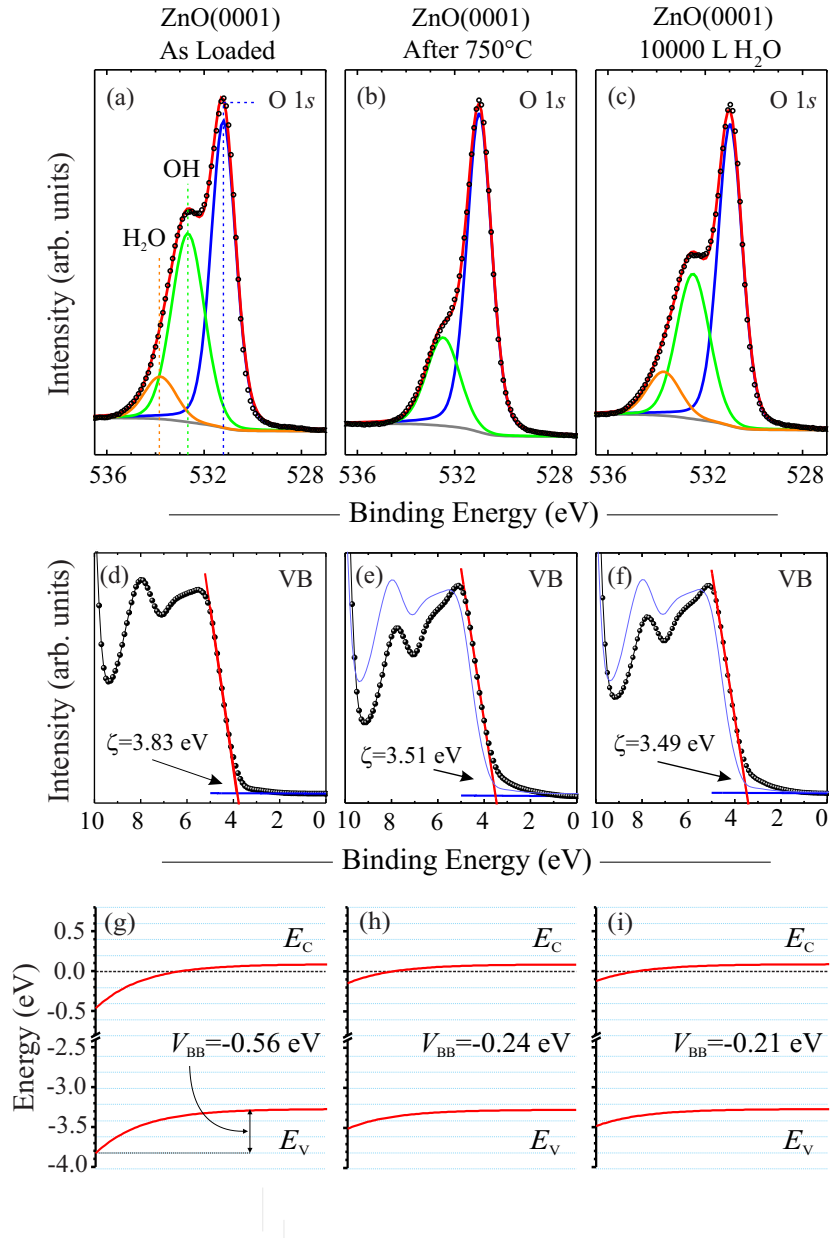

Figure 9.2.: O 1*s* core level XPS at $h\vartheta = 680\,\mathrm{eV}$ with pseudo-Voigt fits in (a – c) for Zn-polar face and the VB region at $h\vartheta = 150\,\mathrm{eV}$ with fits to the leading edge in (d – f). The faint blue line indicates the as-loaded VB position. The calculated surface band bending is presented in (g – i). The carrier concentration of the sample was $1 \times 10^{17}\,\mathrm{cm}^{-3}$.

tribution after annealing at 750 °C. At the same time, the O 1*s* lattice contribution increases in intensity. Following annealing at 750 °C, the OH-reduced samples were subjected to *in situ* H_2O dosing. Dosing experiments are commonly described using Langmuir units, where 1 Langmuir (1 L) represents the exposure of a certain gas at a pressure of 1×10^{-6} Torr for one second. This corresponds to a surface coverage of approximately one monolayer (ML) for a surface with a sticking coefficient of unity.

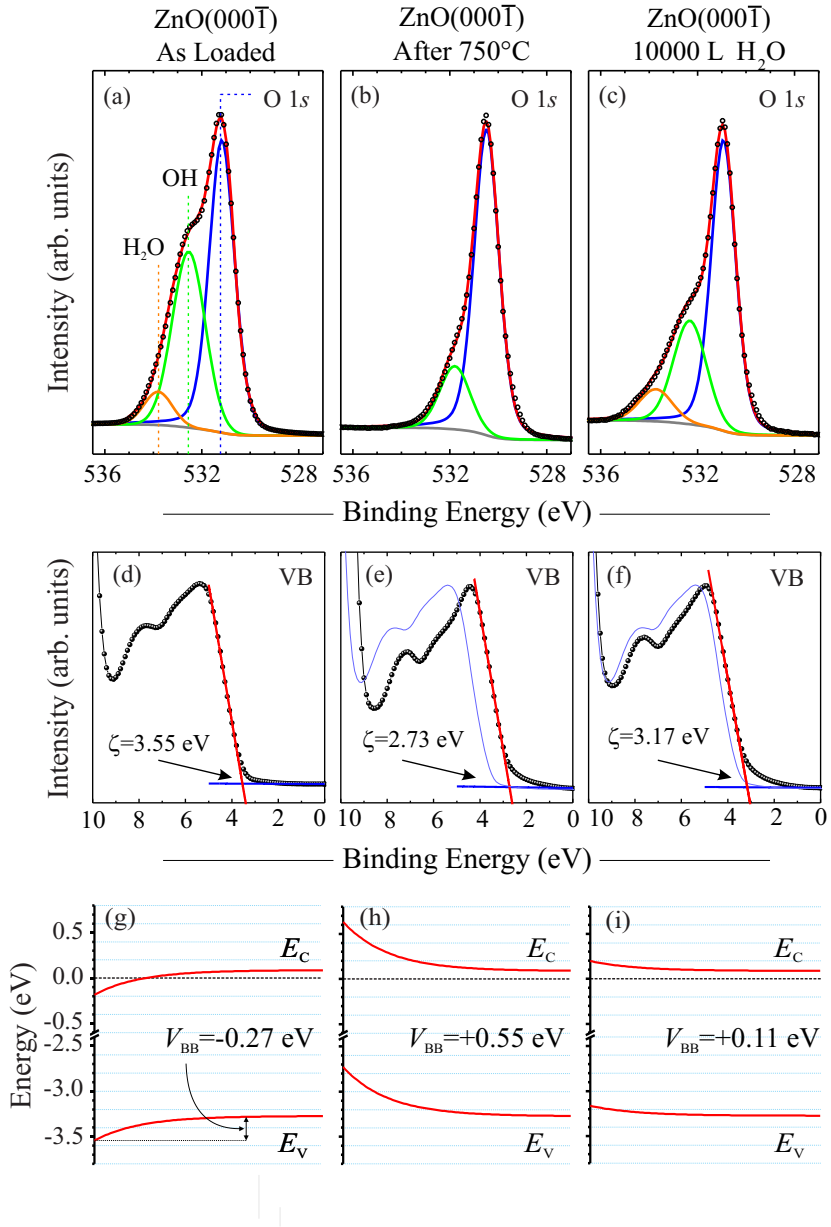

Figure 9.3.: O 1*s* core level XPS at $h\vartheta = 680\,\text{eV}$ with pseudo-Voigt fits in (a – c) for O-polar face and the VB region at $h\vartheta = 150\,\text{eV}$ with fits to the leading edge in (d – f). The faint blue line indicates the as-loaded VB position. The calculated surface band bending is presented in (g – i). The carrier concentration of the sample was $1 \times 10^{17}\,\text{cm}^{-3}$.

In the following, the H_2O and H_2 dose will be given in units of Langmuir. With increasing H_2O exposure, the O 1*s* lattice peak decreases in intensity and the OH/H_2O shoulder significantly increases in strength due to the dissociative adsorption of H_2O ($H_2O \rightarrow OH+H$) on the ZnO surface. After H_2O dosing, the crystals were exposed to atmosphere and re-annealed at 750 °C to create similar starting conditions for H_2 dosing. Compared to H_2O dosing, exposure to molecular hydrogen has a much smaller

effect on the O 1*s* spectra with only a slight increase in the OH shoulder. This can be explained by the low sticking coefficient of molecular hydrogen on ZnO surfaces [241].

All spectra were fitted with pseudo-Voigt functions in order to extract the relative peak areas of the lattice oxygen, OH and H_2O contributions. The top rows in Figs. 9.2 and 9.3 show the three pseudo-Voigt fitting functions, their resulting envelope and the Shirley background for the as-loaded, 750 °C annealed, and 10000 L water-dosed Zn-polar and O-polar surfaces respectively. For the as-loaded Zn-polar face (Fig. 9.2), the O 1*s* lattice peak is located at 531.2 eV with the OH contribution shifted by 1.4 eV toward higher binding energies, at 532.6 eV. The third component at 533.8 eV is attributed to H_2O adsorbed directly onto the ZnO surface or on top of the hydroxyl layer. Following annealing at 750 °C, the H_2O is no longer present and the hydroxyl component is significantly decreased. The loss of OH and H_2O species is partially recoverable by dosing with water, as shown in Fig. 9.2(c). The same behaviour can be observed for the O-polar face in Fig. 9.3(a – c). The shifts in the core level positions are significantly larger on the O-polar face indicating larger changes in surface band bending. The O 1*s* lattice peak shifts from 531.2 eV for the as-loaded O-polar face to 530.5 eV after 750 °C heat treatment and back to 531.0 eV after dosing with 10000 L of water.

The changes in surface band bending (V_{BB}), responsible for the shifts in the energetic position of the O 1*s* core level following different annealing/dosing treatments, can be more accurately extracted from the leading edge of the VB-XPS spectra, using the procedure previously explained in Sec. 3.4.3. Figures 9.2(d – f) and 9.3(d – f) show the intersection of linear fits to the leading edge of the VB-XPS spectra and the instrument background. A negative value of V_{BB} indicates downward band bending and electron accumulation, whereas a positive value indicates upward band bending and electron depletion at the surface. The extracted peak areas for the OH and H_2O contributions and the extracted surface band bending (V_{BB}) are plotted in Fig. 9.4. Both polar faces initially exhibit a similar hydroxyl concentration of 38 – 39 % and a 6 – 9 % contribution from H_2O compared to the overall O 1*s* core level peak area of $A_{O\,lattice+OH+H_2O}$. After *in situ* annealing, the loss of OH is significantly stronger on the O-polar surface. For example, heat treatment at 350 °C results in an OH reduction of 10 % on the O-polar face compared to only 2 % on the Zn-polar face. At this annealing temperature, the H_2O contribution was negligible (under 2 %) being comparable to the fitting error. Annealing at 750 °C reduces the OH concentration to 19 % on the O-polar face and 26 % on the Zn-polar face. While the reduction in the OH component is almost linear with annealing temperature on the O-polar face, the Zn-face shows a sudden 6 % decrease between 650 °C and 750 °C.

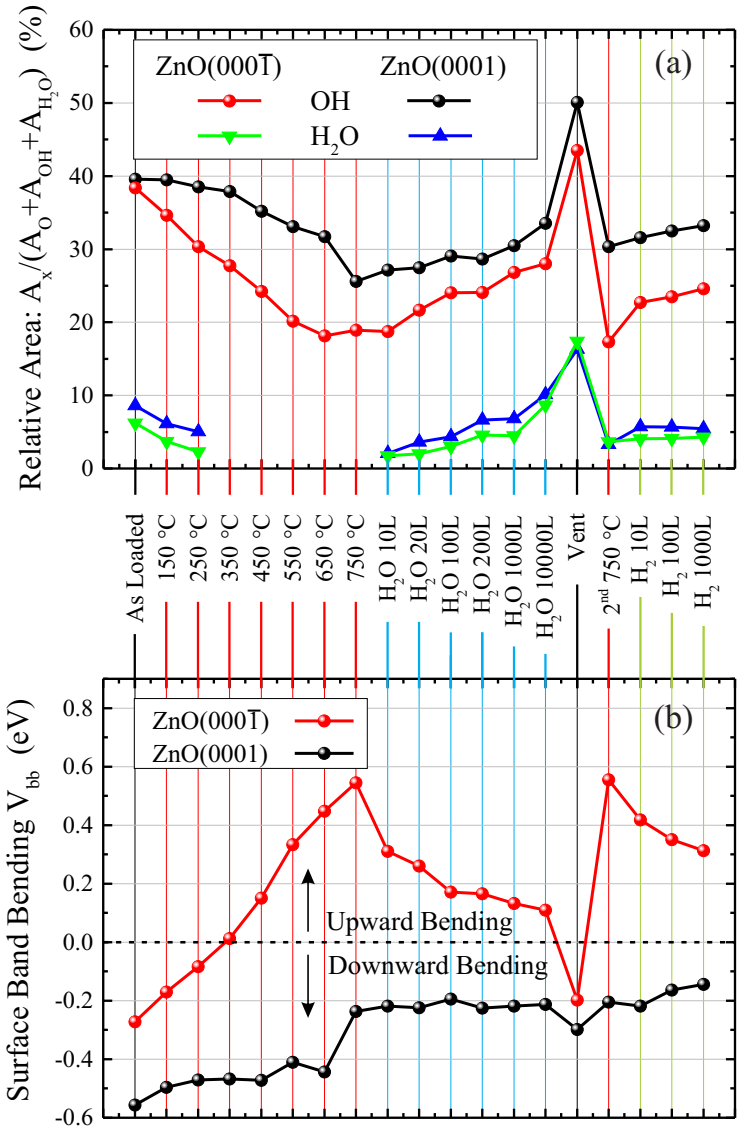

Figure 9.4.: (a) Integrated XPS intensity for the OH and H_2O contributions of the O 1*s* core level for different annealing and dosing conditions and (b) the subsequent change in surface band bending in terms of V_{BB}.

Hydrogen and hydroxyls introduce surface donor states [242]. Removal of these species, therefore, results in a reduction of the downward band bending at the surface. On the Zn-face the reduction is only modest, from $V_{BB} = -0.56\,\text{eV}$ for the as-loaded surface to $-0.24\,\text{eV}$ after 750 °C annealing. Interestingly, most of this change took place between 650 °C and 750 °C in a sudden step which mirrors the step-like reduction in OH concentration for the same temperatures. In contrast, the change in V_{BB} on the O-polar face is almost linear with annealing temperature. Initially, the surface band bending on the as-loaded O-polar face is only $-0.27\,\text{eV}$, significantly smaller than for the as-loaded Zn-polar face (see Fig. 9.2(g) and Fig. 9.3(g)). A flat band condition ($V_{BB} = 0\,\text{eV}$) is achieved after annealing at 350 °C, which corresponds to a transition

from downward to upward band bending. For annealing temperatures above 350 °C the surface bands on the O-polar surface bend increasingly upwards. A maximum upward band bending of +0.55 eV is achieved at 750 °C. This presents a total change in V_{BB} of over +0.8 eV compared to a change of only +0.3 eV for the Zn-polar face. Heating above 750 °C produced no significant further changes in V_{BB} on either the O-polar or Zn-polar face, while there was evidence of irreversible changes such as surface decomposition and significant near-surface impurity aggregation.

Dosing with H_2O, increases both OH and H_2O contributions in the O 1*s* core level. After 10000 L H_2O dosing, OH concentrations of 34 % (28 %) were measured for the Zn-polar (O-polar) face, plus a 9 – 10 % H_2O contribution on both surfaces. Interestingly, the re-hydroxylation does not appear to alter the surface band bending (V_{BB}) on the Zn-polar face at all. On the other hand, V_{BB} decreases to +0.11 eV on the O-polar face, still indicating a slight upward band bending on this surface. Following H_2O dosing, both faces were re-exposed to atmosphere which resulted in a strong increase in OH concentration. This step fully re-introduced the downward bend bending on the O-polar face, with a V_{BB} of −0.20 eV, close to the initial as-loaded value. In contrast, the downward bending on the Zn-polar face increased only slightly from −0.20 eV to −0.30 eV.

To check the reproducibility of the changes in surface band bending and to prepare OH-reduced surfaces for dosing experiments with molecular hydrogen, both polar-face were annealed a second time at 750 °C. The second annealing process resulted in a similar reduction in OH concentration as observed for the first 750 °C heat treatment and nearly identical changes in V_{BB}. This shows that on the O-polar face, the surface band bending can be repeatedly cycled between downward and upward band bending by removing and adding surface hydroxyls via heat treatment and atmospheric exposure. Dosing with molecular hydrogen leads to much smaller changes in the OH concentration and surface band bending compared to H_2O dosing. A modest 3 % increase in OH concentration on the Zn-polar face was observed for a H_2O dose of 1000 L and a corresponding minimal increase in surface band bending from −0.20 eV to −0.15 eV. The O-polar face showed an increase in OH concentration of 7 % for 1000 L of H_2 accompanied by a decrease in V_{BB} to +0.31 eV.

Fig. 9.5 shows the surface band bending V_{BB} versus the monolayer coverage of H or OH for each polar face. The monolayer coverages were calculated using the model presented in Sec. 3.4.3. For the O-polar face, the surface band bending strongly depends on the hydrogen monolayer coverage with the initial as-loaded H-coverage (1.24 ML) slightly greater than a single monolayer. There appears to be a definite correlation between H coverage on the O-polar face and V_{BB}, with decreasing H coverage associated

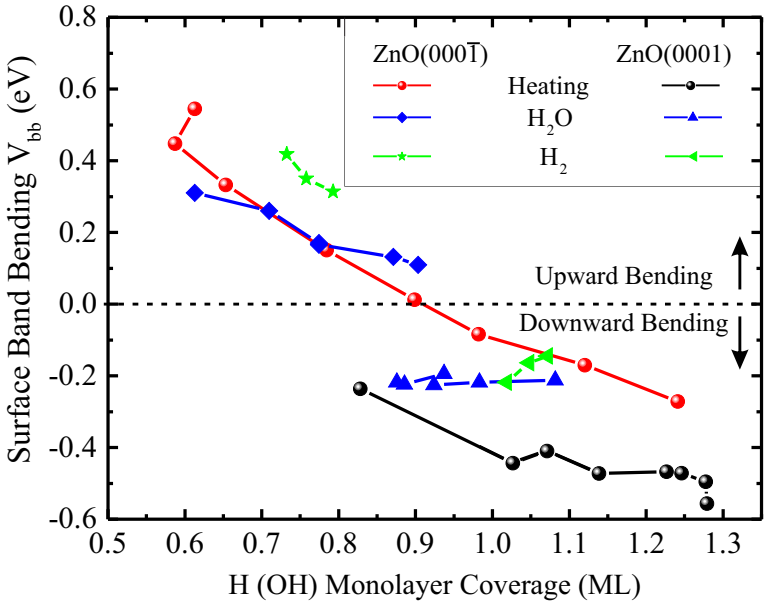

Figure 9.5.: Surface band bending V_{BB} versus OH (H) monolayer coverage for ZnO(0001) and ZnO(000$\bar{1}$) polar face for *in situ* annealing as well as H_2O and H_2 dosing.

with increasing V_{BB}. Flat band conditions are achieved at a coverage of 0.9 ML. At lower H coverages, the bands on the O-polar face show strong upward bending with $V_{BB} = 0.55$ eV for 0.61 ML H-coverage. The predicted H(OH) monolayer coverage for unreconstructed polar ZnO surfaces over a wide range of chemical potentials is 0.5 ML [34, 38].

After each annealing cycle, LEED measurements were performed. No deviations from a sixfold symmetry, indicating an unreconstructed (1×1) surface pattern, were observed. This is in agreement with Kunat *et al.* [40], who proposed that only the completely hydrogen-free O-polar surface exhibits a (1×3) oxygen vacancy reconstruction and that hydrogen coverage inevitably leads to unreconstructed surfaces. Completely hydrogen-free ZnO surfaces have so far only been obtained after extensive Ar^+ sputter-cleaning and annealing cycles which are also likely to change the surface stoichiometry. Although, an annealing-only preparation (as used here) does not yield hydrogen-free O-polar surfaces, this simple method can be used to change the electronic nature of the O-polar face from electron accumulation to electron depletion.

Exposure of depleted O-polar surfaces to H_2O increases the hydrogen monolayer coverage and reduces the upward band bending as water adsorbs dissociatively on the O-polar surface, a process that is indistinguishable from dosing with atomic hydrogen [26]. However, H_2O dosing up to 10000 L did not produce the same monolayer H coverage or downward band bending as observed in the as-loaded samples. Interestingly, exposure to atmosphere was necessary to fully restore the initial downward band

bending. This relatively slow re-hydroxylation is in contrast to the high reactivity of the clean (hydrogen-free) O-polar surface towards H_2O. Schiek *et al.* [243] found that water readily dissociates even below 300 K on the clean, (1×3) terminated O-polar surface. It is possible that water preferably dissociates at oxygen vacancies, which are present in much higher concentrations on H-free, reconstructed O-polar surfaces [244]. Kunat *et al.* [41] proposed that for the (1×3) H-free reconstruction, that is characterised by one missing oxygen atom per unit cell, H_2O molecules are first trapped at these vacancies before dissociating to form OH groups. The O-polar face samples presented here exhibit a residual ~ 0.5 ML OH coverage after UHV annealing and show no surface reconstruction. Therefore, significant numbers of oxygen vacancies are not expected at the surface.

In comparison, the Zn-polar face shows a more complex nature. UHV annealing up to 750 °C reduces the OH monolayer coverage from 1.28 ML to 0.83 ML. However, V_{BB} seems to be largely independent of the OH coverage, certainly for OH coverages greater than 1 ML. In addition, the downward band bending on the Zn-polar face is significantly stronger than that on the O-polar face. The weak link between OH coverage and V_{BB} is also observed after H_2O and H_2 dosing. Although the monolayer OH coverage increases after H_2O dosing, the surface band bending remains almost unchanged. The reason for this effect is unclear.

In addition to hydrogen adsorbed on the surface, hydrogen in the subsurface region could potentially influence the surface band bending and electron accumulation. Traeger *et al.* [245] recently investigated HT ZnO single crystals by means of ^{15}N nuclear reaction analysis and found that hydrogen concentrations in the subsurface region could exceed the bulk concentration by up to a factor of 10. A portion of this subsurface hydrogen was found to anneal out up to 550 °C and, therefore, is less strongly bound than bulk hydrogen. This is not surprising, as hydrogen can occupy a variety of different bonding positions. For a short overview see Sec.2.4. The same authors showed that subsurface hydrogen could be reintroduced by exposure to atomic hydrogen. Figure 9.4 clearly shows that on the O-polar surface, the downward band bending can be restored by exposure to atmospheric conditions. Assuming that the majority of the subsurface hydrogen diffused out during the 750 °C annealing step, the question becomes whether subsurface hydrogen can be replenished by atmospheric water vapour. For the completely hydroxylated rutile $TiO_2(110)$ surface [246], it was found that hydrogen does not desorb from the surface by forming H_2 or H_2O, but migrates into the bulk at room temperature due to a low activation barrier.

Annealing at temperatures above 750 °C did not introduce any significant further change in the band bending of either the Zn-polar or O-polar face. However, new

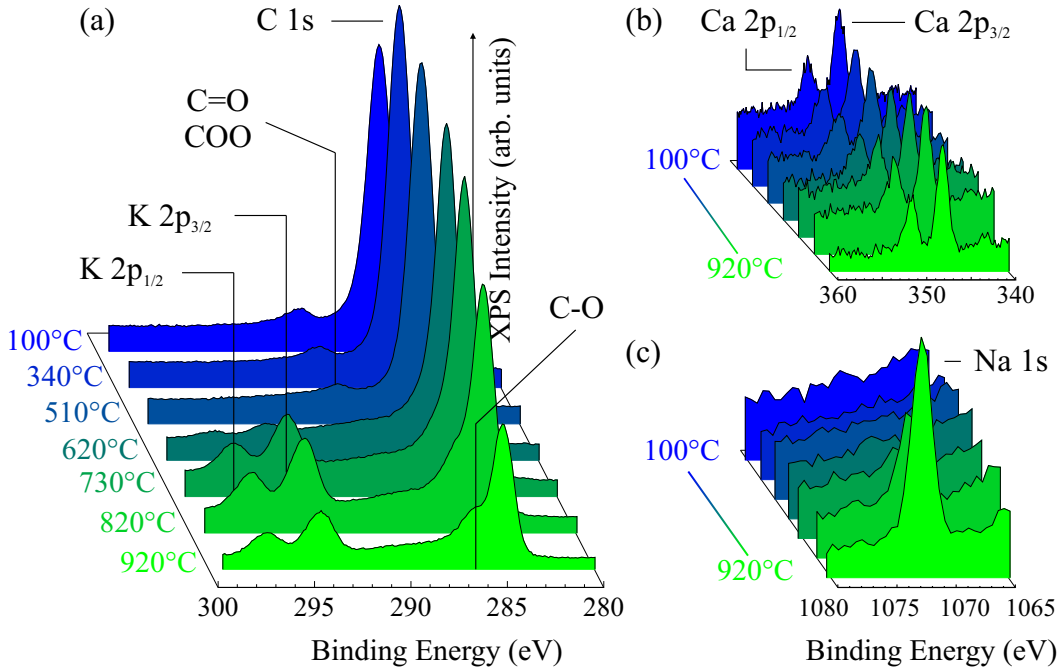

Figure 9.6.: XPS spectrum of (a) C 1*s* and (b) Ca 2*p* core levels recorded at $h\vartheta = 680\,\text{eV}$ on the Zn-polar face for different *in situ* annealing temperatures. (c) Na 1*s* core level recorded at $h\vartheta = 1486.7\,\text{eV}$.

XPS signals from sodium and potassium were observed on both polar faces, as shown for example on the Zn-polar face in Fig. 9.6. The dominant C 1*s* core level emission in 9.6(a) is positioned at 285.4 eV and initially contains a peak on its higher energy side at 289.6 eV. Peaks with higher binding energies than the elemental carbon peak at 285.4 eV originate from carbon atoms bound to one or more oxygen atoms, as the more electronegative oxygen atoms polarise the carbon atoms and induce a chemical shift [111]. Considering its energetic distance of 4.2 eV from the main elemental C 1*s* peak, this peak is attributed to a ketone (C=O) or carboxylic acid group (C=O-O) [247]. Interestingly, for heat treatment above 800 °C, a new shoulder on the higher binding energy side of C 1*s* was observed and is assigned to ether groups (C-O). It seems likely, that with higher annealing temperatures, ketones, and carboxylic acids dissociate into the more basic ether groups, giving rise to the C-O shoulder. At annealing temperatures of 620 °C and above, two peaks at 294.2 eV and 297.1 eV appear, which are assigned to potassium, i.e. K $2p_{\frac{1}{2}}$ and K $2p_{\frac{3}{2}}$. A weak calcium signal is also detected in Fig. 9.6(c) independently of the annealing temperature.

Hydrothermally grown ZnO crystals contain large amounts of group I impurities [9]. On annealing, these impurities tend to diffuse towards the surface where they accumulate (see the SIMS measurements in chapter 4). Although similar behaviour has been observed for Al and Ga in HT ZnO [248] using SIMS, no corresponding

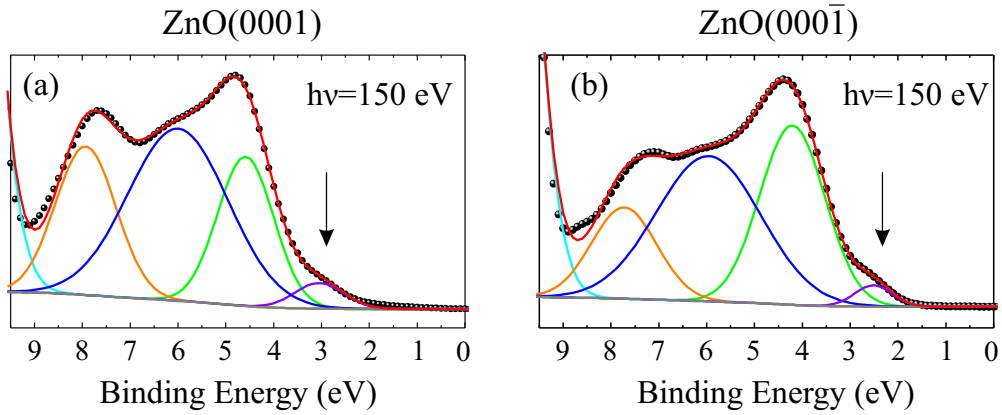

Figure 9.7.: Valence band XPS spectra for (a) Zn-polar and (b) O-polar face after *in situ* annealing at 920 °C. Dots represent measured data points. Arrows indicate electronic states with sub bandgap energies.

XPS signals for these elements could be detected for annealing steps up to 920 °C. The detection of group I elements in the near-surface region, suggests that high temperature annealing, especially above 730 °C, permanently alters the near-surface chemistry. In addition, Kohl *et al.* [249] found an exponential increase in sublimation of Zn atoms from the ZnO surface above 700 °C. Therefore, decomposition and/or sublimation of the ZnO crystal has to be considered for high-temperature UHV annealing. Zn atoms sublimated from the surface can re-adsorb on the crystal surface as metallic Zn, and introduce states in the bandgap. To examine this possibility, the valence band XPS spectra of samples annealed at 920 °C were fitted with four Gaussian peaks. These include the predominantly O $2p$ derived states at 4.5 – 5 eV, the hybridised O $2p$ and Zn $4s$ states at 8 eV [250], and an additional peak between these binding energies to assure a good fit. Interestingly, after annealing to 920 °C, the valence band region also exhibits a broad tail of states in the bandgap, shown in Fig. 9.7 for both polar faces. These states, marked by an arrow, may represent metallic Zn. However, group I elements or Al accumulated in the subsurface region cannot be excluded.

9.1.2 Non-polar and semi-polar faces of ZnO

Non-polar (m-plane and a-plane) and semi-polar (r-plane) surfaces of conventional HT ZnO were prepared by the same organic solvent cleaning process as the polar ZnO surfaces described in Sec. 9.1.1 and then subjected to UHV annealing at temperatures up to 700 °C. The resulting O $1s$ core level spectra, taken at $h\vartheta = 680$ eV, are shown in Fig. 9.8. All three surfaces show large hydroxyl peaks (after loading into the UHV chamber), with relative OH concentrations of 50 % and 54 % for the r- and m-plane faces, respectively, and 67 % for a-plane ZnO (see Fig. 9.9(a)). After initial *in situ* an-

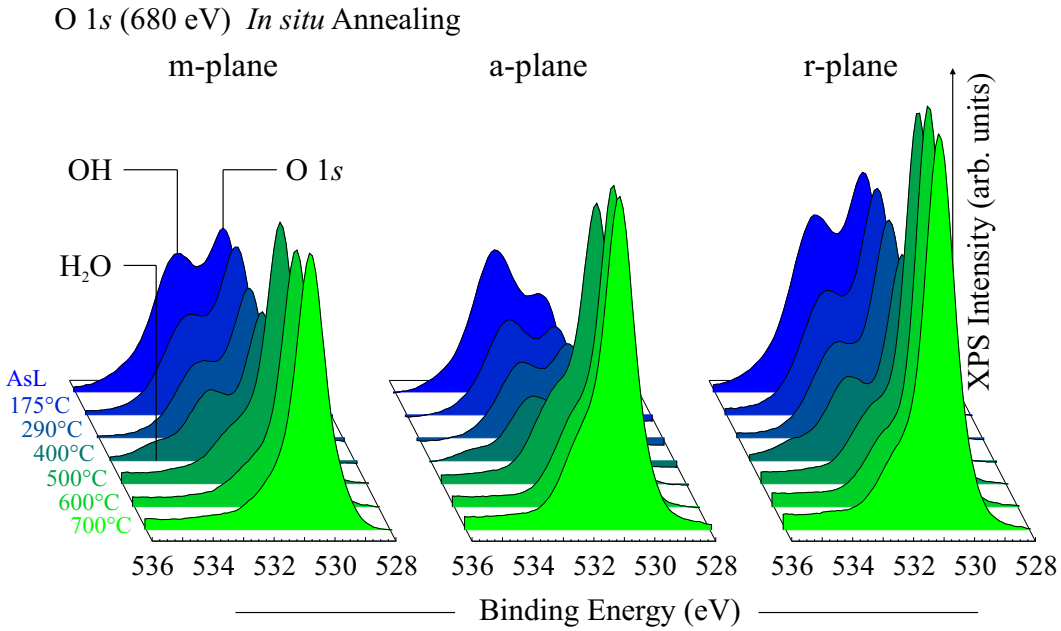

Figure 9.8.: O 1*s* core level XPS spectra at $h\vartheta = 680\,\text{eV}$, of non-polar m- and a- plane, and semi-polar r-plane ZnO surfaces following *in situ* annealing.

nealing for 10 min at 175 °C, all faces showed a loss of 10 – 15% in surface hydroxyl concentration. The OH concentration on the r-plane and m-plane samples at this point is comparable to the O-polar face annealed at a similar temperature. In general, the OH desorption process for the r- and a-plane faces seems to be reasonably linear with annealing temperature, except for a relatively large decrease in OH concentration between 400 °C and 500 °C. This effect is particularly noticeable on the m-plane face for which the OH concentration is almost constant for annealing temperatures of 175 – 400 °C, after which a large step-like decrease is observed. This can also be seen in Fig. 9.8 as after 500 °C annealing, the O 1*s* lattice peak strongly increases in intensity, containing only an OH shoulder rather than a distinct OH peak. After the final 700 °C annealing step, all three surfaces showed OH concentrations of 5 – 11 %, significantly smaller than the 19 – 26 % OH-concentration observed on the polar surfaces after 750 °C annealing.

The surface water component approaches zero after annealing at 300 °C, considering a measurement error of at least ±3 % (Fig. 9.9). Remarkably, a distinct jump in water concentration after 400 °C annealing was observed on all the non-polar and semi-polar faces investigated. A similar observation was made by Martin *et al.* [251], who observed two well defined, H_2O-related peaks using thermal desorption spectroscopy (TDS) at 200 °C and 400 °C in ZnO powders that contained high percentages of non-polar surfaces with the 400 °C peak being significantly stronger.

A comparison of Figs. 9.9(a) and (b) suggests a reasonable correlation between OH concentration and surface band bending (V_{BB}) on the r-plane, a-plane and m-plane

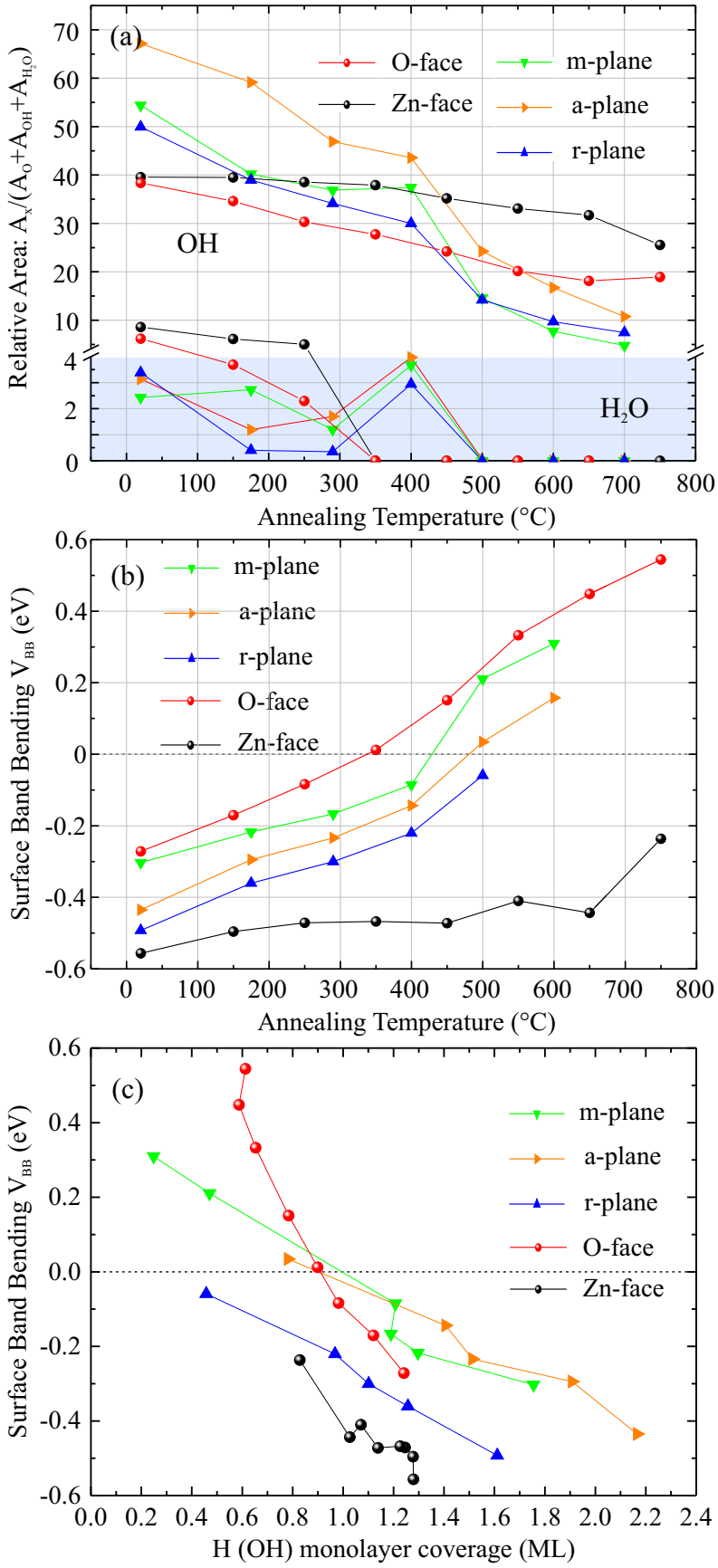

Figure 9.9.: (a) OH/H_2O concentration and (b) surface band bending (V_{BB}) during *in situ* annealing for non-polar and semi-polar planes. (c) Surface band bending (V_{BB}) versus H (OH) monolayer coverage. The carrier concentration of the m-, a- and r-plane wafers were 4×10^{15} cm^{-3}, 2×10^{17} cm^{-3} and 2×10^{15} cm^{-3} respectively.

faces with decreasing OH concentration associated with increasing V_{BB} as the near-surface bands shift upwards. This correlation is further explored in Fig. 9.9(c) which indicates that V_{BB} is directly related to the surface H (OH) coverage, although the nature of this relationship varies with crystallographic polarity. In the case of the m-plane face, annealing up to 400 °C, leads to a relatively small increase in V_{BB}. Further annealing at 500 °C causes a rather sudden transition from downward to upward surface band bending. A rather more linear increase of V_{BB} with annealing temperatures was observed for the a-plane and r-plane faces with almost flat band conditions obtained after 500 °C annealing. Unfortunately, all three of these ZnO crystals became insulating after annealing above 500 – 600 °C, resulting in sample charging and unreliable shifting in the XPS valence band spectra. This behaviour is commonly observed in conventional HT ZnO material containing high concentrations of group I impurities (especially Li). Under these conditions, it was not possible to extract a reasonable band bending parameter (ζ).

The as-loaded m-, a- and r-plane ZnO samples have significantly higher OH concentrations than the polar surfaces and a higher thermal desorption rate during *in situ* annealing. Compared to the Zn-polar and O-polar faces, the surface termination on the non-polar and semi-polar faces is more complex with H, OH and H_2O species likely to be present in a mixed adlayer. In addition, hydrogen bonding between these different surface species will influence their thermal stability. The non-polar faces of ZnO consist of rows of Zn-O dimers separated by trenches. In the case of the m-plane $(10\bar{1}0)$ face, the Zn-O dimers on both sides of these trenches allow a hydrogen-bonded "key-lock" network between adsorbed H_2O molecules and adjacent O surface atoms to form. Meyer *et al.* [252, 253] showed by first principle calculations and surface microscopy studies that, at monolayer coverages, the hydrogen bonding network promotes the partial dissociation of H_2O molecules, leading to the formation of a H, OH and H_2O network with a regular (2×1) periodicity. On the a-plane $(11\bar{2}0)$ surface, the Zn-O dimers run parallel to the trenches and the adsorbed H_2O configuration is less symmetrical. Cooke *et al.* [254] proposed that the lack of molecular H_2O hydrogen bonding on the a-plane face energetically favours full rather than partial H_2O dissociation leading to fully hydroxylated surfaces. The recombination of adsorbed H and OH into molecular H_2O and its subsequent desorption from the ZnO surface seems to be the preferential desorption pathway after the initial hydrogen bonding network is broken. In addition, the non-polar planes are free of out-of-plane electric fields and spontaneous polarisation charges and are electrostatically stable in their unreconstructed bulk-terminated form. Therefore, hydrogen and hydroxyl groups are not needed to electrostatically stabilise the non-polar surfaces. This could be one of the reasons why the H/OH coverage shows a lower thermal stability on these faces.

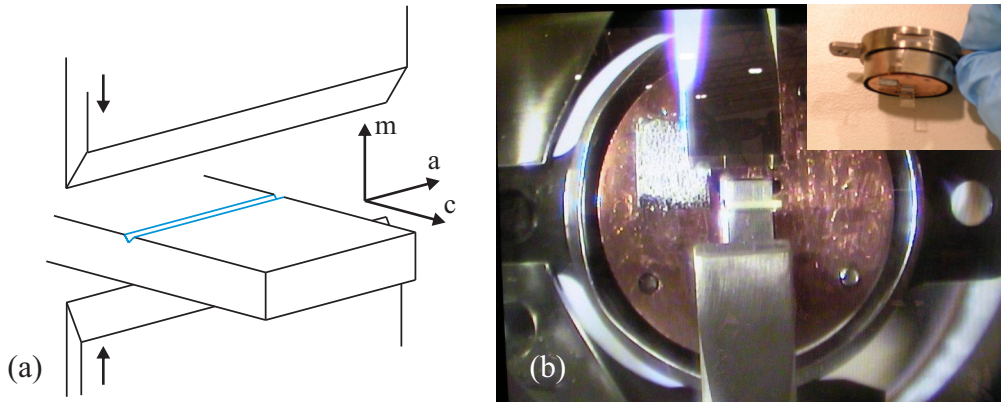

Figure 9.10.: (a) Schematic representation and (b) photograph of the *in situ* cleaving setup at the Australian Synchrotron. The blue line indicates the pre-scratched notch for preferential cleaving.

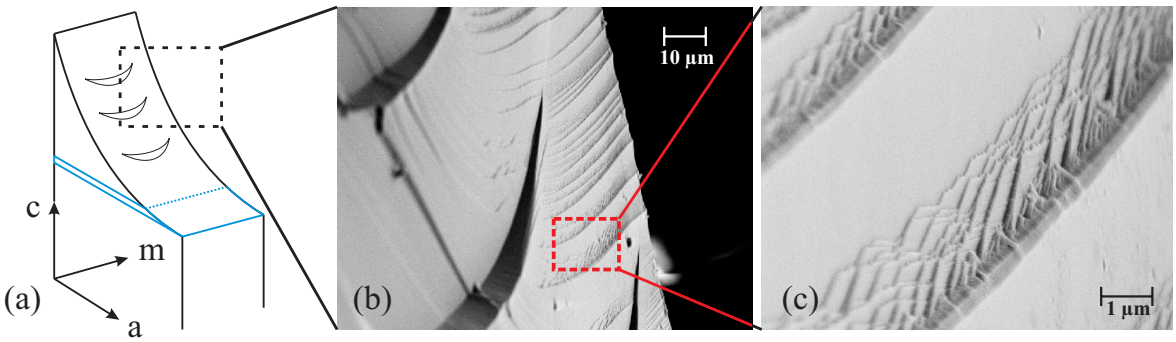

Figure 9.11.: Schematic representation of the cleaved sample. Atomically flat surface could not be obtained. SEM image of the cleaved Zn-polar face for different magnifications in (b) and (c).

9.1.3 In situ cleaving of ZnO

ZnO bulk single crystals were cleaved in ultra-high vacuum ($\sim 5 \times 10^{-10}$ mbar) to provide clean surfaces free of atmospheric contaminants that were subsequently investigated using XPS spectroscopy. The cleavage setup at the Australian Synchrotron consists of two stainless steel knife-edge shears that apply continuous mechanical pressure on to a sample placed between them. Figure 9.10 shows the sample holder with a 1 mm thick m-plane ZnO bulk crystal between the cleaving shears together with the sample orientation. ZnO bulk crystals were mounted in the (+c) and (−c) directions in the sample holder to obtain Zn-polar and an O-polar cleaved faces, respectively.

None of the cleaved samples showed an atomically flat cleavage plane, as shown in the SEM images presented in Fig. 9.11 (b − c). This means that these surfaces will contain a significant density of step edges and other defects. Scratching the surface with a diamond scribe to create a predetermined breaking point did not noticeably improve the quality of the cleaved surface. Generally, a wurtzite crystal will cleave more easily

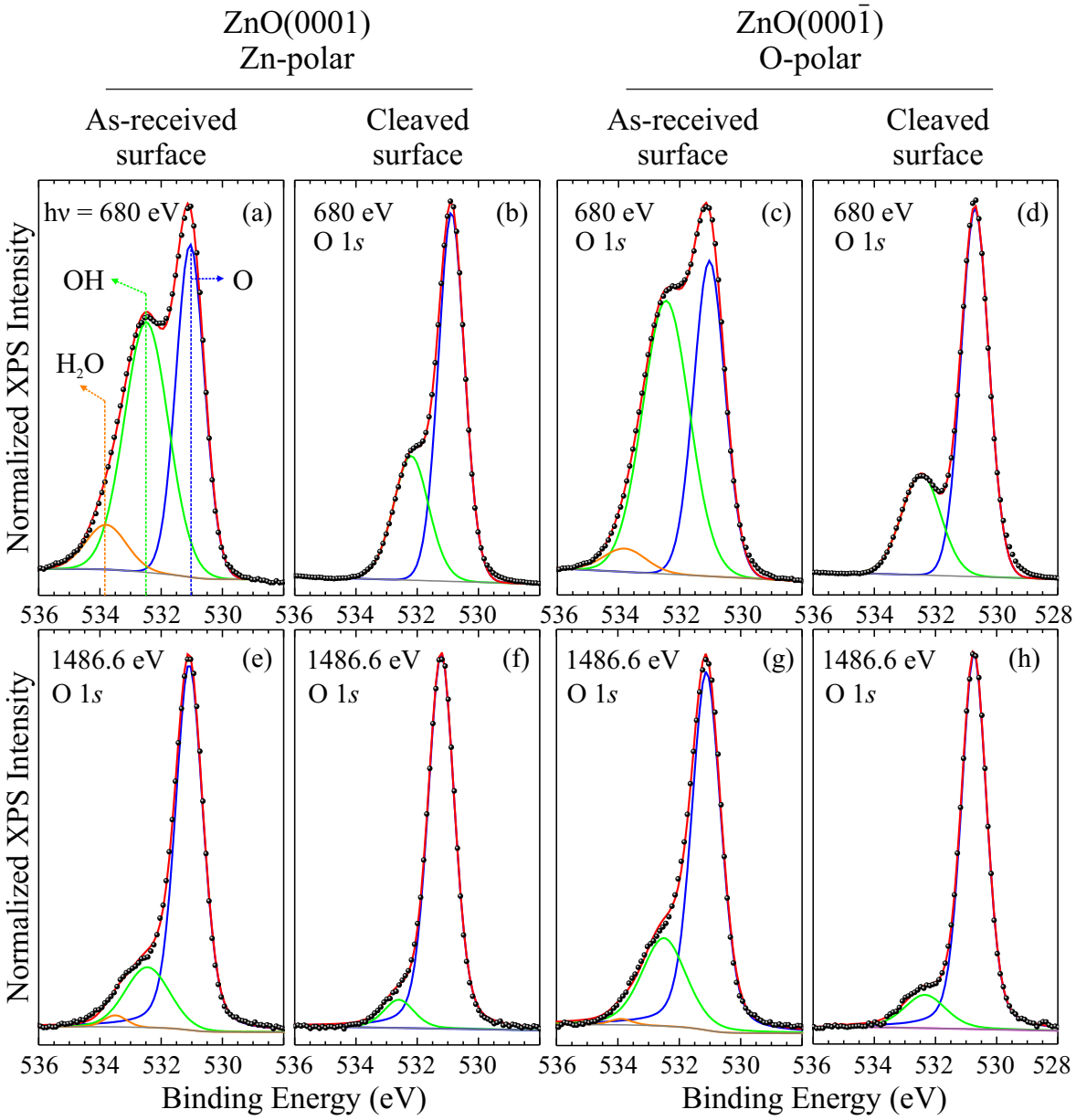

Figure 9.12.: O 1*s* core level spectra using 680 eV and 1486.7 eV x-rays for Zn-polar (a,b,e,f) and O-polar (c,d,g,h) faces of as-received and cleaved HT ZnO single crystals. The black dots represent the actual data with solid lines being the pseudo-Voigt fits for contribution of bulk oxygen (blue), OH (green), H_2O (orange) and the Shirley background (grey) as well as the envelope function (red).

along the non-polar $(10\bar{1}0)$ prism face for electrostatic stability reasons [255].

Synchrotron XPS measurements were carried out at $h\vartheta = 680\,\text{eV}$ to ensure optimal surface sensitivity and at $h\vartheta = 1486.7\,\text{eV}$ for comparison with laboratory based measurements using Al K_α sources. The resulting O 1*s* core level XPS spectra for as-loaded and cleaved Zn-polar and O-polar faces are shown in Fig. 9.12. The data was fitted with three pseudo-Voigt functions for lattice oxygen, hydroxyl groups, and water on

a Shirley background. The extracted concentrations and monolayer coverages for both polar faces are given in Table 9.1.

We first consider the uncleaved reference samples. The as-loaded Zn-polar (O-polar) faces show peak area percentages of 19.2 % (26.4 %) for hydroxyls and a minor water component of 1.8 % (2.6 %) for photon energies of 1486.7 eV. The surface sensitivity increases dramatically with the use of 680 eV photons due to the lower photoelectron escape depth. A O 1*s* core level binding energy of 531 eV would yield photoelectrons with a kinetic energy of 149 eV for 680 eV photons corresponding to a photoelectron mean free path of $\lambda_{\mathrm{IMFP}} \approx 6.2$ Å compared to ≈ 19.5 Å for 1486.7 eV photons. The OH component increases to 49.5 % (54 %) for the Zn-polar (O-polar) faces with a further 8 % (4 %) for the H_2O component using $h\vartheta = 680$ eV photons. The OH monolayer coverage is approximately 1.7 ML for both uncleaved Zn-polar and O-polar faces at $h\vartheta = 680$ eV with a minor contribution from H_2O. This is consistent with Schlepütz *et al.* [256] who observed a (1×1) overlayer of oxygen atoms, in the on-top positions, above the terminating Zn atoms (for ZnO(0001) polar faces) using surface x-ray diffraction (SXRD). These oxygen atoms most likely belong to OH groups as SXRD lacks sufficient sensi-

Table 9.1.: Quantification analysis for as-received and *in situ* cleaved ZnO surfaces.

		As-received surface		Cleaved Surfaces		
		Zn-polar	O-polar	Zn-polar	O-polar	O-polar 12 h in UHV
680 eV	Bulk O	42.5 %	41.9 %	68.8 %	72.3 %	72.1 %
	OH	49.5 %	54.0 %	31.2 %	27.7 %	27.9 %
		1.6 ML	1.7 ML	1.0 ML	0.9 ML	0.9 ML
	H_2O	8.0 %	4.0 %	–	–	–
		0.3 ML	0.1 ML	–	–	–
	ζ	3.71 eV	3.50 eV	3.65 eV	3.25 eV	3.23 eV
	V_{BB}	−0.42 eV	−0.21 eV	−0.36 eV	+0.04 eV	+0.02 eV
1486.7 eV	Bulk O	79.0 %	71.0 %	92.0 %	87.3 %	–
	OH	19.2 %	26.4 %	8.0 %	12.7 %	–
		1.7 ML	2.4 ML	0.7 ML	1.1 ML	–
	H_2O	1.8 %	2.6 %	–	–	–
		0.2 ML	0.2 ML	–	–	–
	ζ	3.45 eV	3.45 eV	3.76 eV	3.15 eV	–
	V_{BB}	−0.18 eV	−0.18 eV	−0.48 eV	+0.12 eV	–

tivity to detect hydrogen atoms.

The XPS spectra immediately after cleaving are shown in Fig. 9.12(b) and (f) for the Zn-polar face and Fig. 9.12(d) and (h) for the O-polar face. Interestingly, in both cases an OH shoulder is still clearly present. Quantification analysis gives a hydroxyl component of 8 % (12.7 %) for Zn-polar (O-polar) faces at a photon energy of 1486.7 eV. At $h\vartheta = 680$ eV these values increase to 31.2 % (27.2 %), which represents a coverage of approximately one monolayer. No H_2O component was observed on any of the cleaved samples.

The presence of OH groups immediately after cleaving is surprising as the cleaved crystals were continually exposed to UHV conditions. It is therefore likely that hydrogen from the bulk or from the sides of the sample has diffused towards the cleaved surface. As outlined in Sec. 2.4, there are several forms of interstitial and molecular hydrogen in hydrothermal ZnO and most of them show a very low diffusion barrier [84, 85]. The fast diffusion process could also be driven by the need to stabilise the electrostatically unstable hydroxyl-free polar faces. Nishidate *et al.* [240] used DFT calculations to show that hydrogen atoms in the subsurface region of the Zn-polar face form hydroxyl groups with lattice oxygen, which subsequently emerge at the surface. This process breaks the back bond of the oxygen atom with the neighbouring Zn atoms. Significant quantities of atomic hydrogen are believed to be trapped in the bulk lattice and in defect complexes. Therefore, hydrogen will always be present in the subsurface region no matter how the ZnO crystal is cleaved. However, the re-hydroxylation from residual hydrogen species must also be considered. The vacuum in the cleaving chamber was $\sim 5 \times 10^{-10}$ mbar, making re-hydroxylation from residual H, H_2, and H_2O in the timeframe (a few minutes) between cleavage and measurement most unlikely. Furthermore, the cleaved crystals showed no further increase in their OH component after 12 h in the UHV chamber. In addition, ZnO crystals annealed *in situ* at 600 °C exhibited significantly reduced hydroxyl surface concentrations and showed no sign of re-hydroxylation with time in the same UHV chamber.

The band bending parameter ζ (i.e. the energetic difference between E_V and E_F in the near-surface region) was extrapolated from the respective VB-spectra (not shown) then used to calculated the surface band bending V_{BB} in Table 9.1. The Zn-polar (O-polar) faces of the uncleaved reference samples exhibit a negative V_{BB} of -0.42 eV (-0.21 eV) consistent with strong downward band bending. Similar values were obtained for the unannealed ZnO crystals in Sec. 9.1.1. The cleaved ZnO(0001) polar face showed a slight increase in V_{BB} to -0.36 eV indicating a negligible change in the downward band bending on this face. However, the cleaved O-polar face exhibited almost flat bands with $V_{BB} = +0.04$ eV. This indicates that the surface accumulation layer has been removed by cleaving on the O-polar face. The respective flat band hydroxyl coverage is 0.9 ML, in excellent agreement with the annealing studies presented in Sec. 9.1.1 for

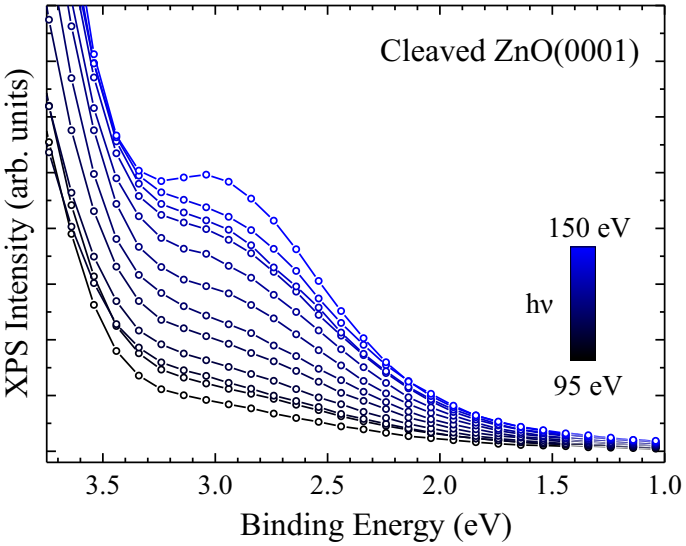

Figure 9.13.: Gap states in the VB-XPS of cleaved ZnO(0001) face for different photon energies between $h\vartheta = 95 - 150\,\mathrm{eV}$. Open circles represent data points.

which the O-polar face showed a transition from downward to upward surface band bending after annealing at 350 °C with a corresponding hydroxyl coverage of 0.89 ML.

Upon cleaving, the valence band spectra of the Zn-polar face exhibits a new low-intensity peak at 3.04 eV, indicating gap states above the valence band edge. Figure 9.13 shows these gap states for various photon energies from 95 eV to 150 eV. It is possible that these states are linked to the formation of OH groups on the cleaved surface by diffusing hydrogen. The adsorption of hydrogen on top of Zn atoms is also possible, but unlikely compared to the formation of hydroxyl groups [34]. Hydrogen in the near-surface region can reduce the ZnO lattice by forming OH groups with lattice oxygen, leaving metallic Zn on the surface [240]. The metallic Zn could then produce the observed gap states. Interestingly, the gap states form a clear maximum at a photon energy of 150 eV and are not observable at $h\vartheta = 680\,\mathrm{eV}$. This indicates that the origin of these sub-bandgap states lies within the first few Zn-O double-layers but are not necessary located at the surface.

9.2 Real-Time XPS

The change in surface band bending during annealing was directly monitored in real-time using a fast XPS acquisition system at Aberystwyth University, specifically designed to study the kinetics of surfaces and interfaces. A description of the setup is given in Sec. 3.4.2. Figure 9.14 shows the evolution of the Zn $2p_{3/2}$ core level emission for both polar faces during *in situ* annealing. The position of the Zn $2p_{3/2}$ peak max-

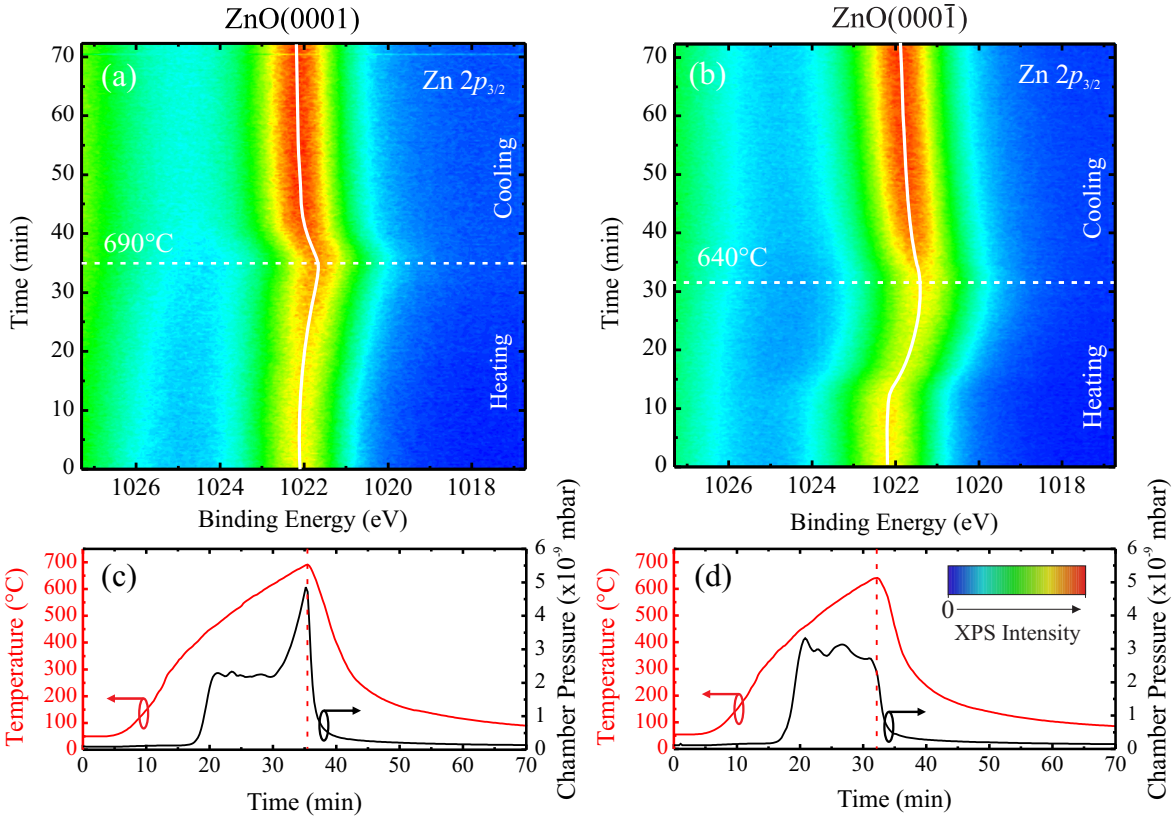

Figure 9.14.: Projection view of real-time evolution of Zn $2p_{3/2}$ core level on the Zn-polar (a) and O-polar face (b) as well as sample temperature and chamber pressure in (c) and (d) for the respective faces.

ima was used to provide a direct indication of the surface band bending (V_{BB}) of each sample i.e. shifts to lower binding energies are associated with positive shifts in V_{BB} and visa versa. All samples were subjected to initial NO plasma cleaning to efficiently remove the adventitious carbon contamination. As indicated by the white solid lines in Fig. 9.14(a – b), the Zn $2p_{3/2}$ peak maxima shift toward lower binding energies during the 35 min annealing cycle. This corresponds to a positive shift in the surface band bending V_{BB}. The white dashed line indicates the point in time at which the highest sample temperature was reached and the subsequent cooling process started. During the cooling process the core level shift is reversed, leading to a decrease in V_{BB}. This was not observed in the synchrotron experiments and is likely caused by surface re-hydroxylation due to the higher residual hydrogen and water partial pressures in the real-time XPS chamber. With increasing sample temperature, the chamber pressure increases, as can be seen in Fig. 9.14(c – d). A strong pressure increase is observed for both polar faces at approximately 400 °C. The chamber pressure for the O-polar face plateaus at this point ($\sim$ 400 °C) for the rest of the heating cycle, whereas the pressure for the Zn-polar face suddenly increases again (to $\sim 5 \times 10^{-9}$ mbar) above 620 °C.

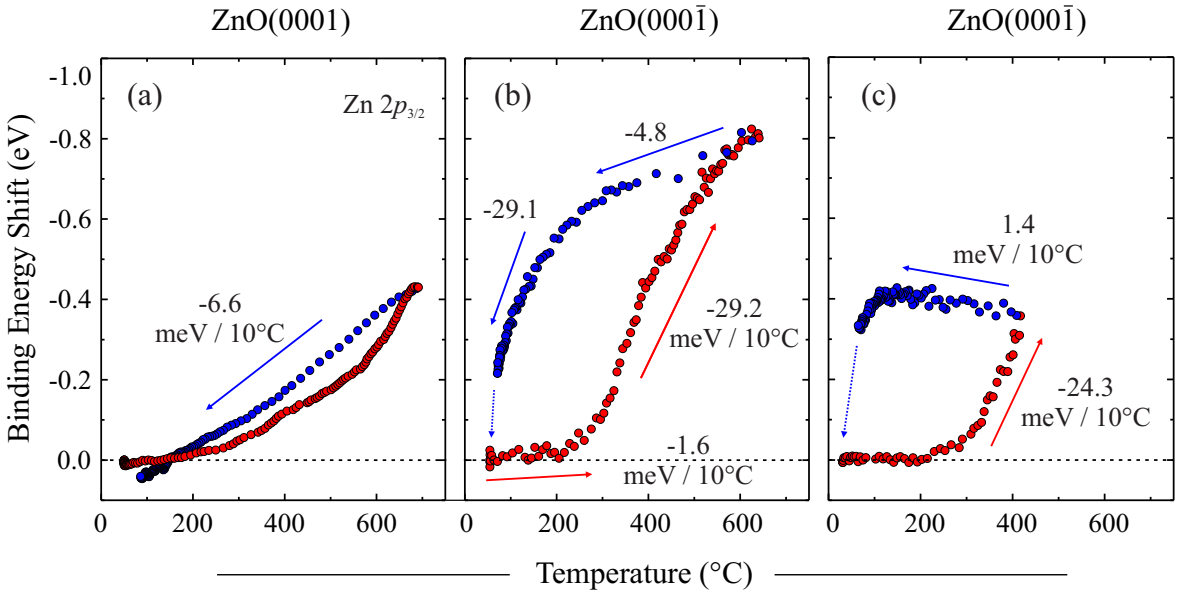

Figure 9.15.: Real-time binding energy shift of Zn $2p_{3/2}$ under *in situ* annealing for the (a) Zn-polar and (b) O-polar faces. A second annealing cycle for the O-polar face up to 400 °C is shown in (c). Data acquisition was carried out by G.T. Williams [257].

The binding energy (BE) shift in the Zn $2p_{3/2}$ core level spectra for both polar faces with temperature is shown in Fig. 9.15. For the Zn-polar face, Fig. 9.15(a), the binding energy shift is almost symmetrical for annealing and cooling, at a rate of approximately 6.6 meV per 10 °C. The maximum binding energy shift for the Zn-polar face was −0.4 eV, corresponding to an increase in V_{BB} of +0.4 eV at 690 °C. In contrast, the O-polar face in Fig. 9.15(b) shows a binding energy shift of −0.8 meV at 640 °C, corresponding to an increase in V_{BB} of +0.8 meV, similar to that observed in the synchrotron experiments. In addition, the core level shift after a complete annealing/cooling cycle on the O-polar face shows a hysteresis-like behaviour in contrast to the linear relationship found on the Zn-polar face. Initially, only a small change in binding energy for temperatures up to ∼ 280 °C is observed; after which the BE shift increases by a factor of almost 20 to −29.2 meV per 10 °C. Upon cooling from 640 °C, the shift in binding energy reverses at a moderate rate of 4.8 meV per 10 °C. The substantial part of the BE recovery on the O-polar face occurs over the course of several hours below 200 °C as the surface slowly re-hydroxylates. A second heating/cooling cycle up to 400 °C yields the same hysteresis-like behaviour, as can be seen in Fig. 9.15(c), and this effect was consistently observed on this face for a number of ZnO crystals (see also Fig. 9.17(a)).

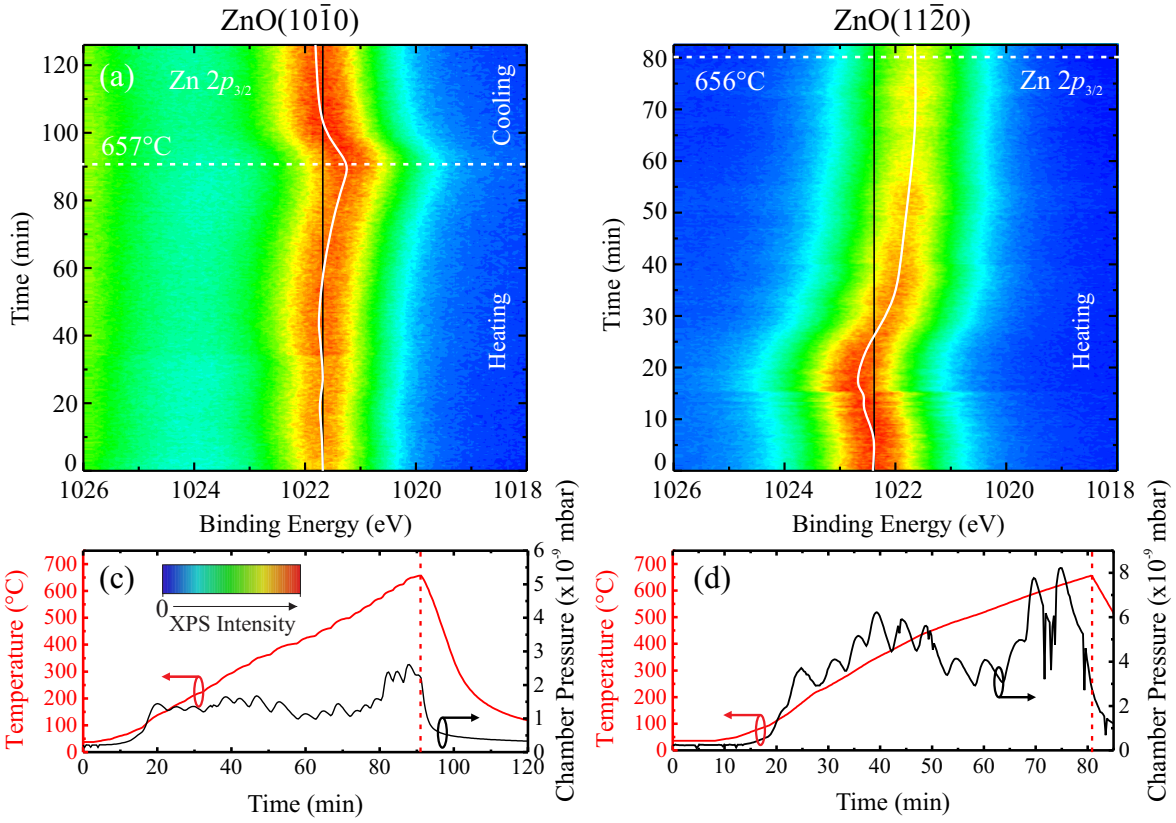

Figure 9.16.: Projection view of the real-time evolution of Zn $2p_{3/2}$ core level for (a) m-plane and (b) a-plane ZnO as well as the sample temperature and chamber pressure in (c) and (d) for the respective faces. The white line indicates the change in peak position whereas the black line represents the initial peak position.

In summary, the changes in surface band bending on the polar faces of ZnO are comparable both during and after annealing as shown by the similarity in the results from the real-time XPS and synchrotron XPS experiments. The O-polar face shows significantly larger changes in surface band bending, compared to the Zn-polar face, including a transition from downward to upward band bending. This excludes the possibility that the changes in V_{BB} during annealing are solely caused by the decrease in bandgap at higher temperatures.

Real-time XPS annealing studies were also carried out on the non-polar m-plane and a-plane faces of HT ZnO, as shown in Fig. 9.16. The m-plane face shows a similar behaviour to the O-polar face with a shift to lower binding energies at higher annealing temperatures. In contrast, the a-plane face exhibits an initial shift to higher binding energies and an oscillating pressure profile with peak pressures up to 8.2×10^{-9} mbar above 600 °C. The binding energy shift of the respective Zn $2p_{3/2}$ core levels is shown for m-plane and a-plane faces in Figs. 9.17(b) and 9.17(c). For comparison, the binding energy shift for two O-polar faces from different wafers are shown in Fig. 9.17(a).

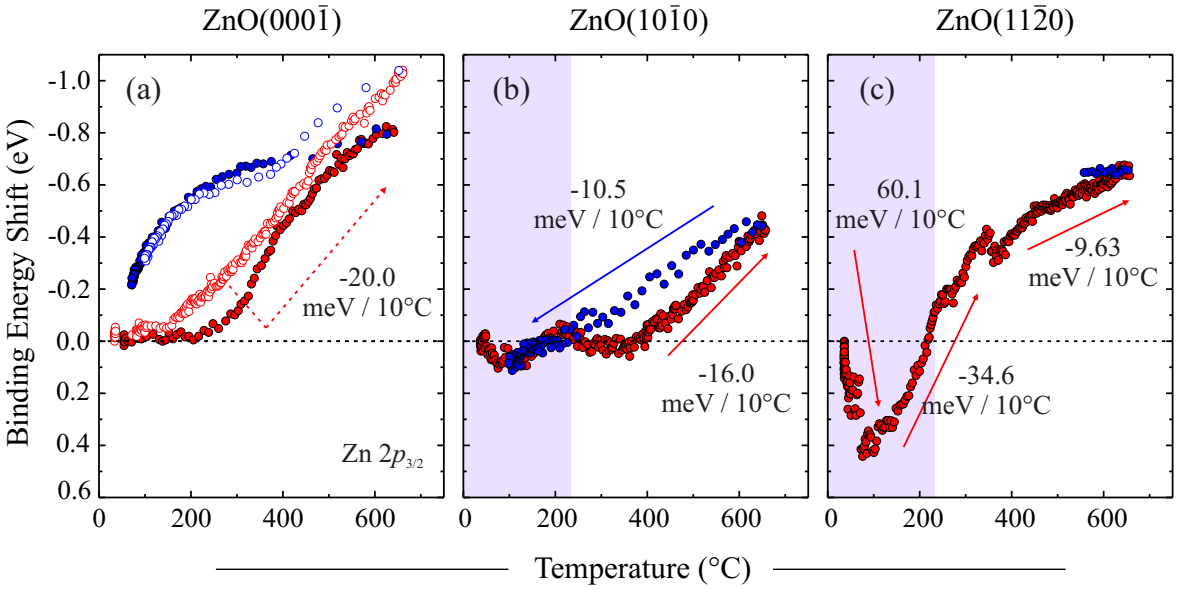

Figure 9.17.: Real-time binding energy shift of Zn $2p_{3/2}$ under *in situ* annealing for (a) two different O-polar faces, (b) m-plane and (c) a-plane ZnO.

The non-polar planes faces were subjected to an initial NO plasma cleaning procedure to remove carbon contamination. For the polar faces, the plasma cleaning was followed by an initial annealing cycle at 130 °C to remove excess oxygen adsorbed on the sample surface from the NO plasma. Williams [257] showed that NO plasma treatment results in a negative BE shift of up to −0.5 eV of the Zn $2p_{3/2}$ core level on the Zn-polar surface for an exposure time of 40 min, which was attributed to the adsorption of electronegative oxygen species on the surface. During subsequent annealing up to 300 °C the surface oxygen adsorbates were removed, reversing the associated negative BE shift. This post-plasma annealing step was not carried out in the case of the non-polar faces, and the initial shift to higher binding energies, shown as shaded areas in Fig. 9.17(b–c), is attributed to oxygen desorbing from the surface. No change in BE was observed between 250 – 350 °C for the m-plane face followed by the onset of a linear negative shift of −16 meV per 10 °C. At the maximum temperature of 660 °C, the total BE shift is −0.4 eV corresponding to an increase in V_{BB} of +0.4 eV. In contrast, the a-plane face exhibits a total BE shift of almost −1.0 eV if the initial increase of +0.4 eV due to surface oxygen adsorption is included.

In addition to real-time XPS, low energy electron diffraction (LEED) measurements were also carried out during *in situ* annealing with the results shown in Fig. 9.18. Both polar surfaces exhibit sixfold symmetric (1×1) patterns as shown for the O-polar face in Fig. 9.18. For high temperatures up to 775 °C, the LEED pattern sharpens , however, no reconstruction, e.g. (1×3) or $(\sqrt{3} \times \sqrt{3})$R30° [38] was observed on either the O-polar or Zn-polar face. The synchrotron XPS experiments showed that annealing at 750 °C

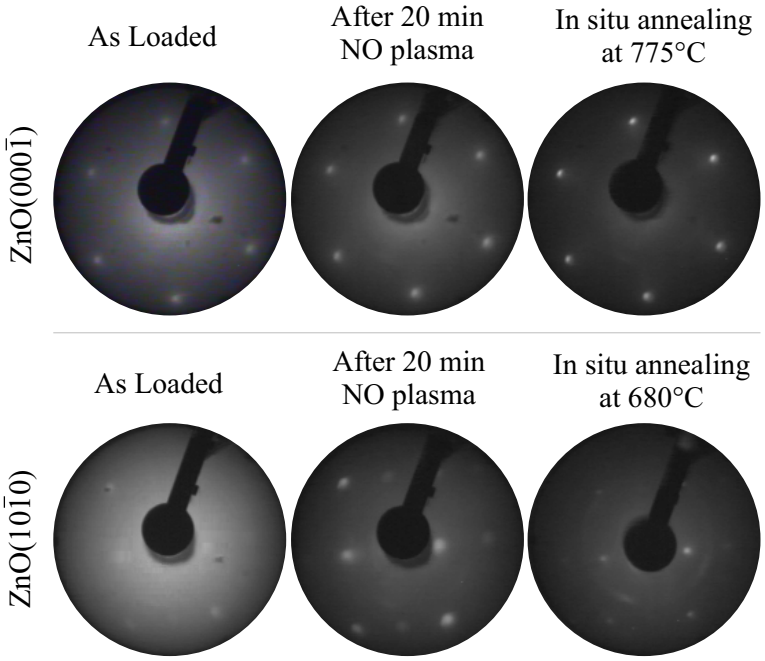

Figure 9.18.: LEED patterns for O-polar and m-plane ZnO recorded at 49 meV and 69 meV respectively.

is not sufficient to completely remove H/OH from the surface with approximately 0.5 ML coverage remaining. This is especially true in the real-time XPS UHV chamber employed here which has a higher background partial pressures of residual H and H_2O. Therefore, it is not surprising that no reconstructions are observed. A clear (1×1) pattern is also observed for both non-polar planes as illustrated for the m-plane face in Fig. 9.18, similar to earlier literature reports [32].

9.3 Real-time Argon Sputtering Experiments

Hydroxyl- and hydrogen-free ZnO surfaces are commonly prepared by repeated cycles of Ar^+ sputtering and UHV annealing [40, 258, 259]. In this section, the H/OH concentration and surface band bending is monitored both during and after Ar^+ sputtering. The XPS experiments were carried out using an Al K_α Kratos XPS spectrometer at the University of Auckland. Low-resistivity, hydrothermally grown ZnO single crystals with low lithium concentration (Low-Li HT ZnO) were investigated to avoid sample charging effects. The analyser chamber had a nominal background pressure of 1.2×10^{-8} mbar and was back-filled with Ar gas for sputtering purposes to 1.3×10^{-7} mbar. A 5 kV Ar^+ beam rastered a 5×5 mm shallow crater which fully contained the x-ray spot (see inset in Fig. 9.19). Two Ar^+ sputter cycles were carried out and the OH concentration was subsequently estimated from the higher BE shoulder of the O 1*s* core level. The

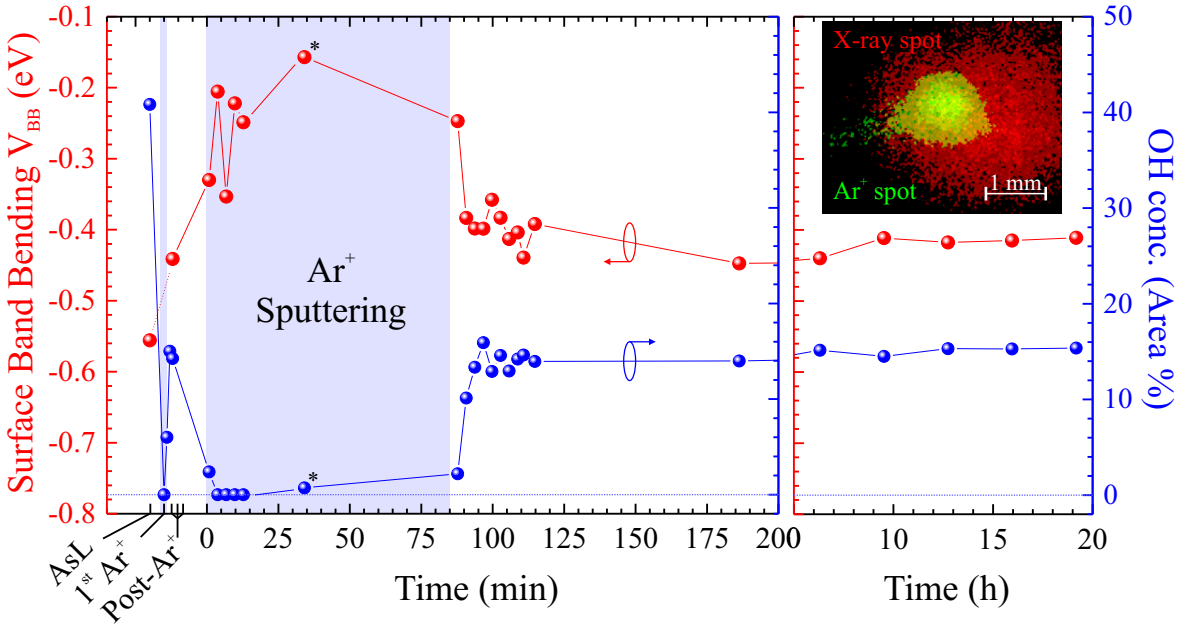

Figure 9.19.: Surface band bending V_{BB} (red) and hydroxyl concentration (blue) before, during (shaded area) and after Ar^+ sputtering on Low-Li O-polar HT ZnO. For comparison, the spot size of impinging Ar^+ atoms (green) and x-ray spot (red) is shown in (b).

surface band bending V_{BB} was estimated from the leading edge of the valence band spectra as explained previously.

A scan of the as-loaded O-polar Low-Li HT ZnO sample (*AsL* in Fig. 9.19) showed a hydroxyl concentration of $\sim$ 41 % (blue scale) and a corresponding V_{BB} of -0.56 eV (red scale) consistent with the expected downward band bending. During an initial 60 s Ar^+ sputtering cycle (*1st Ar+*), the OH shoulder on the O 1*s* core level completely vanished. After the Ar^+ ion gun was turned off, three consecutive O 1*s* core level scans were recorded, each with a duration of 60 s (*Post-Ar+*). After two minutes, the O-polar surface reached a steady OH concentration of $\sim$ 15 % and a $V_{BB} = -0.44$ eV. These initial experiments show that both the removal of OH groups during Ar^+ sputtering and the re-hydroxylation from residual hydrogen containing species in the chamber takes place on a time scale of a few seconds. The amount of re-hydroxylation is likely to be determined by the hydrogen/water partial pressure in the chamber.

A second sputtering cycle resulted in a similar outcome with OH removal on a time scale smaller than an individual scan duration of 90 s. Immediately, prior to the second sputtering cycle a OH concentration of $\sim$ 14 % and surface band bending V_{BB} of -0.44 eV was measured. The first scan, immediately after the Ar^+ ion gun was turned on, yielded an OH concentration of $\sim$ 3 % and an increase in V_{BB} to -0.33 eV. The apparent oscillations of the subsequent values in Fig. 9.19 originates from the

high measurement noise due to fast scanning. Data points marked with an asterisk indicate 30 min scans with the lowest measurement error yielding an OH concentration of $\sim 0.7\,\%$ and $V_{\mathrm{BB}} = -0.16\,\mathrm{eV}$ during the second Ar^+ sputtering cycle. After the ion gun was turned off, the OH concentration and surface band bending returned to their pre-sputtering values in a matter of minutes and stayed constant at an OH concentration of $\sim 15\,\%$ and $V_{\mathrm{BB}} \approx -0.41\,\mathrm{eV}$.

In addition to the removal of OH/H from ZnO surfaces by annealing as demonstrated earlier, OH/H removal can also be accomplished by Ar^+ sputtering and shows similar trends with respect to surface band bending. The extracted OH concentration and surface band bending V_{BB} cannot be directly compared to those presented in previous sections due to different surface sensitivity as a result of the different photon energies used, i.e. VB scans taken at $h\vartheta = 1486.7\,\mathrm{eV}$ here and $h\vartheta = 150\,\mathrm{eV}$ at the Australian Synchrotron. The surface band bending could be changed by approximately $+0.4\,\mathrm{eV}$ on the O-polar face during sputtering as measured using less surface-sensitive 1486.7 eV photons. However, the results from all the different XPS techniques show that the overall correlation between OH concentration and surface band bending on the O-polar face is remarkable.

9.4 Summary

Conventional and real-time XPS measurements, using both synchrotron and laboratory sources, were carried out on as-received ZnO bulk crystal surfaces of different polarity and on ZnO crystal surfaces cleaved *in situ* under UHV conditions. A strong correlation between the surface band bending V_{BB}, extracted from the valence band spectra, and the OH/H surface concentration, obtained from the O $1s$ core level spectra, was established for the O-polar and non-polar faces. The surface band bending on ZnO surfaces is strongly influenced by the concentration of terminating species, the loss of which can lead to a transition from electron accumulation to electron depletion. The key findings can be summarised as follows:

- The stability of the terminating hydroxyl coverage depends on the surface polarity. Both Zn-polar and O-polar faces show a higher thermal stability of their hydroxyl termination compared to the non-polar and semi-polar faces.

- A strong correlation between surface OH/H monolayer coverage and surface band bending was found for the O-polar, r-plane, a-plane and m-plane faces. The loss in surfaces OH/H resulted in a decrease in downward band bending and eventually a transition to upward band bending. The correlation between OH coverage and surface band bending is less obvious in the case of the Zn-polar face.

- The band bending on the O-polar face can be reversibly switched over a range of 0.8 eV between downward and upward band bending by modifying the surface hydrogen coverage via annealing in UHV, H_2O dosing and atmospheric exposure. The transition from downward to upward band bending was achieved after annealing at 350 °C and a corresponding hydrogen coverage of 0.9 ML.

- The Zn-polar face is characterised by a relative small decrease in downward band bending with *in situ* annealing, possibly due to the higher thermal stability of its hydroxyl termination compared to the O-polar face.

- The semi-polar (r-plane) and non-polar (m-plane and a-plane) faces of ZnO show a significant higher concentration of surface H, OH, and H_2O compared to the polar faces. The rate of thermal desorption of these species is also significantly higher resulting in monolayer coverages as low as 0.2 ML on the m-plane $(10\bar{1}0)$ after *in situ* annealing at 600 °C. The surface band bending V_{BB} on the semi-polar and non-polar faces increases monotonically with decreasing adsorbate coverage, similar to the behaviour observed for the O-polar face, eventually resulting in near-surface electron depletion.

- UHV cleaving of the polar surfaces of hydrothermal ZnO does not produce hydroxyl free surfaces. It is possible that hydrogen diffuses immediately from the bulk to the surface in order to electrostatically stabilise the cleaved Zn-polar and O-polar surfaces.

- Real-time XPS measurements indicate a threshold temperature of 280 °C for the O-polar face and 380 °C for the m-plane face, after which a dramatic increase in the rate of upward band bending with temperature occurs.

- Removal of surface adsorbates by Ar^+ sputtering affects the surface band bending in a similar manner to *in situ* annealing.

10 | Conclusions and Outlook

The most significant findings in this thesis relate to the important role played by hydrogen in the photoluminescence and surface band bending of ZnO, particularly in material grown using the hydrothermal technique. Hydrogen is unavoidably introduced into ZnO during its growth and is readily captured by a range of defects and impurities, forming a variety of hydrogen-related complexes with different thermal stabilities. Hydrogen also plays a significant role on the surface of ZnO, forming a persistent hydroxyl termination which appears to strongly influence the electronic properties of the surface. In this chapter, we summarise the main findings and propose models for the behaviour of hydrogen-related complexes in hydrothermal ZnO.

10.1 Hydrogen complexes in ZnO

Several new hydrogen-related emission lines in ZnO have been found via 3 K PL spectroscopy of hydrothermal (HT) and pressurised melt ZnO bulk-grown single crystals. The presence of these hydrogen-related emission lines depends strongly on the ZnO material type and the sample treatment. Table 10.1 summarises the ZnO material and the sample treatment for which the three main hydrogen-related PL emission lines I_4, $I_{4b,c}$, and I_{6-H} were observed. In interpreting these findings it is useful to keep in mind that a key difference between the ZnO single crystal materials in Table 10.1 is in the concentration of lithium (and other group I) impurities. That is, HT ZnO contains relatively high concentrations of Li (~ 2 ppm wt), Low-Li HT ZnO contains relatively low concentrations (< 0.01 ppm wt) while melt-grown ZnO contains only trace amounts of Li. Low-Li HT ZnO has also been post-annealed at high temperatures ($\sim 1400\,^{\circ}$C). Based on the observations in Table 10.1, the following models are proposed:

I_4 and $I_{4b,c}$ emission lines: Although many hydrogen-related defects in ZnO have been identified using IR absorption [75, 76, 78, 83, 85], only the I_4 emission line in the PL spectrum of ZnO, has been unequivocally assigned to hydrogen. However, the high-resolution PL spectroscopy carried out in this thesis has shown that I_4 (3.36272 eV) is

Table 10.1.: Presence (✓) and absence (✗) of the hydrogen-related PL emission lines I_4, $I_{4b,c}$, and I_{6-H} in the 3 K PL spectra of different ZnO bulk single crystal material and various sample treatments.

PL Line	ZnO Material	As-received	600 °C annealing			H/D-Implantation	Al Coverage
			O_2	N_2	FG		
I_4	HT	✗	✗	✗	✗	✓ ≤ 300 °C*	✗
	Low-Li HT	✗	✗	–	✗	✓ ≤ 300 °C*	–
	melt	✓	✗	–	✓	–	–
$I_{4b,c}$	HT	✓	✗	✓	✓	✓ 400–500 °C	✗
	Low-Li HT	✗	✗	–	✗	✗	–
	melt	✗	✗	–	✗	–	–
I_{6-H}	HT	✓	✗	✓	✓	–	✓✓
	Low-Li HT	✗	–	–	✓	✓ ≤ 400 °C*	–
	melt	✗	✗	–	✗	–	–

*The exact annealing temperature for which the PL line can still be observed depends on the implantation dose.

not present in hydrothermally grown ZnO. Instead, two closely lying hydrogen-related emission lines, I_{4b} (3.36237 eV) and I_{4c} (3.36219 eV) are consistently observed in HT ZnO. These lines are only observed in HT ZnO, in contrast to most other forms of ZnO in which I_4 is the only known hydrogen-related emission line. The corresponding ionised donor (D^+X), B-exciton and TES replicas of $I_{4b,c}$ were also clearly observed in HT ZnO. From its TES transition, a donor binding energy of 49.1 meV for $I_{4b,c}$ was extracted compared to the value of 46.1 meV reported for I_4 [17]. Due to the higher localisation energy and higher binding energy of $I_{4b,c}$, compared to I_4, the observation of the ionised donor-bound replica of $I_{4b,c}$ does not contradict Meyer *et al.* [17, 18] who proposed that it was not possible for excitons to bind to the ionised donor of I_4.

Hydrothermally grown ZnO contains significant amounts of group I elements, in particular Li which readily forms complexes with hydrogen in ZnO. As this high Li content is the outstanding difference between HT ZnO and other forms of ZnO, it is reasonable to assume that Li is involved in $I_{4b,c}$ and other hydrogen-related emission lines, such as I_{6-H}, that are unique to HT ZnO.

In other forms of ZnO, I_4 is commonly assigned to hydrogen trapped in an oxygen vacancy (H_O) (see Fig. 10.1(a)). In HT ZnO, $I_{4b,c}$ may also be related to hydrogen occupying an oxygen vacancy. However, instead of being coordinated to four neighbouring Zn atoms, it is proposed that the oxygen vacancy associated with $I_{4b,c}$ is only

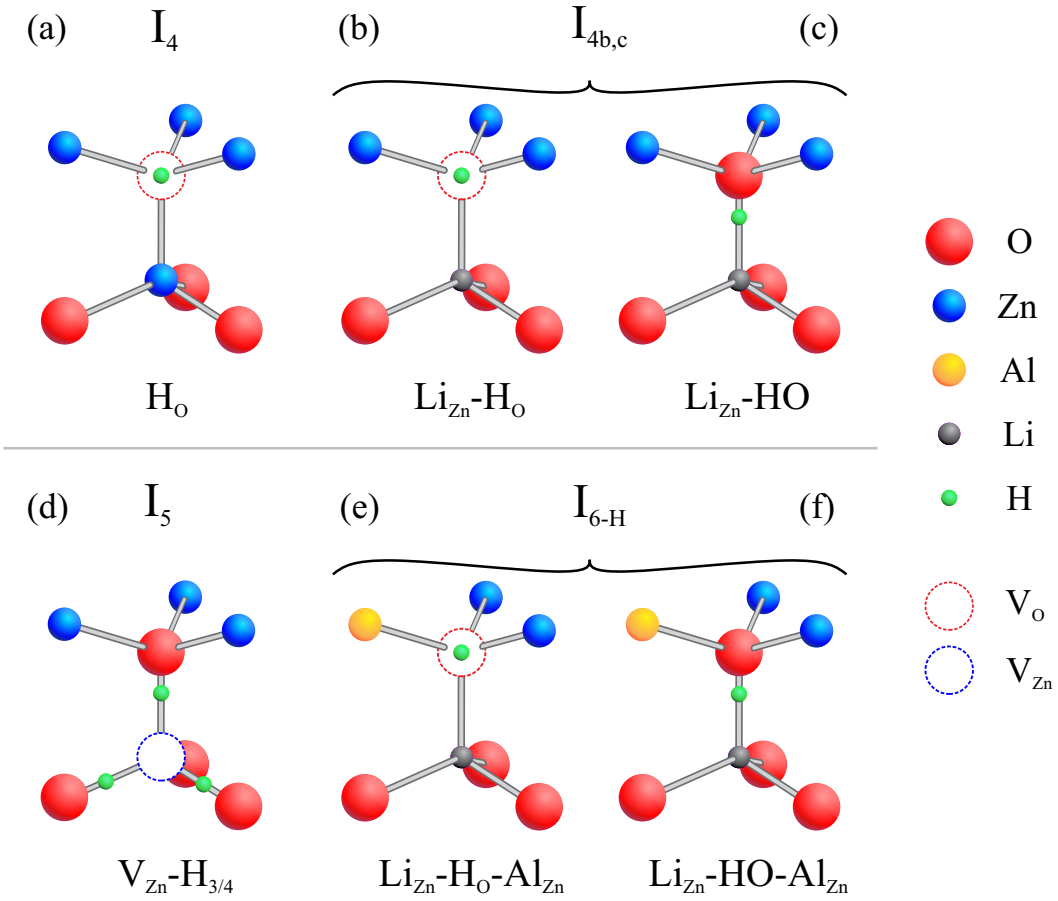

Figure 10.1.: Different hydrogen-related complexes in ZnO and their assigned PL emission line.

coordinated to three neighbouring Zn atoms (probably in the same doublelayer) with the fourth bond involving a substitutional Li_{Zn} atom (probably along the c-axis) as shown in Fig. 10.1(b). This model would explain the close proximity of I_4 and $I_{4b,c}$ in the PL spectra. Furthermore, DFT calculations [260] have suggested that the formation of V_O in the vicinity of Li_{Zn} is energetically favourable in ZnO containing high amounts of Li. An alternative configuration for $I_{4b,c}$ could be hydrogen in a bond-centred position between the Li_{Zn}-O bond, also along the c-axis forming Li_{Zn}-OH (Fig. 10.1(c)). The latter configuration has the lowest formation energy for any Li-OH complex from DFT calculations [86] and is exclusively observed in HT ZnO as a 3577.3 cm^{-1} line in IR absorption measurements [83]. However, this IR line has been shown to exhibit a remarkably high thermal stability of up to 1200 °C for several hours [209]. This is significantly different from the behaviour of the $I_{4b,c}$ emission line which quenches after annealing in oxygen or nitrogen at 600 °C. Therefore, the Li_{Zn}-H_O model is preferred for $I_{4b,c}$. This model would also explain the observed behaviour of $I_{4b,c}$ on annealing: Annealing in nitrogen simply dissociates H_O and the highly mobile hydrogen out-diffuses;

annealing in oxygen would re-occupy V_O while also displacing H_O; while $I_{4b,c}$ reappears after annealing in forming gas (either N_2-H_2 or Ar-H_2) due to the reintroduction of hydrogen and the formation of new oxygen vacancies.

Remarkably, when HT ZnO and Low-Li HT ZnO were implanted with hydrogen or deuterium, I_4 and not $I_{4b,c}$ was introduced and was stable for annealing in oxygen up to 300 °C. This can be explained as follows: The implantation process introduces oxygen vacancies that can trap hydrogen and also removes Li_{Zn} by collision displacement. Consequently, the majority of the implanted hydrogen will be trapped at "normal" oxygen vacancies (which are not coordinated to any neighbouring substitutional Li_{Zn} atoms), leading to the observation of I_4. After oxygen annealing, the majority of the oxygen vacancies, introduced by implantation, are refilled. At the same time Li re-occupies vacant Zn lattice sites, creating Li_{Zn} species. Both these processes will tend to quench I_4. In implanted HT ZnO, the quenching of I_4 is therefore determined by the rate with which O and Li re-occupy vacant lattice positions, rather than the simple out-diffusion of hydrogen and this may explain the lower thermal stability of I_4 in implanted HT ZnO and Low-Li HT ZnO compared to melt-grown and other types of ZnO. Assuming that the formation of V_O in the vicinity of Li_{Zn} is energetically favourable in materials containing high concentrations of Li, residual hydrogen is now more likely to be trapped by oxygen vacancies in the vicinity of Li_{Zn}. Consequently, the Li_{Zn}-H_O complex is formed, giving rise to $I_{4b,c}$ until hydrogen eventually out-diffuses from this complex at 600 °C. In H/D-implanted Low-Li HT ZnO, $I_{4b,c}$ was not observed after the quenching of I_4 as significantly lower concentrations Li_{Zn} are present in this material.

I_{6-H} in Al-covered HT ZnO: When conventional HT ZnO is covered with a thin Al overlayer, $I_{4b,c}$ is completely quenched without the need for any heat treatment while at the same time the I_{6-H} emission line is greatly enhanced on both polar faces particularly after post-deposition annealing at 600 °C. The following model is proposed: The thermally deposited Al atoms have insufficient energy to directly displace substitutional Li_{Zn}, but they are able to occupy V_{Zn} sites close to Li_{Zn}. It was shown in Ref. [260] that Li_{Zn}-V_{Zn} complexes have similar formation energies compared to Li_{Zn}-V_O complexes and are, therefore, also likely to be present. With Al_{Zn} in the vicinity of Li_{Zn}, the Li_{Zn}-H_O complex becomes a Li_{Zn}-H_O-Al_{Zn} complex (Fig. 10.1(e)) (or alternatively Li_{Zn}-HO becomes a Li_{Zn}-HO-Al_{Zn} complex (Fig. 10.1(f))). These are then responsible for the observed I_{6-H} emission line. This would explain the simultaneous decrease in $I_{4b,c}$ emission and increase in I_{6-H} intensity in Al-covered HT ZnO samples.

Lithium, Aluminium and the I_{6-H} line: For conventional HT ZnO crystals a new hydrogen-related recombination line I_{6-H} (3.36081 eV) was observed in this work. This line is not observed in non-hydrothermal forms of ZnO such as melt and vapour-phase wafers suggesting the involvement of Li. The involvement of aluminium in I_{6-H} is also highly likely due to the close proximity of I_{6-H} to the well-known Al-related I_6 emission line and also from its enhancement on Al-covered HT ZnO samples, as mentioned above. Remarkably, I_{6-H} completely quenches after annealing in oxygen gas at 600 °C but is not affected by annealing in nitrogen gas under identical conditions, strongly suggesting the involvement of oxygen vacancies. Furthermore, I_{6-H} was subsequently re-introduced after annealing in forming gas mixtures (such as N_2-H_2 and Ar-H_2, both 95 %/5 %). Significantly, annealing Low-Li HT ZnO in forming gas produced a low intensity I_{6-H} line that was not present beforehand. Furthermore, I_{6-H} could not be introduced in melt-grown ZnO via forming gas annealing (or via any other method). Together, these observations lead to the conclusion that I_{6-H} originates from a defect complex involving aluminium, lithium, hydrogen, and oxygen vacancies. Models for possible versions of this defect complex are shown in Fig. 10.1(e – f) with model (e), the Li_{Zn}-H_O-Al_{Zn} complex, being the most likely candidate. A donor binding energy of 51.6 meV was determined for I_{6-H} from the energetic position of its TES emission. This is close to the 48 meV value for a similar $Al_{Zn} + Li_{Zn}$-H related defect complex proposed by Look [208].

I_{6-H} was also introduced in Low-Li HT ZnO following hydrogen and deuterium implantation and was stable for annealing temperatures up to 300 – 400 °C. The fact that I_{6-H} can be introduced into Low-Li HT ZnO by either hydrogen implantation or forming gas annealing suggests that hydrogen diffusion limits the the formation of I_{6-H}. The thermal stability of I_{6-H} in conventional HT ZnO was observed to increase after hydrogen (and deuterium) implantation with I_{6-H} still observed after annealing at 600 °C. During the implantation process, various structural defects are introduced into the ZnO crystal. These are likely to limit the out-diffusion of hydrogen, which in turn may lead to a higher thermal stability for I_{6-H}. Secondly, oxygen vacancies will be created by the implantation process which can be occupied by the implanted hydrogen, leading to the formation of higher concentrations of the Li_{Zn}-H_O-Al_{Zn} complex responsible for I_{6-H}.

Interestingly, I_{6-H} was not observed after Al implantation and subsequent annealing at 600 °C. Implanted Al atoms are known to displace Li_{Zn} and form a Li-lean region [228] as both species compete for the zinc lattice site. This phenomena was also reported for a range of other implanted elements that all seem to compete for the zinc lattice site [261]. The displacement of Li by Al inhibits the formation of the I_{6-H} defect complex and consequently only the Al-related I_6 emission line is observed.

Li_{Zn}-H_O versus Li_{Zn}-HO: The question of the exact hydrogen configuration responsible for $I_{4b,c}$ and I_{6-H} is of course debatable in the absence of any direct evidence. The close proximity between I_4 and $I_{4b,c}$ does suggest a similar bonding configuration, such as hydrogen occupying an oxygen vacancy via the formation of hydrogen multicentred bonds, as shown in Fig. 10.1(a–b). This assignment would also explain the similar temperature stability observed for I_4 and $I_{4b,c}$. Similarly, the close proximity of I_{6-H} to the well-known Al-related I_6 emission line indicates that I_{6-H} is likely to be due to a Li_{Zn}-H_O-Al_{Zn} complex (Fig. 10.1(e)). This would explain why I_{6-H} quenches after annealing in an oxygen atmosphere but not in nitrogen gas. The Li_{Zn}-HO complex (Fig. 10.1(c)) should form a neutral defect with no shallow donor level in the bandgap and consequently no D^0X transition would be expected. Instead it is likely to provide an appropriate model for the reported 3577 cm^{-1} hydrogen-related IR line, that is characterised by an unusually high thermal stability up to several hours at 1200 °C. However, the high thermal stability of the bond-centred Li_{Zn}-HO complex compared to H_{BC} (hydrogen bond-centred between lattice zinc and oxygen), which is only stable up to 190 °C, appears somewhat strange and may indicate the involvement of additional defects. Johansen *et al.* [262] observed that inversion domains can act as strong trapping sites for migrating H and Li. Structural defects, such as inversion domains, could potentially trap dissociated Li and H even at high temperatures and provide another possible explanation for the unexpected high thermal stability of a Li_{Zn}-HO complex.

I_5 and V_{Zn}-$H_{3/4}$: After hydrogen and deuterium implantation, a new PL emission line at the energetic position of I_5 was observed in Low-Li HT ZnO after annealing in oxygen between 300 – 500 °C. The intensity dependence of I_5 with annealing temperature was identical to that reported for the hydrogen-related 3326.3 cm^{-1} line in IR absorption experiments [77, 216, 219]. In these reports, the IR line was present in vapour-phase- and melt-grown ZnO after annealing in hydrogen. These materials are known to contain only trace amounts of Li and as such it is unlikely that Li is involved in I_5. The 3326.3 cm^{-1} IR line was assigned to a $V_{Zn} - H$ complex which forms after dissociation of molecular hydrogen in ZnO at elevated temperatures. However, $V_{Zn} - H$ is a deep acceptor and only $V_{Zn} - H_3$ or $V_{Zn} - H_4$ (which will be refered to as $V_{Zn} - H_{3/4}$) are thought to form shallow donors [263] which ultimately can be observed in near-bandedge PL. Therefore, I_5 is assigned to the $V_{Zn} - H_{3/4}$ complex. Johansen *et al.* [264] showed that Li_{Zn} acts as the primary trapping site for hydrogen in conventional HT ZnO as the trapping efficiency of V_{Zn} is significantly lower in comparison. This explains our exclusive observation of I_5 in the Low-Li HT ZnO material where much less competing Li_{Zn} is available to capture hydrogen. In addition, V_{Zn} has to capture up to four hydrogen atoms to form one observable recombination centre whereas Li_{Zn} would only need one.

10.2 Surface and polarity effects in ZnO photoluminescence

Consistent differences in the PL spectra of the polar, non-polar and semi-polar faces of hydrothermally grown ZnO were observed in this work. The O-polar $(000\bar{1})$, and a-plane $(11\bar{2}0)$ and r-plane $(1\bar{1}02)$ faces consistently showed a broad Gaussian-shaped feature between 3.367 eV and 3.364 eV that was not present on the Zn-polar (0001) and m-plane $(10\bar{1}0)$ faces. The same difference between the two polar faces of ZnO was also observed in melt-grown ZnO and Low-Li HT ZnO. Similar broad emission features have been widely reported for ZnO nanostructures and were assigned to surface-related donor-bound excitons [167].

Annealing bulk ZnO crystals in oxygen or nitrogen gas at 600 °C significantly reduces the background PL intensity in the spectral region between 3.374 – 3.362 eV, that is dominated by the Gaussian-shaped feature. However, the Gaussian-shaped feature could be re-established on all faces by subsequent annealing at 600 °C in forming gas (either N_2-H_2 or Ar-H_2), even on the Zn-polar face where it was not initially present. Forming gas annealing re-introduces hydrogen into the near-surface region and also tends to cause significant etch damage to the surface. However, declining surface quality is not likely to be the cause of the re-introduction of the Gaussian-shaped feature as further annealing cycles in oxygen and forming gas on the same wafer were able to repeatedly quench and re-introduce the feature with no significant recovery in the morphology of the surface. In addition, the influence of varying surface hydroxyl coverage can be discounted since all samples were exposed to atmospheric conditions following annealing and this is known to immediately re-hydroxylate ZnO surfaces as shown in chapter 9.

Deposition of 10 – 15 nm thick Ti, Au, Al, and IrO_x overlayers onto conventional HT ZnO significantly reduces the PL background intensity in the spectral region between 3.372 eV and 3.363 eV, including the broad Gaussian-shaped feature. This re-inforces a likely surface or near-surface origin for the Gaussian-shaped feature. In contrast, the dominant D^0X emission lines, including the hydrogen-related $I_{4b,c}$ line, were unaffected by these overlayers, with exception of Al layers for which I_{6-H} was significantly enhanced. Surface band bending can also be excluded as the origin of the Gaussian-shaped feature, as both as-received polar surfaces are characterised by strong downward band bending. Furthermore, the deposition of thin overlayers of ohmic (e.g. Ti, Al) and Schottky (e.g. Au, IrO_x) metals, which are known to introduce downward and upward band bending respectively, both caused a reduction in the Gaussian-shaped feature.

In summary, the broad Gaussian-shaped feature has been conclusively linked to hydrogen in the near-surface region. However, it is unlikely to be directly associated

with the ever-present surface hydroxyl coverage or the associated surface downward band bending. This leaves hydrogen-related defects in the near-surface region as the most likely cause.

10.3 Hydroxyl termination and band bending at ZnO surfaces

Hydroxyls and band bending on polar ZnO surfaces: Hydrogen also plays a dominant role in the termination and electronic properties of the ZnO surface. The polar surfaces of ZnO are characterised by a persistent termination of hydroxyl groups (formed by H adsorbed on the O-polar face and OH groups adsorbed on the Zn-polar face) under most laboratory conditions. The thermal stability of these terminating hydroxyl groups and the associated downward band bending is significantly different for the two polar faces. The band bending on the O-polar face could be reversibly switched over a range of 0.8 eV by adjusting the H coverage using simple UHV heat treatments, dosing with H_2O or H_2, and atmospheric exposure. The downward band bending could be steadily reduced by decreasing the surface hydrogen coverage, with a transition from downward to upward band bending occurring at H-coverages of approximately 0.9 ML. Depleted O-polar surfaces with H coverages approaching the 0.5 ML level predicted by first-principles calculations [38, 265] could be prepared via a simple UHV heat treatment at 750 °C. Real-time XPS measurements indicated a threshold temperature at $\sim$ 280 °C after which there was a dramatic increase in the rate of upward band bending with temperature. In contrast, the hydroxyl groups on the Zn-polar face showed a substantially higher thermal stability and depleted Zn-polar surfaces could not be created by UHV heat treatment alone.

The Zn-polar and O-polar faces of UHV-cleaved HT ZnO single crystals showed a residual hydroxyl termination of approximately 0.5 ML immediately after cleaving, even though these cleaved faces were maintained in UHV conditions ($\sim 5\times10^{-10}$ mbar) . The O-polar face showed almost flat bands while the Zn-polar face still showed significant downward band bending after cleaving. It is likely that H/OH diffuses from the bulk to the surface of the crystal immediately after cleaving in order to electrostatically stabilise both polar surfaces.

Hydroxyls and band bending on non-polar ZnO surfaces: The surface band bending on the non-polar faces of ZnO was also found to be directly related to the OH coverage on their surfaces, with a transition from downward to upward band bending (i.e. electron accumulation to electron depletion) observed for sufficiently low OH coverages. Although the OH coverage of as-loaded, non-polar surfaces was consistently larger than for the Zn-polar and O-polar surfaces, the thermal desorption rate of their

OH coverage was also considerably larger, indicating a lower thermal stability. For the non-polar faces, this high desorption rate is likely due to neighbouring H and OH species directly recombining and desorbing as H_2O molecules. Furthermore, non-polar ZnO surfaces are free of bound spontaneous polarisation charges and are electrostatically stable in their unreconstructed bulk-terminated form and as such polar adsorbates are not required to play a surface stabilisation role as they do on the polar surfaces of ZnO.

10.4 Electrical properties of Low-Li HT ZnO

The removal of lithium and other group I impurities from HT ZnO results in less-compensated, lower-resistivity material with carrier concentrations typically 3 – 4 orders of magnitude higher than for conventional HT ZnO. This results in a significant decrease in the series resistance of high quality Schottky contacts on Low-Li HT ZnO, making them suitable for high resolution capacitance-based defect spectroscopy. TAS and DLTS measurements revealed six different trap levels in Low-Li HT ZnO, i.e. E4/E_{560}, E3/E_{305}, T2/E_{190}, E_{160}, E_{115}, and E_{70}. Unlike conventional HT ZnO, the E_{50} defect level was absent from Low-Li HT ZnO. Significantly, E_{50} and the hydrogen-related I_{6-H} PL line are only observed in ZnO wafers containing high concentrations of Li. Therefore, E_{50} can be tentatively assigned to the same Li_{Zn}-H_O-Al_{Zn} complex as I_{6-H}. In the high-temperature annealing and re-grinding process involved in the production of Low-Li HT ZnO, the Li_{Zn}-H_O-Al_{Zn} complex dissociates and both H and Li are subsequently removed from the crystal, explaining the absence of E_{50} and I_{6-H} in Low-Li HT ZnO.

10.5 Outlook

A multitude of new excitonic recombination lines in the photoluminescence of ZnO are described in this thesis. However, making valid conclusions about the chemical origin of these new features using PL alone is far from straight-forward. Future work is needed to further identify excited state transitions and possible acceptor-related transitions. The use of ion implantation has been very helpful in identifying the origin of certain features and may be usefully extended to other impurities.

Several new hydrogen-related PL lines were reported in this work especially in hydrothermal ZnO. However, the simultaneous use of IR absorption and Raman spectroscopy alongside high-resolution PL measurements, especially after hydrogen anneal-

ing and hydrogen / deuterium implantation in different types and polarities of HT ZnO, would be a useful next step in confirming their precise origin. In this work, a Li_{Zn}-H_O-Al_{Zn} complex has been proposed as the origin of the new I_{6-H} emission line. Surprisingly, no matching IR line has been conclusively identified in the literature.

Deposition of ohmic and Schottky contact metal / metal oxide overlayers produced significant changes in the PL emission of ZnO. In the case of Schottky contacts, the width of the depletion region provides a useful variable in controlling the PL probing depth. PL measurements through differently biased Schottky contacts could be a useful tool for investigating the depth profile of optically active donors and structural-related defects.

The thermal stability of the hydroxyl termination on the Zn-polar face of ZnO is significantly larger than for all other crystallographic faces. Consequently, simple UHV heat treatments are not sufficient to produce depleted ZnO surfaces. Extensive Ar^+ sputtering and annealing cycles in UHV environments have been used to produce clean, hydroxyl-free Zn-polar surfaces. However, the extent to which this produces extra electrically active defects has yet to be determined.

A | Appendix

Table A.1.: Exciton line positions in ZnO observed in this thesis.

Line	λ (nm)	E (eV)	E_{loc} (meV)	TES spacing $1s$-$2p$ (meV)	E_{D} (meV)	Identity
A_{L}	367.109	3.37731	–	–	–	–
A_{T}	367.317	3.37540	–	–	–	–
$I^{+}_{\mathrm{4b,c}}$	367.478	3.37392	1.48	–	–	$\mathrm{Li_{Zn}}$-$\mathrm{H_O}$
I^{+}_{5}	367.499	3.37373	1.67	–	–	$\mathrm{V_{Zn}}$-$\mathrm{H_n}$
$I^{+}_{\mathrm{6-H}}$	367.594	3.37286	2.54	–	–	$\mathrm{Li_{Zn}}$-$\mathrm{H_O}$-$\mathrm{Al_{Zn}}$
I^{+}_{6}	367.622	3.37260	2.80	–	–	Al
I^{+}_{6a}	367.655	3.37230	3.10	–	–	–
I^{+}_{7}	367.669	3.37217	3.23	–	–	–
I^{+}_{8}	367.699	3.37189	3.51	–	–	Ga
$I^{+}_{\mathrm{8-Ga}}$	367.742	3.37150	4.04	–	–	Ga
I^{+}_{9}	368.043	3.36874	7.02	–	–	In
$I^{\mathrm{B}}_{\mathrm{4b,c}}$	368.285	3.36653	8.87	–	–	H
$I^{\mathrm{B}}_{\mathrm{5a}}$	368.336	3.36606	9.34	–	–	–
I^{B}_{6}	368.457	3.36496	10.44	–	–	Al
I^{B}_{8}	368.523	3.36435	11.05	–	–	Ga
I_{c}	368.677	3.36295	11.85	–	–	–
I_{b}	368.647	3.36322	12.18	–	–	–

Continued on next page

Table A.1 – continued from previous page

Line	λ (nm)	E (eV)	E_{loc} (meV)	TES spacing $1s$-$2p$ (meV)	E_{D} (meV)	Identity
I_{a}	368.611	3.36355	12.45	–	–	–
I_4	368.702	3.36272	12.68	33.2	47.2	$\mathrm{H_O}$
$I_{4\mathrm{c}}$	368.740	3.36237	13.03	–	–	$\mathrm{Li_{Zn}}$-$\mathrm{H_O}$
$I_{4\mathrm{b}}$	368.760	3.36219	13.21	35.1	49.1	$\mathrm{Li_{Zn}}$-$\mathrm{H_O}$
$I_{4\mathrm{a}}$	368.797	3.36185	13.25	–	–	–
I_{5a}	368.815	3.36169	13.54	–	–	–
I_5	368.844	3.36143	13.99	–	–	$\mathrm{V_{Zn}}$-$\mathrm{H_n}$
$I_{6-\mathrm{H}}$	368.912	3.36081	14.59	36.9	51.6	$\mathrm{Li_{Zn}}$-$\mathrm{H_O}$-$\mathrm{Al_{Zn}}$
I_6	368.940	3.36055	14.85	38.8	52.8	Al
$I_{6\mathrm{a}}$	368.956	3.36041	14.99	–	–	–
I_7	369.001	3.36000	15.40	–	–	–
I_8	369.018	3.35984	15.56	41.0	55.0	Ga
$I_{8-\mathrm{Ga}}$	369.043	3.35961	15.92	41.4	55.4	Ga
$I_{8\mathrm{a}}$	369.083	3.35925	16.15	–	–	–
I_9	369.378	3.35657	18.83	50.7	64.9	In
$I_{10\mathrm{a}}$	369.643	3.35416	21.24	–	–	–
I_{10}	369.768	3.35303	22.37	59.5	73.5	–
$\mathrm{Y_2}$	370.519	3.34623	29.17	–	–	–
$\mathrm{Y_1}$	371.607	3.33643	38.97	–	–	–
$\mathrm{Y_0}$	372.005	3.33286	42.54	63.6	–	–

Table A.2.: Sample list with following abbreviations: TD for Tokyo Denpa and Mitsu. for Mitsubishi, S-XPS for synchrotron- and L-XPS for laboratory-based XPS and RT-XPS for real-time XPS.

Wafer			Type		Technique	Treatment
TD	CGZ-0935	#7	HT	+c	PL	As-Received
TD	CGZ-0907	#6	HT	+c	PL	As-Received
TD	CGZ-0936	#8	HT	−c	PL	As-Received
TD	CGZ-0756	#3	HT	m	PL	As-Received
TD	CGZ-1211	#9	HT	a	PL	As-Received
TD	CGZ-1212	#8	HT	r	PL	As-Received
TD	CGZ-0937	#7	Low-Li	+c	PL	AsR & FG ann.
Cermet	1481-02CVA		Melt	–	PL	AsR & O_2 ann.
Cermet	1501-03AVA		Melt	–	PL	As-Received
Mitsu.	3233-73-8-3		Low-Li	+c	PL	no offcut
Mitsu.	3232-47-8-2		Low-Li	+c	PL	0.5° offcut
TD	CGZ-1208	#6	HT	+c	PL	Temp.-Dep.
TD	CGZ-1208	#6	HT	+c	PL	O_2 & N_2 ann.
TD	CGZ-1208	#9	HT	+c	PL	O_2 & FG/ArH ann.
TD	CGZ-0907	#6	HT	+c	PL	H, D Implantation
TD	CGZ-1210	#8	Low-Li	+c	PL	H, D Implantation
TD	CGZ-0907	#5	HT	+c	PL	Ga Implantation
TD	CGZ-1210	#3	Low-Li	+c	PL	Ga Implantation
TD	CGZ-0907	#7	HT	+c	PL	Al Implantation
TD	CGZ-0907	#4	HT	+c	PL	Pt Implantation
TD	CGZ-1208	#8	HT	+c	PL	Ti Coating
TD	CGZ-1208	#8	HT	+c	PL	Au Coating
TD	CGZ-1208	#5	HT	+c	PL	IrO_x Coating

Continued on next page

Table A.2 – continued from previous page

	Wafer		Type		Technique	Treatment
TD	CGZ-0907	# 9	HT	+c	PL	Al Coating
TD	CGZ-1209	# 7	HT	−c	S-XPS	Anneal.+Dos.
TD	CGZ-0755	–	HT	m	S-XPS	Cleaving
TD	CGZ-0756	# 7	HT	m	S-XPS	Annealing
TD	CGZ-1211	# 1	HT	a	S-XPS	Annealing
TD	CGZ-1212	# 4	HT	r	S-XPS	Annealing
TD	CGZ-1209	# 6	HT	−c	RT-XPS	Annealing
TD	CGZ-0756	# 10	HT	m	RT-XPS	Annealing
TD	CGZ-1211	# 2	HT	a	RT-XPS	Annealing
TD	CGZ-1210	# 1	Low-Li	+c	L-XPS	Ar^+ Sputtering

Bibliography

[1] P. Whittaker. *Iron and zinc interactions in humans.* The American Journal of Clinical Nutrition **68**, 442S (1998). eprint: http://ajcn.nutrition.org/content/68/2/442S.full.pdf+html.

[2] P. J. Nieuwenhuizen. *Zinc accelerator complexes: Versatile homogeneous catalysts in sulfur vulcanization.* Applied Catalysis A: General **207**, 55 (2001). DOI: 10.1016/S0926-860X(00)00613-X.

[3] J. F. Cordaro, C. E. Shipway, J. T. Schott. *Radiation hardness of zinc oxide varistors.* Journal of Applied Physics **61**, 429 (1987). DOI: 10.1063/1.338842.

[4] D. C. Look, D. C. Reynolds, J. W. Hemsky, R. L. Jones, J. R. Sizelove. *Production and annealing of electron irradiation damage in ZnO.* Applied Physics Letters **75**, 811 (1999). DOI: 10.1063/1.124521.

[5] J. Zhou, N. Xu, Z. Wang. *Dissolving Behavior and Stability of ZnO Wires in Biofluids: A Study on Biodegradability and Biocompatibility of ZnO Nanostructures.* Advanced Materials **18**, 2432 (2006). DOI: 10.1002/adma.200600200.

[6] A. J. Huh, Y. J. Kwon. *Nanoantibiotics: A new paradigm for treating infectious diseases using nanomaterials in the antibiotics resistant era.* Journal of Controlled Release **156**, 128 (2011). DOI: 10.1016/j.jconrel.2011.07.002.

[7] C. P. Dietrich, M. Lange, M. Stölzel, M. Grundmann. *Microwire (Mg,Zn)O/ZnO and (Mg,Zn)O/(Cd,Zn)O non-polar quantum well heterostructures for cavity applications.* Applied Physics Letters **100**, 031110 (2012). DOI: 10.1063/1.3678594.

[8] D. Ehrentraut, H. Sato, Y. Kagamitani, H. Sato, A. Yoshikawa, T. Fukuda. *Solvothermal growth of ZnO.* Prog. Cryst. Growth Charact. Mater. **52**, 280 (2006). DOI: 10.1016/j.pcrysgrow.2006.09.002.

[9] V. Avrutin, G. Cantwell, J. Zhang, J. Song, D. Silversmith, Morkoğ. *Bulk ZnO: Current status, challenges, and prospects.* Proc. IEEE **98**, 1339 (2010). DOI: 10.1109/JPROC.2010.2040363.

[10] Y. Yan, J. Li, S.-H. Wei, M. M. Al-Jassim. *Possible Approach to Overcome the Doping Asymmetry in Wideband Gap Semiconductors*. Phys. Rev. Lett. **98** (13 2007), 135506. DOI: 10.1103/PhysRevLett.98.135506.

[11] A. Janotti, C. G. Van de Walle. *Native point defects in ZnO*. Phys. Rev. B **76**, 165202 (2007). DOI: 10.1103/PhysRevB.76.165202.

[12] C. G. Van de Walle, J. Neugebauer. *Universal alignment of hydrogen levels in semiconductors, insulators and solutions*. Nature **423**, 626 (2003). DOI: 10.1038/nature01665.

[13] C. G. Van de Walle. *Hydrogen as a cause of doping in zinc oxide*. Phys. Rev. Lett. **85**, 1012 (2000). DOI: 10.1103/PhysRevLett.85.1012.

[14] A. Janotti, C. G. V. Walle. *Hydrogen multicentre bonds*. Nat. Mater. **6**, 44 (2007). DOI: 10.1038/nmat1795.

[15] D. C. Look, B. Claflin, H. E. Smith. *Origin of conductive surface layer in annealed ZnO*. Appl. Phys. Lett. **92**, 122108 (2008). DOI: 10.1063/1.2903505.

[16] F. Oba, M. Choi, A. Togo, I. Tanaka. *Point defects in ZnO: an approach from first principles*. Sci. Tech. Adv. Mat. **12**, 034302 (2011). DOI: 10.1088/1468-6996/12/3/034302.

[17] B. K. Meyer, H. Alves, D. M. Hofmann, W. Kriegseis, D. Forster, F. Bertram, J. Christen, A. Hoffmann, M. Straßburg, M. Dworzak, U. Haboeck, A. V. Rodina. *Bound exciton and donor - acceptor pair recombinations in ZnO*. phys. stat. sol. (b) **241**, 231 (2004). DOI: 10.1002/pssb.200301962.

[18] B. K. Meyer, J. Sann, S. Lautenschläger, M. R. Wagner, A. Hoffmann. *Ionized and neutral donor-bound excitons in ZnO*. Phys. Rev. B **76**, 184120 (2007). DOI: 10.1103/PhysRevB.76.184120.

[19] R. J. Mendelsberg, M. W. Allen, S. M. Durbin, R. J. Reeves. *Photoluminescence and the exciton-phonon coupling in hydrothermally grown ZnO*. Phys. Rev. B **83**, 205202 (2011). DOI: 10.1103/PhysRevB.83.205202.

[20] H. Wenckstern, H. Schmidt, M. Grundmann, M. W. Allen, P. Miller, R. J. Reeves, S. M. Durbin. *Defects in hydrothermally grown bulk ZnO*. Appl. Phys. Lett. **91**, 022913 (2007). DOI: 10.1063/1.2757097.

[21] F. D. Auret, W. E. Meyer, P. J. J. Rensburg, M. Hayes, J. M. Nel, H. Wenckstern, H. Hochmuth, G. Biehne, M. Lorenz, M. Grundmann. *Electronic properties of shallow level defects in ZnO grown by pulsed laser deposition*. J. Phys.: Conf. Ser **100**, 042038 (2008). DOI: 10.1088/1742-6596/100/4/042038.

[22] M. W. Allen, P. Miller, R. J. Reeves, S. M. Durbin. *Influence of spontaneous polarization on the electrical and optical properties of bulk, single crystal ZnO.* Appl. Phys. Lett. **90**, 062104 (2007). DOI: 10.1063/1.2450642.

[23] R. Heinhold, G. T. Williams, S. P. Cooil, D. A. Evans, M. W. Allen. *Influence of polarity and hydroxyl termination on the band bending at ZnO surfaces.* Phys. Rev. B **88**, 235315 (2013). DOI: 10.1103/PhysRevB.88.235315.

[24] G. Heiland, P. Kunstmann. *Polar surfaces of ZnO.* Surf. Sci. **13**, 72 (1969). DOI: 10.1016/0039-6028(69)90237-4.

[25] E. Schlenker, A. Bakin, T. Weimann, P. Hinze, D. H. Weber, A. Gölzhäuser, H.-H. Wehmann, A. Waag. *On the difficulties in characterizing ZnO nanowires.* Nanotechnology **19**, 365707 (2008). DOI: 10.1088/0957-4484/19/36/365707.

[26] C. Wöll. *The chemistry and physics of zinc oxide surfaces.* Prog. Surf. Sci. **82**, 55 (2007). DOI: 10.1016/j.progsurf.2006.12.002.

[27] C. F. Klingshirn, B. K. Meyer, A. Waag, A. Hoffmann, J. Geurts. *Zinc oxide: From fundamental properties towards novel applications.* Springer Series in Materials Science 120, (2010). DOI: 10.1007/978-3-642-10577-7.

[28] C. R. A. Catlow, A. M. Stoneham. *Ionicity in solids.* J. Phys. C: Solid State Physics **16**, 4321 (1983). DOI: 10.1088/0022-3719/16/22/010.

[29] J. Goniakowski, F. Finocchi, C. Noguera. *Polarity of oxide surfaces and nanostructures.* Reports on Progress in Physics **71**, 016501 (2008). DOI: 10.1088/0034-4885/71/1/016501.

[30] P. W. Tasker. *The stability of ionic crystal surfaces.* Journal of Physics C: Solid State Physics **12**, 4977 (1979). DOI: 10.1088/0022-3719/12/22/036.

[31] A. Wander, F. Schedin, P. Steadman, A. Norris, R. McGrath, T. S. Turner, G. Thornton, N. M. Harrison. *Stability of Polar Oxide Surfaces.* Phys. Rev. Lett. **86**, 3811 (2001). DOI: 10.1103/PhysRevLett.86.3811.

[32] O. Dulub, L. A. Boatner, U. Diebold. *STM study of the geometric and electronic structure of ZnO(0001)-Zn, (000$\bar{1}$)-O, (10$\bar{1}$0), and (11$\bar{2}$0) surfaces.* Surf. Sci. **519**, 201 (2002). DOI: 10.1016/S0039-6028(02)02211-2.

[33] S. Torbruegge, F. Ostendorf, M. Reichling. *Stabilization of zinc-terminated ZnO(0001) by a modified surface stoichiometry.* J. Phys. Chem. C **113**, 4909 (2009). DOI: 10.1021/jp804026v.

[34] G. Kresse, O. Dulub, U. Diebold. *Competing stabilization mechanism for the polar ZnO(0001)-Zn surface.* Phys. Rev. B **68**, 245409 (2003). DOI: 10.1103/PhysRevB.68.245409.

[35] B. Meyer, D. Marx. *Density-functional study of the structure and stability of ZnO surfaces*. Phys. Rev. B **67**, 035403 (2003). DOI: 10.1103/PhysRevB.67.035403.

[36] O. Dulub, U. Diebold, G. Kresse. *Novel stabilization mechanism on polar surfaces: ZnO(0001)-Zn*. Phys. Rev. Lett. **90**, 016102 (2003). DOI: 10.1103/PhysRevLett.90.016102.

[37] V. Staemmler, K. Fink, B. Meyer, D. Marx, M. Kunat, S. Gil Girol, U. Burghaus, C. Wöll. *Stabilization of polar ZnO surfaces: Validating microscopic models by using CO as a probe molecule*. Phys. Rev. Lett. **90**, 106102 (2003). DOI: 10.1103/PhysRevLett.90.106102.

[38] M. Valtiner, M. Todorova, G. Grundmeier, J. Neugebauer. *Temperature Stabilized Surface Reconstructions at Polar ZnO(0001)*. Phys. Rev. Lett. **103**, 065502 (2009). DOI: 10.1103/PhysRevLett.103.065502.

[39] B. Meyer. *First-principles study of the polar O-terminated ZnO surface in thermodynamic equilibrium with oxygen and hydrogen*. Phys. Rev. B **69**, 045416 (2004). DOI: 10.1103/PhysRevB.69.045416.

[40] M. Kunat, S. Gil Girol, T. Becker, U. Burghaus, C. Wöll. *Stability of the polar surfaces of ZnO: A reinvestigation using He-atom scattering*. Phys. Rev. B **66**, 081402 (2002). DOI: 10.1103/PhysRevB.66.081402.

[41] M. Kunat, S. G. Girol, U. Burghaus, C. Wöll. *The interaction of water with the oxygen-terminated, polar surface of ZnO*. J. Phys. Chem. B **107**, 14350 (2003). DOI: 10.1021/jp030675z.

[42] J. V. Lauritsen, S. Porsgaard, M. K. Rasmussen, M. C. R. Jensen, R. Bechstein, K. Meinander, B. S. Clausen, S. Helveg, R. Wahl, G. Kresse, F. Besenbacher. *Stabilization principles for polar surfaces of ZnO*. ACS Nano **5**, 5987 (2011). DOI: 10.1021/nn2017606.

[43] R. Wahl, J. V. Lauritsen, F. Besenbacher, G. Kresse. *Stabilization mechanism for the polar ZnO(000$\bar{1}$)-O surface*. Phys. Rev. B **87**, 085313 (2013). DOI: 10.1103/PhysRevB.87.085313.

[44] K. Ozawa, K. Mase. *Comparison of the surface electronic structures of H-adsorbed ZnO surfaces: An angle-resolved photoelectron spectroscopy study*. Phys. Rev. B **83**, 125406 (2011). DOI: 10.1103/PhysRevB.83.125406.

[45] K. Moorman, Heiland. *Workfunction and band bending on cleaned cleaved ZnO*. Surf. Sci. **80**, 261 (1979). DOI: 10.1016/0039-6028(79)90685-X.

[46] L. F. J. Piper, A. R. H. Preston, A. Fedorov, S. W. Cho, A. DeMasi, K. E. Smith. *Direct evidence of metallicity at ZnO* $(000\overline{1})$-(1×1) *surfaces from angle-resolved photoemission spectroscopy*. Phys. Rev. B **81**, 233305 (2010). DOI: 10.1103/PhysRevB.81.233305.

[47] P. D. C. King, T. D. Veal, D. J. Payne, A. Bourlange, R. G. Egdell, C. F. McConville. *Surface Electron Accumulation and the Charge Neutrality Level in* In_2O_3. Phys. Rev. Lett. **101**, 116808 (2008). DOI: 10.1103/PhysRevLett.101.116808.

[48] P. D. C. King, T. D. Veal, A. Schleife, J. Zúñiga- Pérez, B. Martel, P. H. Jefferson, F. Fuchs, V. Muñoz-Sanjosé, F. Bechstedt, C. F. McConville. *Valence-band electronic structure of CdO, ZnO, and MgO from x-ray photoemission spectroscopy and quasi-particle-corrected density-functional theory calculations*. Phys. Rev. B **79**, 205205 (2009). DOI: 10.1103/PhysRevB.79.205205.

[49] C. Jagadish and S. Pearton, eds. *Zinc Oxide Bulk, Thin Films and Nanostructures*. Elsevier Science, (2011).

[50] T. Nann, J. Schneider. *Origin of permanent electric dipole moments in wurtzite nanocrystals*. Chemical Physics Letters **384**, 150 (2004). DOI: 10.1016/j.cplett.2003.12.017.

[51] M. Allen. *Schottky contact formation to bulk zinc oxide*. PhD thesis. University of Canterbury, (2008).

[52] F. Bernardini, V. Fiorentini, D. Vanderbilt. *Spontaneous polarization and piezoelectric constants of III-V nitrides*. Phys. Rev. B **56**, R10024 (1997). DOI: 10.1103/PhysRevB.56.R10024.

[53] A. Mang, K. Reimann, S. Rübenacke. *Band gaps, crystal-field splitting, spin-orbit coupling, and exciton binding energies in ZnO under hydrostatic pressure*. Solid State Communications **94**, 251 (1995). DOI: 10.1016/0038-1098(95)00054-2.

[54] W. R. L. Lambrecht, A. V. Rodina, S. Limpijumnong, B. Segall, B. K. Meyer. *Valence-band ordering and magneto-optic exciton fine structure in ZnO*. Phys. Rev. B **65**, 075207 (2002). DOI: 10.1103/PhysRevB.65.075207.

[55] W. Y. Liang, A. D. Yoffe. *Transmission spectra of ZnO single crystals*. Phys. Rev. Lett. **20**, 59 (1968). DOI: 10.1103/PhysRevLett.20.59.

[56] M. R. Wagner, J.-H. Schulze, R. Kirste, M. Cobet, A. Hoffmann, C. Rauch, A. V. Rodina, B. K. Meyer, U. Röder, K. Thonke. Γ_7 *valence band symmetry related hole fine splitting of bound excitons in ZnO observed in magneto-optical studies*. Phys. Rev. B **80**, 205203 (2009). DOI: 10.1103/PhysRevB.80.205203.

[57] D. C. Reynolds, C. W. Litton, T. C. Collins. *Zeeman effects in the edge emission and absorption of ZnO*. Phys. Rev. **140**, A1726 (1965). DOI: 10.1103/PhysRev.140.A1726.

[58] S. Adachi, K. Hazu, T. Sota, S. Chichibu, G. Cantwell, D. C. Reynolds, C. W. Litton. *Biexcitons and their dephasing processes in ZnO*. phys. stat. sol. (c) **2**, 890 (2005). DOI: 10.1002/pssc.200460332.

[59] K. Hazu, S. F. Chichibu, S. Adachi, T. Sota. *Valence-band-ordering of a strain-free bulk ZnO single crystal identified by four-wave-mixing spectroscopy technique*. J. Appl. Phys. **111**, 093522 (2012). DOI: 10.1063/1.4711103.

[60] E. Ohshima, H. Ogino, I. Niikura, K. Maeda, M. Sato, M. Ito, T. Fukuda. *Growth of the 2-in-size bulk ZnO single crystals by the hydrothermal method*. J. Cryst. Growth **260**, 166 (2004). DOI: 10.1016/j.jcrysgro.2003.08.019.

[61] D. Ehrentraut, K. Maeda, M. Kano, K. Fujii, T. Fukuda. *Next-generation hydrothermal ZnO crystals*. J. Cryst. Growth **320**, 18 (2011). DOI: 10.1016/j.jcrysgro.2011.01.005.

[62] K. Maeda, M. Sato, I. Niikura, T. Fukuda. *Growth of 2 inch ZnO bulk single crystal by the hydrothermal method*. Semicond. Sci. Technol. **20**, S49 (2005).

[63] Cermet. *Webpage ZnO substrate leaflet: www.cermetinc.com*. 2013. URL: http://www.cermetinc.com/materials/ZnO_substrate_product_lit.pdf.

[64] A. Laufer, N. Volbers, S. Eisermann, K. Potzger, S. Geburt, C. Ronning, B. K. Meyer. *Determination of secondary ion mass spectrometry relative sensitivity factors for polar and non-polar ZnO*. J. Appl. Phys. **110**, 094906 (2011). DOI: 10.1063/1.3660417.

[65] S. Lautenschläger, J. Sann, N. Volbers, B. K. Meyer, A. Hoffmann, U. Haboeck, M. R. Wagner. *Asymmetry in the excitonic recombinations and impurity incorporation of the two polar faces of homoepitaxially grown ZnO films*. Phys. Rev. B **77**, 144108 (2008). DOI: 10.1103/PhysRevB.77.144108.

[66] S. Lautenschläger, S. Eisermann, G. Haas, E. A. Zolnowski, M. N. Hofmann, A. Laufer, M. Pinnisch, B. K. Meyer, M. R. Wagner, J. S. Reparaz, G. Callsen, A. Hoffmann, A. Chernikov, S. Chatterjee, V. Bornwasser, M. Koch. *Optical signatures of nitrogen acceptors in ZnO*. Phys. Rev. B **85** (2012), 235204. DOI: 10.1103/PhysRevB.85.235204.

[67] D. C. Look, J. W. Hemsky, J. R. Sizelove. *Residual native shallow donor in ZnO*. Phys. Rev. Lett. **82** (1999), 2552–2555. DOI: 10.1103/PhysRevLett.82.2552.

[68] A. F. Kohan, G. Ceder, D. Morgan, C. G. Van de Walle. *First-principles study of native point defects in ZnO*. Phys. Rev. B **61**, 15019 (2000). DOI: 10.1103/PhysRevB.61.15019.

[69] F. A. Selim, M. H. Weber, D. Solodovnikov, K. G. Lynn. *Nature of Native Defects in ZnO*. Phys. Rev. Lett. **99**, 085502 (2007). DOI: 10.1103/PhysRevLett.99.085502.

[70] M. Grundmann. *The physics of semiconductors*. 2nd. Springer Berlin / Heidelberg, (2010).

[71] E. Mollwo. *Die Wirkung von Wasserstoff auf die Leitfähigkeit und Lumineszenz von Zinkoxydkristallen*. Zeitschrift für Physik **138**, 478 (1954). DOI: 10.1007/BF01340694.

[72] D. G. Thomas, J. J. Lander. *Hydrogen as a donor in zinc oxide*. The Journal of Chemical Physics **25**, 1136 (1956). DOI: 10.1063/1.1743165.

[73] M. G. Wardle, J. P. Goss, P. R. Briddon. *First-Principles Study of the Diffusion of Hydrogen in ZnO*. Phys. Rev. Lett. **96**, 205504 (2006). DOI: 10.1103/PhysRevLett.96.205504.

[74] E. V. Lavrov, F. Börrnert, J. Weber. *Photoconductivity and infrared absorption study of hydrogen-related shallow donors in ZnO*. Phys. Rev. B **72**, 085212 (2005). DOI: 10.1103/PhysRevB.72.085212.

[75] E. V. Lavrov, F. Herklotz, J. Weber. *Identification of two hydrogen donors in ZnO*. Phys. Rev. B **79**, 165210 (2009). DOI: 10.1103/PhysRevB.79.165210.

[76] E. V. Lavrov, J. Weber, F. Börrnert, C. G. Van de Walle, R. Helbig. *Hydrogen-related defects in ZnO studied by infrared absorption spectroscopy*. Phys. Rev. B **66**, 165205 (2002). DOI: 10.1103/PhysRevB.66.165205.

[77] F. Herklotz, E. V. Lavrov, V. Kolkovsky, J. Weber, M. Stavola. *Charge states of a hydrogen defect with a local vibrational mode at 3326 cm^{-1} in ZnO*. Phys. Rev. B **82**, 115206 (2010). DOI: 10.1103/PhysRevB.82.115206.

[78] M. McCluskey, S. Jokela. *Sources of n-type conductivity in ZnO*. Physica B: Cond. Mat. **401**, 355 (2007). DOI: 10.1016/j.physb.2007.08.186.

[79] G. A. Shi, M. Saboktakin, M. Stavola, S. J. Pearton. *Hidden hydrogen in as-grown ZnO*. Appl. Phys. Lett. **85**, 5601 (2004). DOI: 10.1063/1.1832736.

[80] D. Bastin, E. V. Lavrov, J. Weber. *Metastable state of the $V_{Zn}H_2$ defect in ZnO*. Phys. Rev. B **83**, 195210 (2011). DOI: 10.1103/PhysRevB.83.195210.

[81] E. V. Lavrov, F. Börrnert, J. Weber. *Dominant hydrogen-oxygen complex in hydrothermally grown ZnO*. Phys. Rev. B **71**, 035205 (2005). DOI: 10.1103/PhysRevB.71.035205.

[82] L. E. Halliburton, L. Wang, L. Bai, N. Y. Garces, N. C. Giles, M. J. Callahan, B. Wang. *Infrared absorption from OH^- ions adjacent to lithium acceptors in hydrothermally grown ZnO*. J. Appl. Phys. **96**, 7168 (2004). DOI: 10.1063/1.1806531.

[83] G. A. Shi, M. Stavola, W. B. Fowler. *Identification of an OH-Li center in ZnO: Infrared absorption spectroscopy and density functional theory*. Phys. Rev. B **73**, 081201 (2006). DOI: 10.1103/PhysRevB.73.081201.

[84] E. V. Lavrov, F. Herklotz, J. Weber. *Identification of Hydrogen Molecules in ZnO*. Phys. Rev. Lett. **102**, 185502 (2009). DOI: 10.1103/PhysRevLett.102.185502.

[85] M.-H. Du, K. Biswas. *Anionic and Hidden Hydrogen in ZnO*. Phys. Rev. Lett. **106**, 115502 (2011). DOI: 10.1103/PhysRevLett.106.115502.

[86] M. G. Wardle, J. P. Goss, P. R. Briddon. *Theory of Li in ZnO: A limitation for Li-based p-type doping*. Phys. Rev. B **71**, 155205 (2005). DOI: 10.1103/PhysRevB.71.155205.

[87] S. J. Jokela, M. D. McCluskey. *Unambiguous identification of nitrogen-hydrogen complexes in ZnO*. Phys. Rev. B **76**, 193201 (2007). DOI: 10.1103/PhysRevB.76.193201.

[88] M. E. Zvanut, D. M. Matlock, R. L. Henry, D. Koleske, A. Wickenden. *Thermal activation of Mg-doped GaN as monitored by electron paramagnetic resonance spectroscopy*. J. Appl. Phys. **95**, 1884 (2004). DOI: 10.1063/1.1639954.

[89] M. Matsubara, M. N. Amini, R. Saniz, D. Lamoen, B. Partoens. *Attracting shallow donors: Hydrogen passivation in (Al,Ga,In)-doped ZnO*. Phys. Rev. B **86** (2012), 165207. DOI: 10.1103/PhysRevB.86.165207.

[90] D. M. Hofmann, A. Hofstaetter, F. Leiter, H. Zhou, F. Henecker, B. K. Meyer, S. B. Orlinskii, J. Schmidt, P. G. Baranov. *Hydrogen: A Relevant Shallow Donor in Zinc Oxide*. Phys. Rev. Lett. **88**, 045504 (2002). DOI: 10.1103/PhysRevLett.88.045504.

[91] P. Blood, J. W. Orton. *The Electrical Characterization of Semiconductors: Majority Carriers and Electronic States*. Academic Press, (1992).

[92] W. Shockley, W. T. Read. *Statistics of the Recombinations of Holes and Electrons*. Phys. Rev. **87**, 835 (1952). DOI: 10.1103/PhysRev.87.835.

[93] S. M. Sze. *The Physics of Semiconductor Devices*. Wiley, New York, (1981).

[94] D. L. Losee. *Admittance spectroscopy of impurity levels in Schottky barriers*. J. Appl. Phys. **46**, 2204 (1975). DOI: 10.1063/1.321865.

[95] J. L. Pautrat, B. Katircioglu, N. Magnea, D. Bensahel, J. Pfister, L. Revoil. *Admittance spectroscopy: A powerful characterization technique for semiconductor crystals: Application to ZnTe*. Solid-State Electron. **23**, 1159 (1980). DOI: 10.1016/0038-1101(80)90028-3.

[96] D. V. Lang. *Deep-level transient spectroscopy: A new method to characterize traps in semiconductors*. J. Appl. Phys. **45**, 3023 (1974). DOI: 10.1063/1.1663719.

[97] L. Dobaczewski, A. R. Peaker, K. Bonde Nielsen. *Laplace-transform deep-level spectroscopy: The technique and its applications to the study of point defects in semiconductors*. J. Appl. Phys. **96**, 4689 (2004). DOI: 10.1063/1.1794897.

[98] I. Pelant, J. Valenta. *Luminescence Spectroscopy of Semiconductors*. Oxford University Press, (2012). DOI: 10.1093/acprof:oso/9780199588336.001.0001.

[99] W. Martienssen, H. Warlimont. *Handbook of condensed matter and materials data: Condensed matter and materials data*. Springer Berlin / New York, (2005).

[100] A. Sedhain, J. Li, J. Y. Lin, H. X. Jiang. *Probing exciton-phonon interaction in AlN epilayers by photoluminescence*. Appl. Phys. Lett. **95**, 061106 (2009). DOI: 10.1063/1.3206672.

[101] A. I. Ekimov, F. Hache, M. C. Schanne-Klein, D. Ricard, C. Flytzanis, I. A. Kudryavtsev, T. V. Yazeva, A. V. Rodina, A. L. Efros. *Absorption and intensity-dependent photoluminescence measurements on CdSe quantum dots: assignment of the first electronic transitions*. J. Opt. Soc. Am. B **10**, 100 (1993). DOI: 10.1364/JOSAB.10.000100.

[102] C. F. Klingshirn. *Semiconductor optics*. Springer Berlin / Heidelberg, (2005).

[103] J. Frenkel. *On the Transformation of light into Heat in Solids. I*. Phys. Rev. **37**, 17 (1931). DOI: 10.1103/PhysRev.37.17.

[104] G. H. Wannier. *The Structure of Electronic Excitation Levels in Insulating Crystals*. Phys. Rev. **52**, 191 (1937). DOI: 10.1103/PhysRev.52.191.

[105] P. Y. Yu, M. Cardona. *Fundamentals of Semiconductors*. Springer Berlin / Heidelberg, (2005).

[106] H. Wenckstern. *Doping, contacting, defect levels and transport properties of ZnO*. PhD thesis. Universität Leipzig, 2008.

[107] D. Thomas. *The exciton spectrum of zinc oxide*. J. Phys. Chem. Solids **15**, 86 (1960). DOI: 10.1016/0022-3697(60)90104-9.

[108] A. Baudrant. *Silicon Technologies: Ion Implantation and Thermal Treatment*. 1st ed. Wiley, (2013).

[109] H. Hertz. *Ueber einen Einfluss des ultravioletten Lichtes auf die electrische Entladung*. Ann. Phys. **267**, 983 (1887). DOI: 10.1002/andp.18872670827.

[110] A. Einstein. *Über einen die Erzeugung und Verwandlung des Lichtes betreffenden heuristischen Gesichtspunkt*. Ann. Phys. **322**, 132 (1905). DOI: 10.1002/andp.19053220607.

[111] S. Hüfner. *Photoelectron Spectroscopy: Principles and Application*. Springer Berlin / Heidelberg, (2010).

[112] M. P. Seah, W. A. Dench. *Quantitative electron spectroscopy of surfaces: A standard data base for electron inelastic mean free paths in solids*. Surf. Interface Anal. **1**, 2 (1979). DOI: 10.1002/sia.740010103.

[113] I. O. Standardisation. *18115:2001, Surface chemical analysis - Vocabulary, (ISO 18115:2001/Amd 1:2006; ISO 18115:2001/Amd 2:2007)*. International Organisation for Standardisation, 2001.

[114] C. Powell, A. Jablonski. *Progress in quantitative surface analysis by X-ray photoelectron spectroscopy: Current status and perspectives*. J. Electron Spectrosc. Relat. Phenom. **178**, 331 (2010). DOI: 10.1016/j.elspec.2009.05.004.

[115] S. Tanuma, C. J. Powell, D. R. Penn. *Calculations of electron inelastic mean free paths. V. Data for 14 organic compounds over the 50-2000 eV range*. Surf. Interface Anal. **21**, 165 (1994). DOI: 10.1002/sia.740210302.

[116] S. Tougaard. *Quantitative Analysis of Surfaces by Electron Spectroscopy*. URL: http://www.quases.com/products/quases-imfp-tpp2m/.

[117] J. Yeh, I. Lindau. *Atomic subshell photoionization cross sections and asymmetry parameters: $1 \leq Z \leq 103$*. Atomic Data and Nuclear Data Tables **32**, 1 (1985). DOI: 10.1016/0092-640X(85)90016-6.

[118] B. Henke, E. Gullikson, J. Davis. *X-Ray Interactions: Photoabsorption, Scattering, Transmission, and Reflection at E = 50-30,000 eV, Z = 1-92*. Atomic Data and Nuclear Data Tables **54**, 181 (1993). DOI: 10.1006/adnd.1993.1013.

[119] O. Roberts. *The application of real-time photoelectron spectroscopy to carbon based semiconductors*. PhD thesis. Aberystwyth University, 2009.

[120] C. A. Dukes, R. A. Baragiola. *Compact plasma source for removal of hydrocarbons for surface analysis*. Surface and Interface Analysis **42**, 40 (2010). DOI: 10.1002/sia.3138.

[121] R. Hesse, P. Streubel, R. Szargan. *Product or sum: comparative tests of Voigt, and product or sum of Gaussian and Lorentzian functions in the fitting of synthetic Voigt-based X-ray photoelectron spectra*. Surf. Interface Anal. **39**, 381 (2007). DOI: 10.1002/sia.2527.

[122] Y. Joseph, W. Ranke, W. Weiss. *Water on FeO(111) and Fe3O4(111): Adsorption behavior on different surface terminations*. J. Phys. Chem. B **104**, 3224 (2000). DOI: 10.1021/jp9932012.

[123] A. Önsten, D. Stoltz, P. Palmgren, K. Yu, T. Claesson, M. Göthelid, U. O. Karlsson. *SO_2 interaction with Zn(0001) and ZnO(0001) and the influence of water*. Surf. Sci. **608**, 31–43 (2013). DOI: 10.1016/j.susc.2012.09.007.

[124] S. A. Chambers, T. Droubay, T. C. Kaspar, M. Gutowski. *Experimental determination of valence band maxima for $SrTiO_3$, TiO_2, and SrO and the associated valence band offsets with Si(001)*. J. Vac. Sci. Technol. B **22**, 2205 (2004). DOI: 10.1116/1.1768525.

[125] A. Carvalho, A. Alkauskas, A. Pasquarello, A. K. Tagantsev, N. Setter. *A hybrid density functional study of lithium in ZnO: Stability, ionization levels, and diffusion*. Phys. Rev. B **80**, 195205 (2009). DOI: 10.1103/PhysRevB.80.195205.

[126] P. H. Kasai. *Electron spin resonance studies of donors and acceptors in ZnO*. Phys. Rev. **130**, 989 (1963). DOI: 10.1103/PhysRev.130.989.

[127] O. Schirmer. *The structure of the paramagnetic lithium center in zinc oxide and beryllium oxide*. J. Phys. Chem. Solids **29**, 1407 (1968). DOI: 10.1016/0022-3697(68)90193-5.

[128] P. D. Bievre, P. Taylor. *IUPAC Recommended Isotopic Abundances*. Int. J. of Mass Spect. Ion Phys. **123**, 149 (1993).

[129] M. W. Allen, R. J. Mendelsberg, R. J. Reeves, S. M. Durbin. *Oxidized noble metal Schottky contacts to n-type ZnO*. Appl. Phys. Lett. **94**, 103508 (2009). DOI: 10.1063/1.3089871.

[130] S. K. Cheung, N. W. Cheung. *Extraction of Schottky diode parameters from forward current-voltage characteristics*. Appl. Phys. Lett. **49**, 85 (1986). DOI: 10.1063/1.97359.

[131] L. Vines, E. Monakhov, B. Svensson. *Effect of high temperature treatments on defect centers and impurities in hydrothermally grown ZnO*. Physica B: Cond. Mat. **404**, 4386 (2009). DOI: 10.1016/j.physb.2009.09.029.

[132] L. Vines, E. V. Monakhov, R. Schifano, W. Mtangi, F. D. Auret, B. G. Svensson. *Lithium and electrical properties of ZnO*. J. Appl. Phys. **107**, 103707 (2010). DOI: 10.1063/1.3415551.

[133] R. Schifano, E. Monakhov, B. Svensson, W. Mtangi, P. J. Rensburg, F. Auret. *Shallow levels in virgin hydrothermally grown n-type ZnO studied by thermal admittance spectroscopy*. Physica B: Cond. Mat. **404**, 4344 (2009). DOI: 10.1016/j.physb.2009.09.030.

[134] F. D. Auret, W. Meyer, P. J. Rensburg, M. Hayes, J. Nel, H. Wenckstern, H. Schmidt, G. Biehne, H. Hochmuth, M. Lorenz, M. Grundmann. *Electronic properties of defects in pulsed-laser deposition grown ZnO with levels at 300 and 370 meV below the conduction band*. Physica B: Cond. Mat. **401-402**, 378 (2007). DOI: 10.1016/j.physb.2007.08.192.

[135] F. Schmidt, S. Müller, H. Wenckstern, C. P. Dietrich, R. Heinhold, H.-S. Kim, M. W. Allen, M. Grundmann. *Comparative study of deep defects in ZnO microwires, thin films and bulk single crystals*. Appl. Phys. Lett. **103**, 062102 (2013). DOI: 10.1063/1.4817824.

[136] Y. Jiang, N. C. Giles, L. E. Halliburton. *Persistent photoinduced changes in charge states of transition-metal donors in hydrothermally grown ZnO crystals*. J. Appl. Phys. **101**, 093706 (2007). DOI: 10.1063/1.2723872.

[137] F. D. Auret, S. A. Goodman, M. J. Legodi, W. E. Meyer, D. C. Look. *Electrical characterization of vapor-phase-grown single-crystal ZnO*. Appl. Phys. Lett. **80**, 1340 (2002). DOI: 10.1063/1.1452781.

[138] M. Schmidt, M. Ellguth, R. Karsthof, H. v. Wenckstern, R. Pickenhain, M. Grundmann, G. Brauer, F. C. C. Ling. *On the T2 trap in zinc oxide thin films*. phys. stat. sol. (b) **249**, 588 (2011). DOI: 10.1002/pssb.201147271.

[139] F. Oba, A. Togo, I. Tanaka, J. Paier, G. Kresse. *Defect energetics in ZnO: A hybrid Hartree-Fock density functional study*. Phys. Rev. B **77**, 245202 (2008). DOI: 10.1103/PhysRevB.77.245202.

[140] T. Frank, G. Pensl, R. Tena-Zaera, J. Zúñiga-Pérez, C. Martínez-Tomás, V. Muñoz-Sanjosé, T. Ohshima, H. Itoh, D. Hofmann, D. Pfisterer, J. Sann, B. Meyer. *Energetically deep defect centers in vapor-phase grown zinc oxide*. English. Appl. Phys. A **88**, 141 (2007). DOI: 10.1007/s00339-007-3963-3.

[141] M. Schmidt, M. Ellguth, F. Schmidt, T. Lüder, H. v. Wenckstern, R. Pickenhain, M. Grundmann, G. Brauer, W. Skorupa. *Defects in a nitrogen-implanted ZnO thin film*. phys. stat. sol. (b) **247**, 1220 (2010). DOI: 10.1002/pssb.200945534.

[142] M. Hayes, F. D. Auret, P. J. Janse van Rensburg, J. M. Nel, W. Wesch, E. Wendler. *Electrical characterization of He^+ irradiated n-ZnO*. phys. stat. sol. (b) **244**, 1544 (2007). DOI: 10.1002/pssb.200675135.

[143] M. Hayes, F. Auret, P. J. Rensburg, J. Nel, W. Wesch, E. Wendler. *Electrical characterization of H^+ ion irradiated n-ZnO*. Nuc. Inst. Meth. Phys. Res. B **257**, 311 (2007). DOI: 10.1016/j.nimb.2007.01.033.

[144] L. Vines, J. Wong-Leung, C. Jagadish, E. Monakhov, B. Svensson. *Ion implantation induced defects in ZnO*. Physica B: Cond. Mat. **407**, 1481 (2012). DOI: 10.1016/j.physb.2011.09.066.

[145] V. Quemener, L. Vines, E. V. Monakhov, B. G. Svensson. *Iron related donor-like defect in zinc oxide*. Appl. Phys. Lett. **102**, 232102 (2013). DOI: 10.1063/1.4809941.

[146] M. J. Henseler. *Optoelectrical studies on ZnO*. PhD thesis. University of Canterbury, (2009).

[147] S. F. Chichibu, T. Sota, G. Cantwell, D. B. Eason, C. W. Litton. *Polarized photoreflectance spectra of excitonic polaritons in a ZnO single crystal*. J. Appl. Phys. **93**, 756 (2003). DOI: 10.1063/1.1527707.

[148] S. F. Chichibu, T. Onuma, M. Kubota, A. Uedono, T. Sota, A. Tsukazaki, A. Ohtomo, M. Kawasaki. *Improvements in quantum efficiency of excitonic emissions in ZnO epilayers by the elimination of point defects*. J. Appl. Phys. **99**, 093505 (2006). DOI: 10.1063/1.2193162.

[149] B. K. Meyer, J. Sann, S. Eisermann, S. Lautenschlaeger, M. R. Wagner, M. Kaiser, G. Callsen, J. S. Reparaz, A. Hoffmann. *Excited state properties of donor bound excitons in ZnO*. Phys. Rev. B **82**, 115207 (2010). DOI: 10.1103/PhysRevB.82.115207.

[150] M. R. Wagner. *Fundamental properties of excitons and phonons in ZnO: A spectroscopic study of the dynamics, polarity, and effects of external fields*. PhD thesis. Technische Universität Berlin, (2010).

[151] D. W. Hamby, D. A. Lucca, M. J. Klopfstein. *Photoluminescence of mechanically polished ZnO*. J. Appl. Phys. **97**, 043504 (2005). DOI: 10.1063/1.1840102.

[152] A. Teke, Ü. Özgür, S. Doğan, X. Gu, H. Morkoç, B. Nemeth, J. Nause, H. O. Everitt. *Excitonic fine structure and recombination dynamics in single-crystalline ZnO*. Phys. Rev. B **70**, 195207 (2004). DOI: 10.1103/PhysRevB.70.195207.

[153] N. Syrbu, I. Tiginyanu, V. Zalamai, V. Ursaki, E. Rusu. *Exciton polariton spectra and carrier effective masses in ZnO single crystals*. Physica B: Cond. Mat. **353**, 111 (2004). DOI: 10.1016/j.physb.2004.09.007.

[154] T. Gruber, G. M. Prinz, C. Kirchner, R. Kling, F. Reuss, W. Limmer, A. Waag. *Influences of biaxial strains on the vibrational and exciton energies in ZnO*. J. Appl. Phys. **96**, 289 (2004). DOI: 10.1063/1.1755433.

[155] A. Schleife, C. Rödl, F. Fuchs, J. Furthmüller, F. Bechstedt. *Strain influence on valence-band ordering and excitons in ZnO: An ab initio study*. Appl. Phys. Lett. **91**, 241915 (2007). DOI: 10.1063/1.2825277.

[156] J. Sann. *Photolumineszenz gebundener Exzitonen in Zinkoxid*. PhD thesis. Justus-Liebig-Universität Giessen, (2008).

[157] M. Strassburg, A. Rodina, M. Dworzak, U. Haboeck, I. Krestnikov, A. Hoffmann, O. Gelhausen, M. Phillips, H. Alves, A. Zeuner, D. Hofmann, B. Meyer. *Identification of bound exciton complexes in ZnO*. phys. stat. sol. (b) **241**, 607 (2004). DOI: 10.1002/pssb.200304187.

[158] K. Johnston, M. O. Henry, D. McCabe, E. McGlynn, M. Dietrich, E. Alves, M. Xia. *Identification of donor-related impurities in ZnO using photoluminescence and radiotracer techniques*. Phys. Rev. B **73**, 165212 (2006). DOI: 10.1103/PhysRevB.73.165212.

[159] H. J. Ko, Y. F. Chen, S. K. Hong, H. Wenisch, T. Yao, D. C. Look. *Ga-doped ZnO films grown on GaN templates by plasma-assisted molecular-beam epitaxy*. Appl. Phys. Lett. **77**, 3761 (2000). DOI: 10.1063/1.1331089.

[160] R. Schneider, M. Schirra, A. Reiser, G. M. Prinz, W. Limmer, R. Sauer, K. Thonke, J. Biskupek, U. Kaiser. *Incorporation of Ga in ZnO/GaN epitaxial films*. Appl. Phys. Lett. **92**, 131905 (2008). DOI: 10.1063/1.2905284.

[161] M. Schilling, R. Helbig, G. Pensl. *Bound exciton luminescence of Ar- and Al-implanted ZnO*. J. Lumin. **33**, 201 (1985). DOI: 10.1016/0022-2313(85)90018-3.

[162] F. Bertram, J. Christen, A. Dadgar, A. Krost. *Complex excitonic recombination kinetics in ZnO: Capture, relaxation, and recombination from steady state*. Appl. Phys. Lett. **90**, 041917 (2007). DOI: 10.1063/1.2432259.

[163] A. V. Rodina, M. Strassburg, M. Dworzak, U. Haboeck, A. Hoffmann, A. Zeuner, H. R. Alves, D. M. Hofmann, B. K. Meyer. *Magneto-optical properties of bound excitons in ZnO*. Phys. Rev. B **69**, 125206 (2004). DOI: 10.1103/PhysRevB.69.125206.

[164] O. Brandt, C. Pfüller, C. Chèze, L. Geelhaar, H. Riechert. *Sub-meV linewidth of excitonic luminescence in single GaN nanowires: Direct evidence for surface excitons*. Phys. Rev. B **81**, 045302 (2010). DOI: 10.1103/PhysRevB.81.045302.

[165] J. Grabowska, A. Meaney, K. K. Nanda, J.-P. Mosnier, M. O. Henry, J.-R. Duclère, E. McGlynn. *Surface excitonic emission and quenching effects in ZnO nanowire/nanowall systems: Limiting effects on device potential*. Phys. Rev. B **71**, 115439 (2005). DOI: 10.1103/PhysRevB.71.115439.

[166] V. Travnikov, A. Freiberg, S. Savikhin. *Surface excitons in ZnO crystals*. J. Lumin. **47**, 107 (1990). DOI: 10.1016/0022-2313(90)90006-W.

[167] M. Biswas, Y. S. Jung, H. K. Kim, K. Kumar, G. J. Hughes, S. Newcomb, M. O. Henry, E. McGlynn. *Microscopic origins of the surface exciton photoluminescence peak in ZnO nanostructures*. Phys. Rev. B **83**, 235320 (2011). DOI: 10.1103/PhysRevB.83.235320.

[168] J. Sann, J. Stehr, A. Hofstaetter, D. M. Hofmann, A. Neumann, M. Lerch, U. Haboeck, A. Hoffmann, C. Thomsen. *Zn interstitial related donors in ammonia-treated ZnO powders*. Phys. Rev. B **76**, 195203 (2007). DOI: 10.1103/PhysRevB.76.195203.

[169] D. Bimberg, M. Sondergeld, E. Grobe. *Thermal Dissociation of Excitons Bounds to Neutral Acceptors in High-Purity GaAs*. Phys. Rev. B **4**, 3451 (1971). DOI: 10.1103/PhysRevB.4.3451.

[170] H. Shibata. *Negative thermal quenching curves in photoluminescence of solids*. Jpn. J. Appl. Phys **37**, 550 (1998). DOI: 10.7567/JJAP.37.550.

[171] D. W. Hamby, D. A. Lucca, M. J. Klopfstein, G. Cantwell. *Temperature dependent exciton photoluminescence of bulk ZnO*. J. Appl. Phys. **93**, 3214 (2003). DOI: 10.1063/1.1545157.

[172] D. Dumcenco, Y. Huang, D. Kuo, K. Tiong. *Photoluminescence characterization of vertically aligned ZnO microrods*. J. Lumin. **132**, 1890 (2012). DOI: 10.1016/j.jlumin.2012.02.037.

[173] J. Gutowski, N. Presser, I. Broser. *Acceptor-exciton complexes in ZnO: A comprehensive analysis of their electronic states by high-resolution magnetooptics and excitation spectroscopy*. Phys. Rev. B **38**, 9746 (1988). DOI: 10.1103/PhysRevB.38.9746.

[174] C. Morhain, T. Bretagnon, P. Lefebvre, X. Tang, P. Valvin, T. Guillet, B. Gil, T. Taliercio, M. Teisseire-Doninelli, B. Vinter, C. Deparis. *Internal electric field in wurtzite ZnO/$Zn_{0.78}Mg_{0.22}O$ quantum wells*. Phys. Rev. B **72**, 241305 (2005). DOI: 10.1103/PhysRevB.72.241305.

[175] X. W. Sun, H. S. Kwok. *Optical properties of epitaxially grown zinc oxide films on sapphire by pulsed laser deposition*. J. Appl. Phys. **86**, 408 (1999). DOI: 10.1063/1.370744.

[176] Y. S. Jung, W. K. Choi, O. V. Kononenko, G. N. Panin. *Luminescence of bound excitons in epitaxial ZnO thin films grown by plasma-assisted molecular beam epitaxy*. J. Appl. Phys. **99**, 013502 (2006). DOI: 10.1063/1.2150602.

[177] S. Lautenschläger, S. Eisermann, M. N. Hofmann, U. Roemer, M. Pinnisch, A. Laufer, B. K. Meyer, H. Wenckstern, A. Lajn, F. Schmidt, M. Grundmann, J. Blaesing, A. Krost. *Morphological, structural and electrical investigations on non-polar a-plane ZnO epilayers*. Journal of Crystal Growth **312**, 2078 (2010). DOI: 10.1016/j.jcrysgro.2010.04.029.

[178] R. Aggarwal, H. Zhou, C. Jin, J. Narayan, R. J. Narayan. *Semipolar r-plane ZnO films on Si(100) substrates: Thin film epitaxy and optical properties*. J. Appl. Phys. **107**, 113530 (2010). DOI: 10.1063/1.3406260.

[179] T. Sekiguchi, S. Miyashita, K. Obara, T. Shishido, N. Sakagami. *Hydrothermal growth of ZnO single crystals and their optical characterization*. J. Cryst. Growth **214**, 72 (2000). DOI: 10.1016/S0022-0248(00)00065-8.

[180] J. Mass, M. Avella, J. Jiménez, M. Callahan, E. Grant, K. Rakes, D. Bliss, B. Wang. *Spectrally Resolved Cathodoluminescence (SRCL) of Hydrothermal ZnO crystals*. MRS Proceedings **878** (2005). DOI: 10.1557/PROC-878-Y1.7.

[181] H. Sasaki, H. Kato, F. Izumida, H. Endo, K. Maeda, M. Ikeda, I. Kashiwaba, Y. Kashiwaba. *Photoluminescence properties of ZnO single crystals with polar and non-polar faces*. phys. stat. soli. (c) **3**, 1034 (2006). DOI: 10.1002/pssc.200564752.

[182] R. E. Sherriff, D. C. Reynolds, D. C. Look, B. Jogai, J. E. Hoelscher, T. C. Collins, G. Cantwell, W. C. Harsch. *Photoluminescence measurements from the two polar faces of ZnO*. J. Appl. Phys. **88**, 3454 (2000). DOI: 10.1063/1.1288159.

[183] D. C. Oh, T. Kato, H. Goto, S. H. Park, T. Hanada, T. Yao, J. J. Kim. *Comparative study of photoluminescences for Zn-polar and O-polar faces of single-crystalline ZnO bulks*. Appl. Phys. Lett. **93**, 241907 (2008). DOI: 10.1063/1.3033224.

[184] A. Yamamoto, Y. Moriwaki, K. Hattori, H. Yanagi. *A comparative study of photoluminescence of Zn-polar and O-polar faces in single crystal ZnO using moment analysis*. Appl. Phys. Lett. **98**, 061907 (2011), 061907. DOI: 10.1063/1.3554722.

[185] P. J. Dean, J. D. Cuthbert, D. G. Thomas, R. T. Lynch. *Two-Electron Transitions in the Luminescence of Excitons Bound to Neutral Donors in Gallium Phosphide*. Phys. Rev. Lett. **18**, 122 (1967). DOI: 10.1103/PhysRevLett.18.122.

[186] A. Schildknecht, R. Sauer, K. Thonke. *Donor-related defect states in ZnO substrate material*. Physica B: Cond. Mat. **340**, 205 (2003). DOI: 10.1016/j.physb.2003.09.029.

[187] M. R. Wagner, G. Callsen, J. S. Reparaz, J.-H. Schulze, R. Kirste, M. Cobet, I. A. Ostapenko, S. Rodt, C. Nenstiel, M. Kaiser, A. Hoffmann, A. V. Rodina, M. R. Phillips, S. Lautenschläger, S. Eisermann, B. K. Meyer. *Bound excitons in ZnO: Structural defect complexes versus shallow impurity centers*. Phys. Rev. B **84**, 035313 (2011). DOI: 10.1103/PhysRevB.84.035313.

[188] J. R. Haynes. *Experimental Proof of the Existence of a New Electronic Complex in Silicon*. Phys. Rev. Lett. **4**, 361 (1960). DOI: 10.1103/PhysRevLett.4.361.

[189] M. Brandt, H. Wenckstern, G. Benndorf, M. Lange, C. P. Dietrich, C. Kranert, C. Sturm, R. Schmidt-Grund, H. Hochmuth, M. Lorenz, M. Grundmann, M. R. Wagner, M. Alic, C. Nenstiel, A. Hoffmann. *Identification of a donor-related recombination channel in ZnO thin films*. Phys. Rev. B **81**, 073306 (2010). DOI: 10.1103/PhysRevB.81.073306.

[190] E. Tomzig, R. Helbig. *Band-edge emission in ZnO*. J. Lumin. **14**, 403 (1976). DOI: 10.1016/0022-2313(76)90009-0.

[191] H. Shibata, M. Watanabe, M. Sakai, K. Oka, P. Fons, K. Iwata, A. Yamada, K. Matsubara, K. Sakurai, H. Tampo, K. Nakahara, S. Niki. *Characterization of ZnO crystals by photoluminescence spectroscopy.* phys. stat. sol. (c) **1**, 872 (2004). DOI: 10.1002/pssc.200304149.

[192] D. C. Look, D. C. Reynolds, C. W. Litton, R. L. Jones, D. B. Eason, G. Cantwell. *Characterization of homoepitaxial p-type ZnO grown by molecular beam epitaxy.* Appl. Phys. Lett. **81**, 1830 (2002). DOI: 10.1063/1.1504875.

[193] J. G. Reynolds, J. C. L. Reynolds, A. Mohanta, J. F. Muth, J. E. Rowe, H. O. Everitt, D. E. Aspnes. *Shallow acceptor complexes in p-type ZnO.* Appl. Phys. Lett. **102**, 152114 (2013). DOI: 10.1063/1.4802753.

[194] D. Stichtenoth, C. Ronning, T. Niermann, L. Wischmeier, T. Voss, C.-J. Chien, P.-C. Chang, J. G. Lu. *Optical size effects in ultrathin ZnO nanowires.* Nanotechnology **18**, 435701 (2007).

[195] T. Hirai, Y. Harada, S. Hashimoto, N. Ohno, T. Itoh. *Luminescence of bound excitons in ZnO:Zn phosphor powders.* J. Lumin. **113** (2005), 115–120. DOI: 10.1016/j.jlumin.2004.09.114.

[196] I. Robin, P. Marotel, A. El-Shaer, V. Petukhov, A. Bakin, A. Waag, M. Lafossas, J. Garcia, M. Rosina, A. Ribeaud, S. Brochen, P. Ferret, G. Feuillet. *Compared optical properties of ZnO heteroepitaxial, homoepitaxial 2D layers and nanowires.* Journal of Crystal Growth **311**, 2172 (2009). DOI: 10.1016/j.jcrysgro.2008.10.078.

[197] B. Wang, M. Callahan, L. Bouthillette, C. Xu, M. Suscavage. *Hydrothermal growth and characterization of nitrogen-doped ZnO crystals.* Journal of Crystal Growth **287**, 381 (2006). DOI: 10.1016/j.jcrysgro.2005.11.049.

[198] H. Alves, D. Pfisterer, A. Zeuner, T. Riemann, J. Christen, D. Hofmann, B. Meyer. *Optical investigations on excitons bound to impurities and dislocations in ZnO.* Optical Materials **23** (2003), 33–37. DOI: 10.1016/S0925-3467(03)00055-7.

[199] K. Thonke, T. Gruber, N. Teofilov, R. Schönfelder, A. Waag, R. Sauer. *Donor-acceptor pair transitions in ZnO substrate material.* Physica B: Cond. Mat. **308**, 945 (2001). DOI: 10.1016/S0921-4526(01)00877-8.

[200] S. Graubner, C. Neumann, N. Volbers, B. K. Meyer, J. Bläsing, A. Krost. *Preparation of ZnO substrates for epitaxy: Structural, surface, and electrical properties.* Appl. Phys. Lett. **90**, 042103 (2007). DOI: 10.1063/1.2434170.

[201] F. Leiter, H. Alves, A. Hofstaetter, D. Hofmann, B. Meyer. *The oxygen vacancy as the origin of a green emission in undoped ZnO*. phys. stat. sol. (b) **226**, R4 (2001). DOI: 10.1002/1521-3951(200107)226:1<R4::AID-PSSB99994>3.0.CO;2-F.

[202] R. Dingle. *Luminescent transitions associated with divalent copper impurities and the green emission from semiconducting Zinc Oxide*. Phys. Rev. Lett. **23**, 579 (1969). DOI: 10.1103/PhysRevLett.23.579.

[203] B. Meyer, J. Sann, A. Zeuner. *Lithium and sodium acceptors in ZnO*. Superlattices and Microstructures **38**, 344 (2005). DOI: 10.1016/j.spmi.2005.08.006.

[204] J. Sann, A. Hofstaetter, D. Pfisterer, J. Stehr, B. K. Meyer. *Acceptor doping in ZnO with group-I elements*. phys. stat. soli. (c) **3**, 952 (2006). DOI: 10.1002/pssc.200564635.

[205] Özgur, Y. I. Alivov, C. Liu, A. Teke, M. A. Reshchikov, S. Doğan, V. Avrutin, S.-J. Cho, H. Morkoğ. *A comprehensive review of ZnO materials and devices*. J. Appl. Phys. **98**, 041301 (2005). DOI: 10.1063/1.1992666.

[206] A. Boonchun, W. R. L. Lambrecht. *Electronic structure of defects and doping in ZnO: Oxygen vacancy and nitrogen doping*. phys. stat. sol. (b) **250**, 2091–2101 (2013). DOI: 10.1002/pssb.201300010.

[207] A. N. Mariano, R. E. Hanneman. *Crystallographic polarity of ZnO crystals*. J. Appl. Phys. **34**, 384 (1963). DOI: 10.1063/1.1702617.

[208] D. Look. *Unusual electrical properties of hydrothermally grown ZnO*. Superlattices Microstruct. **42**, 284 (2007). DOI: 10.1016/j.spmi.2007.04.058.

[209] E. V. Lavrov, J. Weber. *Comment on "Infrared absorption spectroscopy on OH–Ni complex in hydrothermally grown ZnO" [J. Appl. Phys. 105, 093516 (2009)]*. J. Appl. Phys. **106**, 086104 (2009). DOI: 10.1063/1.3253333.

[210] M. Schirra, R. Schneider, A. Reiser, G. M. Prinz, M. Feneberg, J. Biskupek, U. Kaiser, C. E. Krill, K. Thonke, R. Sauer. *Stacking fault related 3.31 eV luminescence at 130 meV acceptors in zinc oxide*. Phys. Rev. B **77**, 125215 (2008). DOI: 10.1103/PhysRevB.77.125215.

[211] K. Ip, M. E. Overberg, Y. W. Heo, D. P. Norton, S. J. Pearton, S. O. Kucheyev, C. Jagadish, J. S. Williams, R. G. Wilson, J. M. Zavada. *Thermal stability of ion-implanted hydrogen in ZnO*. Appl. Phys. Lett. **81**, 3996 (2002). DOI: 10.1063/1.1524033.

[212] J.-K. Lee, M. Nastasi, D. W. Hamby, D. A. Lucca. *Optical observation of donor-bound excitons in hydrogen-implanted ZnO*. Appl. Phys. Lett. **86**, 171102 (2005). DOI: 10.1063/1.1906330.

[213] Z. Zhang, D. C. Look, R. Schifano, K. M. Johansen, B. G. Svensson, L. J. Brillson. *Process dependence of H passivation and doping in H-implanted ZnO*. J. Phys. D: Appl. Phys. **46**, 055107 (2013). DOI: 10.1088/0022-3727/46/5/055107.

[214] E. V. Monakhov, J. S. Christensen, K. Maknys, B. G. Svensson, A. Y. Kuznetsov. *Hydrogen implantation into ZnO for n^+-layer formation*. Appl. Phys. Lett. **87**, 191910 (2005). DOI: 10.1063/1.2128059.

[215] K. S. Chan, L. Vines, K. M. Johansen, E. V. Monakhov, J. D. Ye, P. Parkinson, C. Jagadish, B. G. Svensson, J. Wong-Leung. *Defect formation and thermal stability of H in high dose H implanted ZnO*. J. Appl. Phys. **114**, 083111 (2013). DOI: 10.1063/1.4819216.

[216] M. D. McCluskey, S. J. Jokela, K. K. Zhuravlev, P. J. Simpson, K. G. Lynn. *Infrared spectroscopy of hydrogen in ZnO*. Appl. Phys. Lett. **81**, 3807 (2002). DOI: 10.1063/1.1520703.

[217] E. Lavrov, F. Börrnert, J. Weber. *Hydrogen motion in ZnO*. Physica B: Condensed Matter **401**, 366 (2007). Proceedings of the 24th International Conference on Defects in Semiconductors. DOI: 10.1016/j.physb.2007.08.189.

[218] X.-B. Li, S. Limpijumnong, W. Q. Tian, H.-B. Sun, S. B. Zhang. *Hydrogen in ZnO revisited: Bond center versus antibonding site*. Phys. Rev. B **78**, 113203 (11 2008). DOI: 10.1103/PhysRevB.78.113203.

[219] G. A. Shi, M. Stavola, S. J. Pearton, M. Thieme, E. V. Lavrov, J. Weber. *Hydrogen local modes and shallow donors in ZnO*. Phys. Rev. B **72**, 195211 (2005). DOI: 10.1103/PhysRevB.72.195211.

[220] F. Friedrich, N. H. Nickel. *Resonant Raman scattering in hydrogen and nitrogen doped ZnO*. Appl. Phys. Lett. **91**, 111903 (2007). DOI: 10.1063/1.2783222.

[221] T. Schmidt, K. Lischka, W. Zulehner. *Excitation-power dependence of the near-band-edge photoluminescence of semiconductors*. Phys. Rev. B **45**, 8989 (1992). DOI: 10.1103/PhysRevB.45.8989.

[222] Z. Yang, D. C. Look, J. L. Liu. *Ga-related photoluminescence lines in Ga-doped ZnO grown by plasma-assisted molecular-beam epitaxy*. Appl. Phys. Lett. **94**, 072101 (2009). DOI: 10.1063/1.3080204.

[223] S. Limpijumnong, P. Reunchan, A. Janotti, C. G. Van de Walle. *Hydrogen doping in indium oxide: An ab initio study*. Phys. Rev. B **80**, 193202 (2009). DOI: 10.1103/PhysRevB.80.193202.

[224] F. Reuss, C. Kirchner, T. Gruber, R. Kling, S. Maschek, W. Limmer, A. Waag, P. Ziemann. *Optical investigations on the annealing behavior of gallium- and nitrogen-implanted ZnO*. J. Appl. Phys. **95**, 3385 (2004). DOI: 10.1063/1.1650899.

[225] P. Dahan, V. Fleurov, P. Thurian, R. Heitz, A. Hoffmann, I. Broser. *Isotope shift in semiconductors with transition-metal impurities: Experiment and theory applied to ZnO:Cu*. Phys. Rev. B **57**, 9690 (1998). DOI: 10.1103/PhysRevB.57.9690.

[226] D. Byrne, F. Herklotz, M. O. Henry, E. McGlynn. *Unambiguous identification of the role of a single Cu atom in the ZnO structured green band*. J. Phys.: Condens. Matter **24**, 215802 (2012). DOI: 10.1088/0953-8984/24/21/215802.

[227] Z. Q. Chen, M. Maekawa, S. Yamamoto, A. Kawasuso, X. L. Yuan, T. Sekiguchi, R. Suzuki, T. Ohdaira. *Evolution of voids in Al^+-implanted ZnO probed by a slow positron beam*. Phys. Rev. B **69**, 035210 (2004). DOI: 10.1103/PhysRevB.69.035210.

[228] T. Børseth, J. Christensen, K. Maknys, A. Hallén, B. Svensson, A. Kuznetsov. *Annealing study of Sb^+ and Al^+ ion-implanted ZnO*. Superlattices Microstruct. **38**, 464 (2005). DOI: 10.1016/j.spmi.2005.08.017.

[229] K. Okamoto, I. Niki, A. Shvartser, Y. Narukawa, T. Mukai, A. Scherer. *Surface-plasmon-enhanced light emitters based on InGaN quantum wells*. Nat. Mater. **3**, 601 (2004). DOI: 10.1038/nmat1198.

[230] J.-P. Richters, A. Dev, S. Múller, R. Niepelt, C. Borschel, C. Ronning, T. Voss. *Influence of metallic coatings on the photoluminescence properties of ZnO nanowires*. phys. stat. soli. (RRL) **3**, 166 (2009). DOI: 10.1002/pssr.200903176.

[231] Y. J. Fang, J. Sha, Z. L. Wang, Y. T. Wan, W. W. Xia, Y. W. Wang. *Behind the change of the photoluminescence property of metal-coated ZnO nanowire arrays*. Appl. Phys. Lett. **98**, 033103 (2011). DOI: 10.1063/1.3543902.

[232] A. Dev, J. P. Richters, J. Sartor, H. Kalt, J. Gutowski, T. Voss. *Enhancement of the near-band-edge photoluminescence of ZnO nanowires: Important role of hydrogen incorporation versus plasmon resonances*. Appl. Phys. Lett. **98**, 131111 (2011). DOI: 10.1063/1.3569951.

[233] R. J. Mendelsberg, J. V. Kennedy, S. M. Durbin, R. J. Reeves. *Unique photoluminescence from ZnO grown by eclipse pulsed laser deposition*. **27**, 1698 (2009). DOI: 10.1116/1.3137968.

[234] K. W. Liu, Y. D. Tang, C. X. Cong, T. C. Sum, A. C. H. Huan, Z. X. Shen, L. Wang, F. Y. Jiang, X. W. Sun, H. D. Sun. *Giant enhancement of top emission from ZnO thin film by nanopatterned Pt*. Appl. Phys. Lett. **94**, 151102 (2009). DOI: 10.1063/1.3116617.

[235] T. H. Gfroerer. *Photoluminescence in Analysis of Surfaces and Interfaces. Encyclopedia of Analytical Chemistry*. John Wiley & Sons, Ltd, 2006. DOI: 10.1002/9780470027318.a2510.

[236] J. Tersoff. *Schottky barrier heights and the continuum of gap states*. Phys. Rev. Lett. **52**, 465 (1984). DOI: 10.1103/PhysRevLett.52.465.

[237] S. Kuehn, S. Friede, S. Sadofev, S. Blumstengel, F. Henneberger, T. Elsaesser. *Surface excitons on a ZnO (000$\bar{1}$) thin film*. Applied Physics Letters **103**, 191909 (2013). DOI: 0.1063/1.4829466.

[238] Y. Dong, Z.-Q. Fang, D. C. Look, G. Cantwell, J. Zhang, J. J. Song, L. J. Brillson. *Zn- and O-face polarity effects at ZnO surfaces and metal interfaces*. Applied Physics Letters **93**, 072111 (2008). DOI: 10.1063/1.2974983.

[239] M. W. Allen, D. Y. Zemlyanov, G. I. N. Waterhouse, J. B. Metson, T. D. Veal, C. F. McConville, S. M. Durbin. *Polarity effects in the x-ray photoemission of ZnO and other wurtzite semiconductors*. Appl. Phys. Lett. **98**, 101906 (2011), 101906. DOI: 10.1063/1.3562308.

[240] K. Nishidate, M. Hasegawa. *Hydrogen-induced disruption of the ZnO (0001) polar surface*. Phys. Rev. B **86**, 035412 (2012). DOI: 10.1103/PhysRevB.86.035412.

[241] M. Kunat, U. Burghaus, C. Wöll. *Adsorption of hydrogen on the polar O-ZnO surface: a molecular beam study*. Phys. Chem. Chem. Phys. **5**, 4962 (2003). DOI: 10.1039/B307955D.

[242] V. E. Henrich, P. A. Cox. *The surface science of metal oxides*. Cambridge University Press, (1996).

[243] M. Schiek, K. Al-Shamery, M. Kunat, F. Traeger, C. Wöll. *Water adsorption on the hydroxylated H-(1x1) O-ZnO(000$\bar{1}$) surface*. Phys. Chem. Chem. Phys. **8**, 1505 (2006). DOI: 10.1039/B515418A.

[244] H. Noei, H. Qiu, Y. Wang, E. Loffler, C. Wöll, M. Muhler. *The identification of hydroxyl groups on ZnO nanoparticles by infrared spectroscopy*. Phys. Chem. Chem. Phys. **10**, 7092 (2008). DOI: 10.1039/B811029H.

[245] F. Träger, M. Kauer, C. Wöll, D. Rogalla, H.-W. Becker. *Analysis of surface, subsurface, and bulk hydrogen in ZnO using nuclear reaction analysis*. Phys. Rev. B **84**, 075462 (2011). DOI: 10.1103/PhysRevB.84.075462.

[246] X.-L. Yin, M. Calatayud, H. Qiu, Y. Wang, A. Birkner, C. Minot, C. Wöll. *Diffusion versus Desorption: Complex Behavior of H Atoms on an Oxide Surface*. Chem. Phys. Chem. **9**, 253 (2008). DOI: 10.1002/cphc.200700612.

[247] H. Ago, T. Kugler, F. Cacialli, W. R. Salaneck, M. S. P. Shaffer, A. H. Windle, R. H. Friend. *Work Functions and Surface Functional Groups of Multiwall Carbon Nanotubes*. J. Phys. Chem. B **103**, 8116 (1999). DOI: 10.1021/jp991659y.

[248] R. Heinhold, H.-S. Kim, F. Schmidt, H. v. Wenckstern, M. Grundmann, R. J. Mendelsberg, R. J. Reeves, S. M. Durbin, M. W. Allen. *Optical and defect properties of hydrothermal ZnO with low lithium contamination*. Appl. Phys. Lett. **101**, 062105 (2012). DOI: 10.1063/1.4739515.

[249] D. Kohl, M. Henzler, G. Heiland. *Low temperature sublimation processes from clean cleaved polar surfaces of zinc oxide crystals during first heating*. Surf. Sci. **41**, 403 (1974). DOI: 10.1016/0039-6028(74)90057-0.

[250] W. Göpel, J. Pollmann, I. Ivanov, B. Reihl. *Angle-resolved photoemission from polar and nonpolar zinc oxide surfaces*. Phys. Rev. B **26**, 3144 (1982). DOI: 10.1103/PhysRevB.26.3144.

[251] L. P. Martin, D. Dadon, M. Rosen, D. Gershon, K. I. Rybakov, A. Birman, J. P. Calame, B. Levush, Y. Carmel, R. Hutcheon. *Effects of anomalous permittivity on the microwave heating of zinc oxide*. J. Appl. Phys. **83**, 432 (1998). DOI: 10.1063/1.366735.

[252] B. Meyer, D. Marx, O. Dulub, U. Diebold, M. Kunat, D. Langenberg, C. Wöll. *Partial Dissociation of Water Leads to Stable Superstructures on the Surface of Zinc Oxide*. Angew. Chem. Int. Ed. **43**, 6641 (2004). DOI: 10.1002/anie.200461696.

[253] O. Dulub, B. Meyer, U. Diebold. *Observation of the Dynamical Change in a Water Monolayer Adsorbed on a ZnO Surface*. Phys. Rev. Lett. **95**, 136101 (2005). DOI: 10.1103/PhysRevLett.95.136101.

[254] D. J. Cooke, A. Marmier, S. C. Parker. *Surface Structure of (10$\bar{1}$0) and (11$\bar{2}$0) Surfaces of ZnO with Density Functional Theory and Atomistic Simulation*. J. Phys. Chem. B **110**, 7985 (2006). DOI: 10.1021/jp0564445.

[255] H. Lüth. *Solid Surfaces, Interfaces and Thin Films*. Springer-Verlag Berlin Heidelberg, (2010).

[256] C. M. Schlepütz, Y. Yang, N. S. Husseini, R. Heinhold, H.-S. Kim, M. W. Allen, S. M. Durbin, R. Clarke. *The presence of a (1x1) oxygen overlayer on ZnO(0001) surfaces and at Schottky interfaces*. J. Phys.: Condens. Matter **24**, 095007 (2012). DOI: 10.1088/0953-8984/24/9/095007.

[257] G. T. Williams. *Monitoring in-situ processing of solid surfaces with real-time x-ray photoelectron spectroscopy*. PhD thesis. The University of Wales, Aberystwyth, 2011.

[258] G. Zwicker, K. Jacobi. *Site-specific interaction of H2O with ZnO single-crystal surfaces studied by thermal desorption and UV photoelectron spectroscopy*. Surf. Sci. **131**, 179 (1983). DOI: 10.1016/0039-6028(83)90127-9.

[259] E. D. Batyrev, J. C. Heuvel. *Modification of the ZnO(0001)-Zn surface under reducing conditions*. Phys. Chem. Chem. Phys. **13**, 13127 (2011). DOI: 10.1039/C1CP20330D.

[260] R. Vidya, P. Ravindran, H. Fjellvåg. *Ab-initio studies on Li doping, Li-pairs, and complexes between Li and intrinsic defects in ZnO*. Journal of Applied Physics **111**, 123713 (2012). DOI: 10.1063/1.4729774.

[261] A. Y. Azarov, K. E. Knutsen, P. T. Neuvonen, L. Vines, B. G. Svensson, A. Y. Kuznetsov. *Impurity Sublattice Localization in ZnO Revealed by Li Marker Diffusion*. Phys. Rev. Lett. **110**, 175503 (2013). DOI: 10.1103/PhysRevLett.110.175503.

[262] K. Johansen, H. Haug, Ø. Prytz, P. Neuvonen, K. Knutsen, L. Vines, E. Monakhov, A. Kuznetsov, B. Svensson. *Li and OH-Li Complexes in Hydrothermally Grown Single-Crystalline ZnO*. Journal of Electronic Materials **40**, 429 (2011). DOI: 10.1007/s11664-010-1404-0.

[263] S. Z. Karazhanov, E. S. Marstein, A. Holt. *Hydrogen complexes in Zn deficient ZnO*. Journal of Applied Physics **105**, 033712 (2009). DOI: http://dx.doi.org/10.1063/1.3074304.

[264] K. M. Johansen, A. Zubiaga, F. Tuomisto, E. V. Monakhov, A. Y. Kuznetsov, B. G. Svensson. *H passivation of Li on Zn-site in ZnO: Positron annihilation spectroscopy and secondary ion mass spectrometry*. Phys. Rev. B **84**, 115203 (2011). DOI: 10.1103/PhysRevB.84.115203.

[265] M. Valtiner, M. Todorova, J. Neugebauer. *Hydrogen adsorption on polar ZnO(0001)-Zn: Extending equilibrium surface phase diagrams to kinetically stabilized structures*. Phys. Rev. B **82**, 165418 (2010). DOI: 10.1103/PhysRevB.82.165418.

List of Abbreviations

Constants

$\hbar$	reduced Planck Constant - $6.58212\,\mathrm{eV}\cdot\mathrm{s}$
$\lambda \cdot E$	Vacuum PL Conversion - $1239.84187\,\mathrm{eV}\cdot\mathrm{nm}$
k_B	Boltzmann Constant - $8.61733\,\mathrm{eV}\cdot\mathrm{K}^{-1}$

Abbreviations

(e, A^0)	Free to Bound Acceptor Transition
$\mathrm{D}^+\mathrm{X}$	Ionised Donor-Bound Excitons
$\mathrm{D}^0\mathrm{X}$	Neutral Donor-Bound Excitons
Ar-H_2	Forming Gas on Argon Basis ($95\,\%\,\mathrm{Ar} + 5\,\%\,\mathrm{H}_2$)
AS	Australian Synchrotron
AsR	As Received
BE	Binding Energy
C-V	Capacitance-Voltage Measurements
CBM	Conduction Band Minimum
CCD	Charged-Coupled Device
CL	Cathodoluminescence Spectroscopy
DAP	Donor Acceptor Pair Transition
DFT	Density Functional Theory
DLTS	Deep Level Transient Spectroscopy
EMA	Effective-Mass Approach

EPR	Electron Paramagnetic Resonance
FAT	Fixed Analyser Transmission Mode
FG	Forming Gas ($95\,\%\,N_2 + 5\,\%\,H_2$)
FWHM	Full Width at Half Maximum
HSA	Hemispherical Sector Analyser
HT	Hydrothermal Growth
IMFP	Inelastic Mean Free Path
J-V	Current Density-Voltage Measurements
KE	Kinetic Energy
LEED	Low Energy Electron Diffraction
Low-Li HT	Bulk ZnO with Low Lithium Concentrations
LVM	Local Vibrational Mode
PL	Photoluminescence Spectroscopy
PLD	Pulsed Laser Deposition
PMT	Photomultiplier Tube
SCVT	Seeded Chemical Vapour Transport
SEM	Scanning Electron Microscopy
SIMS	Secondary Ion Mass Spectrometry
SX	Surface Exciton
SXR	Soft X-ray Beamline
SXRD	Surface X-ray Diffraction
TAS	Thermal Admittance Spectroscopy
TDH	Temperature-Dependent Hall Effect
TDS	Thermal Desorption Spectroscopy
UHV	Ultra-High Vacuum, $p \leq 10^{-9}\,\mathrm{mbar}$

VB	Valence Band
XPS	X-ray Photoelectron Spectroscopy

Variables

λ	Wavelength
λ_{IMFP}	Inelastic Mean Free Path
ω	Angular Frequency
ϕ	Work Function
σ	Conductivity or Apparent Trap Cross Section
ε_0	Vacuum Permittivity
ε_{s}	Specific Permittivity
ϱ	Resistivity
C	Capacitance
E	Energy
e	Elementary Charge
E_{A}	Acceptor Binding Energy
E_{C}	Conduction Band Minimum
E_{D}	Donor Binding Energy
E_{F}	Fermi Energy
E_{g}	Bandgap
E_{loc}	Localisation Energy
E_{V}	Valence Band Maximum
f	Frequency
G	Conductance
m_0	Electron Rest Mass in Vacuum
m_e^*	Effective Electron Mass

n	Free Carrier Concentration
T	Temperature
t	Time
V	Applied Voltage
V_{bi}	Build-in Potential
w	Depletion Region Width
$\mathrm{R_p}$	Projected Range